Politecnico di Torino

ScuDo
Scuola di Dottorato ~ Doctoral School
WHAT YOU ARE, TAKES YOU FAR

Doctoral Dissertation
Doctoral Program in Civil and Environmental Engineering (38^{th}cycle)

Integrated Monitoring and Eco-Morphodynamic Modeling of Coastal Dunes

By

Davide Demichele

******

Supervisor(s):
Prof. Carlo Vincenzo Camporeale, Supervisor
Prof. Marco Piras, Co-Supervisor
PhD Elena Belcore, Co-Supervisor

Doctoral Examination Committee:
Prof. Orencio Durán Vinent, Texas A&M University, United States of America
Prof. Edyta Wozniak, Space Research Centre of the Polish Academy of Sciences, Poland
Prof. Giovanni Besio, University of Genoa, Italy
Prof. Vincenzo Nava, Polytechnic of Turin, Italy

Politecnico di Torino
2026

Declaration

I hereby declare that, the contents and organization of this dissertation constitute my own original work and does not compromise in any way the rights of third parties, including those relating to the security of personal data.

Davide Demichele
2026

* This dissertation is presented in partial fulfillment of the requirements for **Ph.D. degree** in the Graduate School of Politecnico di Torino (ScuDo).

Acknowledgements

Firstly, I am deeply grateful to my supervisors, Carlo, Marco, and Elena, for mentoring me throughout these three PhD years, which passed incredibly fast. Their guidance gave me the opportunity to grow both professionally and personally.

I would also like to thank all my wonderful colleagues in the department, and especially my beloved office mates of the Ammezzato, where I found not only colleagues but also sincere and dear friends.

Lastly, I thank my family for supporting me in all my life choices, and most importantly, my partner Giulia, for her constant love, patience, and encouragement.

Abstract

Coastal dunes are extremely dynamic ecotones where marine and land processes merge together. They provide essential ecosystem services, including biodiversity conservation, natural protection against coastal hazards, and support for local economies. Despite their importance, dune systems worldwide are increasingly threatened by climate change, shoreline erosion, invasive species, and human pressures, leading to degradation of their protective and ecological functions. Effective management and restoration of coastal dunes therefore require improved understanding of the co-evolution of biotic and abiotic dynamics across multiple spatial and temporal scales.

This PhD thesis develops a fine-scale integrated monitoring and predictive framework for coastal dunes, with a particular emphasis on vegetation as a key indicator and driver of dune dynamics.
The research addresses critical gaps in long-term monitoring and in the integration of geomatics-derived observations with physically based hydrodynamic and eco-morphodynamic models, with the sandy dunes on the coast of Migliarino–San Rossore–Massaciuccoli Regional Park serving as a test bed.

The first part of the thesis focuses on the monitoring phase, evaluating the feasibility and effort required to construct an integrated, multi-temporal dataset combining airborne observations (e.g. RGB and multispectral optical imagery, LiDAR point clouds), ground-based measurements (e.g. vegetation surveys and ground control points), and marine data (e.g. multibeam-derived bathymetric point clouds).

The processing and analysis of these heterogeneous datasets provide a quantitative and qualitative assessment of coastal dune dynamics, allowing the investigation of the mutual interactions among geomorphology, hydrodynamics, and vegetation in controlling coastal dune evolution.

Finally, the work converges on the formulation of a predictive eco-morphodynamical model, addressing the specific task of estimating the post-storm recovery time of dunal vegetation, a process that remains poorly understood and insufficiently explored in the scientific literature. While the proposed model is still in its infancy and remains to be fully explored and generalized, it lays the groundwork for future developments and has the potential to significantly support more effective coastal dune restoration and conservation strategies.

Contents

List of Figures

List of Tables

Chapter 1

Introduction

Coastal dunes stand as vital ecosystems that play a pivotal role in maintaining coastal resilience and supporting diverse forms of life [1–3]. As nature's protective barrier between land and sea, they reserve biodiversity, and mitigate the impacts of climate change-induced events [4–6].

Beyond the intrinsic value of the natural heritage, coastal dunes foster biodiversity and promote ecological balance by hosting intricate ecosystems teeming with flora and fauna specialized to survive to harsh coastal conditions [7]. For example, sand-burial tolerant species like *Ammophila arenaria* (or beachgrass) increases sand accumulation, stabilizes sand and prevents erosion [8–10], whereas species less tolerant to burial, such as *Helichrysum stoechas*, are considered to be important in stabilizing low-elevation backdune areas [11] contributing to the overall health of coastal ecosystems.

Moreover, coastal dunes act as natural buffers against the impact of coastal storms, hurricanes, and tidal surges, protecting inland communities and infrastructure from severe damage. This protective function is particularly critical considering that approximately 40% of the global population lives within 100km of the coastline, and about 10% lives within 5km [12].

Their ability to dissipate wave energy and reduce coastal flooding not only protects human lives and property, but also preserves invaluable coastal habitats and cultural heritage sites. The resilience of coastal dunes in the face of relentless natural disturbances underscores their indispensable role in enhancing coastal resilience and adaptation strategies. Furthermore, coastal dunes hold immense economic value by supporting a wide array of job opportunities and recreational activities, thereby

enhancing regional economies and local tourism industries [13].
However, despite their ecological and socioeconomic importance, the dunes are subjected to several threats, from habitat degradation due to invasive species proliferation [14] to unsustainable human activities joint with climate change-induced alterations like coastal erosion which is estimated to impact about 70% of the Earth's sandy beach environments and around 42% of Italian sandy coasts [15, 16].
The degradation of coastal dune ecosystems not only compromises their ability to provide crucial ecosystem balance but also increases coastal vulnerability to erosion, flooding, and habitat loss.

Restoration interventions often become necessary where the functioning of the dune has been severely compromised. Such interventions may involve stabilizing or re-vegetating dunes, but also, in some cases, promoting dune mobility (e.g., through de-vegetation) depending on the natural state of the system and restoration objectives [17, 16]. Due to the intrinsic complexity of dune ecosystems and their variability across climates and regions, restoration approaches need to be adapted to local conditions and cannot rely on a single universal methodology.

Sustainable management, therefore, requires a multi-scale understanding of coastal processes—from short-term erosion and vegetation feedbacks to long-term shoreline evolution and regional-scale ecosystem transitions [16, 18–20]. This understanding depends on the integration of geological, physical, and ecological knowledge, supported by robust historical and spatial records of dune morphology, vegetation distribution, and shoreline change. Unfortunately, most beaches worldwide are not regularly monitored, limiting our ability to forecast future change and design effective adaptation strategies.

1.1 State of the Art and Research Gaps

Coastal dunes can recover and grow naturally when sediment supply, hydrodynamic forcing, and vegetation dynamics are favorable [21, 22]. However, climate-driven sea-level rise, changing storm patterns, and coastal development are increasing the frequency and severity of erosion and flooding hazards [23–26]. Exposure to these hazards is commonly assessed by comparing storm-induced total water levels to dune morphology metrics derived from airborne surveys [27, 28]. For instance, LiDAR surveys provide high spatial resolution at regional scales and are widely

used for flood mapping, dune-grading assessments, and coastal change analysis [29–33]. However, data acquisition is often episodic—typically following major storms—resulting in snapshots that do not fully capture the seasonal or interannual evolution of dunes.

Other monitoring techniques, such as RTK-GPS surveys, terrestrial laser scanning, and UAV photogrammetry, offer high resolution and operational flexibility [34]. However, their deployment over extensive coastlines is limited by cost and logistics, and infrequent data collection risks missing key phases of erosion or recovery. These limitations affect both hazard assessments and predictive modeling.

Advances in understanding dune evolution have benefited from studies focused on specific morphological units (nearshore, beach, foredune) and from integrated eco-morphodynamic approaches linking hydrodynamics, sediment transport, and vegetation processes. These insights have informed a range of modeling approaches. Conceptual and empirical models describe general trajectories of beach-dune evolution [35, 36, 27, 37]. Reduced-complexity models—such as DUBEVEG [38], the model of Zhang et al. [39], or the Cross-Shore (CS) model [40]—simulate dune-beach dynamics using rule-based systems that are computationally efficient for long-term and large-scale analysis.

More recently, process-based models have emerged, coupling nearshore hydrodynamics with dune evolution (e.g., Windsurf [41], XBeach-Duna [42]). These models offer the potential to predict coastal change holistically and support climate-change adaptation by testing management scenarios [43]. Nonetheless, their performance must be evaluated across diverse environments, and many models remain constrained by limited datasets, site-specific tuning, and high computational demands.

On the management side, numerous international initiatives—such as REST-COAST [44], and multiple LIFE projects (e.g., Blue Natura, SOSS DUNES [45])—aim to protect and restore coastal ecosystems. The recent EU Restoration Law further supports such efforts, with networks such as MEDPAN [46] promoting coordinated action. A persistent challenge, however, is the need for restoration methodologies capable of accounting for the complex ecological, physical, and socio-economic interactions that characterize coastal zones, together with uncertainties in future climate projections.

The current state of knowledge reveals several persistent gaps:

1. Insufficiently unified process-based frameworks. Many models emphasize wind-driven sand transport while underrepresenting processes such as precipitation, groundwater, tidal inundation, and environmental stochasticity. Eco-morphodynamic models are often deterministic and neglect probabilistic forcing.

2. Limited long-term monitoring programs. Multi-year datasets documenting dune evolution or evaluating restoration effectiveness remain rare, hindering understanding of mid- to long-term trends.

3. Weak integration between geomatics and mechanistic modeling. Despite the growing availability of UAV, remote-sensing, and machine-learning-derived products, these data streams are seldom assimilated into physically based models driven by waves, run-up, and wind.

4. Sparse and heterogeneous marine and coastal observations. Differences among sensors, acquisition methods, and spatial coverage reduce interoperability and limit their usefulness for both science and coastal management.

5. Challenges in cross-scale integration. Current approaches struggle to link fine-scale, short-term processes with broader morphological evolution spanning decades or larger spatial domains.

Overall, more comprehensive approaches are needed—ones that integrate geomorphology, ecology and climate forcing; incorporate stochasticity; and support both restoration and management. Emerging frameworks such as digital twins offer promising opportunities to testing alternative scenarios [47, 48], but many models remain site-specific and insufficiently validated.

1.2 Research Questions and Dissertation Outline

This thesis contributes to the development of a monitoring and predictive framework for coastal dunes (Fig. 1.1), using vegetation as a key indicator of dune dynamics. The research focuses on three dune systems within the Migliarino–San Rossore–Massaciuccoli Regional Park, monitored between 2021 and 2025 and characterized by different morphologies, exposure to environmental forcing, and degrees of anthropogenic pressure.

Here, we specifically address research gaps 2 and 3 through the following questions:

- What monitoring frequency, spatial resolution, and combination of morphological, hydrodynamic, and ecological indicators are required to assess mid- to long-term coastal dune dynamics?
- How can geomorphological and ecological information be processed and validated for effective assimilation into physically based eco-morphodynamic models, and which modeling architectures best support this integration to improve predictions under different meteo-hydrological forcing conditions?

The outline of the thesis is reported below.

Chapter 2, titled *'Data Collection and Processing'*, describes extensively the study site, —from physiological, ecological and climatic standpoints— field measurements techniques and data processing methods, including hydrodynamic modeling and geomorphological analysis.

Chapter 3, titled *'Pattern Analysis of Coastal Dune Vegetation'* present a detailed spatial analysis of coastal vegetation species, discussed in the following publication:

Demichele, D., Belcore, E., Piras, M., Camporeale, C. Species-by-species pattern analysis of coastal dune vegetation. *Journal of Geophysical Research: Biogeosciences* 130.2 (2025): e2024JG008419. https://doi.org/10.1029/2024JG008419

Chapter 4, titled *'Recovery Time of Coastal Dune Vegetation'* describes a novel theoretical framework to address the post-storm recovery time of coastal dune vegetation, using a stochastic approach.

Finally, chapter 5 synthesizes the key findings and outlines directions for future research.

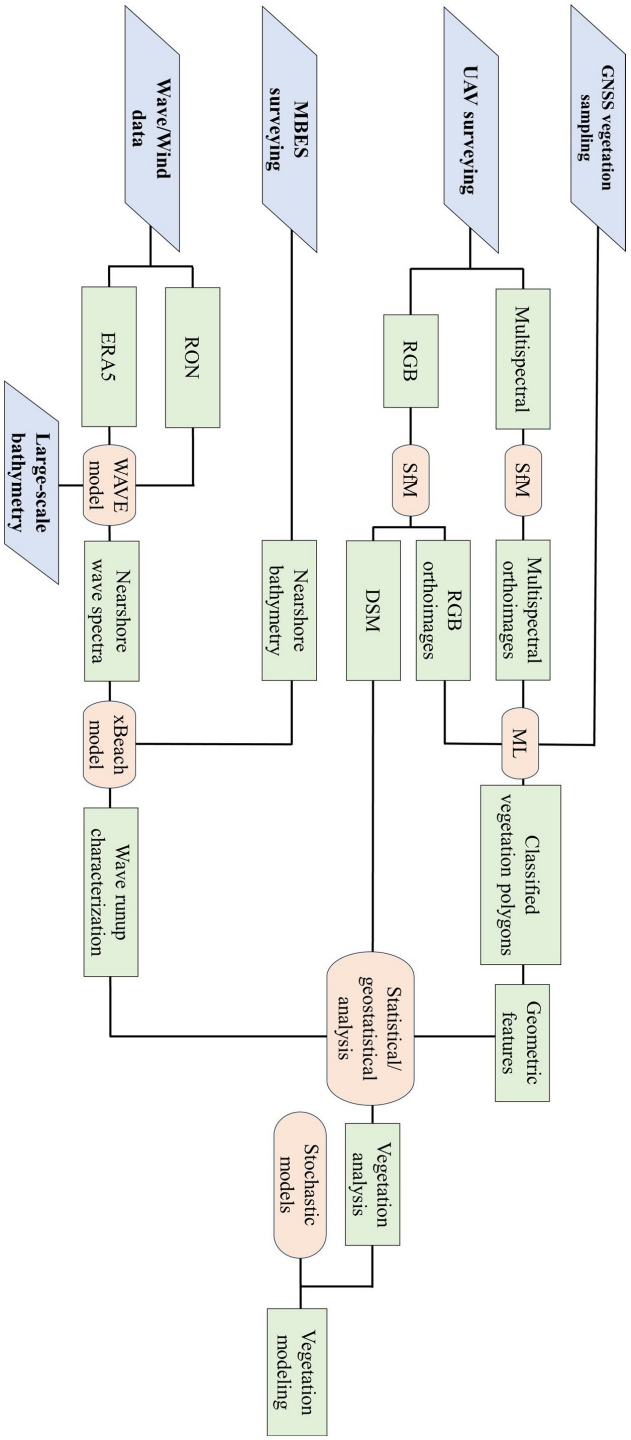

Fig. 1.1 Workflow of the proposed multi-disciplinary approach for coastal dune vegetation monitoring and modeling. Blue boxes represent input data, acquired in the field or retrieved by other datasets; red boxes represent processing operations; green boxes represent output products.

Chapter 2

Data Collection and Processing

2.1 Case Study

The study site is the Migliarino-Sanrossore-Massacciuccoli Regional Park (Fig.2.1a-b), covering about 30km of the Tuscan coastline between Livorno and Viareggio encompassing approximately 394 hectares of dune habitats that have been mapped and classified according to EU Directive 92/43/EEC . In 2004, the $23,000$ hectares park has also been designated as a Biosphere Reserve by UNESCO [49] for its ecological and landscape value of primary importance.
During the last decades the physical and biological state of the park was subject to constant monitoring by research groups [50–53] and many interventions of habitat restoration have been successfully attempted [54].
Furthermore, the park served as a pilot site for integrated monitoring approaches combining geological, biological, and technological methods including UAV flights and wireless sensor networks to assess coastal dune evolution [55]. Agricultural activities within the park boundaries cover approximately $1,500$ hectares of utilized agricultural area, with farming practices showing improved environmental sustainability over recent decades, including reduced fertilizer use and decreased industrial crop production [56]. The park has been utilized as a case study for applying Life Cycle Assessment methodologies to analyze territorial sustainability, particularly regarding biodiversity and environmental accessibility [57].
The dune field, in particular, although having a limited extension, is a scenario of incredible biological richness and diversity and sadly exhibits all the symptoms of

climate change and anthropic pressure (e.g. coastal erosion, marine litter deposition, disruption by over-trampling, human-induced dune blowout, sand removal for construction purposes, etc.), even in the 11km of coastline subjected to protective restrictions [54].

We focused our attention on three main areas along the coastline (A1, A2 and A3 shown in fig.2.1), where measurement campaigns have been undertaken from 2021 to 2025 -as we will discuss later on- plus an extra area (A2-bis) right next A2, where wind measurements have been carried out in 2025. In total, we covered a coastal stretch of about 1.6km in length and approximately 400m in the cross-shore direction, enough to include the entire dune system that is composed of the shoreline, the foredune, the backdune slack, the fixed dune and part of the inland pine tree forest (Fig.2.1c-e).
The first area (Fig.2.1c) is located in correspondence of Lecciona Beach ($43°49'51''N$, $10°15'11''E$), a very popular destination for seaside tourism and watersports. The strong impact of anthropic activities prevented the proliferation of psammophyte species, so there is no foredune in this area, instead, there is a series of parallel embryonic dunes, populated by evergreen shrubs and junipers scattered quite homogeneously. The second and third areas (Fig.2.1d-e) are located to the south Serchio River's mouth ($43°46'05''N$, $10°16'23''E$) and to the south of Morto Nuovo River ($43°43'48''N$, $10°16'41''E$), respectively, and they lie inside the restricted area of the park, with little or no direct anthropic impact, although loads of marine litter and woody debris transported by longshore currents can be found on the beach. In these areas, there are the richest communities of psammophyte species and the tallest dunes, which can reach up to 5m high. Moreover, the shore is not very steep (less than 10) and thin (less than 20m at low tide), accentuating the effect of storm-driven overwash and wind erosion on the seaward slope of the foredune, significantly affecting the vegetation zonation.
In all three areas, exotic species like *Yucca gloriosa*, become invasive, displacing local communities, hindering their evolution towards mature stages [58].

2.1.1 Geographical and Geomorphological Setting

The Migliarino-San Rossore-Massaciuccoli Regional Park is located along the coastal plain of northern Tuscany, between Livorno and Viareggio. This low-lying coastal

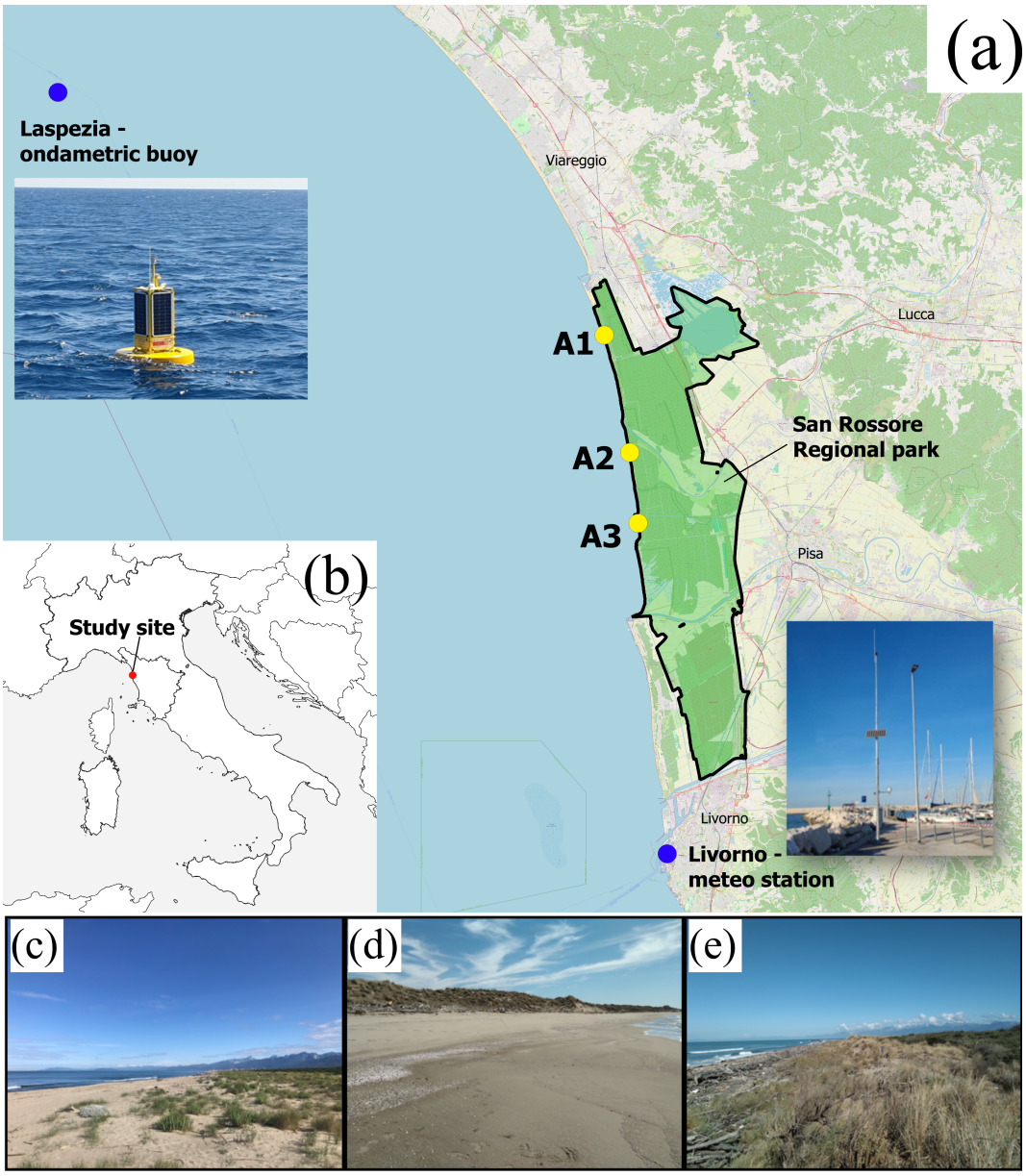

Fig. 2.1 Location of Sanrossore-Migliarino-Massacciuccoli Regional Park (Tuscany, Italy). a)Map of tuscanian coast stretch within the park. Are highlighted the positions of the three study areas (yellow dots) and the nearest *Rete Mareografica Nazionale* gauge stations (blue dots). Pictures of the La Spezia ondametric buoy and Livorno meteo station are provided; b)Location of study site; c-d)Vegetated foredunes in A1 (c); A2 (d); A3 (e). The photos were taken by the Author during a field survey

sector owes its geomorphological configuration primarily to the sedimentary supply of the Arno River of about $1,524,000$t/yr, with a more limited contribution from the Serchio River, $23,000$t/yr [59]. The Arno has historically acted as the dominant control on coastal dynamics, generating a bidirectional littoral drift: southwards towards Livorno and northwards as far as Marina di Pietrasanta, where it converges with the opposite sediment transport derived from the Magra River [60]. A significant portion of the study area corresponds to the Arno delta, which began to develop approximately $2,500$ years ago in response to enhanced sediment input linked to widespread deforestation within the drainage basin [61]. Its morpho-sedimentary evolution, characterized by alternating phases of progradation and erosion, has been documented using satellite imagery [62] and LiDAR data [63]. These studies revealed a close relationship between demographic changes in the Arno basin and delta dynamics: periods of rapid accretion led to the formation of numerous low dune ridges, whereas slower progradation favoured the vertical growth of fewer but higher

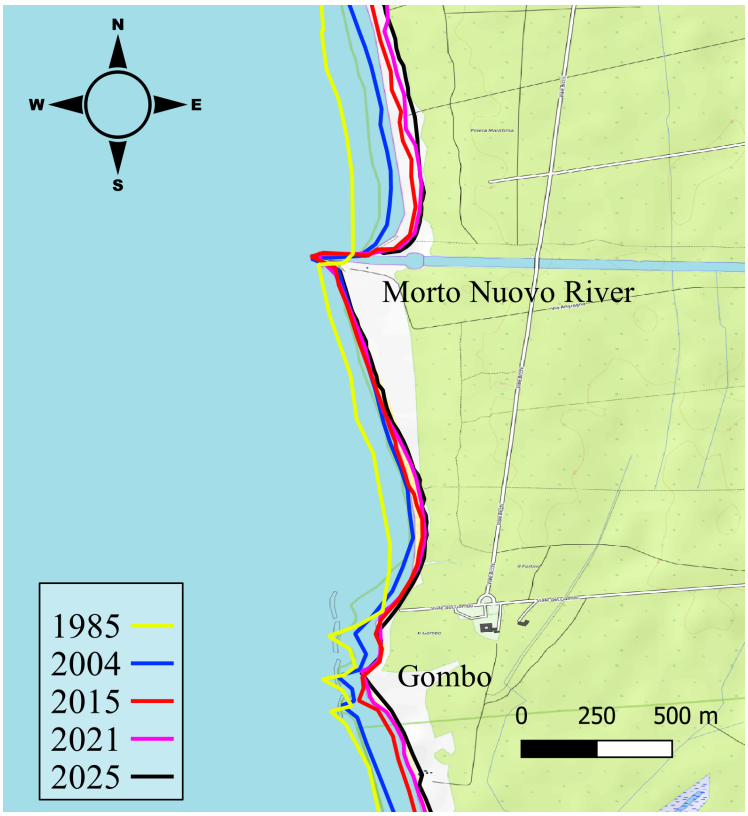

Fig. 2.2 Coastal erosion around Morto Nuovo River from 1985 to 2025. Shorelines have been derived from Landsat satellite imagery.

ridges. At present, the dune system reaches a maximum width of about 5.8 km, with ridge elevations typically ranging between 2 and 3m, and locally exceeding 8 m where coastal stability allowed vertical accretion in accordance with Psuty's conceptual model [64, 65].

Landward of the dune belt lies a depressed zone, with elevations from -3 to $+1$m a.s.l. [66]. This sector includes the Lake and Marsh of Massaciuccoli, a wetland complex of ca. $12,100$ ha extending between the Camaiore canal to the north and the Serchio River to the south. Together with the Fucecchio Marsh, it represents the last remnant of the once widespread wetlands that characterized the Tuscan coastal plain until the early modern period [67]. Archaeological evidence indicates human presence in this area since the Neolithic [68].

Coastal erosion became a major issue from the late 19th century onwards, initially affecting the cuspate delta and subsequently propagating along the shoreline [69]. The first coastal defences were built in the early 20th century around Marina di Pisa, where urban settlements were at risk. Today, the two-kilometre-long urban frontage is protected by a dense system of hard defences consisting of shore-parallel and shore-connected breakwaters, groynes and revetments, with a structural density of approximately 2.3km of barriers per km of coastline [70]. In contrast, the northern lobe of the delta, left unprotected due to the absence of settlements, has undergone retreat of about $1,300$m since 1881, leading to significant asymmetry at the river mouth and requiring the construction of a training wall to prevent channel migration and siltation [71]. Additional interventions were implemented at Gombo, where severe erosion threatened the presidential estate: five detached breakwaters were built between 1962 and 1965 and later modified in 1985; these structures promoted beach widening but also triggered erosion downdrift [72]. Similar engineering works were carried out at the mouth of the Fiume Morto Nuovo canal, where jetties built to avoid siltation disrupted the northward sediment drift. While favouring local sediment accumulation, they accelerated erosion in the adjacent downdrift sector, where retreat rates now reach about 5m/yr (Fig.2.2) [73]. At Le Lame, a sector where storm surges frequently caused saline intrusion into freshwater wetlands, nine groynes were constructed between 2001 and 2003, four of which extend offshore as submerged barriers. This work, combined with the nourishment of $65,000$m^3 of gravel, temporarily reversed the erosional trend and stabilized the shoreline [71]. A 2009 intervention involved the construction of an artificial tombolo using geotextile tubes, designed to connect the Gombo breakwaters to the mainland and prevent the

development of a wide embayment between the Arno mouth and the jetties of the Fiume Morto Nuovo canal [54, 13].

2.1.2 Climatic Characterization

Available Data

Wind and wave data were obtained from the open database of the National Wave and Tide Gauge Network (Rete Mareografica Nazionale), which is operated by the Italian Institute for Environmental Protection and Research (ISPRA).
Wind measurements were provided by the Livorno meteorological station, located within the Porto Mediceo harbor ($43°32'46.63''N$, $10°17'57.62''E$), approximately 20 km from the study site (Fig. 2.1a). For this work, we analyzed a 15-year time series of wind speed and direction, spanning from January 2010 (the earliest available record) to September 2025, with a temporal resolution of one measurement every ten minutes.
Wave parameters were obtained from the La Spezia wave buoy, deployed offshore of Porto Venere harbor at an average water depth of 85 m ($43°55'45''N$, $9°49'40''E$), approximately 40 km from the study area (Fig. 2.1a). We used a 4-year time series of significant wave height (H_s), direction and peak wave period (T_p), from May 2021 to September 2025 recorded at a frequency of two measurements per hour.

Winds

Research on Mediterranean coastal wind patterns has revealed complex seasonal variations driven by the mutual interaction of synoptic-scale dynamics and localized phenomena. Tyrrhenian coastlines, in particular, are characterized by three distinct wind patterns: two synoptic-dominated patterns (i.e., regulated by large-scale atmospheric dynamics, such as Atlantic perturbations) with persistent SW-to-NE winds (e.g., *Libeccio* wind), and a sea breeze regime (e.g., diurnal oscillations driven by land–sea thermal contrasts) [74, 75]. Seasonal characteristics show synoptic circulation dominates in winter, spring, and autumn with high ventilation conditions, while summer features stronger, more frequent sea breeze regimes creating intense air recirculation. Summer conditions produce maximum land-sea temperature differences during daytime, generating strong diurnal breezes but weak nocturnal breezes,

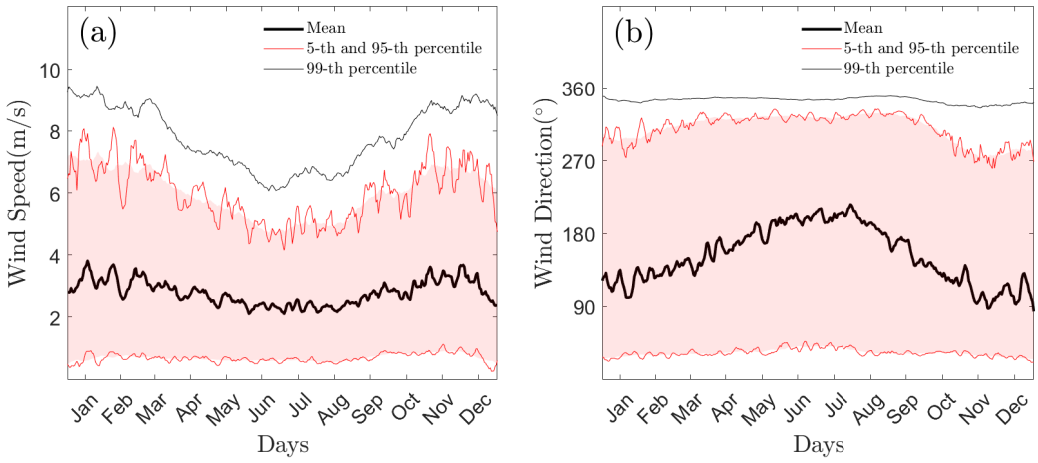

Fig. 2.3 Annual cycle of wind (a) speed and (b) direction. Daily mean values (thick black lines), 5-th and 95-th percentiles (red lines) and 99-th percentiles are portrayed. The shaded area highlights the daily interval between 5-th and 95-th percentiles.

while winter shows the opposite pattern with intense nocturnal breezes [74, 76].

The local wind regime in the study site region exhibits a marked seasonal variability, both in terms of intensity and direction. As shown in Figure 2.3a, the annual cycle of wind speed is characterized by lower mean values during late spring and summer (approximately $2-3$m/s), with a gradual increase in fall and maximum values in winter, when daily means occasionally exceed $3.5-4$ m/s and extreme events (represented by 99-th percentiles) can surpass 9m/s. Wind direction (Fig.2.3b) also displays a clear seasonal modulation: during winter and fall, NE winds dominate, often associated with synoptic-scale circulation, while during spring and summer the pattern shifts towards multi-modal flows, mainly NE-W winds (e.g., *Levante* wind) in summer (Fig.2.4c), reflecting the prominence of sea-land breeze systems, and NE-W-S winds during spring season.
The seasonal wind roses (Fig.2.4) further confirm this duality, with the spring and summer season showing a bimodal distribution between westerly sea breezes and weaker easterly land breezes (Fig.2.4b,c), whereas the fall and winter regime is more strongly aligned with northeasterly flows of higher intensity (Fig.2.4a,d). This seasonal transition highlights the interplay between large-scale atmospheric circulation and local thermally driven processes, aligning with existing literature.

Waves

The northern Tyrrhenian Sea basin presents a complex geomorphology and heterogeneous coastal stretches, exerting major control on the hydrodynamics and on the wave processes. The closed geomorphological shape of the basin strongly influences wind exposure, fetch lengths, and the development of mesoscale coastal circulation structures [77, 78], thereby conditioning air–sea interaction processes and exerting a major influence on wave characteristics [79, 80].

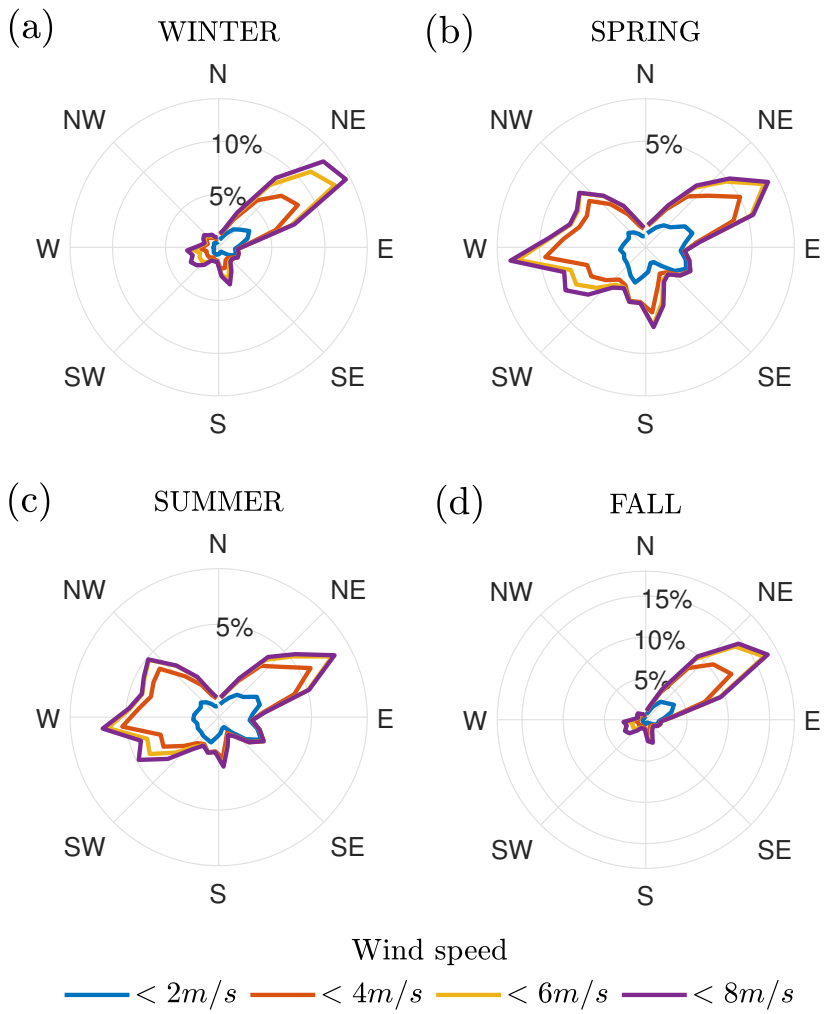

Fig. 2.4 Seasonal wind-roses of (a)winter, (b)spring, (c)summer and (d)fall. The radial coordinates represents the percentage of sampled data along each of the 32 angular bins. Contour lines are percentages of wind records below 2, 4, 6, 8m/s.

The waves analyzed in this study correspond to offshore deep-water conditions, rather than shallow-water waves close to the shoreline. As will be further discussed, wave height, period, and direction undergo systematic modulation during propagation towards the coast due to refraction processes induced by seabed interaction with the orbital motion of water particles [81–83]. Their coastal impact (e.g., wave runup) is further modulated by tidal variability. The tidal regime along the northern Tuscan coast is microtidal, with an astronomical tidal range of approximately 35 cm, and additional atmospheric contributions ranging from $+20$ to -18 cm, depending on local pressure anomalies in this sector of the Ligurian Sea [84].

The annual cycle of significant wave height H_s (Fig.2.5a) exhibits a marked step-like reduction around mid-April, at the onset of spring, with average values decreasing from approximately 1m to 0.5m, followed by a gradual increase throughout

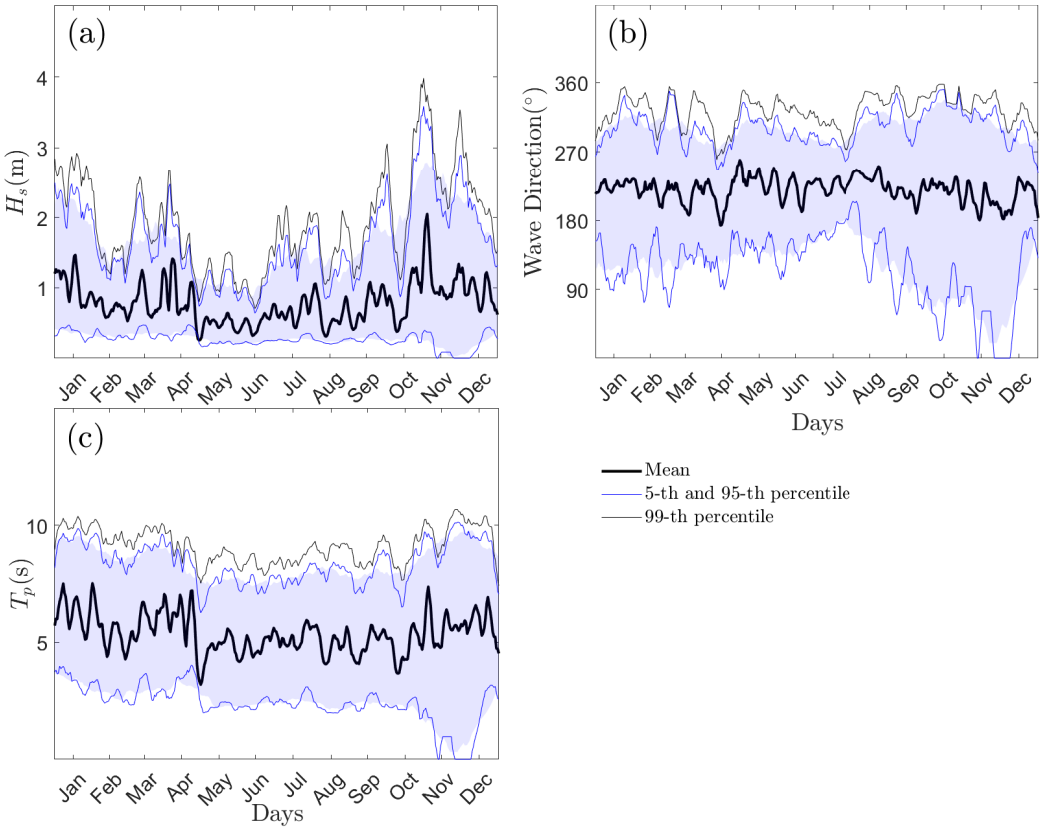

Fig. 2.5 Annual cycle of wave (a) significant height, H_S, (b) incoming direction direction and (c) peak period, T_p. Daily mean values (thick black lines), 5-th and 95-th percentiles (blue lines) and 99-th percentiles are portrayed. The shaded area highlights the daily interval between 5-th and 95-th percentiles.

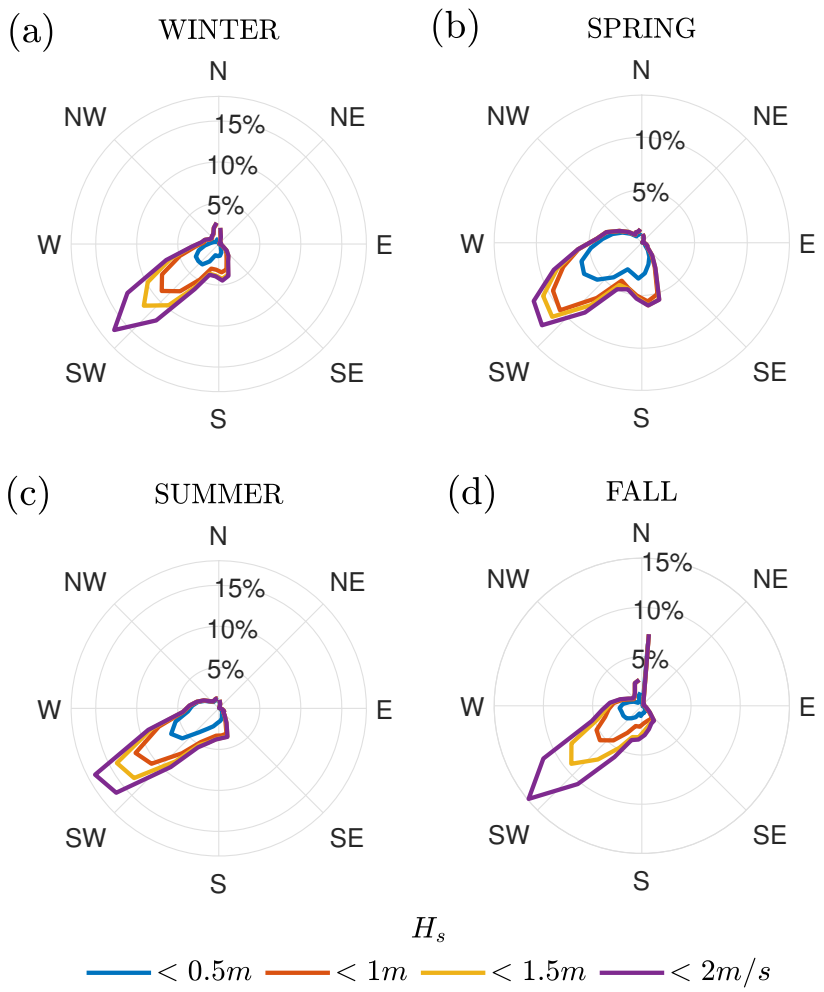

Fig. 2.6 Seasonal wave-roses of (a)winter, (b)spring, (c)summer and (d)fall. The radial coordinates represents the percentage of sampled data along each of the 32 angular bins. Contour lines are percentages of H_S records below 0.5, 1, 1.5, 2m.

the rest of the year. The highest mean H_s values occur during winter and autumn, consistent with enhanced storminess, and extreme events can reach up to 4 m. It is important to note, however, that the peaks identified in the bivariate histogram (Fig.2.7) correspond to *modal* values of H_s and T_p, which do not necessarily coincide with the seasonal mean values shown in Fig.2.5.

The mean wave direction (Fig.2.5b) is relatively stable throughout the year, predominantly from the southwest. Nonetheless, an increase in directional variability is observed during summer and autumn. This pattern is consistent with the analysis of wind data, which indicates a transition from a unimodal northeasterly regime

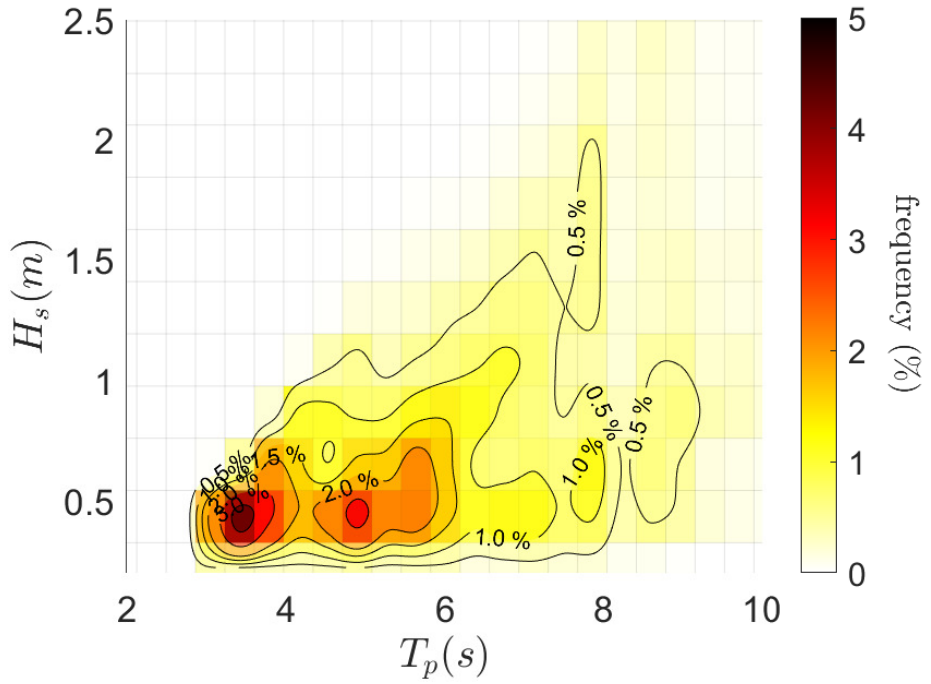

Fig. 2.7 Joint probability density function of H_s and T_p at La Spezia ondametric buoy.

in winter to a bimodal NE–W configuration in spring and summer (Fig.2.3b and Fig.2.4). Wave roses, however, highlight a somewhat different seasonal evolution: from unimodal SW waves in winter (Fig.2.6a) to bimodal SW-S waves in spring (Fig.2.6b), before returning to predominantly unimodal regimes during summer and autumn (Fig.2.6c,d). A secondary but narrow peak from the north is also detected in autumn (Fig.2.6d). The prevalence of SW-directed waves is coherent with the dominant NW wind regime in the region, confirming that local wind forcing represents the primary generation mechanism for waves at this site.

The temporal evolution of peak wave period T_p (Fig.2.5c) mirrors that of H_s, with a stepwise decrease in mid-April (from ~ 6 s to ~ 5s), followed by a gradual increase during the subsequent months. Despite the relatively short time series (four years), the interannual variability of daily T_p cycles, as indicated by the spread of the distribution (blue band in Fig.2.5c), remains nearly constant across the annual cycle.

The joint distribution of H_s and T_p (Fig.2.7) identifies two dominant modal regimes, both associated with the highest contributions to wave power ($P \propto H_s^2 T_p$; [85]), centered at $\{T_p, H_s\} = \{3.5s, 0.4m\}$ and $\{4.9s, 0.4m\}$.

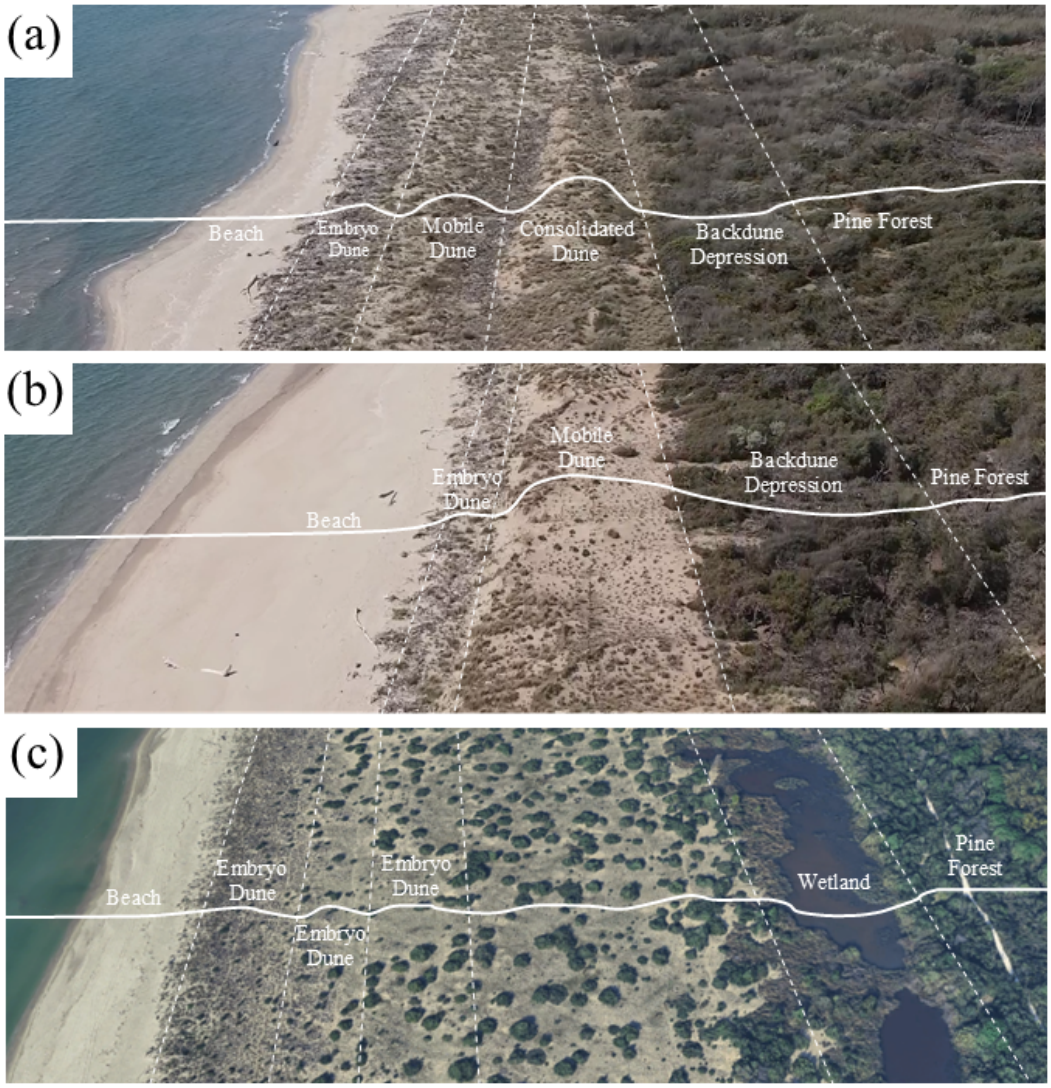

Fig. 2.8 Examples of morphological units successions along in three different locations along the coastline of San Rossore Park: (a)*Spiaggia del Serpente* ($43°46'41''N$, $10°16'7''E$); (b)*La casermetta* ($43°46'23''N$, $10°16'11''E$); (c)*Spiaggia della Lecciona* ($43°54'22''N$, $10°17'05''E$). Perpendicular transects representing the dune morphology characteristic of each location are marked with white lines, while the dashed mark the boundaries between each morphological unit.

2.1.3 Vegetation Characterization

The dune systems in San Rossore Park host the most significant examples of psammophilous vegetation in northern Tuscany, embedded in a highly dynamic context affected by long-term erosive processes and anthropogenic pressures [86]. Vegeta-

tion follows a clear zonation pattern parallel to the shoreline, reflecting the typical successional dynamics of Mediterranean sandy coasts, but here strongly altered by coastal retreat and human disturbance [87]. Along different stretches of the coastline, diverse sequences of morphological units can be observed, leading to distinct phytocoenotic successions (Fig.2.8). An overview of the typical plant communities associated with each main physiognomic unit of the dunal landscape within the park is here presented.

The pioneer communities belong to the *Salsolo kali - Cakiletum maritimae*, dominated by annual halonitrophilous species such as *Cakile maritima*, *Salsola kali*, *Atriplex latifolia* and *Euphorbia paralias* which colonize organic deposits on the beach. These ephemeral communities represent the initial stage of the psammophilous succession [88, 86].

At the base of the embryonic dunes, perennial communities occur, dominated by *Spartina juncea* and *Agropyron junceum* (*Elymo farcti - Spartinetum junceae*), often accompanied by stands of *Otanthus maritimus* and *Eringium maritimum*, typical of unstable sandy mounds [89].

Moving inland, the mobile dunes are colonized by the *Echinophoro spinosae - Ammophiletum arundinaceae*, with *Ammophila littoralis* and *Echinophora spinosa* as key species stabilizing the sandy substrates [90].

Consolidated dunes host chamaephytic communities dominated by *Helichrysum stoechas*, ecologically related to the *Pycnocomo rutifolii - Crucianelletum maritimae*, although here lacking *Crucianella maritima*, an indication of degradation and fragmentation of the dune series [91, 89]. In mosaic with these communities, therophytic grasslands dominated by *Vulpia membranacea* (*Sileno coloratae - Vulpietum membranaceae*) frequently occur. Their presence is considered an indicator of disturbance and regression of the dune dynamics, often linked to trampling and coastal erosion [88, 86].

The interdunal and back-dune depressions host halophilous and hygrophilous communities. Among them are the *Suaedo maritimae - Salicornietum patulae*, pioneer stands dominated by succulent Chenopodiaceae; the halophilous rush meadows *Juncetum acuti* dominated by *Juncus acutus*; and the *Junco maritimi - Spartinetum junceae*, dense stands of *Spartina juncea* [92]. In more disturbed contexts, dense stands of *Imperata cylindrica* occur, resulting from a combination of coastal erosion, forest degradation, and grazing pressure [93, 86].

Back-dune and consolidated dunes are also characterized by the presence of *Juniperus oxycedrus* subsp. *macrocarpa*. This habitat corresponds to the association *Pistacio-Juniperetum*,located in the transition zones between strictly psammophilous vegetation and forest vegetation.

Retrodunal wetlands also support reed beds (*Phragmitetum australis*) and relic hygrophilous woodlands dominated by *Ulmus minor*, *Alnus glutinosa*, and *Fraxinus oxycarpa*, which are of high conservation value [89].

Finally, the most inland portions of the dune system are characterized by artificial formations, such as maritime pine forests (*Pinus pinaster*), originally established as protective belts against marine winds, and stabilization plantings with alien species such as *Tamarix* spp. and *Hippophae rhamnoides*, now partially degraded [86].

Table 2.1 Characterization of dune vegetation in the San Rossore Park.

Ecological zone	**Main communities/associations**	**Examples of characteristic species**
Beach	*Salsolo kali - Cakiletum maritimae*	*Cakile maritima Scop.*, *Salsola kali L.*, *Atriplex latifolia Wahlenb.*, *Euphorbia paralias L.*
Embryonic dunes	*Elymo farcti - Spartinetum junceae*; stands of *Otanthus maritimus*	*Spartina juncea (Michx.) Willd.*, *Agropyron junceum (L.) Beauv.*, *Otanthus maritimus (L.) Hoffmgg. et Link*, *Eryngium maritimum L.*
Mobile dunes	*Echinophoro spinosae - Ammophiletum arundinaceae*	*Ammophila littoralis (Beauv.) Rothm.*, *Echinophora spinosa L.*
Consolidated dunes	*Helichrysum stoechas* stands; *Sileno coloratae - Vulpietum membranaceae*	*Helichrysum stoechas (L.) Moench.*, *Vulpia membranacea (L.) Link*, *Silene canescens Ten.*
Interdune and back-dune	*Suaedo maritimae - Salicornietum patulae*; *Juncetum acuti*; *Junco maritimi - Spartinetum junceae*; stands of *Imperata cylindrica*; *Pistacio-Juniperetum macrocarpae*	*Suaeda maritima (L.) Dumort.*, *Salicornia patula Douval-Jouve*, *Juncus acutus L.* , *Spartina juncea (Michx.) Willd.*, *Imperata cylindrica (L.) Beauv.*, *Juniperus oxycedrus* subsp. *macrocarpa*
Wetlands	*Phragmitetum australis*; relic hygrophilous forests	*Phragmites australis (Cav.) Trin*, *Alnus glutinosa*, *Fraxinus oxycarpa*
Inland areas	Artificial pine forests (*Pinus pinaster*); stabilization plantations with alien species	*Pinus pinaster*, *Tamarix* sp.pl., *Hippophae rhamnoides*

2.2 Data Collection

The monitoring of coastal dune systems presents unique challenges due to their dynamic morphology, spatial heterogeneity, and sensitivity to both natural and anthropogenic drivers. Reliable data acquisition is therefore fundamental to capturing the processes that shape these environments and to developing effective monitoring frameworks. In this study, a multi-disciplinary approach to data collection was employed, combining in-situ measurements with a suite of remote sensing techniques, including Real Time Kinematic Global Navigation Satellite System (RTK GNSS) surveying, LiDAR (Light Detection and Ranging) and photogrammetry from UAV and Multi-Beam Echo Sounder (MBES) hydrography. This integrated strategy was motivated by the recognition that no single method can comprehensively address the diverse and complex dynamics governing coastal dunes.

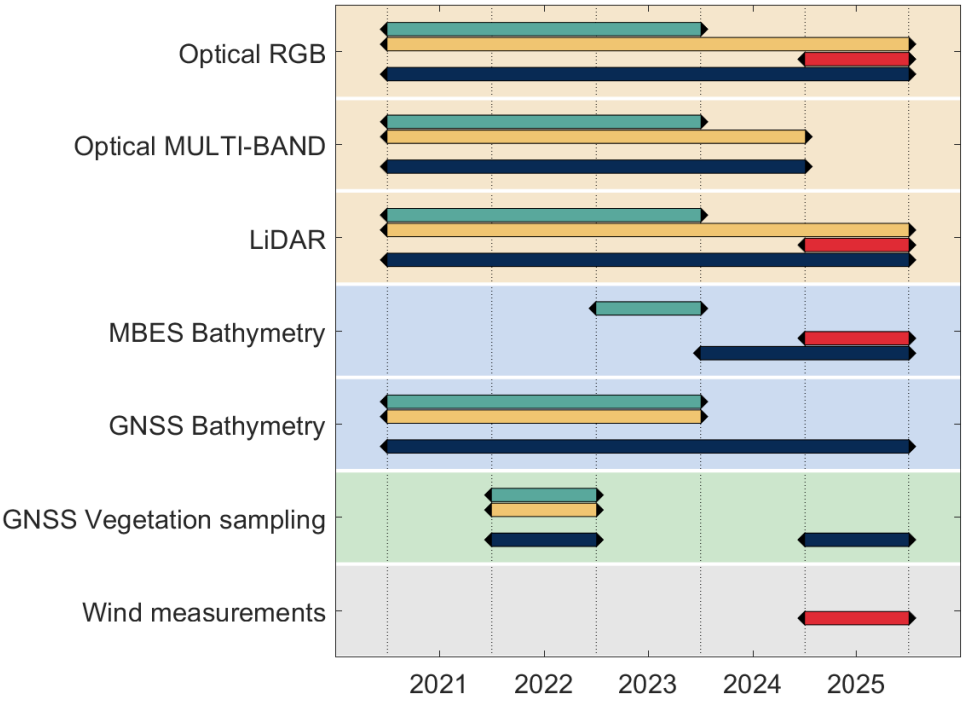

Fig. 2.9 Gantt diagram of field activities. The color of lines marks the area where the measurements are carried out: A1 (green), A2 (yellow), A2-bis (red), A3 (dark blue). Background color shade indicates the semantic area of the measurements: land (orange), water (blue), vegetation (green), wind (gray).

Despite the richness of the acquired dataset, the temporal resolution of monitoring remained constrained. Measurements were carried out on an annual basis from 2021 to 2025 (Fig.2.9), always in late-spring to early-autumn period, due to milder weather conditions and richer vegetation. This relatively low frequency is dictated by the logistical complexity, time requirements, and high costs associated with both data acquisition and processing. However, this limitation was balanced by the exceptionally high spatial resolution achieved through the combination of field and remote sensing methods.

2.2.1 UAV Surveys

Uncrewed Aerial Vehicles (UAVs), are aircraft operated without an onboard pilot. Over the past decade, UAVs have become a standard in scientific research, especially in geospatial studies, due to their ability to collect high-quality data at lower costs compared to traditional field surveys or crewed aerial photography [94]. Their versatility further increases when equipped with different sensors, including optical and hyperspectral cameras, Light Detection and Ranging sensors (LiDAR), Synthetic Aperture Radar (SAR), GPS, and Inertial Measurement Units (IMU) [95, 96].
Compared to other types of land survey techniques, UAVs cover larger areas in shorter times, and their efficiency makes repeated surveys feasible, enabling multi-temporal monitoring. Furthermore, unlike satellites, UAVs allow on-demand deployment, extremely useful in post-disaster surveying to quantify the magnitude and damages caused by extreme climatic events where fieldwork poses risks to personnel [97].
Despite the extreme flexibility, UAV operations are strongly affected by weather conditions: rain, fog, or strong winds can limit or prevent data collection. Payload capacity and battery life further constrain their use [98].
For geoscience, mini- and micro-UAVs (i.e., with operational range less than 10km) are the most common choices, especially multirotor platforms. These systems provide stability and flexible maneuverability, allowing data acquisition from multiple perspectives, including oblique angles.

A state-of-the-art deployment procedure has been followed for all UAV surveys carried out during the numerous campaigns to ensure the best data quality.
The process begins with careful survey planning, where the Areas of Interests (AoI) are assessed in terms of boundaries, topography, and potential obstacles. Flight plans are then prepared using mission-planning software (e.g., USGS, Mission Planner,

BLY3D, ecc.), specifying parameters such as altitude, flight path, image frequency and overlap. At this stage, regulatory requirements are also considered, including permissions for operation, checking for no-fly zones and compliance with national aviation guidelines (e.g., National Civil Aviation Authority, ENAC).
Prior to deployment, pre-flight preparations are carried out to guarantee that both equipment and site conditions are suitable. This includes visual inspection of the

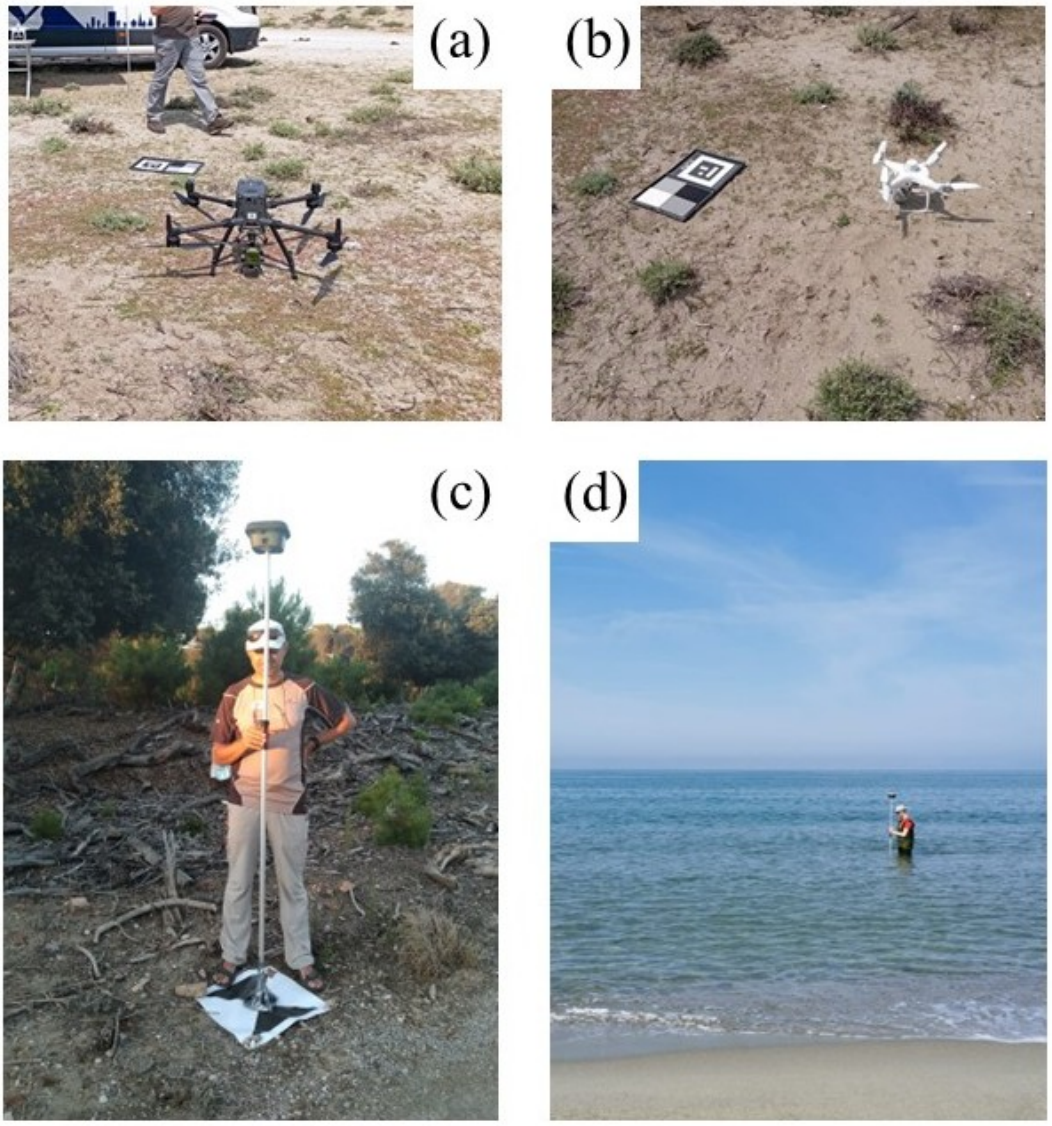

Fig. 2.10 (a)*DJI Matrice M300 RTK* with the reflectance calibration panel; (b) *DJI Phantom 4* with reflectance calibration panel; (c) GCP marker position measured with GNSS antenna; (d) Shallow water bathymetry measurements with GNSS antenna.

UAV, calibration of onboard sensors such as cameras, GNSS, and IMU, and the placement of markers (commonly large, clearly visible sheets) across the survey area to serve as Ground Control Points (GCPs). These markers are accurately measured and recorded with RTK-GNSS antennas (Fig.2.10c) to enable high-precision georeferencing of the aerial data and subsequent alignment of images and the generation of accurate orthomosaics and digital elevation models.
The survey itself is autonomously executed in Real-Time Kinematic (RTK) mode, with the UAV following the pre-programmed flight plan. During flight, onboard sensors collect imagery or LiDAR data, typically with nadiral orientation, although oblique acquisitions have also been performed to better capture spots that would otherwise remain hidden.
Two UAV platforms have been employed for all aerial surveys: *(i) DJI Matrice M300 RTK* quad-rotor drone with dual-frequency GNSS receiver (Fig.2.10a), equipped with *DJI Zenmuse L1* LiDAR or *DJI Zenmuse P1* optical camera; *(ii) DJI Phantom 4 (P4)* quad-rotor drone with dual frequency GNSS receiver (Fig.2.10b), equipped with *DJI P4 multispectral* camera. Drones and sensors characteristics are reported in tables 2.4, 2.5 and 2.6.

2.2.2 RTK GNSS Survey

As previously mentioned, to achieve high accuracy, surveys often use Ground Control Points (GCPs) which require a Global Navigation Satellite System (GNSS). GNSS is the general term for satellite constellations that send signals to receivers on the ground, allowing them to calculate location and time anywhere in the world. Major systems include Galileo (Europe), GPS (USA), GLONASS (Russia), and BeiDou (China). Modern dual-frequency receivers can combine signals of different frequencies from each constellation, reducing atmospheric bias and improving accuracy from several meters down to a few decimeters. Accuracy is improved even further by Real-Time Kinematic networks (NRTK). This survey technique is a relative positioning method with a carrier-phase signal. It relies on networks of permanent reference stations or Continuously Operating Reference Station (CORS) with precisely known positions, connected to control centers. The stations compute the differences between the instantaneous measured positions from satellite and the reference one and transmit them as "corrections", generally via Internet. The Receivers in the field can apply the received correction assuming similar atmospheric

conditions over the emitting CORS and the receiver (standard condition approximately 60 km). NRTK allows real-time acquisition, even kinematics ones, with 1-3 cm on the horizontal component and $3-5$ cm on the vertical component. if the ambiguity is correctly fixed. With this setup, surveyors only need one GNSS receiver in the field instead of two and internet connection. This approach greatly simplifies and improves data collection.

In this study, GNSS surveys were conducted for three main purposes: *(i)*Establishing GCPs coordinates (Fig.2.10c); *(ii)*collecting measurements along the beach, swash zone, and shallow nearshore areas (Fig.2.10d); *(iii)*vegetation sampling. Over the years, three different GNSS receivers were used, always in NRTK mode: *(i)Leica GS18*; *(ii)Stonex S900*$^{+}$; *(iii)Emlid Reach RS2+*. Main receiver's characteristics are summarized in table 2.3 and in table 2.2 are reported the number of points manually acquired during field campaigns.

Anno	**Area**	**GCPs**	**Bathymetry**	**Vegetation**
2021	A1	4	85	n.d.
	A2	5	84	n.d.
	A3	3	166	n.d.
2022	A1	7	200	201
	A2	8	134	338
	A3	8	160	339
2023	A1	8	116	n.d.
	A2	7	66	n.d.
	A3	7	109	n.d.
2024	A2	6	n.d.	n.d.
	A3	3	269	n.d.
2025	A2	4	n.d.	n.d.
	A2-bis	0	n.d.	n.d.
	A3	5	100	221

Table 2.2 Number of GCPs, near-shore bathymetry points and plants locations acquired through manual GNSS surveying.

Model	Purpose	Type	Update rate	RTK accuracy
Leica GS18T	GCP / Bathymetry / vegetation sampling	Multi-frequency	20 Hz	H: 8 mm + 1 ppmV: 15 mm + 1 ppm
Stonex S900^{+}	GCP / Bathymetry / vegetation sampling	Multi-frequency	20 Hz	H: 5 mm + 0.5 ppmV: 10 mm + 0.5 ppm
Emlid Reach RS2+	Bathymetry	Multi-frequency	10 Hz	H: 7 mm + 1 ppmV: 14 mm + 1 ppm

Table 2.3 Specifications of the GNSS receivers used in the surveys.

Model	Type	Purpose	Sensor Equipped	Georeferencing Mode	Navigation Sensors
DJI Matrice M300	Quad-rotor	RGB, LiDAR	DJI Zenmuse P1, L1	RTK	Dual-frequency GNSS antenna / IMU
DJI Phantom 4	Quad-rotor	Multi-spectral	DJI P4 multispectral	RTK	Dual-frequency GNSS antenna / IMU

Table 2.4 Specifications of UAV models used in the survey.

Model	Resolution	Focal length	Pixel size	Bands
DJI Zenmuse P1	8192 x 5460px	35mm	4.39 x 4.39μm	RGB
DJI P4	1600 x 1300px	5.74mm	3.01 x 3.01μm	Red (650$\pm$16nm), Green (560$\pm$16nm), Blue (450$\pm$16nm), Red Edge (730$\pm$16nm), Near Infrared (840$\pm$26nm)

Table 2.5 Specifications of used optical sensors.

Model	Point Rate	Ranging Accuracy	Number of Returns
DJI Zenmuse L1	240,000 - 480,000 pts/s	3cm - 100m	3

Table 2.6 Specifications of used LiDAR sensor.

Anno	Area	N° GCPs	RGB					Multispectral					LiDAR
			N° img	Alt. (m.a.s.l.)	Area (km^2)	Res. (cm/px)	GCP RMSE (mm)	N° img	Alt. (m.a.s.l.)	Area (km^2)	Res. (cm/px)	GCP RMSE (mm)	Pts/m^2
2021	A1	4	1085	63.9	0.182	3	25.2	424	77.3	0.114	3	12.2	763
	A2	5	1481	104	0.182	2	95.7	359	75.8	0.098	3	28.5	998
	A3	3	526	97.2	0.257	1.5	-	246	89.1	0.122	5	11.8	540
2022	A1	7	430	77.5	0.217	1	93.9	674	63.9	0.176	4	5.4	788
	A2	8	668	61	0.113	1	49.3	494	61.8	0.087	3	1.7	366
	A3	8	632	80.5	0.147	1	79.2	271	86.9	0.043	3	-	685
2023	A1	8	515	128	0.202	2	40.2	739	95	0.168	3	-	913
	A2	7	421	127	0.153	2	45.7	312	92.5	0.117	5	-	623
	A3	7	330	97	0.135	1	-	396	94.9	0.118	4.5	-	918
2024	A2	6	323	107	0.059	3	77.0	323	64.3	0.059	3	-	638
	A3	3	145	31.7	0.011	1	13.2	431	64.5	0.033	3	5.4	1227
2025	A2	4	302	51.5	0.123	3	38.7	n.d.	n.d.	n.d.	n.d.	n.d.	700
	A2-bis	0	148	53.9	0.147	4	12.6	n.d.	n.d.	n.d.	n.d.	n.d.	869
	A3	5	334	48.7	0.110	3	-	n.d.	n.d.	n.d.	n.d.	n.d.	963

Table 2.7 Summary of UAV Surveys with Optical, Multispectral, and LiDAR sensors.

2.2.3 MBES Survey

General aspects

The Multibeam Echosounder (MBES) is the primary instrument used for seafloor morphological mapping and has been accessible to the scientific community for nearly five decades.

Early multibeam systems were originally developed for the U.S. Navy in 1964 [99] to map deep-water environments using frequencies between 12 and 30kHz, primarily for submarine navigation and ballistic missile guidance across ocean basins. Subsequent commercial applications emerged to support the design and placement of submarine communication cables [100]. By 1977, the first declassified systems

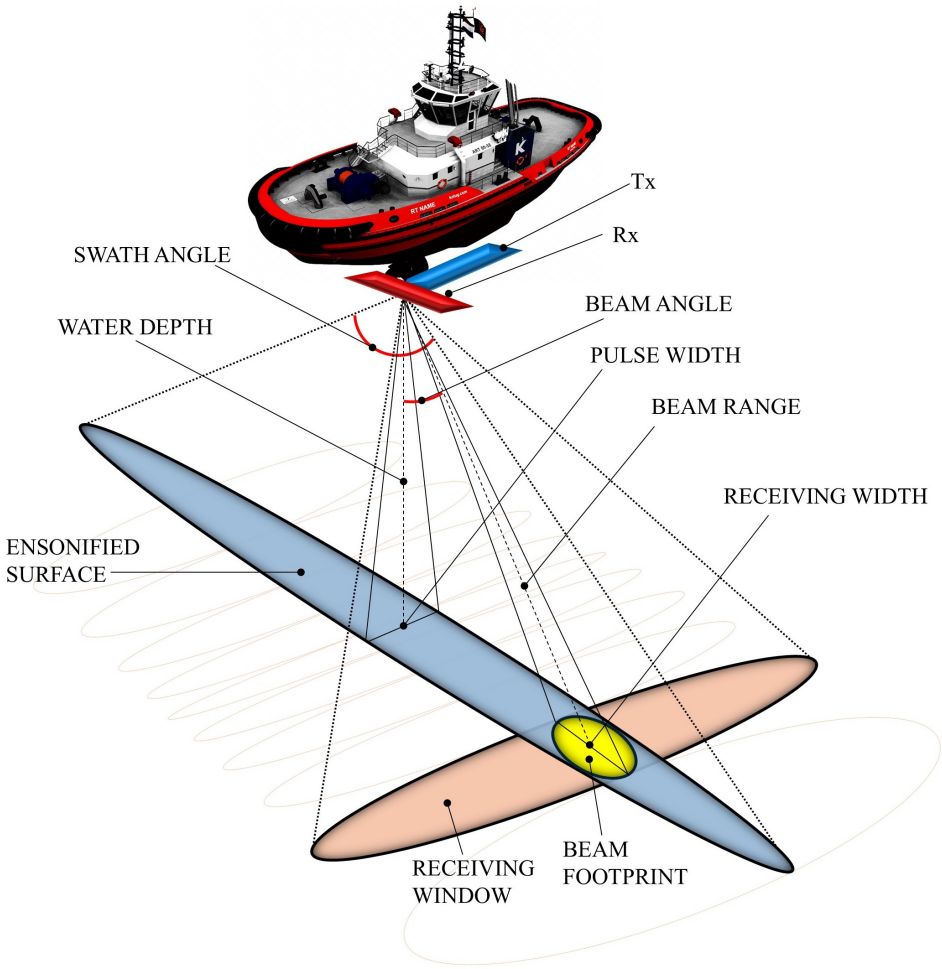

Fig. 2.11 Representation scheme of MBES beamforming.

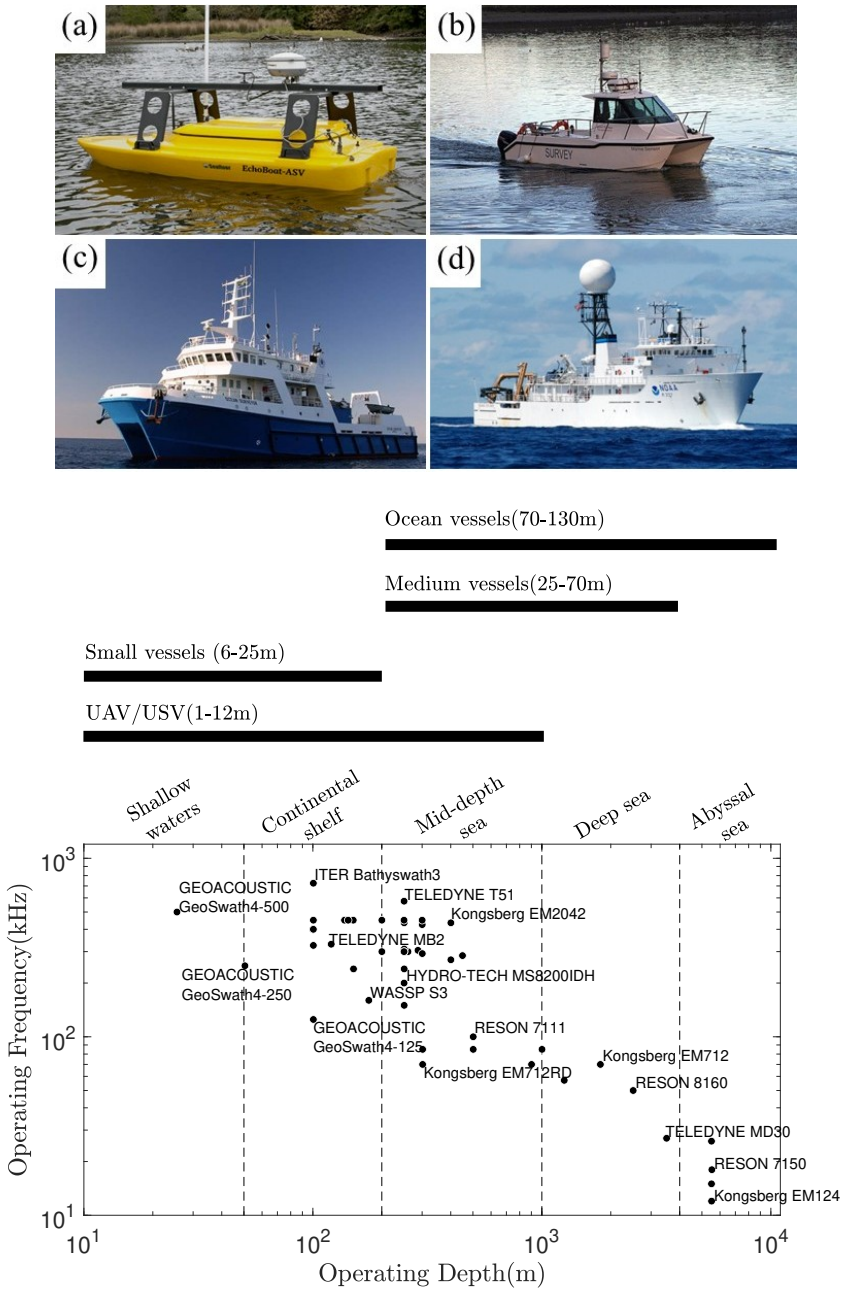

Fig. 2.12 Scatterplot of Typical operating depths and frequencies of most of commercial MBES and operative depth ranges of different hydrographic vessels, subdivided into four size classes, from smallest to largest. Pictures of vessel representing each class are also shown: (a)UAV/USV, (b)small, (c)medium and (d)ocean-going vessels.

became available for scientific studies of submarine geomorphology [101]. Since then, academic research fleets have progressively adopted hull-mounted multibeam systems as standard equipment, revolutionizing our understanding of seafloor processes and topography.
The first shallow-water multibeam systems (500—1000 kHz) were developed in 1984 to support offshore oil and gas infrastructure [102]. Operating at higher frequencies allowed these systems to resolve seabed features with wavelengths of less than 10m. Soon after, shallow-water MBES technology was increasingly adopted for mapping coastal and continental shelf geomorphology [103].

The fundamental operating principle of the MBES —similar to that of a single-beam echosounder— involves the transmission of an acoustic pulse by a transmitter, traveling through the water column. The pulse reflects or scatters off the seafloor and returns to the receiver. By measuring the two-way travel time (TWTT) of the pulse and knowing the sound velocity profile of seawater—primarily governed by temperature, salinity, and pressure [104–108]—the travel time can be converted into distance. Combining this distance with the known beam angle, and applying corrections based on vessel motion and positioning data from ancillary systems (e.g., IMU and GNSS antennas), enables precise three-dimensional positioning of the backscattering points (latitude, longitude, and depth).
Unlike conventional single-beam echosounders, which emit only one acoustic pulse, modern multibeam systems use transducer arrays capable of generating hundreds of simultaneous beams (up to 800 [109]).

Multi beam sonars are composed of a piezoelectric transmitter (Tx) and a receiver (Rx), the former is disposed along the fore-aft direction, and the latter is mounted across-track, perpendicularly to each other.
Tx emits an acoustic wave pulse that insonifies a surface narrow in the fore-aft direction and wide across-track, while Rx is composed by an array of sensors pointing at different angles, able to recive a pulses from spatial windows which are wide in the fore-aft direction and narrow in the across-track direction.
The "beam" is the reflected pulse coming from intersection between the insonified surface and the reciever window (Fig 2.11).

These beams are distributed in a fan-shaped swath —often up to 150 degrees wide— perpendicular to the vessel's track [110, 111], effectively blanketing the seafloor with acoustic pulses. The geometric distance between the centers of the

footprint in each beam approximates the spatial resolution of bathymetric data collected from multi beam echo sounders. The size of the beam footprint is governed by two primary factors: *(i)*beam width and *(ii)*water depth.
A narrower beam width results in a small sonar footprint on the seafloor, resulting in a finer spatial resolution —most MBES use a beam width that can vary from 0.5 degrees to 2 degrees—. In the same way, as the sonar pulse travels away from the transducer array, it is subject to spherical spreading, meaning that the area affected by the ping gets broader with increasing distance. The resulting point cloud is then processed and interpolated to produce high-resolution bathymetric grids that accurately represent seafloor morphology.

Over the years, continuous technological advancements have led to the development of a wide range of MBES systems, each optimized for specific survey environments and scientific objectives. Variations in operating frequency, beam configuration, and swath coverage now allow MBES instruments to effectively address diverse mapping requirements, from ultra-high-resolution shallow-water surveys to deep-ocean bathymetric exploration (Fig.2.12).

The selection of an appropriate sonar frequency must be optimized according to the depth of the survey area. The operational range of a multibeam echosounder (MBES) depends on maintaining an adequate signal-to-noise ratio (SNR). Range performance is influenced by two primary factors: a geometric spreading loss, which is independent of frequency, and a frequency-dependent attenuation caused by sound absorption along the propagation path [112]. Consequently, lower-frequency systems which experience reduced absorption are generally preferred for deep-water operations. As depth increases, the swath width initially expands approximately linearly until the outermost beams approach the minimum usable SNR threshold. Beyond this limit, the effective swath width begins to decrease, and the associated outer-beam detections become increasingly uncertain. An optimal MBES configuration is therefore one in which the SNR threshold is not reached within the edge of swath extent. In practice, systems operating at the lowest commonly used frequencies (around $\sim$ 12kHz) typically maintain sufficient SNR down to depths of approximately 2000—3000m.
Another factor limiting the feasible range of the MBES is vessel self-generated noise, which increases with cruising speed [100].

If the maximum reachable range is predominantly dependent on the pulse frequency, the range resolution (i.e., how well objects at different distances can be discriminated) is proportional to the pulse duration or, equivalently, the pulse length. For instance, a sonar emitting a 12kHz and 10 wavelengths long pulse, produces a best range resolution of about $\sim$ 1m, while a 20 wavelengths pulse results a $\sim$ 2m resolution; for 200kHz sonar pulse, is $\sim$ 5cm at 10 wavelengths and $\sim$ 10cm at 20 wavelengths [100].

Finally, the effective spatial resolution of a MBES is determined by the spacing of detected points and the size of the projected acoustic footprint on the seafloor. To adequately resolve a seabed feature of a given minimum wavelength (λ), both the along- and across-track sampling space intervals must be less than half that wavelength ($< \lambda/2$), in accordance with the Nyquist sampling criterion. Furthermore, the projected beam footprint should not exceed this same dimension to prevent spatial aliasing.
Each beam-derived depth estimate inherently contains measurement uncertainty. When the amplitude of true seabed relief is comparable to (or smaller) than the random detection noise, small-scale morphological features may be obscured. To mitigate this effect, redundant sampling is achieved by overlapping adjacent beam footprints, thereby improving the reliability and precision of the derived bathymetry through statistical averaging of multiple independent observations. In practice, survey lines are typically planned with 20% overlap to compensate for degradation in outer-beam data and to ensure seamless coverage in the final bathymetric mosaic [109].
As the across-track beam spacing controls the amount of overlap, the vessel cruising speed, along-track spacing is controlled by the vessel speed and ping rate.
When wider swath sectors are used, each beam must cover a larger area, reducing both overlap and the ability to suppress noise. Conversely, narrowing the swath angle increases overlap between beams in both directions, significantly improving seabed definition and reducing random noise.

Positioning

As already discussed, echosounders by themselves estimeates the distance from the sensor to the seafloor by measuring the TWTT of a sound pulse, but, in order for the measure to have a meaning, it has to be referred to a spatial reference system. For

this reason, MBES measurements must be tightly integrated with a suite of ancillary positioning sensors [113, 100].

Accurate data integration depends on the consistent definition and transformation between several reference frames. Each sensor on board the survey platform operates within its own coordinate system, and their interrelations must be precisely known to convert measured ranges and angles into georeferenced seabed positions (Fig. 2.13a) [114].
The principal reference frames used are the vessel reference frame (VRF), a three-dimensional Cartesian coordinate system fixed to the hull of the survey vessel. It provides a common geometric basis to which all sensor measurements are referred. The VRF is conventionally defined with its origin at the vessel Reference Point (RP), the *X-axis* positive forward along the vessel's longitudinal axis, the *Y-axis* positive to starboard, and the *Z-axis* positive downward following the right-handed marine convention [115]. This local frame is essential because all sensor positions, orientations, and motion data are expressed within it before being transformed into a global geographic coordinate system (e.g., WGS84).

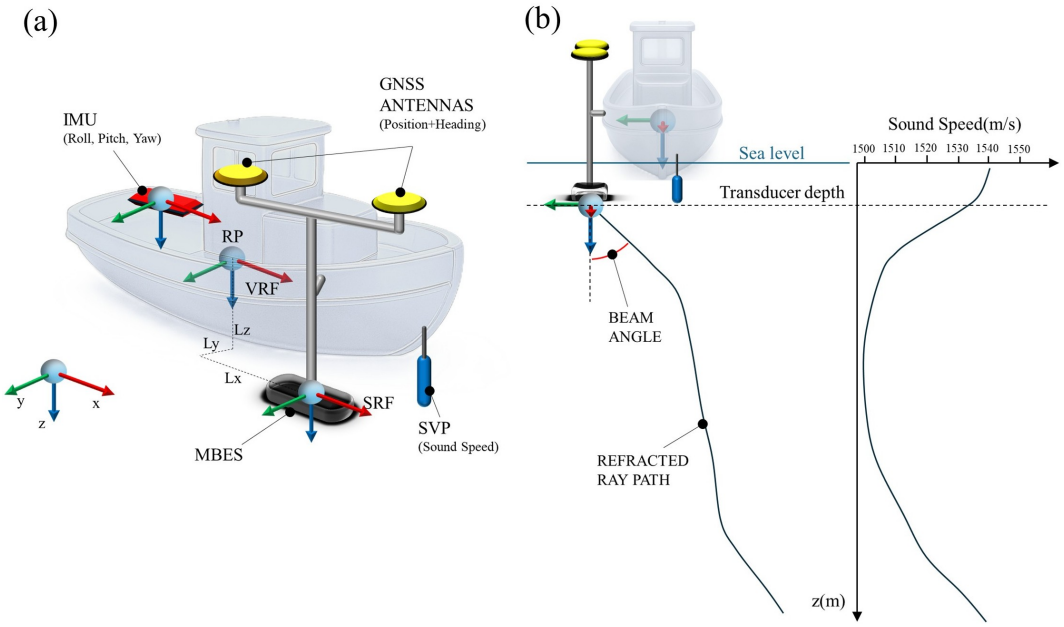

Fig. 2.13 (a)Instrument integration on a hydrographic vessel with the reference systems of the vessel (VRF), transducer (SRF) and IMU. L_x, L_y and L_z are the measures of the offset of the transducer respect to the RP. (b)Effect of the the sound speed variation on the path of the pulse.

The RP is a precisely defined physical point on the vessel that serves as the origin of the VRF. Its location is selected to minimize error propagation and to simplify offset measurements between sensors. Commonly, the VRP is placed near the center of gravity, at the IMU's reference center, or at a fixed structural point that is stable and well-defined. The lever-arm offsets of each sensor—such as the GNSS antenna, IMU, and transducer—are then measured relative to this point, typically through a high-precision survey (e.g., with a total station). These offsets must be known to within a few millimeters to ensure depth accuracy at the centimeter level.
Lastly, the local Sonar Reference Frame (SRF) of the sonar itself describes the local coordinate system of the MBES transducer. Its origin corresponds to the acoustic center of the array, with the *X-axis* aligned along the transmit array, the *Y-axis* across the receive array, and the *Z-axis* normal to the face of the transducer. During acquisition, the sonar measures beam angles and ranges within this local frame. To obtain accurate seabed positions, these measurements are transformed into the VRF using the known lever-arm offsets and boresight angles—the small rotations that describe the orientation difference between the SRF and VRF.

Building upon this spatial framework, the integration of ancillary sensors allows the multibeam system to transform raw acoustic ranges into georeferenced depth measurements.
The GNSS antenna provides the vessel's geographic position and heading, serving as the absolute reference within the global coordinate system —typically, modern setups utilizes a dual-antennas system to enhance positioning.
The real-time vessel attitude —roll, pitch, yaw, and heave—parameters, describing the instantaneous orientation of the vessel reference frame, are measured by an IMU and are applied to correct the beam geometry during acquisition [116].

Sound speed

Accurate modeling of sound propagation through the water column is essential for reliable MBES measurements. The speed of sound in seawater is not constant but varies primarily with temperature, salinity, and pressure, typically ranging between 1400 and 1550 m/s [108]. These variations influence the refraction of acoustic beams and the travel time of sound pulses, directly affecting both depth and horizontal positioning accuracy (Fig. 2.13b) [114, 117, 110]. To quantify these variations,

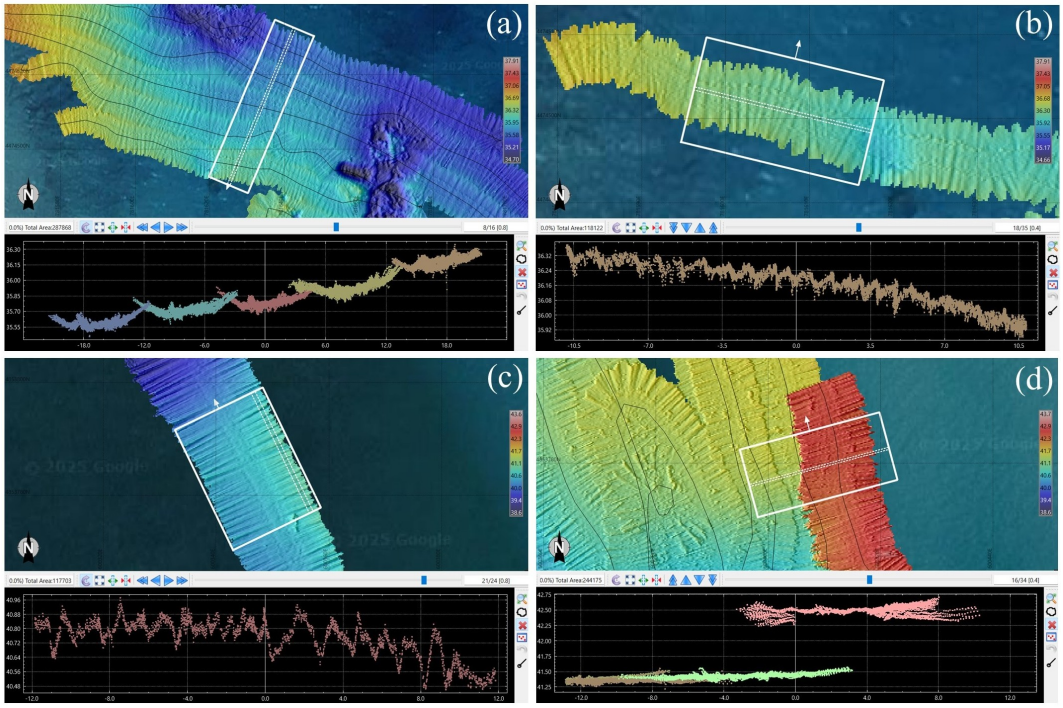

Fig. 2.14 Examples of systematic errors in MBES surveys. (a)Refraction artifacts caused by a wrong estimation of the SVP. The cross-section of multiple parallel tracks shows a "smiley" pattern, meaning that the sound speed has been underestimated; (b)Wobbles caused by heave motion latency. Typically, the pattern is a series of cylindrical waves; (c)Wobbles caused by roll motion latency. Differently from heave artifacts, the pattern is a series of alternating out-of-phase waves between the tribord and starbord side, but flatter in the center; (d)Plane offset between two different tracks, caused by wrong alignment of transducer position.

hydrographic surveys routinely collect Sound Speed Profiles (SVP), which represent the vertical distribution of sound velocity from the surface to the seafloor. SVPs are acquired using dedicated profilers or Conductivity-Temperature-Depth (CTD) sensors, from which sound speed is derived using empirical equations [104–108]. The measured profiles are applied to ray-tracing algorithms that correct the beam path curvature within the water column [118–120]. In addition, a near-surface sound speed value —measured by a sensor mounted under the keel of the vessel, in front of the transducer— is used for real-time beam steering [117].

Errors in MBES measurements

Multibeam measurements can be affected by several types of systematic and dynamic errors that arise from imperfect integration of the sonar, motion, and positioning sensors [114, 121]. These errors can generally be grouped into three categories: *(i)*motion-related, *(ii)*alignment, and *(iii)*sound-speed–related. Each of these errors produce distinctive artifacts in the bathymetric data, well known by the hydrographers community.

—Motion-related errors—
Motion-related errors often arise from time delays in the motion sensor outputs to the processing unit, or from unexpected flexures of the mounting pole. Such errors create dynamic motion residuals that manifest as periodic "wobbles" or across-track ribbing in the bathymetry (Fig.2.14b-c), typically orthogonal to the ship's track [103, 114, 121, 122]. In fact, a few milliseconds of latency in the roll signal can generate systematic tilting of the swath, producing ripples in depth data. Similarly, unmeasured pole flex causes apparent roll and heave motions that are not captured by the Motion Reference Unit, introducing alternating upslope and downslope features along the swath [114, 123, 124].

—Alignment errors—
Alignment errors occur when the physical offsets or angular misalignments between sensors are not correctly defined (e.g., the x, y and z offsets in the VRF of the IMU center, antennas lever arms and transducer head). These lead to apparent positional shifts or vertical offsets that can vary dynamically with vessel motion (Fig.2.14d) [114, 103].

—Sound-speed errors—
These errors occur when the sound velocity near the transducer or within the water column (i.e., the sound velocity profile, SVP) is inaccurately measured. This results in an incorrect estimation of the beam steering angles along the acoustic path, leading to errors in the calculated beam ranges. Typically, this type of error appears as a symmetric curvature of the swath —either downward ("smiles") or upward ("frowns")— depending on whether the sound speed has been underestimated or overestimated, respectively (Fig.2.14a) [110, 114, 117, 125, 126].

Despite these being the main systematic errors that could occur during a MBES survey, other non-systematic errors may occur, caused by additional environmental

noise (presence of fish and algae, bad weather, sounding multi-path, external interference, etc.) or platform-induced noise (bubbles at transducer head, propeller-induced vibrations, etc.).
These errors produce isolated or clustered outlier points in the point cloud [127].

The combined effect of these errors is a distortion of the true seabed topography, since small-scale undulations, tilts, oscillations and outlier points can obscure seabed features. Correcting them requires precise time synchronization (e.g., Pulse Per Second —PPS— method [121, 128], accurate sensor offsets measurements and alignment (e.g., the Patch Test [129], robust motion compensation (e.g., Kalman filtering [130, 131]), and post-processing techniques (e.g., outliers cleaning [132], spline interpolation [133, 134], surface smoothing [121], sound-speed refraction correction [117, 110], etc.).

Patch Test

As previously noted, an accurate hydrographic survey requires the precise determination of position and orientation of each instrument within the complex ensemble that constitutes an MBES system as well as the vertical sound speed profiles. Upon these measurements, the exact alignment of the transducer head is often difficult to determine each time a bathymetric survey is undertaken.
For these reasons, a standard procedure, called 'Patch Test' fulfills the task of determining *(i)*the offsets of the mounting angles (roll, pitch, and yaw) of a MBES transducer head with respect to the VRF and *(ii)*the time latency between the reception of the GNSS position and its integration by the acquisition system [129, 135].
First, a suitable location needs to be found. Preferably, a slope with a flat and deep end (Fig.2.15a). If such a slope is not available, then any features like sand dunes, dredging tracks or a pipeline can be also exploited.
The ship course pattern to perform the test consists of three pairs of reciprocal lines, two of which are parallel to the slope gradient and the third perpendicular and bisecting the first two (Fig.2.15b). Each pair of lines is run in opposite directions with a 100% swath overlap, while an overlap of about 50% is required between the line pairs.
In modern hydrographic practice, the residual misalignment angles are computed automatically by dedicated processing software, upon data acquisition as described above. The software compares point clouds obtained from the different survey

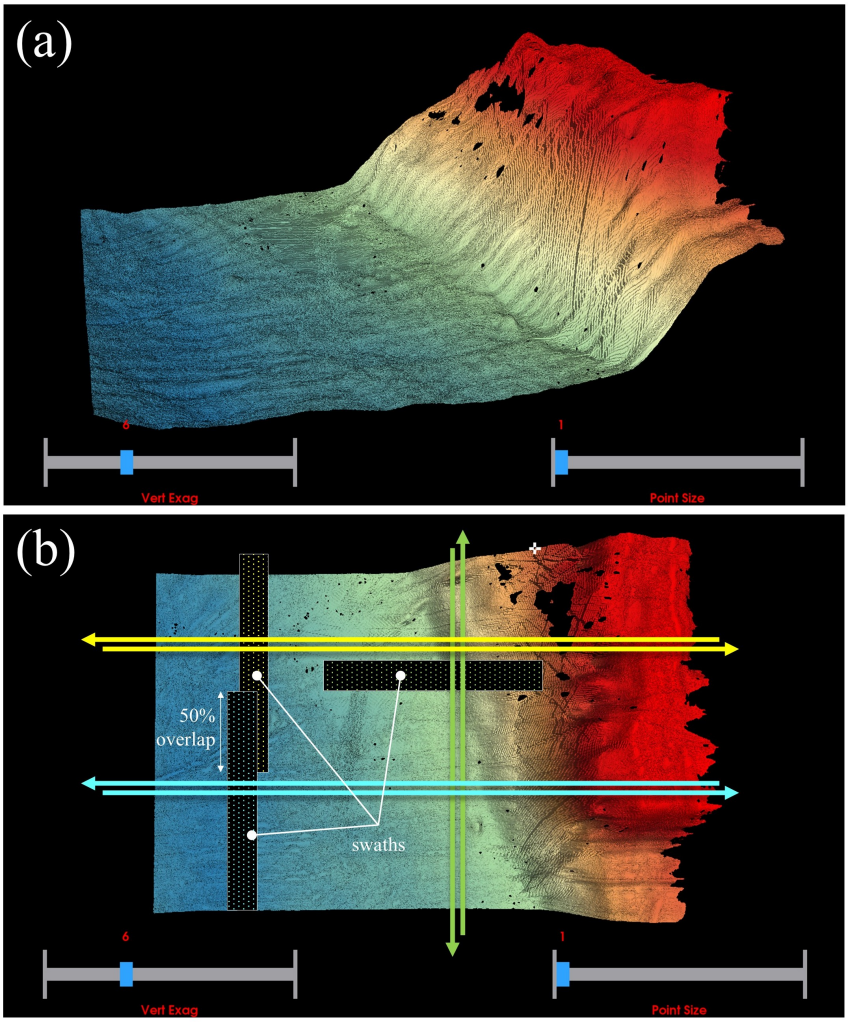

Fig. 2.15 (a)Example of an ideal sloped seabed topography to perform the Patch Test; (b)Line pattern of a standard Patch Test: two pairs of parallel lines (yellow and blue) with a swath overlap of 50%, running parallel to the slope gradient, and a pair perpendicular to the slope (green).

lines and optimizes the alignment parameters to minimize discrepancies between overlapping datasets.

USVs

Among the wide variety of vessels for hydrographic surveying with MBES, Uncrewed Surface Vehicles (USVs) (Fig.2.12a) —also referred to as Autonomous Surface Vehicles (ASVs)— have emerged as a versatile option for a wide range

of maritime applications, offering safer, cost-effective, and more efficient alternatives to traditional manned operations. Advances in automation and remote sensing broadened their use to include mine sweeping, environmental monitoring, scientific surveying, and technology testbeds [136–138]. Modern USVs, typically under 15 m in length, integrate state-of-the-art technologies such as GNSS navigation, waypoint following, wireless communication, and autonomous control frameworks [139, 140], enabling both supervised and fully autonomous operations [141]. Particularly in shallow-water contexts, compact USVs such as ACES [137], ROAZ [142], MESSIN [143], SESAMO [144], and DELFIM [145] have demonstrated effective performance for bathymetric and environmental surveys in depths as shallow as one meter. Over the past decade, the growing demand for efficient and repeatable hydrographic surveys has accelerated the adoption of ASVs in coastal, estuarine and lacustrine applications. Their ability to operate in areas inaccessible or unsafe for crewed vessels makes them particularly advantageous for mapping confined or hazardous environments such as ports and estuaries [146]. These systems not only minimize operational risks to personnel but also enable high-frequency, autonomous monitoring with consistent data quality.
The emergence of small, low-cost, yet highly capable USVs—enabled by advances in miniaturized sensors and open-source control architectures such as Arduino® and Raspberry Pi®—offers a transformative opportunity for high-resolution monitoring of these sensitive and dynamic areas [147] Despite limitations related to endurance, communication reliability, and acoustic interference, the continuous evolution of marine robotic technologies positions USVs as essential assets for the future of hydrographic and environmental survey operations.

USV prototype *"Clementina"*

Near-shore bathymetric surveys have been carried out using a USV prototype, named *"Clementina"* (Fig.2.16), developed and built in collaboration with MSH-USV (www.msh-usv.it). The structure of the USV is a 3D-printed double-keeled hull made with fiberglass-reinforced thermopolymer (Table 2.8).
The system is powered by two E-bike 36V batteries and propelled by two thrusters, ensuring about 2 hours of autonomy at a cruising speed of 1m/s.
The hull hosts an ensemble of instruments, integrating a complex system that man-

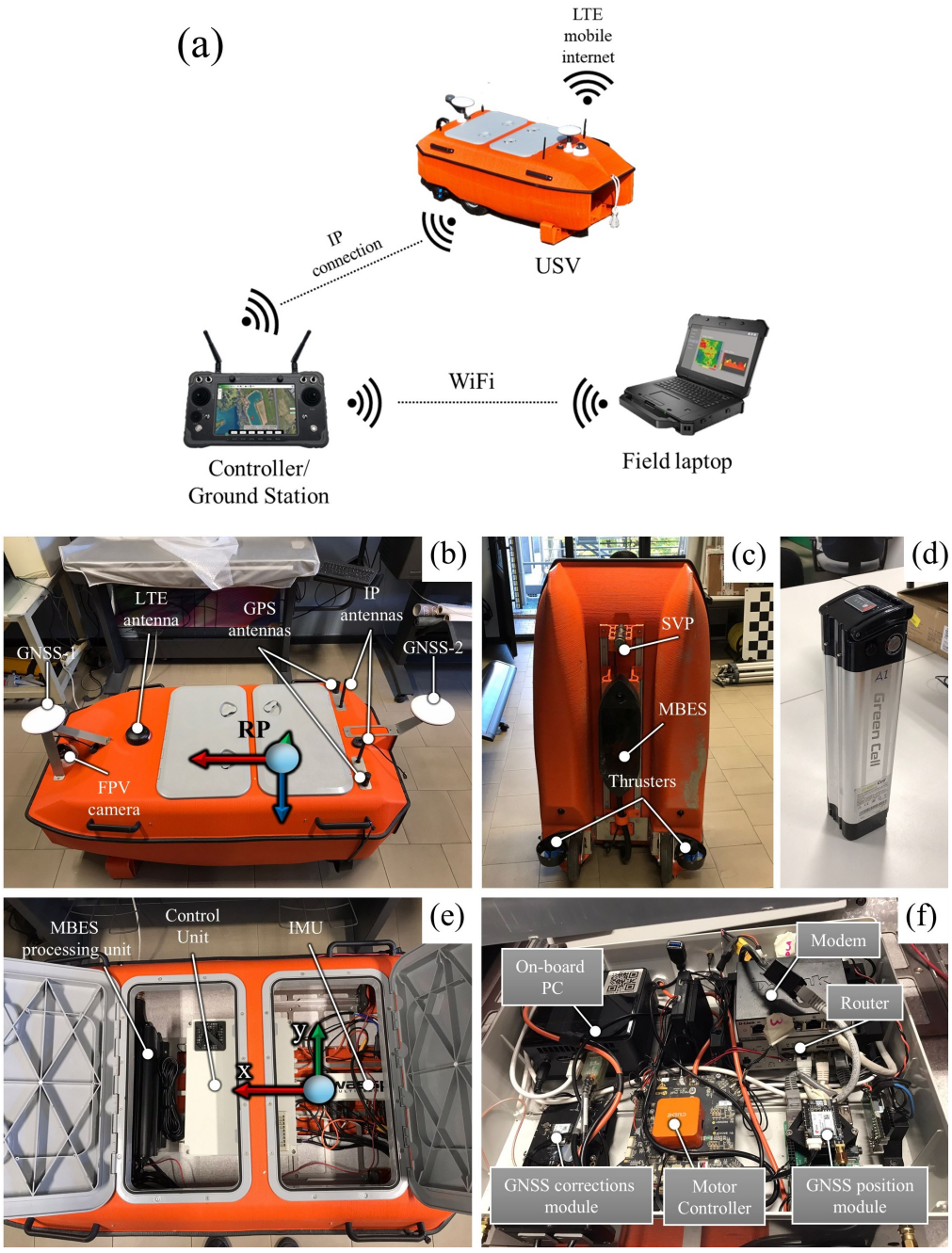

Fig. 2.16 (a)Radio link communication scheme; (b)Top-view picture of the hull with top-mounted antennas; (c)Bottom-view picture of the hull with bottom-mounted sensors and thrusters; (d)36V battery powering the USV; (e)Top-view picture of the hull with open hatches and internal-mounted components; (f)Picture of the inside components in the control unit box.

ages autonomous navigation and data transmission (Fig.2.16f, Fig.2.17, Tab.2.9) with a WASSP S3r MBES kit, composed of transducer, sound velocity probe, processing unit, IMU and two GNSS antennas (Fig. 2.16b,c,e). Technical details of the WASSP S3 transducer are reported in table 2.10.

The communication system of the Unmanned Surface Vehicle (USV) is organized around three main components: the USV itself, a controller/ground station (GS), and a field laptop (Fig. 2.16a).
The Ground Station (GS) acts as both the main controller and a communication bridge between the USV and the field laptop. Through the GS interface, operators can either manually control the USV or plan and upload autonomous navigation routes (e.g., QGroundControl app).
The USV transmits its position and navigation data to the GS using its dual GPS antennas. Communication between the USV and the GS occurs over a Wi-Fi network via an IP connection, allowing real-time data exchange and control commands.

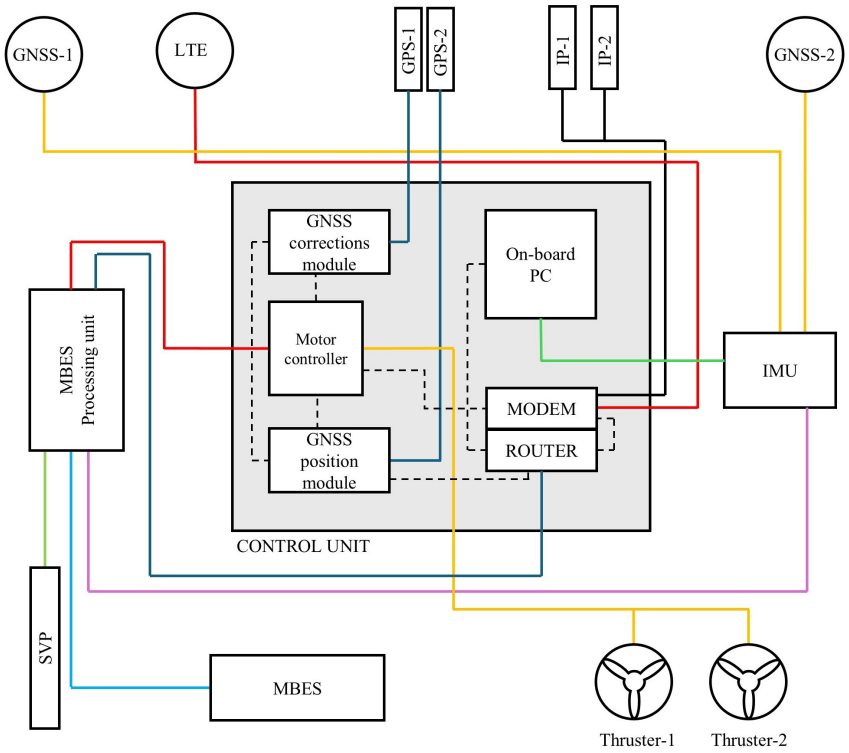

Fig. 2.17 Block diagram of the hardware architecture of *Clementina* system. Solid lines represent links between different elements of the system, while dashed lines represents the links within control unit components.

Additionally, the USV can access the internet through an LTE mobile connection, enabling remote monitoring if needed.
The GS and the field laptop communicate via a Wi-Fi link established through a local hotspot. This connection allows the laptop to receive mission data, visualize navigation information, and remotely access the USV's onboard computer through a LAN (remote desktop) connection.
In summary, the Ground Station functions as a radio and network relay between the USV and the field laptop, ensuring continuous data flow and control during field operations.

Size	
Length (mm)	1505
Width (mm)	815
Height (mm)	522
Total weight (hull+instruments) (kg)	60
Power system	
Motors	Blue Robotics thrusters T200
Batteries	Green Cell E-bike battery—36V/15Ah/540Wh
Performance	
Cruise speed (m/s)	1
Battery endurance (hrs)	2
Data communication range (m)	200

Table 2.8 *Clementina* basic specifications.

Component	**Model**	**Usage**
	Antennas	
GNSS	—	-Dual multi-frequency RTK GNSS antennas to achieve precise position and heading for the integration of sonar data.
GPS	—	-Positioning for autonomous/manual navigation.
LTE	Poynting Puck Antenna WiFi	-Mobile internet access for the on-board PC.
IP	—	-Connection between GS and USV.
	Sensors	
MBES	WASSP S3	-Sonar transducer for hydrographic surveying.
SVP	Valeport SVS	-Near-surface sound speed.
IMU	SBG Ellipse-D	-Integrates position and heading from GNSS antennas with the attitude (roll, pitch, heading).
FPV Camera	—	-Real-time ahead view during navigation.
	Control unit	
On-board PC	Intel® NUC	-MBES data visualization and management.
Modem	—	-Mobile internet access.
Router	D-Link DGS-1100	-Internet data management.
Motor controller	Cube Orange	-Thrust power management to allow autonomous/manual navigation.
GNSS position module	u-blox C101-D9C	-Receives GNSS position for autonomous/manual navigation.
GNSS corrections module	u-blox ZED-F9P	-Receives corrections from base stations.
MBES processing unit	WASSP IP66 DRX-32	-Transceiver that elaborates and transmits raw signal from MBES transducer to the on-board PC.

Table 2.9 List of components with a brief description of their usage.

Feature	Value
Center frequency (kHz)	160
Frequency range (kHz)	120—200
Max. swath angle (°)	120
Number of beams	224
Max. bandwidth (kHz)	60
Max. range resolution (mm)	18.55
Beam width (port-starbord) (°)	4.5
Beam width (fore-aft) (°)	3.2
Min. depth (m)	1
Max. depth (m)	350 (with 53° swath)
Max. ping rate (Hz)	100
Operating temperature (°C)	0—50

Table 2.10 Specifications of WASSP S3.

Deployment procedure

Prior to the deployment of the USV, the GNSS antennas and transducer lever arms relative to the RP in the VRF (Fig.2.13a) have been carefully measured with a total station (Table 2.11).

The vessel RP has been identified with the center of measurement of the IMU

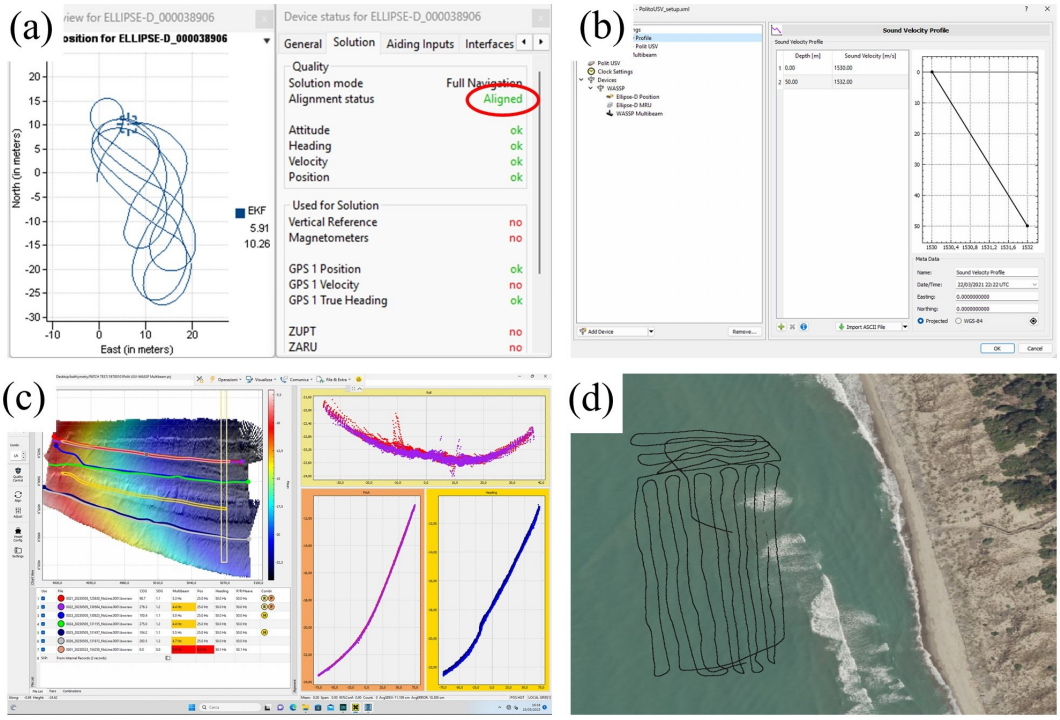

Fig. 2.18 (a)Display of *sbgCenter* during heading calibration; (b)sound speed profile setting screen in *BeamworX NavAQ*; (c)automatic calibration of attitude angle offset calibration in *BeamworX AutoPatch*; (d)survey track following parallel lines pattern.

(Fig.2.16e), while the VRF follows the marine convention (x positive forward, y positive to starboard and z positive downward).
Survey with USV follows three steps: *(i)*heading calibration; *(ii)*near-surface sound speed setup; *(iii)*patch test; *(iv)*actual survey.

—Heading calibration—
In this phase, the internal Kalman filter of the IMU estimates internal sensor errors to optimize navigation accuracy. A typical pattern to follow is doing "figure of eights" for a few minutes. For SBG systems, this phase can be supervised through *sbgCenter* software and the calibration ends when the "Alignment status" turns green (Fig.2.18a).

—Near-surface sound speed setup—
Near-surface sound speed is measured through the probe in front of the transducer (Fig.2.16c) and can be set in *BeamworX NavAQ* software before starting the data acquisition (Fig.2.18b).

—Patch test—
An exploratory survey is performed to check if a suitable seabed topography is available in the study area for the patch test (a steep slope followed by a flat). Data are acquired using *BeamworX NavAQ* following a sailing pattern of three (or more) pairs of straight lines, as described in the dedicated paragraph. Raw data are processed with *BeamworX AutoPAtch* software, which automatically estimates mounting angles residuals and data communication latency (Fig.2.18c).

—Survey—
The actual survey is performed preferably following parallel trajectories with an overlap of at least 20% between adjacent swaths (Fig.2.18d).

Antennas	
GNSS-1 x (mm)	1105
GNSS-1 y (mm)	-5
GNSS-1 z (mm)	-338
GNSS-2 x (mm)	-417
GNSS-2 y (mm)	-5
GNSS-2 z (mm)	-338
MBES Transducer	
MBES x (mm)	513
MBES y (mm)	-5
MBES z (mm)	253

Table 2.11 GNSS antennas and transducer lever arms measurements

2.2.4 Vegetation Sampling

During the field campaigns conducted between 2022 and 2025, a total of 1099 individual plants were manually geolocated using high-precision GNSS antennas and subsequently classified according to their taxonomic characteristics.
The surveyed specimens represent 12 distinct plant species occurring within the coastal dune vegetation, primarily composed of grasses and shrub species adapted to sandy and saline environments.
A comprehensive list of the identified species, along with their scientific names and ecological characteristics, is presented in Table 3.1 (Chapter 4).

2.3 Processing

2.3.1 Photogrammetric processing

Both RGB and multi-spectral UAV imagery have been processed in *Agisoft Metashape* using a standard approach of Structure from Motion (SfM) [148–150].

SfM is a photogrammetric technique that reconstructs three-dimensional (3D) structures from a series of two-dimensional (2D) overlapping images captured from different viewpoints. The fundamental principle of SfM relies on identifying and matching distinctive features—such as corners, edges, or texture patterns—across multiple images to establish correspondences [151]. These matched features enable the estimation of camera positions and orientations through bundle adjustment, an optimization process that simultaneously refines the 3D coordinates of scene points and camera parameters to minimize reprojection error [152, 149]. The resulting sparse point cloud represents the geometric structure of the scene, which can be further densified using Multi-View Stereo (MVS) algorithms [153, 154]. SfM model is inherently generated in an arbitrary, relative coordinate system lacking real-world scale, orientation, and position. To georeference the model, manually-acquired GCPs are integrated into the reconstruction process. By incorporating GCPs, the SfM solution is constrained and transformed into a global coordinate reference frame —WGS84-UTM 32N—, ensuring centimetric accuracy and spatial consistency [149, 155]. Although the georeferencing and scaling of the model can be achieved more recently using RTK-GNSS data associated with the camera projection centre,

this procedure is called direct photogrammetry or direct georeferencing. However, the accuracy of this process depends directly on the accuracy of the GNSS data used. With the introduction of onboard NRTK and RTK systems on drones, direct photogrammetry techniques now allow for direct georeferencing of the model with centimetric precision. Nevertheless, the uncertainty of the 3D reconstruction adds to the GNSS positioning uncertainty. For this reason, during the data collection phase, GCPs are often acquired and used to evaluate the accuracy of the SfM reconstruction.

Digital Elevation Models (DEMs) and orthomosaics are key products derived from photogrammetric processing workflows as it is SfM.
After the SfM stage establishes camera positions and a sparse 3D point cloud, MVS algorithms are applied to generate a dense point cloud that captures fine surface details by estimating depth information for each pixel across multiple overlapping images. From this dense point cloud, a Digital Surface Model (DSM) is typically produced by interpolating the 3D points onto a regular grid, representing the elevation of all visible surfaces.
The ortho-photo, or orthorectified image, is then generated by geometrically correcting each image using the DEM (or DSM) and the estimated camera parameters. This process removes distortions caused by camera tilt and terrain relief, projecting each image pixel to its true orthogonal position on the ground. The result is a planimetrically accurate image where distances, areas, and spatial relationships correspond directly to real-world measurements. Multiple ortho-rectified images are mosaicked together using radiometric balancing and seamline optimization to create a seamless orthomosaic.

Previews of SfM-generated DEMs/ortho-mosaics are presented in Appendices A and B, while in Table 2.7 are reported the resolutions of the final products as well as the area covered and the number of images acquired on every flight.

2.3.2 MBES data processing

The raw MBES data collected were processed using *BeamworX Autoclean*, an advanced yet user-friendly software designed for cleaning and managing bathymetric and LiDAR point clouds.
The program offers automated and manual data-correction capabilities, employing sophisticated algorithms—including spline-based filtering, statistical and spatial

coherence analysis, and least-squares surface fitting—to remove noise, validate data integrity, and adjust for tidal discrepancies. Additionally, users can directly interact with the dataset, manually editing, shifting, or removing individual points as needed [156, 157].

Previews of processed bathymetries are reported in Appendix C.

2.4 Post-Processing

2.4.1 Hydrodynamic Modeling

A comprehensive multi-scale modeling framework designed to analyze and simulate hydrodynamic processes in coastal regions is here presented. The final aim will be to characterize the wave runup on the foreshore of the study area A3, where a high-resolution near-shore bathymetry is available (Fig. C.2). As will be extensively discussed later on, wave runup is the main hydrodynamic process at the sea-land boundary that directly affects coastal vegetation patterns.
The framework (Fig. 2.19) mainly consists of two steps: *(i)*A large-scale wave model (Delft3D-WAVE) to compute the wave field modulation from off-shore to near-shore; *(ii)*a near-shore fine-scale hydrodynamic model (Delft3D-XBeach) to evaluate the wave runup in the swash zone.

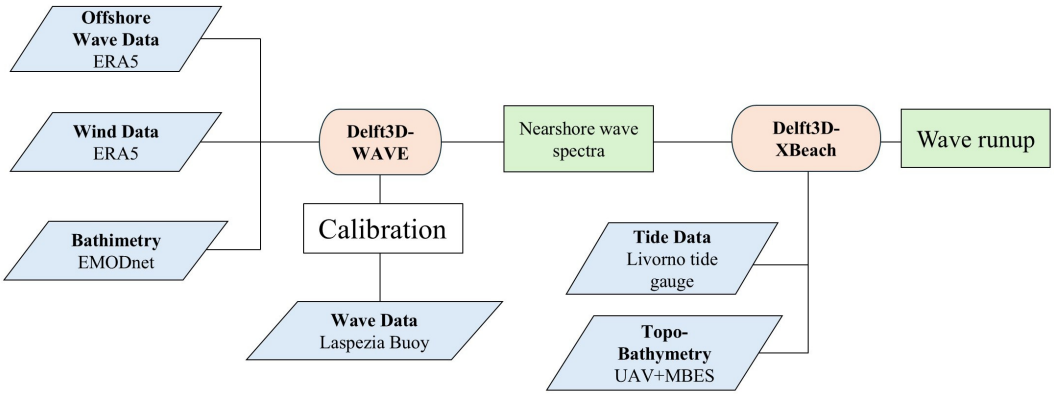

Fig. 2.19 Workflow of the the integrated hydrodynamic model.

Numerical Models

Delft3D is an advanced hydrodynamic modeling suite developed by Deltares, widely used for simulating water movement, sediment transport, waves, and water quality in rivers, estuaries, coastal zones, and seas.
One of Delft3D's key strengths lies in its modular design — integrating hydrodynamics (FLOW), waves (WAVE), sediment and morphology (MOR), and water quality (WAQ) module.
Delft3D is extensively used in coastal engineering, flood risk management, and environmental impact assessments, supporting decision-making for sustainable water management and infrastructure planning worldwide.

—Delft3D-WAVE—
Delft3D-WAVE module runs the Simulating Waves Nearshore(SWAN) model, a fully spectral, third-generation wave model [158, 159]. SWAN can simulate the generation, propagation, transformation, breaking, and associated hydrodynamic forces of short-crested, wind-generated random waves. SWAN has traditionally been used for coastal and shallow waters, However, numerous significant tests applying the SWAN model in deep waters for the study of hydrodynamic and wave variables associated with hurricanes proved its validity in a wider range of scenarios [160–165].

In SWAN the waves are described with the two-dimensional wave action density spectrum, $N(f,\theta)$, where f is the relative frequency (i.e., the frequency of the wave as observed in a frame of reference moving with the current velocity—in presence of a local current) and θ is the wave direction (i.e., the direction normal to the wave crest of each spectral component).
The evolution of the wave spectrum in space and time is described by the spectral action balance equation [166, 167]:

$$\frac{\partial N}{\partial t}+\frac{\partial}{\partial x}(c_{g,x}N)+\frac{\partial}{\partial y}(c_{g,y}N)+\frac{\partial}{\partial \sigma}(c_{g,f}N)+\frac{\partial}{\partial \theta}(c_{g,\theta}N)=\frac{S(f,\theta)}{f} \tag{2.1}$$

Where $\frac{\partial N}{\partial t}$ is the local rate of change of action density N, $\frac{\partial}{\partial \bullet}(c_{g,\bullet}N)$ are the propagation of N in geographical space $((x,y)$ and spectral space (f,θ) with $c_{g,\bullet}$ being the group celerity (i.e., the velocity of propagation of wave energy) in the same

spaces [167–169].
$S(f,\theta)$ is the sum of all sources of wave generation, dissipation and non-linear interactions, in terms of energy density (dE/dt): $S = S_{in} + S_w + S_b + S_{br}$, where

- S_{in} is the wind input term, accounting for the transfer of wind energy to the waves through resonance and feedback mechanism [170, 171].
- S_w is the whitecappig dissipation term, accounting for the wave steepness dissipation [166, 172, 173].
- S_b is the dissipation term accounting for bottom friction and interaction with the seabed [174–176].
- S_{br} is the depth-induced wave braking dissipation term [177, 178].

—Delft3D XBeach—
XBeach is an open-source numerical model which is originally developed to simulate hydrodynamic and morphodynamic processes and impacts on sandy coasts [179–181, 27].
The model includes the hydrodynamic processes of short wave transformation (refraction, shoaling and breaking), long wave (infragravity wave) transformation (generation, propagation and dissipation), wave-induced setup and unsteady currents, as well as overwash, runup and inundation.
Depending on the application, XBeach runs different hydrodynamic models from the simplest to more complex ones:

- Stationary mode: solves the phase averaged stationary action balance equation [182, 183], resolving wave propagation, directional spreading, shoaling, refraction, bottom dissipation and wave breaking but do not include wave growth or wave period variations.

$$\frac{\partial}{\partial x}(c_{g,x}N) + \frac{\partial}{\partial y}(c_{g,y}N) + \frac{\partial}{\partial \theta}(c_{g,\theta}N) = -\frac{D_w}{f} \tag{2.2}$$

  Where D_w is the wave energy dissipation function.

- Surf-beat (instationary) mode: solves the full action balance equation, resolving the variation of short-wave hight envelope and also longer-period

infragravity waves and unsteady currents driven by short-waves dissipation [182, 179, 184].

$$\frac{\partial N}{\partial t}+\frac{\partial}{\partial x}(c_{g,x}N)+\frac{\partial}{\partial y}(c_{g,y}N)+\frac{\partial}{\partial \theta}(c_{g,\theta}N)=-\frac{D_w}{f} \tag{2.3}$$

- Non-hydrostatic mode: solves the non-linear 2-D shallow water equations [185, 186], including a non-hydrostatic pressure to compute depth-averaged flow due to waves and currents [187].

$$\frac{\partial u}{\partial t}+u\frac{\partial u}{\partial x}+v\frac{\partial u}{\partial y}-\nu_h\left(\frac{\partial^2 u}{\partial x^2}+\frac{\partial^2 u}{\partial y^2}\right)=\frac{\tau^E_{sx}-\tau^E_{bx}}{\rho h}-g\frac{\partial \eta}{\partial x}+\frac{F_x}{\rho h} \tag{2.4}$$

$$\frac{\partial v}{\partial t}+u\frac{\partial v}{\partial x}+v\frac{\partial v}{\partial y}-\nu_h\left(\frac{\partial^2 v}{\partial x^2}+\frac{\partial^2 v}{\partial y^2}\right)=\frac{\tau^E_{sy}-\tau^E_{by}}{\rho h}-g\frac{\partial \eta}{\partial y}+\frac{F_y}{\rho h} \tag{2.5}$$

$$\frac{\partial \eta}{\partial t}+\frac{\partial hu}{\partial x}+\frac{\partial hv}{\partial y}=0 \tag{2.6}$$

Where ν_h is the kinematic viscosity, $\tau^E_{s|b}$ are the bed shear-stresses, ρ is the water density, h is the water depth, η is the water surface level and $F_{x|y}$ are wave-induced stresses.

Delft3d—WAVE

—Computational Domain—

The computational domain of the large-scale WAVE model (Fig. 2.20) consists of a rectangular mesh with a total of 4828 cells having size varying from 4km in the offshore part, down to 250m in the shallow waters region near A3. The total size of the domain is 85km in the N-S direction and 95km in the E-W direction.
The bathymetry underlying the mesh has been derived from the European Marine Observation and Data Network (EMODnet) Bathymetry database [188], composed by thousands of hydrographic surveys in the European seas, performed by different authorities and providing an open-access harmonized bathymetric dataset with $1/16$arcmin resolution ($\approx$ 115m).

Two observation points have been inserted within the domain: an off-shore point ($\approx$ 83m water depth), corresponding with the location of the Laspezia wave gauge (LWG), and a near-shore point, in the shallow waters right off the coastline of the study area A3 ($\approx$ 5m water depth).

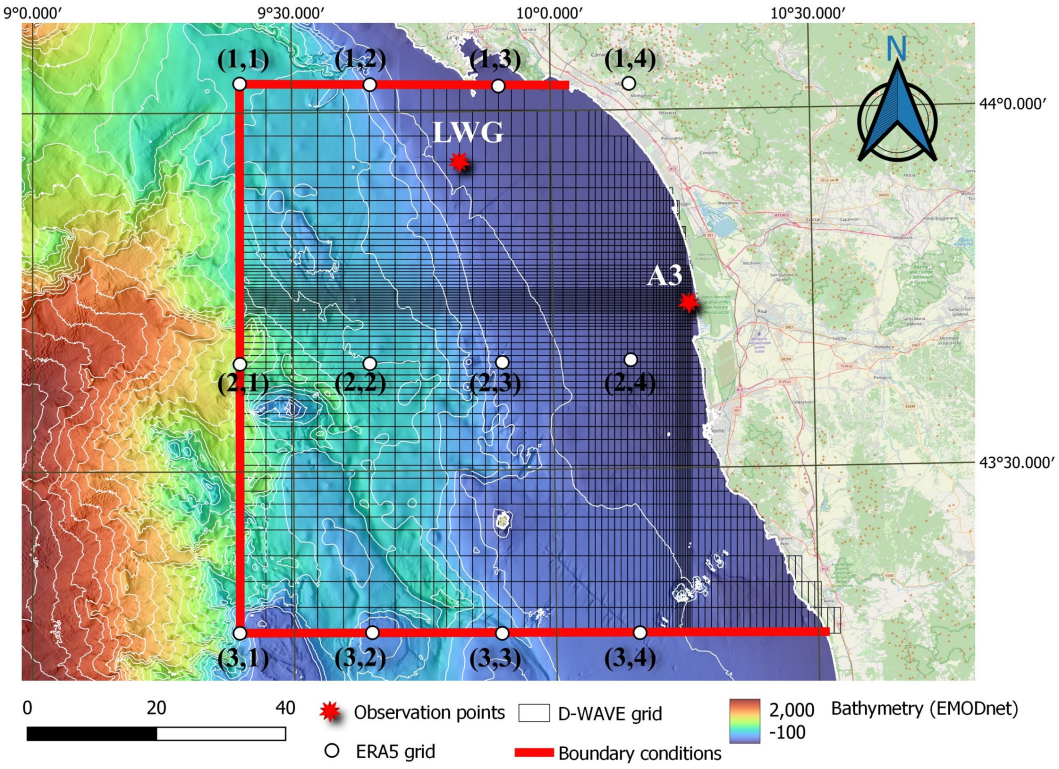

Fig. 2.20 Delft3D-WAVE computational domain.

The former serves the purpose of calibration and validation of the hydrodynamic model by comparing the simulated wave field parameters with those measured by the wave gauge; the latter is needed to derive the time-series of wave spectra that will be used as boundary conditions in the XBeach model.

—Boundary Conditions—

Two types of boundary conditions were applied in the WAVE model: *(i)* wave spectra at the model boundaries, and *(ii)* wind forcing applied uniformly in the nodes of the computational mesh.

Both wave and wind data were obtained from the *ERA5* reanalysis dataset (European Centre for Medium-Range Weather Forecasts, ECMWF), providing hourly time series extracted at the centroids of the ERA5 grid cells (indicated by white dots in Figure 2.20) from January 1-st 2023 to December 31-st 2024.

Waves at the domain boundary are modeled using the two-dimensional Joint North Sea Wave Project (JONSWAP) spectrum shape [176]:

$$E(f,\theta) = D(\theta)E(f) \tag{2.7}$$

with $E(f)$ being the one-dimensional JONSWAP wave spectrum and $D(\theta)$ the directional distribution of the wave field.

$$E(f) = \alpha g^2 (2\pi)^{-4} f^{-5} \exp\left[-\frac{5}{4}\left(\frac{f}{f_p}\right)^{-4}\right] \gamma^{\exp\left[-\frac{1}{2\sigma^2}\left(\frac{f}{f_p}-1\right)^2\right]} \tag{2.8}$$

$$D(\theta) = \cos^m(\theta - \theta_p); \int_0^{2\pi} D(\theta) = 1 \tag{2.9}$$

In equation 2.8, $\alpha(\propto H_s)$ is the energy scale parameter, $f_p = 1/T_p$ is the peak frequency, γ is the peak enhancement factor (usually set at 3.3) and $\sigma(\propto f_p)$ is the width of the spectrum peak. In equation 2.9, θ_p is the peak wave direction and m is the power that controls the width of the distribution. The first and second moments of the directional distribution $D(\theta)$ are, respectively, the mean wave direction θ_m and the directional spreading σ_θ.
In WAVE, the JONSWAP spectrum is parameterized by four parameters: the significant wave height H_s and peak period T_p to characterize the 1-D spectrum $E(f)$, and the mean wave direction θ_m and directional spreading σ_θ defining the directional distribution $D(\theta)$.

Wave boundary conditions were imposed along three sides of the computational domain —the western, northern, and southern boundaries— highlighted with red lines in Figure 2.20. The spatial variation of the wave parameters values along the domain boundary is set as follows:

- Along the western boundary, parameters vary linearly between ERA5 grid points $(1,1)$ and $((3,1)$.
- Along the southern boundary, parameters vary linearly between grid point $(3,1)$ and the coastline (where $H_s = 0$).
- Along the northern boundary, parameters vary linearly between grid point $(1,1)$ and the coastline.

For the wind forcing, a time series of the horizontal wind components (u, v) at 10 m above sea level were employed. The wind forcing was applied uniformly over the entire computational mesh, using the spatial average of the wind components from the four outermost ERA5 grid points: $(1,1)$, $(1,4)$, $(3,1)$, and $(3,4)$.

—Model Calibration—

To assess the ability of the Delft3D-WAVE model to reproduce real-world wave conditions, a sensitivity analysis was carried out by varying selected model parameters.

A key limitation in this calibration process is that model results were compared with observations from only one offshore measurement point (LWG). In fact, numerical parameters that predominantly affect wave propagation in shallow areas—such as depth-induced breaking, bed friction, and refraction—could not be easily tuned due to the lack of nearshore wave measurements.

Consequently, the calibration primarily constrains those parameters influencing wave

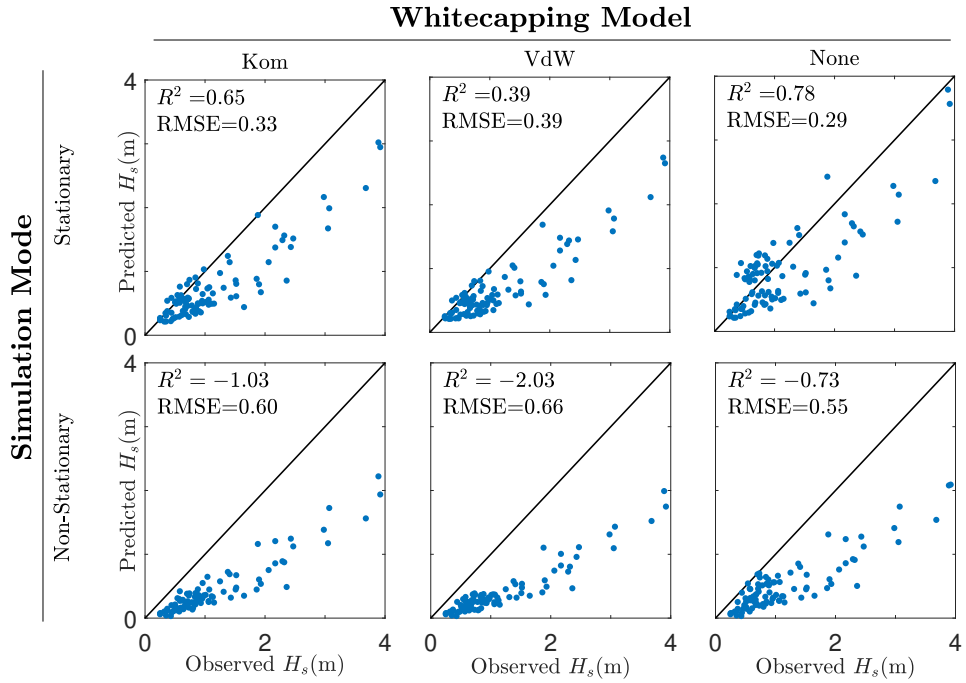

Fig. 2.21 Results of the WAVE model sensitivity analysis. Each panel shows the observed against predicted H_s (blue dots) compared with the plane bisector (black line). In the top-left corners are reported the performance metrics of each simulation.

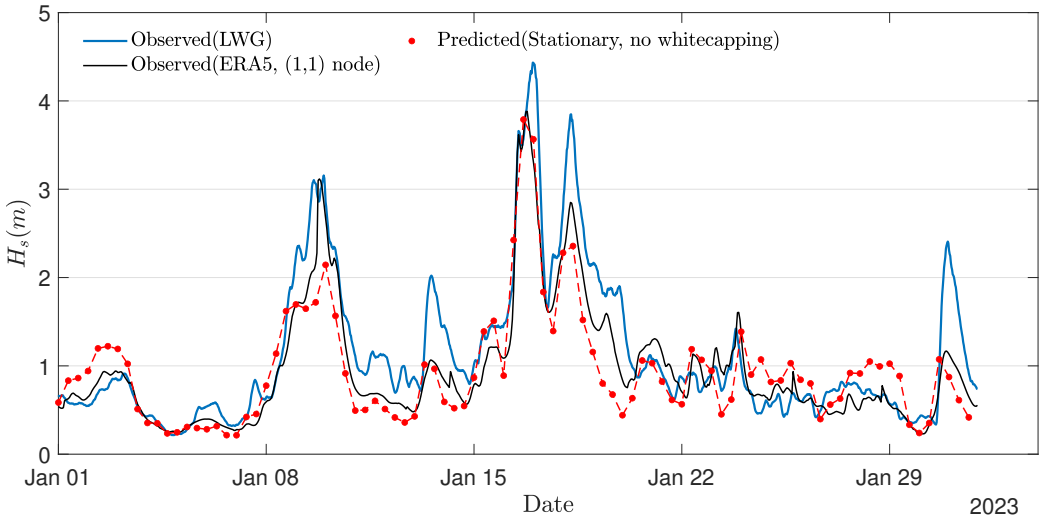

Fig. 2.22 Comparison between H_s observed at LWG (solid blue line) and ERA5 boundary node (1,1) (solid black line), and predicted by the stationary WAVE model with no whitecapping dissipation (red dots).

dynamics in deep waters, specifically *(i)*the whitecapping dissipation model (Komen, Van der Westhuysen, or none), and *(ii)*the computation mode (stationary or non-stationary).
The calibration strategy involved six simulations, corresponding to all combinations of the two varying parameters. Each simulation covered a one-month period, from January 1-st to January 31-st, 2023. This duration was chosen as a balance between computational efficiency and the need for a sufficiently long dataset to include a range of wave conditions—from calm to stormy events—allowing for statistically meaningful comparisons.
Model performance was evaluated by comparing simulated and observed significant wave height (H_s) using two statistical indicators: the coefficient of determination (R^2) and the root mean square error ($RMSE$).
The parameters used to set up the simulations are listed in Table 2.12.

Results of the calibration (Figure 2.21) indicate that the best overall model performance, in terms of both R^2 and $RMSE$ scores, was achieved without whitecapping dissipation and using the stationary computation mode ($R^2 = 0.78$, $RMSE = 0.29$).

One possible explanation for the general underestimation of the modeled H_s compared to observations, even in the best-performing setup, is that the ERA5-derived H_s values themselves, used as boundary conditions, tend to underestimate the wave

Parameters class	Parameter	Value
General	Directional convention	nautical
	Simulation mode	[stationary; non-stationary]
	Output time-step (h)	8
Spectral domain	Number of directions	36
	Number of frequencies	50
	Min. frequency (Hz)	0.03
	Max. frequency (Hz)	1
Physical Processes	Physics mode	third generation
	Wind growth	on
	Quadruplets	on
	Refraction	on
	Frequency shifting	on
	Depth-induced breaking α	1
	Depth-induced breaking Γ	0.73
	Bed friction model	JONSWAP
	Bed friction coeff	0.067
	Whitecapping model	[Komen; Van der Westhuysen; none]
	Wave-wave interaction triad α	0.05
	Wave-wave interaction triad β	2.5
Wave BC	Spectrum formulation	JONSWAP
	Peak enhancement factor	3.3
	Time-step (h)	4
Wind BC	Input type	Per timepoint
	Time-step (h)	8

Table 2.12 Delft3D-WAVE model setup parameters.

heights, especially those medium-high wave peaks in the $2-3$ m range, as shown in Figure 2.22. This systematic bias in the boundary input likely propagates throughout the model domain, leading to an overall underestimation of simulated wave heights, even in the presence of wind energy input. Consequently, the model's apparent under-performance may be partly attributed to inaccuracies in the offshore forcing data rather than to deficiencies in the model parameterization itself.

—Off-shore to near-shore wave modulation—

The optimal model setup achieved in the calibration phase is used to run a two-year simulation from January 1-st 2023 to December 31-st 2024.

Simulation output is presented in Figure 2.23, which shows the full time series of H_s at the observation points LWG and A3 (Fig.2.23a,b), along with an example of the evolution of the wave field during an extreme storm event that occurred in December 2023. Figures2.23c–h portrait the spatial distribution of H_s and mean wave direction, θ, across the 2-D computational domain, highlighting several key features: *(i)* attenuation of wave height from deep to shallow waters; *(ii)* a change in wave direction as waves propagate shoreward; and *(iii)*the sheltering effect caused by

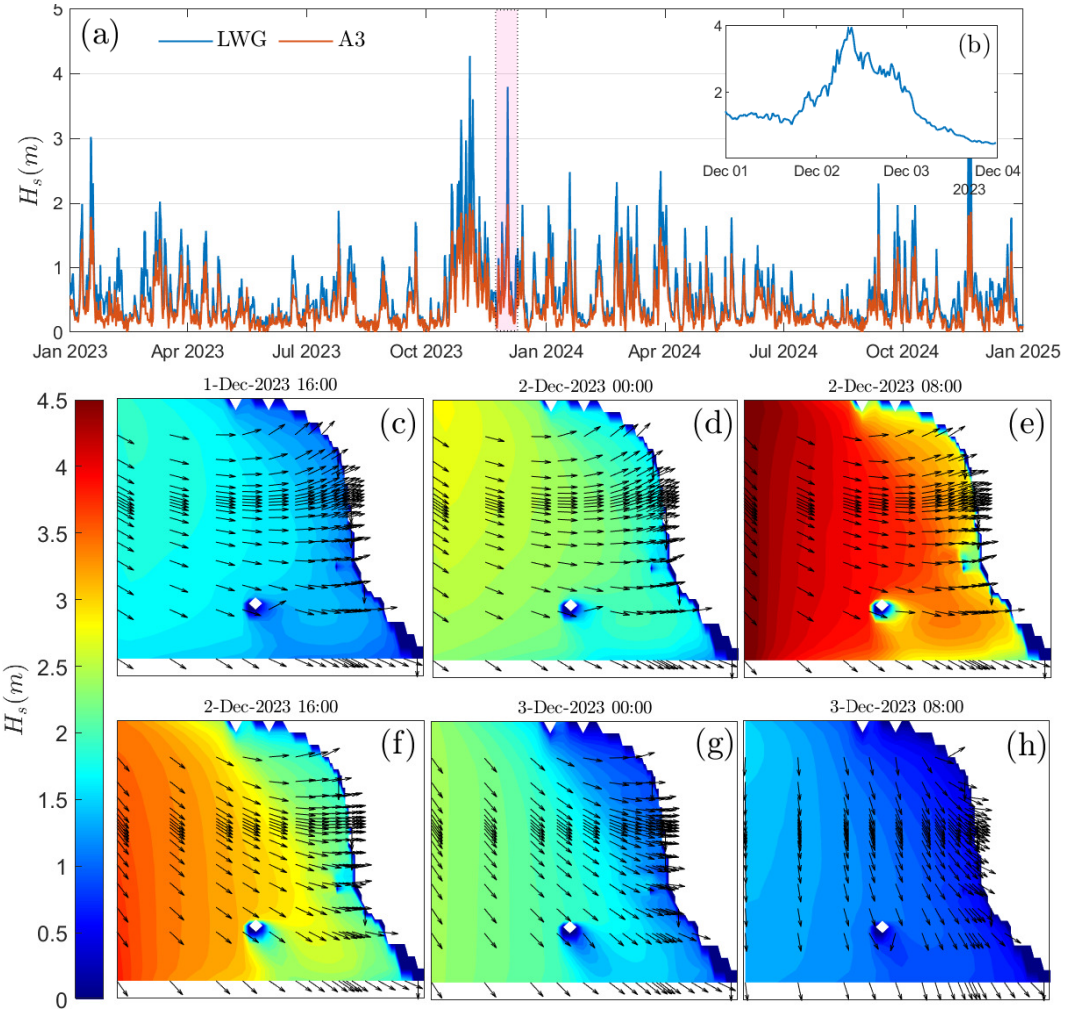

Fig. 2.23 Delft3D-WAVE simulation output. (a)Time series of H_s at observation points LWG (blue line) and A3 (red line). A particular extreme storm event is highlighted with a pink shade. (b)Expanded view of H_s time series during an extreme storm event (pink shade), occurred between December 1-st and 4-th, 2023. (c)-(h)Evolution of the wave field during the extreme event. Color gradient indicates H_s values, while black arrows indicates the mean wave directions.

the presence of an obstacle (white area in the lower part of the domain, representing *Gorgona Island*, one of the largest islands in the *Ligurian Sea*), which significantly reduces wave heights in its lee.

Figure 2.24 displays a comparison of output data at the offshore and nearshore observation points, highlighting the modulation of the wave characteristics propagating from deep to shallow waters.

Probability density functions (PDFs) of H_s (Fig. 2.24a,b) show how the offshore site

(LWG) exhibits larger and more variable wave heights, with a mean $H_s = 0.56$m and standard deviation of 0.49m, compared to the shallower site (A3), where H_s is lower

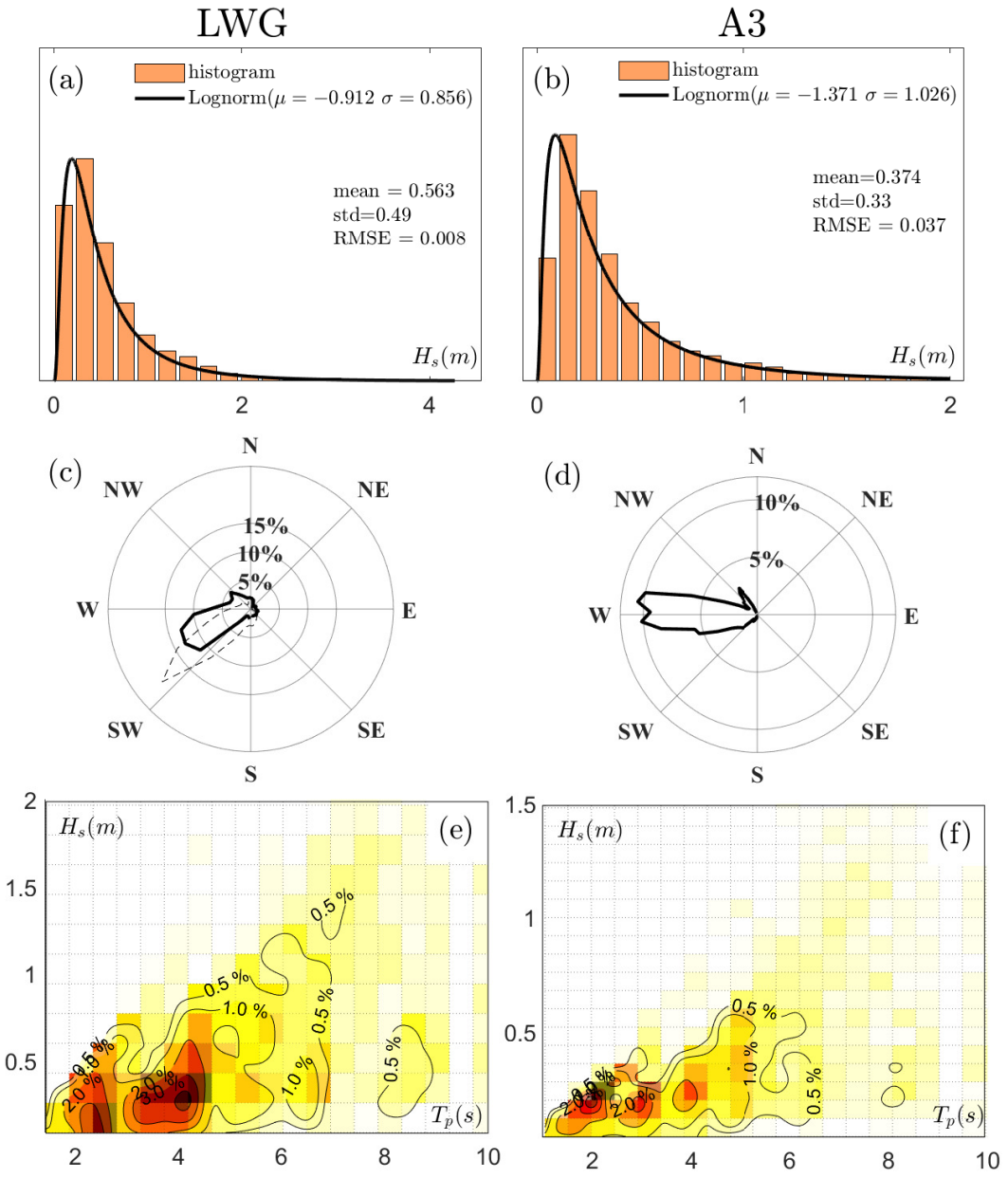

Fig. 2.24 Comparison between the features of the wave field in open sea (at observation point LWG) and near-shore (at A3 observation point). (a)- (b)PDFs of H_s. (c)-(d)Wave-roses. Solid lines indicates the polar distributions of simulated mean wave directions, while the dashed line represents the distribution of measured mean wave directions at LWG. (e)- (f)Joint probability density function of H_s and T_p.

on average (0.37m) and less variable (0.33m). The lognormal fits well-describe both datasets, with low *RMSE* values (0.008 for LWG and 0.037 for A3).
In figures 2.24c,d, wave roses show a shift in the dominant wave direction, from South-West (at LWG) to West (at A3), the latter being quasi-perpendicular to the coastal stretch direction of the study area A3. This 'steering' of wave direction is a well-known phenomenon caused by the refraction of waves in shallow waters due to the interaction between the seabed and the orbital motion of water particles.
Figures 2.24e,f present the joint probability distributions of H_s and peak period (T_p). Offshore waves at LWG exhibit higher H_s and longer T_p values, reflecting more energetic conditions, while A3 shows a concentration of lower H_s and shorter T_p, consistent with wave energy dissipation and transformation in shallow water.
Overall, these results illustrate an expected attenuation and shortening of waves as they propagate from deep to shallow environments.

Delft3D—XBeach

—Computational Domain—

A one-dimensional computational mesh have been used as base elevation model in the Delft3D XBeach model (v1.24) to minimize computational cost while maintaining sufficient spatial detail for resolving nearshore hydrodynamics.

The model domain was constructed using the topo-bathymetric surface (Fig. 2.25a) produced by merging the Digital Terrain Model (DTM) and bathymetry surveyed in 2024 campaign (Fig.B.3d and Fig.C.2a).
From this combined surface, a representative 1-D bathymetric profile (Fig. 2.25b) was extracted as the cross-shore average of the topo-bathymetry. The resulting profile clearly shows the presence of a distinct shallow sand bar seaward of the shoreline, which plays an important role in wave transformation processes.

The computational grid extends for a total of 195m in the cross-shore direction and it's formed by 225 cells with variable size, decreasing from 5 m in the offshore region to 0.5 m in the surf and swash zones to accurately capture wave shoaling, breaking and runup.
The offshore limit of the domain reaches a maximum water depth of approximately 4.5m.

—Boundary conditions and model setup—

Two types of boundary conditions were imposed in the XBeach model: *(i)*tides and *(ii)*waves boundary conditions.

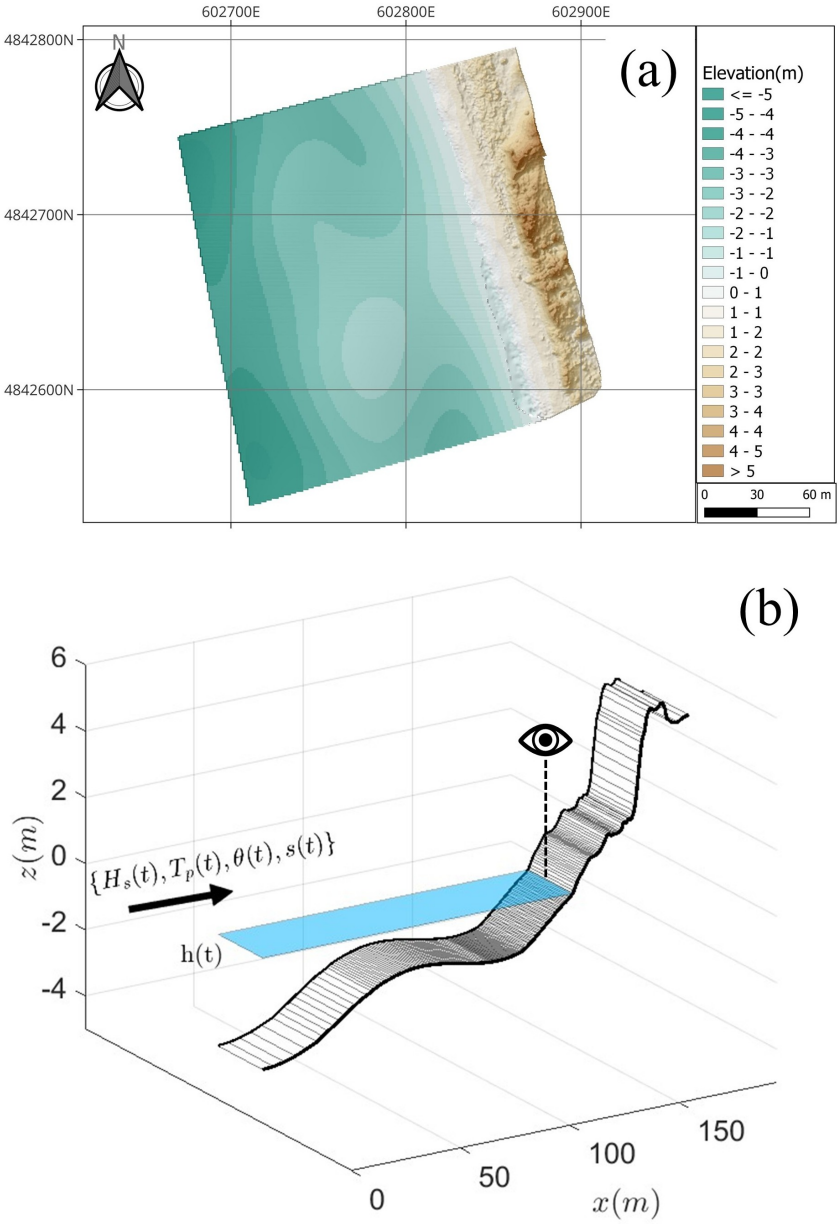

Fig. 2.25 (a) Topo-bathymetry of the A3 study site. (b) XBeach 1-D model mesh. The black arrow identifies where wave boundary conditions are imposed, and the blue shading represents the 0-m elevation reference level. The eye symbol represent a runup virtual observation point.

Tidal forcing was imposed as a uniform temporal variation of the mean sea level across the entire model domain (Fig.2.25b). The tidal time series was obtained from water-level records at the Livorno meteorological station (Fig. 2.1a).

A spectral wave boundary condition was applied at the offshore edge of the computational domain (Fig.2.25b). The offshore forcing consisted of a time series of JONSWAP wave spectra, parametrized through the significant wave height H_s, peak period T_p, mean wave direction θ, and s, proportional to the directional spreading σ_θ through the relation

$$\sigma_\theta = \sqrt{\frac{2}{s+1}s} \tag{2.10}$$

All spectral parameters were extracted from the WAVE model output at the nearshore observation point A3 with a time-step of 8 hours.

For the simulations presented in this study, the seabed was treated as *non-erodible*. Although this choice is not ideal for representing fully coupled hydro–morphodynamic processes, it is justified by the absence of observational data against which modeled morphological changes could be validated.
Furthermore, the primary objective of this work is the characterization of wave runup from a purely hydrodynamic perspective; therefore, detailed morphodynamic evolution lies outside the scope of the present analysis. The use of a fixed bed allows us to isolate hydrodynamic processes and evaluate runup behavior without introducing uncertainties associated with unvalidated sediment transport and morphological processes.

Because the available wave forcing consisted of a time series of JONSWAP spectra rather than an observed sequence of individual waves or water levels, the boundary condition provides only the statistical properties of the sea state for each 8-hour time-step. In XBeach, such spectral translates in a series of stochastic wave realizations matching the prescribed spectral characteristics. Consequently, performing long and costly 8-hour simulations for each spectrum does not necessarily introduce additional physical information compared to shorter simulations; instead, it merely prolongs the duration over which statistically equivalent random waves are produced.
To reduce computational demand while retaining the essential hydrodynamic forcing, each 8-hour spectrum was therefore represented by only 16 minutes of model time, corresponding to a time-compression factor of 2 minutes/1 hour.

Therefore, a 2-year simulation is reduced to about 24 days, enough to contain a sufficient number of waves to produce statistically meaningful runup estimates.

A virtual observation point (Fig. 2.25b) was also integrated into the model to track directly the on-shore wave dynamics by providing a time series of the peak water level and distance reached within the swash zone with sampling frequency of 1Hz.

A summary of the main parameters of the simulation is reported in table 2.13.

Parameters class	**Parameter**	**Value**
General	Computational mode	Non-hydrostatic
	Courant number (CFL)	0.8
	Simulation duration (d)	24
	Output time-step (s)	1
Morphology	Sediment transport	off
	Bed composition—D50 (mm)	0.5
	Bed composition—D90 (mm)	0.7
Wave boundary conditions	Type	Spectral—JONSWAP
	Time-step (min)	16
Tide boundary conditions	Type	uniform
	Time-step (min)	2

Table 2.13 Delft3D-XBeach model setup parameters.

—Wave runup—

The prediction of wave runup, commonly relies on empirical Iribarren-based parameterizations (i.e., runup is scaled with the Iribarren number, $\xi = \beta_f / \sqrt{H/L}$) such as those proposed by Stockdon et al. (2006) [189]. However, these formulations were not originally developed to represent extreme marine conditions, thus motivating the need for further evaluation, potentially through numerical modeling approaches.

In this context, XBeach offers a robust tool for simulating runup dynamics during extreme storm surges because it directly resolves wave setup and low-frequency oscillations, which typically dominate runup behavior under highly dissipative storm conditions [190]. The use of XBeach for runup prediction is particularly relevant because direct field measurements during severe storms are difficult to acquire; strong hydrodynamic forces and rapid morphological changes may damage instruments or introduce substantial uncertainty into the topographic datasets required for analysis. Moreover, accurate runup estimates are essential for assessing the performance and

safety of coastal defense structures operating in the collision regime, as they influence the determination of crest elevations, especially for rare, high-return-period events.

Wave runup, R, is defined as the sequence of local maxima of the water level reached on the foreshore relative to the mean water level (MWL) (Fig.3.6a). The

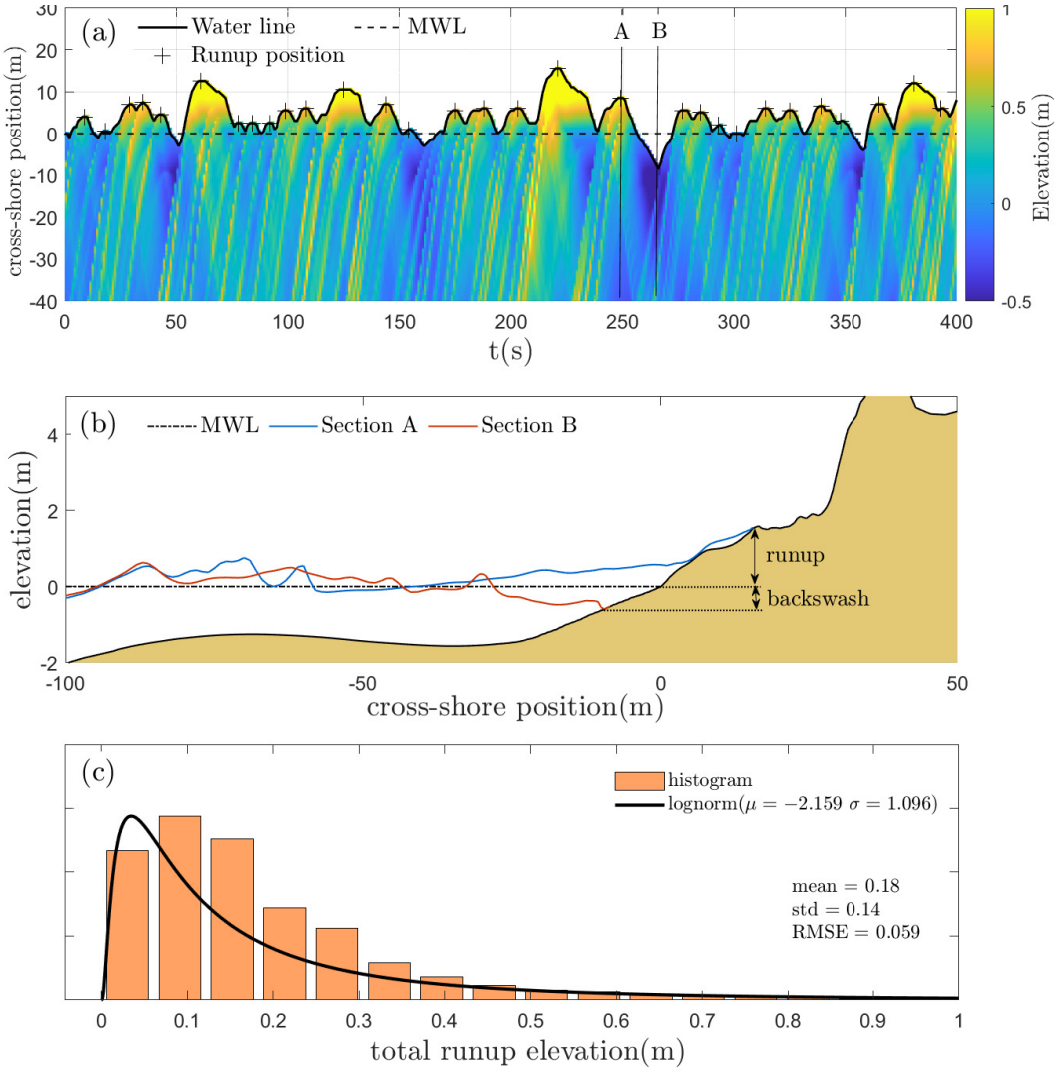

Fig. 2.26 Summary of XBeach model outputs. (a)Time stack of water surface elevation profiles over a 400 s interval. Two cross sections are highlighted, sections A and B, corresponding to a runup and a backwash. (b) Cross-shore sections of successive runup (section A) and backwash (section B) cycle. Dashed line represents the mean water level. (c)PDF of total runup elevation ($h+R$).

total runup elevation results from the combination of MWL fluctuations due to tides (h), wave setup ($\langle\eta\rangle$) and swash (S).

Wave setup, $\langle\eta\rangle$, denotes the time-averaged increase in water level at the shoreline, produced by cross-shore gradients in radiation stress generated during wave breaking. These gradients transfer wave momentum to the water column during the breaking phase and drive an onshore-directed force that elevates the water level above the MWL [189, 191–193].

Superimposed on this mean increase is the swash component, S, which represents the vertical oscillations of the shoreline around the setup elevation. Swash is controlled primarily by the deep-water significant wave height H_0 and the beach slope β_f, and it originates from the dissipation of wave energy on the beach slope. It consists of an uprush phase, during which water propagates landward after wave breaking and attains the runup elevation, followed by a backwash phase in which the flow recedes seaward under the influence of gravity (Fig.3.6b).
In the existing literature, the swash spectrum of shoreline water level fluctuations is generally characterized by two dominant frequency bands (Fig. 2.27b), each associated with distinct physical forcing mechanisms and beach dynamic conditions (e.g., dissipative versus reflective beaches). The incident band (S_{Inc}), comprising frequencies > 0.05Hz, reflects the direct influence of short-wave processes such as wind-generated sea and swell. In contrast, the infragravity band (S_{IG}), defined by frequencies < 0.05Hz, arises from nonlinear wave-wave interactions, group forcing, and shoaling processes that amplify low-frequency energy as waves approach the shore. These infragravity motions become particularly prominent on dissipative beaches, where wave breaking and energy dissipation enhance the generation and propagation of long-period oscillations.

A general relationship has been proposed by Stockdon et al. (2006) for the extreme runup values, corresponding to the 2% exceedance runup series (Fig. 2.27a), generated in a given sea and beach state:

$$R_{0.02}(H_0, T_0, \beta_f) = 1.1\left[\langle\eta\rangle + \frac{S}{2}\right] \tag{2.11}$$

With $S = \sqrt{S_{Inc}^2 + S_{IG}^2}$, while H_0 and T_0 significant wave height and wave period in deep-water.

A preliminary characterization of total on-shore water elevation (tide+runup) at study site A3 is shown in Figure 3.6c. It exhibits a distribution that is best represented by a lognormal model ($RMSE = 0.059$). The 50-th, 95-th, and 99-th percentiles of this distribution—where the 99th percentile corresponds to runup levels associated with extreme storm events—are 0.18m, 0.70m, and 1.48m, respectively.

A comparison between the XBeach simulation results and the empirical runup formulation proposed by Stockdon et al. (2006) (hereafter S06) is therefore a natural step. Each runup component obtained from the model is compared with its corresponding parameterized expression from S06.

Because the S06 expressions depend on deep-water wave parameters through the Iribarren-like term $\sqrt{H_0 L_0}$, the first step consisted of estimating the deep-water significant wave height H_0 and the deep-water wavelength L_0. At the offshore boundary the water depth $d \approx 4.5$m falls in the range of the intermediate-waters ($\frac{1}{20} < \frac{d}{L} < \frac{1}{2}$); therefore, the significant wave height H_s and wavelength L imposed to the boundary must be back-shoaled to deep water.

In linear wave theory, the wave period $T (= T_p)$ is conserved during the shoaling because nonlinear and breaking effects are neglected. T_p is therefore used to compute the deep-water wavelength L_0 from the dispersion relation:

$$L = \frac{g T_p}{2\pi} \tanh\left(\frac{2\pi d}{L}\right) \tag{2.12}$$

To determine a depth sufficiently representative of deep-water conditions, the ratio d/L was evaluated for a range of depths. A depth of approximately 27 m yielded $d/L > 1/2$ for the conditions considered and was thus adopted to compute H_0 and L_0.

The deep-water significant wave height H_0 was obtained by inverting the shoaling transformation:

$$H_0 = K_{sh} H_s = \sqrt{\frac{c_{g0}}{c_{g1}}} H_s \tag{2.13}$$

where the shoaling coefficient is $K_{sh} = \sqrt{\frac{c_{g0}}{c_{g1}}}$ and c_{g0} and c_{g1} are the group velocities in deep and intermediate water, computed from linear wave theory:

$$c_g = \frac{1}{2}\left(1 + \frac{2kd}{\sinh(2kd)}\right)\sqrt{\frac{g}{k}\tanh(kd)} \tag{2.14}$$

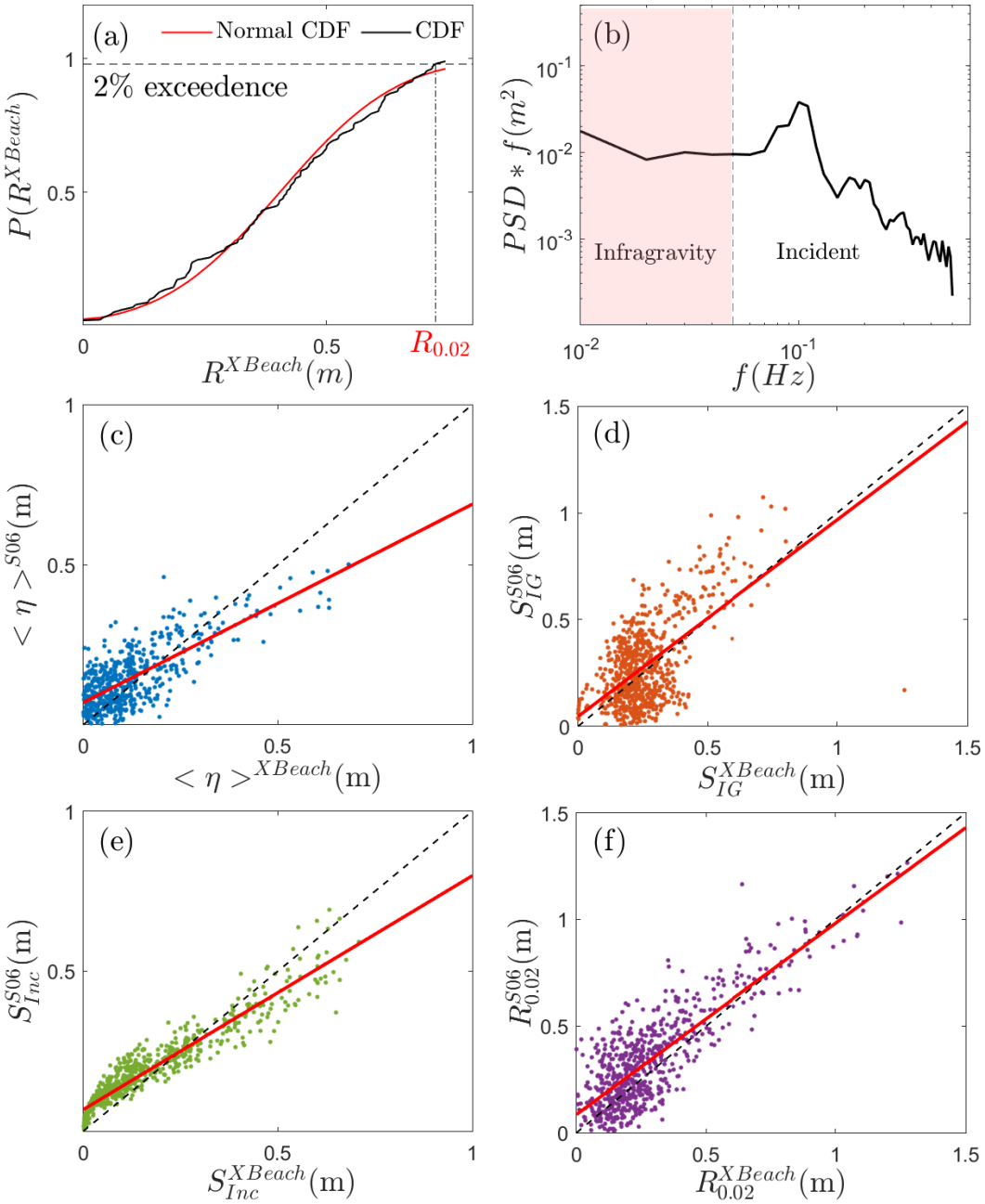

Fig. 2.27 Comparison between runup components from XBeach simulation and empirical model by Stockdon et al., 2006 (S06). (a)Computation of the 2% exceedence runup; (b)pre-multiplied power spectral density (PSD). Infragravity and incident wave spectra are highlighted; (c)Simulated vs empirical setup $\langle\eta\rangle$; (d)Simulated vs empirical infragravity swash S_{IG}; (e)Simulated vs empirical incident swash S_{Inc}; (f)Simulated vs empirical 2% exceedence runup $R_{0.02}$. Solid red lines in panel (c)-(f) represents data linear regression.

with $k = 2\pi/L$ being the wavenumber.

Given a foreshore slope β_f ($\beta_f = 0.12$ in this case), the S06 expressions for mean setup, incident-band swash, and infragravity swash read:

$$\langle \eta \rangle^{S06} = 0.35\beta_f \sqrt{H_0 L_0} \tag{2.15}$$

$$S_{Inc}^{S06} = 0.75\beta_f \sqrt{H_0 L_0} \tag{2.16}$$

$$S_{IG}^{S06} = 0.06\sqrt{H_0 L_0} \tag{2.17}$$

while the corresponding expressions to compute runup components from the simulation output data read as follows:

$$\langle \eta \rangle^{XBeach} = \frac{1}{T}\int_0^T \eta(t)dt \tag{2.18}$$

$$S_{Inc}^{XBeach} = 4\sqrt{\int_{0.05}^{f_s/2} S_\eta(f)df} \tag{2.19}$$

$$S_{IG}^{XBeach} = 4\sqrt{\int_0^{0.05} S_\eta(f)df} \tag{2.20}$$

where $\eta(t)$ is the on-shore level time series, f_s is the sampling frequency of $\eta(t)$ (1Hz) and $S_\eta(f)$ is the power spectral density (PSD) of the detrended time series of the on-shore level, depurated from the setup, $\eta(t) - \langle \eta \rangle$.

	a	b	R^2	$RMSE$	ρ_{xy}
$\langle \eta \rangle$	0.6198	0.0694	0.3769	0.0875	0.6863
S_{Inc}	0.7307	0.0675	0.8186	0.0621	0.9515
S_{IG}	0.9214	0.0461	0.316	0.1871	0.6047
$R_{0.02}$	0.8966	0.0854	0.5954	0.1724	0.8051

Table 2.14 Statistics describing the agreement between runup parameters computed using XBeach 1-D and S06 model. a and b are the coefficient of the linear regression ($y = ax + b$); R^2 and $RMSE$ are the coefficient of determination and root mean square error of the data (points) relative to the 1 : 1 line; ρ_{xy} is the correlation coefficient between XBeach and S06 data.

The results of the comparison between XBeach-derived runup parameters and the empirical formulations of S06 are presented in figure 2.27c-f and a summary of the performance statistics is reported in table 2.14.

Figure 2.27c shows moderate correspondence of $\langle\eta\rangle$ between the two approaches ($R^2 = 0.38$, $RMSE = 0.09$), with a regression slope below the 1:1 line, reflecting the tendency of S06 to slightly overestimate the setup at low values compared to XBeach, while underestimating at higher values. A good linear correlation emerges between the two datasets, with $\rho_{xy} = 0.69$.

The infragravity swash data S_{IG} (Fig. 2.27d) presents a linear regression that, among the others, is the closest to the $1:1$ line ($a = 0.92$, the closest to 1, and $b = 0.04$, the closest to 0), meaning that, on average, the data are 'well-balanced' around that line —except for the fewer values in the higher range that are overestimated by S06, compared to XBeach. However, it shows the highest degree of dispersion ($R^2 = 0.31$, $RMSE = 0.18$) and a moderate level of linear correlation ($\rho_{xy} = 0.6$).

For S_{Inc} (Fig. 2.27e), like $\langle\eta\rangle$, S06 predicts slightly overestimated values compared to XBeach in the lower range of values, and moderately underestimates the modeled values in the higher range of values. Overall, the data dispersion around the bisector line is extremely limited ($R^2 = 0.81$, $RMSE = 0.06$) and it shows a very high linear correlation ($\rho_{xy} = 0.95$). The incident component of the swash is by far the parameter that shows the best agreement between XBeach and S06.

Finally, the 2% exceedance runup data $R_{0.02}$ (Fig. 2.27f), despite presenting a moderate level of dispersion ($R^2 = 0.6$, $RMSE = 0.17$), shows a linear regression very close to the $1:1$ line and a strong linear correlation ($\rho_{xy} = 0.81$). Overall, the 1-D XBeach model and S06 data show a good level of consistency in predicting runup extreme values.

Final Remarks

The comparison between XBeach-derived runup parameters and the empirical S06 formulation — tuned on field data— demonstrates a generally consistent relationship across the setup and swash components, though with varying performance depending on the underlying physical processes.
While this consistency is encouraging, particularly given the simplicity and computational efficiency of the empirical expression, the present results also highlight the need of validating both approaches against high-quality field measurements, which are currently lacking. As demonstrated by Stockdon et al. (2014) [190], systematic

biases can persist in numerical models due to uncertainties in boundary conditions, hydrodynamic formulations, and beach profile representation. A targeted comparison with in situ observations would allow for the calibration of XBeach to local conditions, correction of systematic deviations, and overall improvement of its predictive skill.
Such calibration is especially critical for the infragravity and setup components, where the numerical model's process-based nature should theoretically offer an advantage but may still require tuning to reproduce field behavior accurately.
Nevertheless, the fact that, for identical boundary conditions, the empirical S06 formulation demonstrates such strong agreement with a demanding, process-resolving numerical model lends confidence to its continued use in practical situations — at least in the cases with gently-sloping sandy beaches with no significant seabed morphological changes— especially if a near-shore bathymetry is not available.

Most importantly, it suggests that the commonly employed two-step hydrodynamic modeling approach—a large-scale wave propagation model and, subsequently, a computationally demanding high-resolution nearshore simulation—may be unnecessary when the objective is limited to runup estimation.
If the large-scale model is well-calibrated, its output can be coupled directly with the S06 empirical formulas to provide reliable runup predictions, thereby eliminating the need for the more resource-intensive XBeach phase. Under this framework, the burden of accuracy shifts toward the large-scale wave simulation, which can be further enhanced through integration of a hydrodynamic flow model (e.g., Delft3D-FLOW) and constrained via multiple field observations, including buoy measurements and remote sensing techniques. This modeling simplification offers a computationally efficient pathway for operational runup forecasting while maintaining high predictive fidelity.

2.4.2 Geomorphological Analysis

In this section, we analyze the geomorphological changes occurring within the dune fields of study areas A2 and A3, with the aim of characterizing the main sediment-transport dynamics, volumetric variations, and coastal erosion/accretion processes observed during the field measurement campaigns conducted between 2021 and 2025. These morphological changes are then interpreted in relation to local wave and wind forcing. Study area A1 was excluded from this analysis because elevation

data are available only for the period 2021–2023, whereas A2 and A3 provide a longer and more consistent dataset (2021–2025), which is essential for assessing the multi-year coastal evolution of the San Rossore Regional Park.

As illustrated in Figure 2.28, the spatial extent of the surveyed regions varied among campaigns. To ensure a coherent comparison across years, we selected, for each study area, the intersection of all annual survey footprints (black rectangles in Figures 2.28a,b), guaranteeing the availability of elevation data for every campaign.

Because our focus is on terrain-surface changes, the first step of the analysis involved extracting the bare-earth topography from the elevation models derived from UAV imagery, eliminating all the possible features, such as vegetation and beached woody debris.
The DEMs for the study areas were processed in QGIS to generate Digital Terrain Models (DTMs) following this workflow: *(i)* a slope-based DTM filter was applied to the DSMs [194] to remove above-ground features such as vegetation and other objects; *(ii)* a multilevel B-spline interpolation algorithm [195] was used to fill gaps in the filtered DEMs.

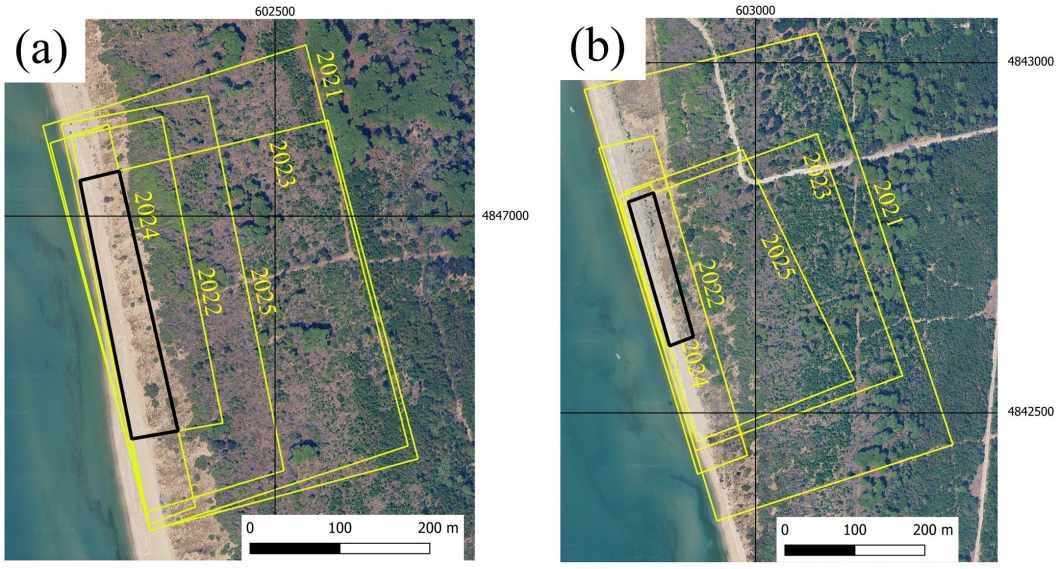

Fig. 2.28 Spatial extent of the surveyed regions (yellow polygons) within study areas A2 (a) and A3 (b) during the measurement campaigns conducted from 2021 to 2025. The black rectangles indicate the overlapping surveyed areas where morphological evolution was examined.

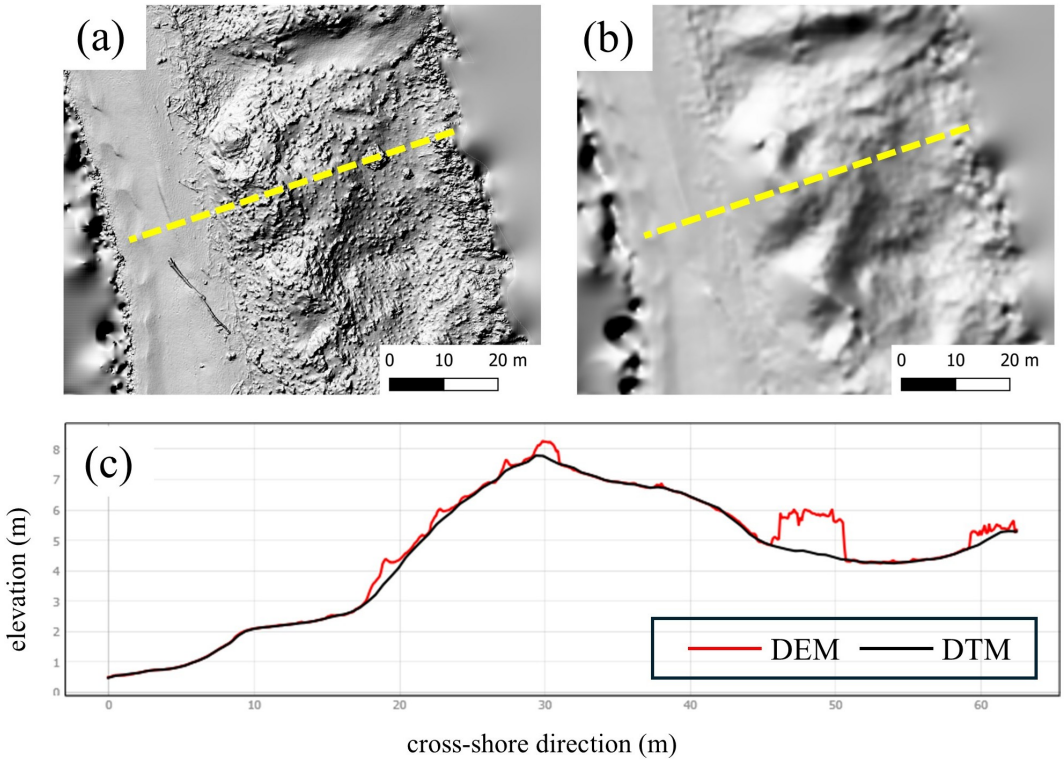

Fig. 2.29 Example of DEM (a) versus DTM (b). All the feature present in the DEM, including vegetation and large woody debris, are eliminated in the DTM. (c) Elevation profiles of the cross sections marked with the yellow dashed line in panels (a) and (b).

Down-scaled DTMs, with resolution of 0.5m are used to carry on the following analysis.

Environmental Forcings

To relate the observed morphological changes to the main environmental forcings, wind and wave data were obtained from the national monitoring network previously described in the section on local climatic characterization.
As a matter of fact, these forcings play distinct yet complementary roles in shaping coastal evolution: while wind regimes exert primary control over the long-term morphodynamics of the subaerial beach, influencing dune accretion or erosion, as well as nutrient transport to coastal vegetation. Wave conditions, conversely, govern short- to medium-term shoreline dynamics, driving beach erosion and modulating the annual sediment supply associated with longshore drift processes.

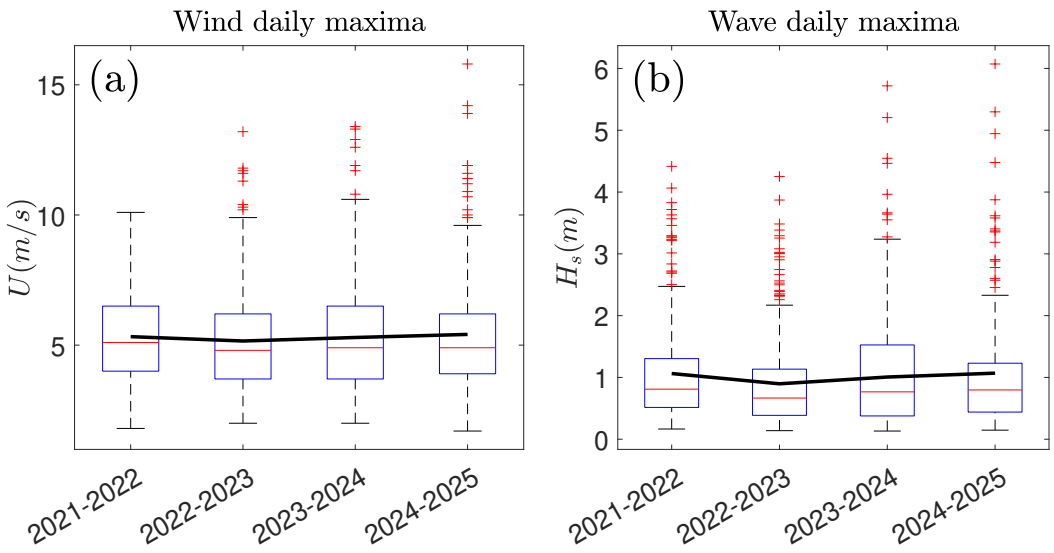

Fig. 2.30 Boxplots representing yearly distributions of daily maxima of (a) wind speed and (b) significant wave height. Black lines marks the trend of yearly mean values.

Figure 2.30 shows the distributions of daily maxima of wind speed and significant wave height in the time spans between each measurement campaign, namely:

- From September, 2021 to May, 2022 (2021 – 2022).
- From May, 2022 to May, 2023 (2022 – 2023).
- From May, 2023 to July, 2024 (2023 – 2024).
- From July, 2024 to July, 2025 (2024 – 2025).

As for the wind (Fig. 2.30a), the mean values and dispersion of daily maxima barely change throughout the years, with a slight decrease in the first two years, followed by a gradual increase till 2025. More notably, the magnitude and frequency of extreme events—indicated by boxplot outliers (red crosses)—exhibit a clear increasing trend, reflecting a progressive intensification of storminess.
Unsurprisingly, waves heights (Fig. 2.30b) show a similar pattern to the wind speed, with negligible variations of mean values, but a general increase of extreme events, denoting the strong interdependence between the two processes.

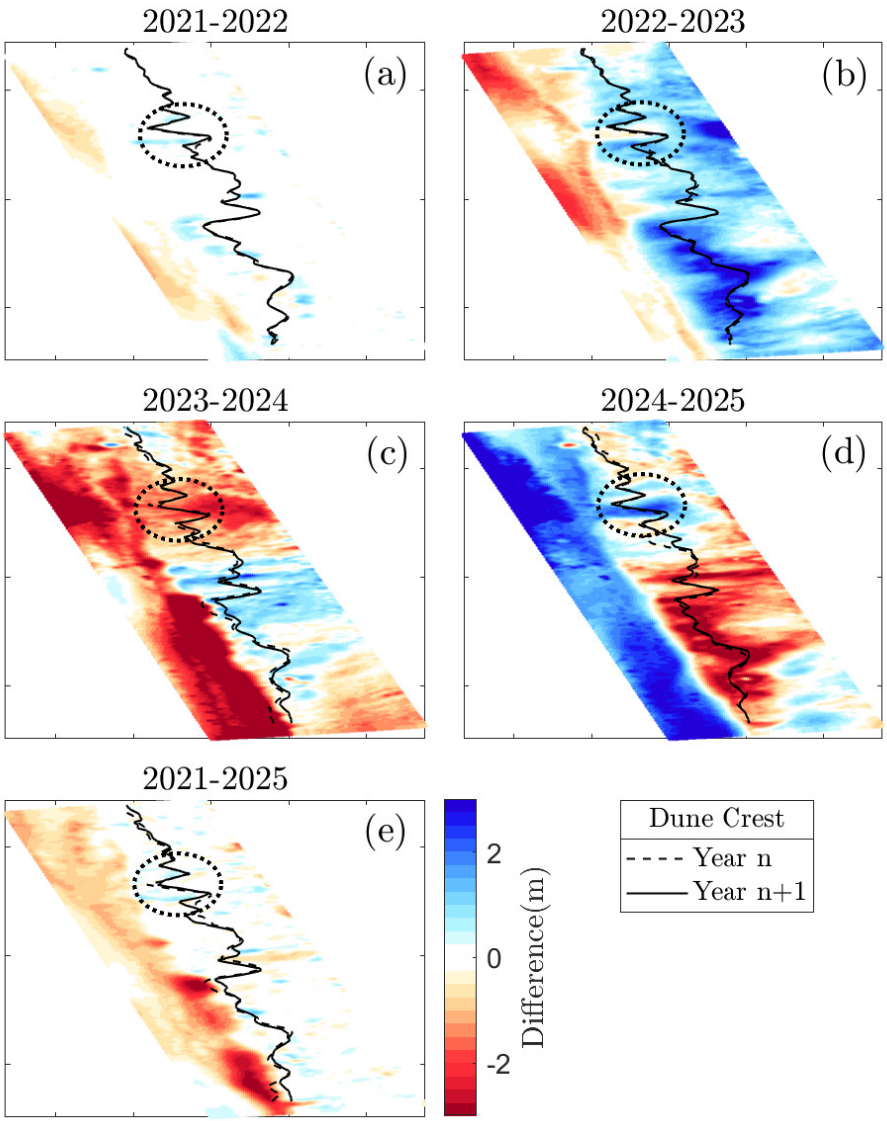

Fig. 2.31 (a)-(d) Temporal DEM of Difference(DoD) in A2, representing terrain elevation changes between each subsequent yearly campaign ($\Delta Z = Z_{Year\ n+1} - Z_{Year\ n}$).(e) DoD between elevation in the first a and last year (2021-2025). Red-ish colors represent erosion, while blu-ish colors represent deposition. Black lines represents the foredune crest positions in two subsequent years. Black circle marks the location of a dune blowout.

Volumetric Changes

Quantifying volumetric change is a central objective in many studies focused on landform evolution.

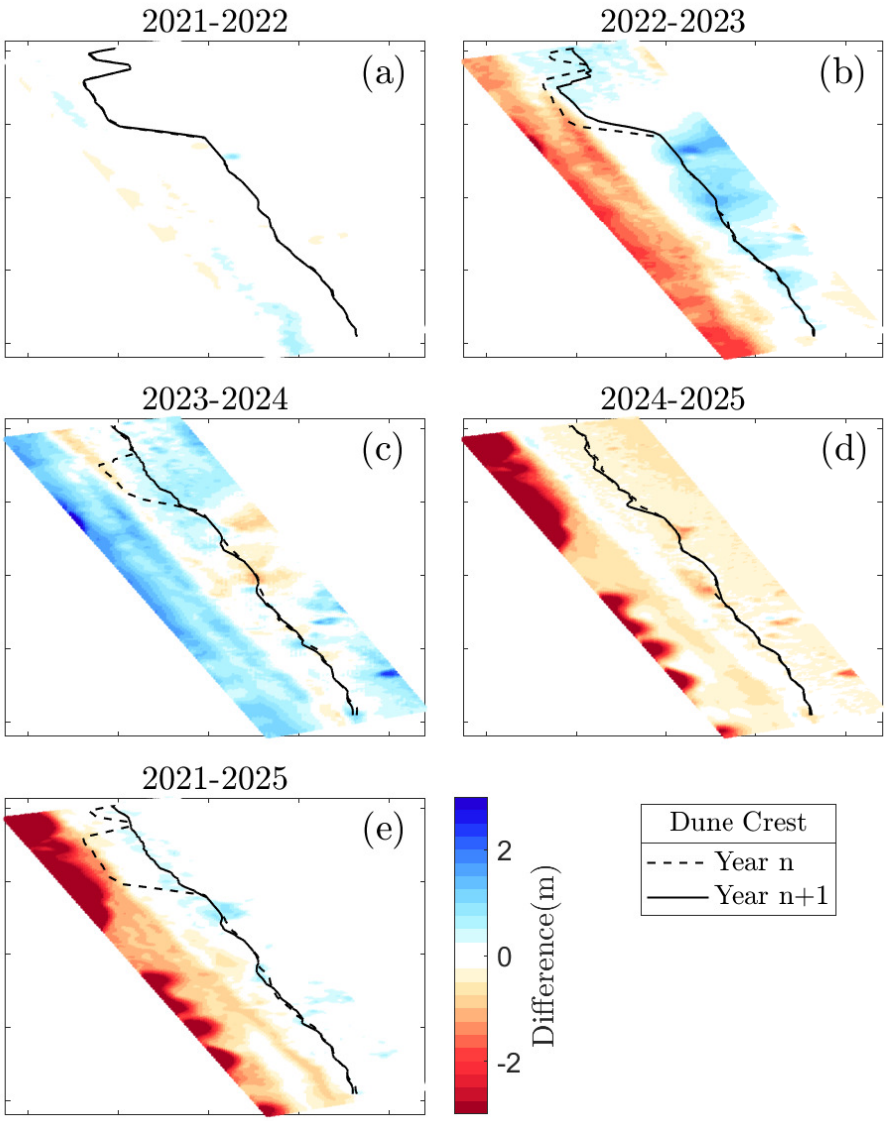

Fig. 2.32 (a)-(d) Temporal DEM of Difference (DoD) in A3, representing terrain elevation changes between each subsequent yearly campaign ($\Delta Z = Z_{Year\ n+1} - Z_{Year\ n}$).(e) DoD between elevation in the first a and last year (2021-2025). Redish colors represent erosion, while blu-ish colors represent deposition. Black lines represents the foredune crest positions in two subsequent years.

The most robust and widely adopted approach for monitoring topographic and volumetric variations is the DEM of Difference (DoD) technique, which has been extensively applied across a broad range of environmental settings [196–199].
This method involves generating digital elevation models from surveys conducted at different times and subtracting them to identify spatial patterns of erosion and

deposition processes. An error propagation analysis is also essential to distinguish genuine geomorphological signals from measurement noise, particularly when the DEMs originate from different survey methodologies [196, 197].

The series of panels in Figure 2.31 illustrates spatiotemporal patterns of topographic change within the A2 dune field for consecutive annual intervals and for the full 2021 – 2025 period. In each yearly DoD, zones of red shading indicate elevation loss associated with sand erosion, whereas blue regions correspond to areas of sediment deposition.

Figure 2.31a shows, in 2021 – 2022 period, modest volumetric variations with local patches of deposition near the foredune crest (black line) and erosion in the foreshore area. This observation well-correlates with the milder meteorological conditions, shown in figure 2.30a.

In 2022 – 2023 (Fig. 2.31b), an increase in wind field intensity, but wave ranges

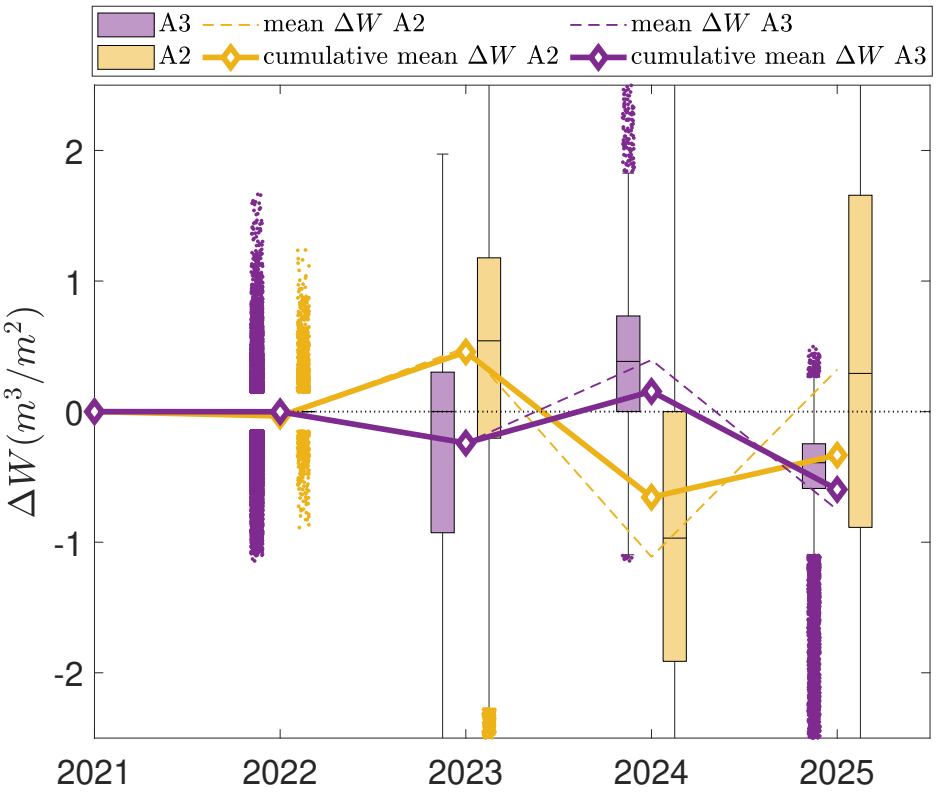

Fig. 2.33 Sand volumetric variation per unit area, from 2021 on. The distributions of ΔW values for each subsequent year are represented with boxplots (yellow for A2, purple for A3). Dashed lines represent trends of mean values of ΔW, while solid lines represent cumulative ΔW value.

similar to the previous period $2021-2022$, produced a pronounced aggradation of the foredune crest (up to ≈ 2.5m) and moderate erosion of large patches of the beach, on the order of magnitude of ≈ 1m.
Figure 2.31c portrays extreme erosion (> 2m) in the foreshore region, protruding into the landward side of the dune in correspondence with a dune blowout (marked with a black circle). In this case, the increasing magnitude of extreme events —both wind and waves— could have produced an overwash of the dune blowout. This accentuates the local depression, enforcing a 'funnel' effect which locally accelerates the air flow and, consequently, sand mobilization.
The $2024-2025$ DoD (Fig. 2.31d) reveals a pronounced spatial contrast, characterized by intense dune-crest erosion—locally reaching up to 3m—paired with substantial sediment accumulation on the foreshore. This pattern is likely associated with instability on the seaward face of the foredune, driven by an increased frequency and magnitude of extreme wave events (Fig. 2.30b), which may have ultimately triggered partial slope collapse. On the other hand, the marked aggradation observed on the foreshore may further reflect the combined influence of higher frequency of occurrence and magnitude of extreme wave events and enhanced sediment supply from the Arno River, with river-derived sand being deposited during the washover phases of high-energy events. Additionally, the blowouts show considerable infilling, with increases in surface elevation of up to 2m, indicating significant sediment delivery into these depressions.
Overall, when aggregated over the full $2021-2025$ period, the long-term DoD (Fig. 2.31e) highlights net beach erosion, but shows almost negligible net elevation changes of the foredune crest and leeward slope.

Similarly to figure 2.31, figure 2.32 represents DoDs of A3, although showing radically different erosion/deposition trends, compared to A2.
Figure 2.32a shows almost absent volumetric changes, reflecting the low energy wind and wave fields characterizing the period $2021-2022$, analogously to figure 2.31a.
In $2022-2023$ period (Fig.2.32b), uniform erosion has taken place in the foreshore —on the order of ≈ 1m— and moderate deposition has occurred on the crest and landward foredune slope. A similar pattern is observed in A2 on the same period (Fig.2.31b), with different magnitudes of beach erosion and crest accretion.
Figure 2.32c shows generalized moderate deposition on the beach and leeward side of the foredune, while portraying local erosion patches on the crest. This trend is in

opposition to A2 (Fig.2.31c) in which the dune crest exhibits local accretions and the foreshore is eroded.
In 2024 – 2025 period a generalized erosion is shown in figure 2.32d, involving both the beach and the foredune, with accentuated patches near the shoreline.
Similarly to what was observed in A2 (Fig.2.31e), the overall volumetric changes between 2021 and 2025, shown in figure 2.32e, portrays a net erosion of the beach and patches of moderate sand deposition on the crestline.

Analyzing the overall trends of volume variations, shown in figure 2.33, emerges an out-of-phase pattern between mean volume changes in A2 and A3: when A2 exhibits net erosion, A3 exhibits net deposition (and vice-versa). Despite these oscillating patterns, in the time span between 2021 and 2025, both A2 and A3 show an average eroding trend with approximately $0.3m^3/m^2$ sand loss in A2 and $0.6m^3/m^2$ sand loss in A3.

Foredune Dynamics

This section examines in detail the spatio-temporal evolution of the foredune system between 2021 and 2025. Figures 2.34a,b present the altimetric evolution of the mean cross-shore elevation profile, providing a complementary and more synthetic perspective on the DoDs discussed in the previous section.

In A2, the most substantial elevation changes occurred between 2022 and 2023, marked by pronounced accretion in the crest/backdune sector — peaking at the dune crest, where the mean elevation increased by more than 1m (from 5.2m to 6.4m) — and by severe beach erosion of approximately 3m. Notably, the crest/backdune profiles for 2021 and 2025 are almost identical, and the shoreline elevation in 2025 is only a few decimeters lower than in 2021. The seaward slope, however, experienced net erosion, resulting in a significantly steeper profile in 2025.
Overall, the foredune underwent an almost complete deposition/erosion cycle over the four-year window, particularly in the crest region, where the mean elevation returned to values comparable to those at the beginning of the observation period (Fig.2.35a).

In A3, the most pronounced elevation changes also occurred in 2022–2023, with a net mean increase of approximately 0.6m in the crest/backdune area (Fig.2.34b). The most critical alteration in the coastal sector, however, was observed between

2024 and 2025, when mean erosion reached up to 3m near the shoreline.
As in A2, the foredune crest in A3 underwent a full accretion/erosion cycle, though with different magnitudes (Fig.2.35b).

Visual inspection of the planimetric evolution of the crestline (Figs.2.34c,d), represented through its plan-view projection in the E-N plane, does not reveal a clear trend.
A more reliable quantification is provided in Figs.2.35c,d, which summarize crestline

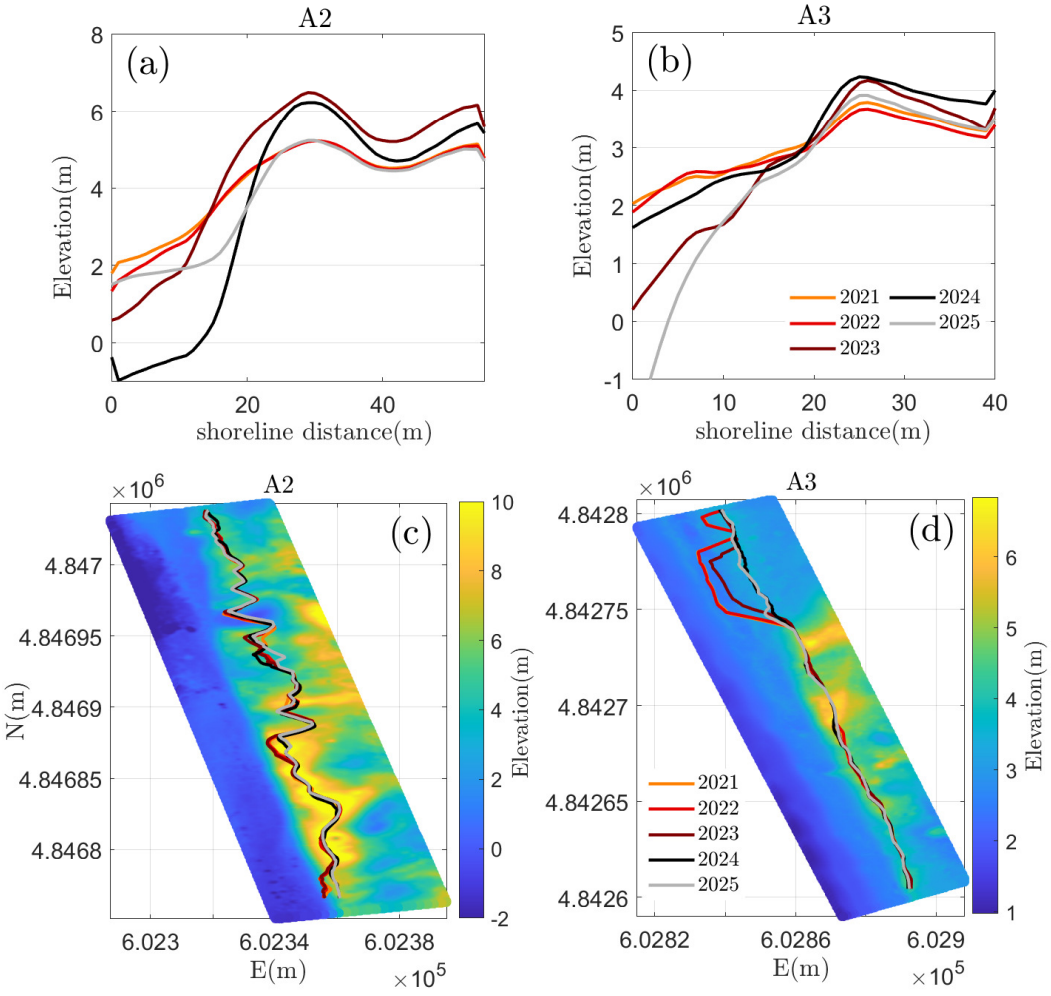

Fig. 2.34 Altimetric and planimetric dynamics of the foredune. Evolution of the mean cross-shore elevation profile in (a) A2 and (b) A3. Planimetric evolution of the foredune crestline in (c) A2 and (d) A3. As a topographic reference, in the background of panels (c) and (d) are shown DTMs of A2 and A3 relative to the year 2021.

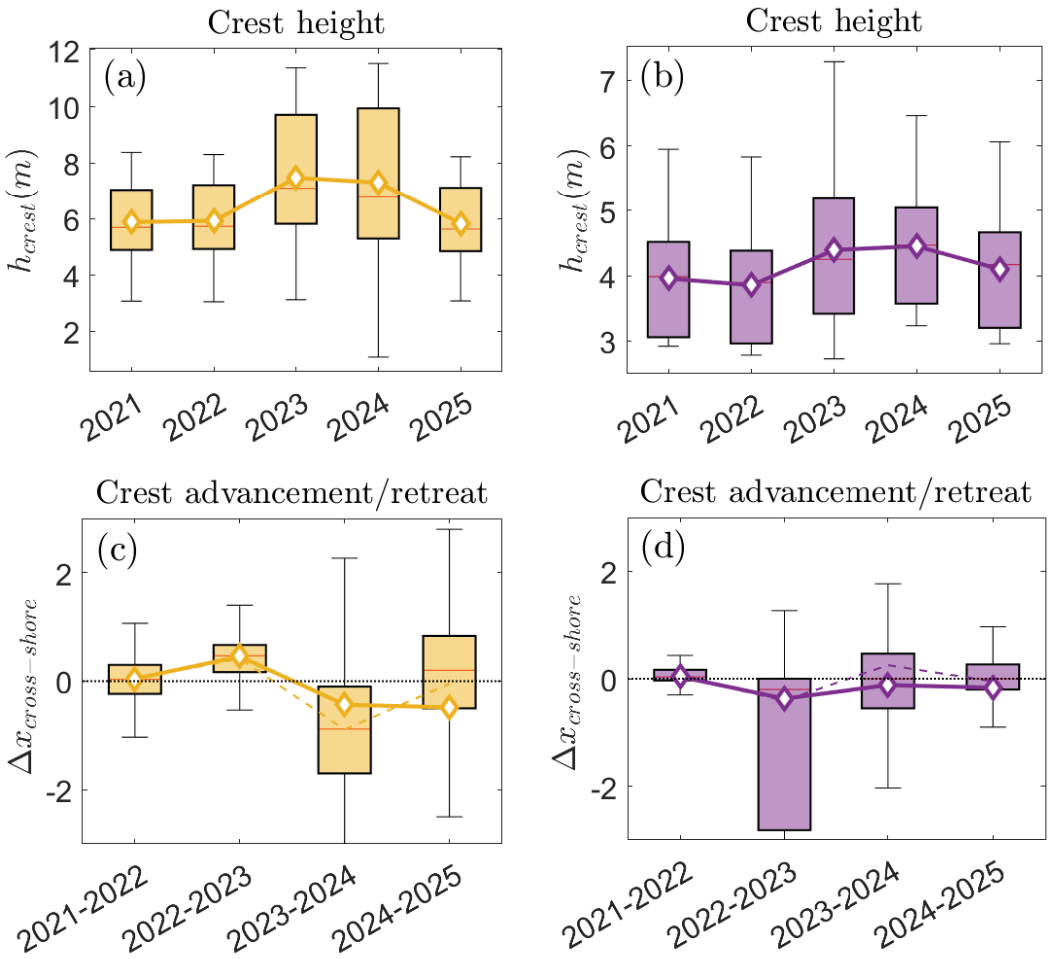

Fig. 2.35 Statistics of altimetric and planimetric evolution of the foredune crestline. The yellow items are referred to data relative to A2, while purple ones are related to A3. Panels (a) and (b) show the distribution of the crest heights (boxplots) for each year. The trends of the mean crest heights are represented with solid lines. Panels (c) and (d) show the distributions (boxplots) of planimetric variations of the dune crestline in the cross-shore direction ($\Delta x_{cross-shore}$) and their mean trend (dashed lines) for each period. Positive values of $\Delta x_{cross-shore}$ denote advancement towards the shoreline, while negative values denote a retreat towards the land. Solid lines in panels (c)-(d) represent the cumulative advancement/retreat of the crestline from 2021 on.

displacements. A2 and A3 exhibit opposing oscillatory patterns in annual mean cross-shore crestline displacement ($\Delta x_{cross-shore}$), mirroring the opposite-phase behavior observed in volumetric changes (Fig. 2.33): when A2 experiences a seaward advance

($\Delta x_{cross-shore} > 0$), A3 experiences a landward retreat ($\Delta x_{cross-shore} < 0$), and vice-versa.

In A2 (Fig.2.35c), annual displacements reach values on the order of 1m, with the largest change occurring in $2023 - 2024$, when the crestline retreated by 0.9m on average. In contrast, displacements in A3 are an order of magnitude smaller (10^{-1}m).
The cumulative trends (Figs.2.35c,d) indicate a net crestline retreat of 0.48m in A2 and 0.16m in A3 over the full observation period.

Given the 0.5m spatial resolution of the DTMs, these planimetric variations fall within the positional uncertainty of individual pixels. Therefore, mean planimetric displacements should be considered negligible, whereas altimetric and volumetric changes represent the dominant morphodynamic features of the foredune system in the study areas.

2.4.3 Vegetation analysis

A detailed analysis of the coastal dune vegetation is not presented in this chapter, as it is addressed extensively in the subsequent two chapters. In there, are discussed the spatial patterns and recovery dynamics of vegetation, highlighting their implications for ecology and management of coastal dunes. For this reason, vegetation-related considerations are omitted from the data collection and processing provided in this chapter.

Chapter 3

Pattern Analysis of Coastal Dune Vegetation

This chapter provides a comprehensive analysis of the spatial patterns of coastal dune vegetation. The interrelations among the adaptive strategies of individual plant species, local geomorphology, and environmental stressors are discussed here.

The contents presented in this chapter are also discussed in the article:
Demichele, D., Belcore, E., Piras, M., Camporeale, C. Species-by-species pattern analysis of coastal dune vegetation. *Journal of Geophysical Research: Biogeosciences* 130.2 (2025): e2024JG008419. https://doi.org/10.1029/2024JG008419

3.1 Introduction

The role of vegetation as the primary driving factor for the dynamics of coastal dunes has been established and extensively studied in the last decades [37, 200–202]. As coastal dunes are being either stabilized or mobilized in response to the changes in the rates of sand and dune movement, the vegetation cover and composition are expected to vary reflecting the differences in the sedimentary conditions [203, 204]. Disturbances such as changes in sand supply, intrusion of invasive species [58], and anthropic activities (agriculture, forestry, infrastructure, urban development and tourist pressure) may modify these fragile spatial patterns [205]. Dune plant patterns originate as a result of the spatial nature of environmental gradients, processes of

succession, or both. It is thus understood that, on one hand, vegetation distribution and biomass depend on several different factors, such as wind exposure [206], hydrodynamic regimes [207], salt spray [208, 209]; on the other hand, vegetation characteristics exert a major control on the development of the topographic features mediating these same abiotic governing factors. Hence, these topographic features such as elevation, slope, and distance from the shoreline have been identified as main habitat descriptors for different dune plant species [210, 211].

The concurrent characterization of vegetation distribution and dune topography has been historically addressed through time-demanding field sampling techniques such as the point count sampling method, transect sampling methods or so-called *quadrant counting methods* [212, 213]. Despite their simplicity, these methods are highly subjective because the estimation precision mostly depends on the estimator's experience and cannot be applied to large study areas for practical reasons [214].

In recent times, remote sensing has provided a comprehensive and cost-effective approach for analyzing vegetation patterns at different spatial and temporal scales, facilitating decision-making for land management, conservation, and environmental monitoring purposes [215, 216]. The ever-increasing data availability with high spatial and spectral resolution is facilitated using satellite, airborne, and ground-based sensors, which capture information across different wavelengths of the electromagnetic spectrum. A plethora of vegetation indices (e.g. NDVI, NDWI, EVI, MCARI, RI, etc.) can be deducted by multi-spectral imagery to quantify vegetation parameters such as health and density, based on the spectral reflectance [217–219].

Additionally, machine learning (ML) algorithms have been also applied to remote sensing data for land cover (LC) analysis [220–223]. Amongst all, Object-Based Image Analysis (OBIA) algorithms have gained popularity for LC classification for their improved accuracy and low sensitivity to noise, compared to other algorithms like pixel-based ones [224, 225]. These algorithms can perform segmentation, which partitions images into meaningful segments using algorithms like mean shift or graph-based segmentation and feature extraction to extract spectral, textural, and contextual attributes from segments. Classification algorithms like Decision Trees, Random Forests or Neural Networks are then used to assign to each segment LC classes based on these features. Although these techniques have been successfully applied across various research fields such as forestry, land management, environmental monitoring, and ecological conservation, there remains a notable gap in the literature concerning

highly detailed vegetation characterization studies. Specifically, tasks like species identification and biomass density estimation in coastal areas, which often contain small, sparse, and mixed populations of herbaceous plants, are still underrepresented [226, 227]. Only since the last decade has been proposed approaches using OBIA algorithms over Ultra-High Resolution (UHR) imagery, having less than 10 cm of spatial resolution, acquired through Uncrewed Aerial Veichle (UAV), performed on a multi-temporal scale [228–230]. This approach is shown to be suitable for fine land cover classification in coastal environments, although being more time and resource-demanding than using methods based on satellite imagery.

In this study, we took advantage of a novel classification model proposed by [231] based on an OBIA algorithm and applied to UHR multispectral UAV imagery to obtain a wide vegetation dataset composed of georeferenced and classified polygons at the single-plant level. The present work aims to provide a detailed qualitative and quantitative description of vegetation spatial patterns using statistical and geostatistical tools like spatial correlation [210, 232] and point pattern analysis [233–235], well-established for vegetation pattern studies in coastal environments as well as in forests, woodlands and many other environments. Moreover, we combined vegetation distribution studies with topography and hydrodynamic forcings analysis to better understand their effect on each plant species. In particular, the research focuses on examining the following aspects: *(i)* the interplay of hydraulic forces and the distribution of vegetation; *(ii)* the relationship between topography, vegetation distribution and vegetation geometrical features; *(iii)* the impact of human activities on vegetation distribution, as this park stands out as one of the few dune areas in Italy under complete protection, but still situated close to heavily frequented bathing areas.

The overall structure of the study is organized in the following way: The second chapter focuses on describing the study site, data retrieval and data analysis methods. Chapter three presents a thorough examination and discussion of the results. In the fourth chapter, we draw conclusions, emphasizing the key findings of the study and exploring their potential applications.

3.2 Material and Methods

3.2.1 Case study and data collection

A comprehensive description of the three study sites located within the San Rossore-Migliarino Regional Park, along with the procedures for data collection and processing employed in the following analysis, is provided in Chapter 2.

3.2.2 Runup computation

The effect of the hydrodynamic forcing on the vegetation has been addressed through an analysis of the wave runup, namely, the maximum elevation gain reached by the water on the shoreline. The elevation gain is due to the conversion of part of the kinematic energy of the wave into potential energy [236].

For this analysis, data have been collected from the National wave-metric and tide-gauge network open database, run by the Italian Institute for Environmental Protection and Research (ISPRA). We retrieved the time series of the spectral significant height H_0 and the spectral peak period T_p over 30 minutes of deep water waves collected by the wave buoy of La Spezia and the time series of mean water levels η collected by the hydrometer of Livorno, with a sampling period of 10 minutes. The time span of collected data is from 2021/06/01 to 2022/12/31 (the original dataset is available on https://www.mareografico.it).

For the computation of the runup we adopted the model proposed by [189]

$$R_u = (H_0 L_0)^{1/2}[0.385\beta_f + (0.17\beta_f^2 + 0.0012)^{1/2}], \tag{3.1}$$

where L_0 is the spectral significant wavelength in deep waters, defined by the dispersion relation $L_0 = gT_0^2/2\pi$; T_0 is the spectral significant wave period in deep waters, defined by $T_0 = 0.95T_p$, where T_p is the peak spectral period; β_f is the beach steepness, i.e., the tangent of the slope angle of the water's edge, θ (Figure 3.1). An average β_f has been calculated for each study area by extracting from the DTMs 100 equally-spaced transects perpendicular to the shoreline and computing for each one the beach steepness $\beta_f = \langle 2/(x_2 - x_i)\rangle$, where x_0 and x_2 are the coordinates in the cross-shore direction of points at elevations 0 m and 2 m above sea level, respectively

(Figure 3.1a). This choice is justified by the fact that the region between 0 and 2 m elevation lies within the shoreline and the foredune toe and the slope is steady. Total water level h is then computed as the sum of the mean sea level η and the runup R_u, namely $h = \eta + R_u$.

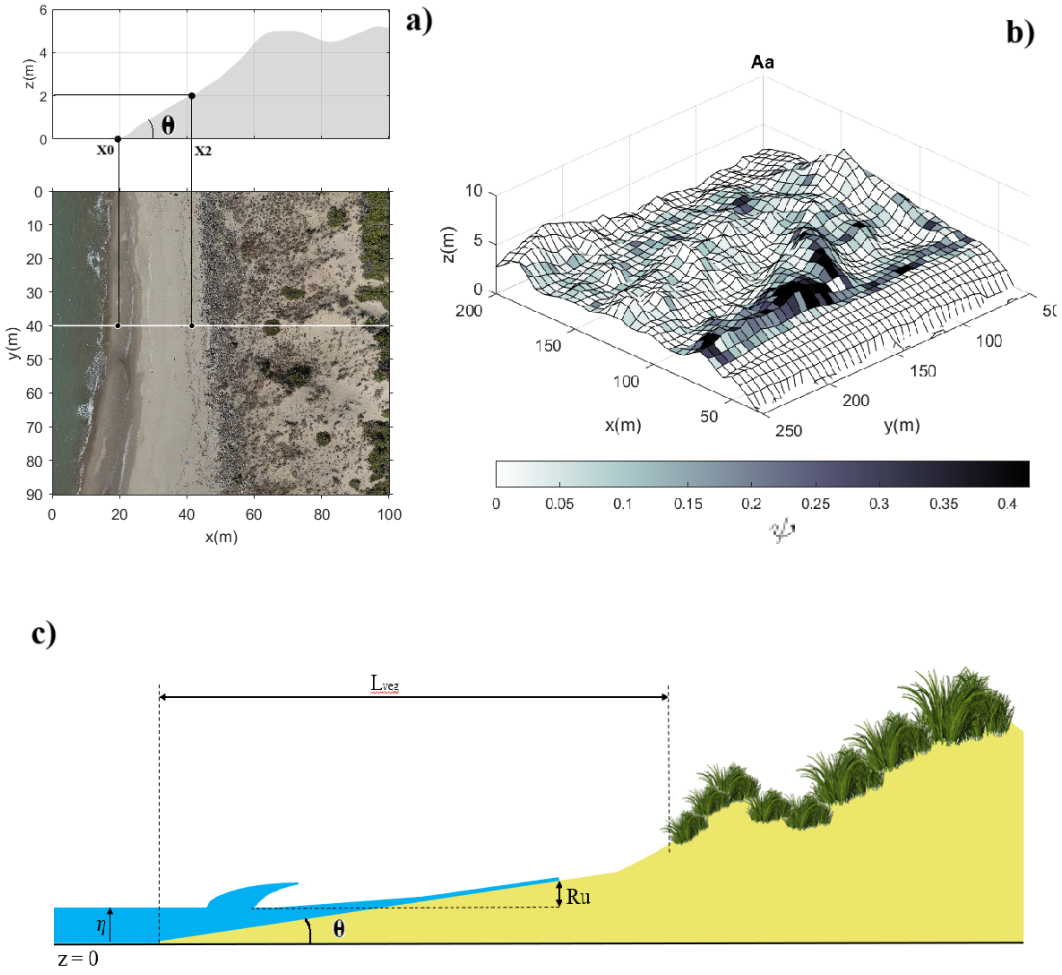

Fig. 3.1 (a) Example section (top) extracted from the Digital Terrain Model (DTM) used to compute $\beta_{f,i}$. The orthoimagery (bottom) highlights a transect marked by a solid white line, with points at elevations of 0 m and 2 m indicated. (b) Two-dimensional vegetation cover map of Ammophila arenaria in A3 with 5 m resolution, overlaid on the DTM of the study area. The shading of each cell represents the corresponding ψ value. (c) Geometric configuration of the considered beach-dune profile. The sea water level h is the sum of wave runup R_u (function of the beach slope θ) and the mean water level fluctuation due to tides η. Because of marine disturbance, vegetation can grow only beyond the threshold distance L_{veg} from the shoreline.

3.2.3 Vegetation pattern classification

The starting point of the present study on the vegetation pattern is a field-based dataset derived from the object-based image analysis (OBIA) recently proposed by our research group [231], which detects and classifies twelve different plant species —as well as sand and debris— (Table 3.1) from UHR multispectral UAV images acquired during campaigns in September 2021 in the three study areas.
The classification workflow consists of a preliminary phase of image segmentation, producing polygons representing the canopy cover of the single plant, —i.e., the area covered by the vertical projection of the outermost perimeter of the natural spread of foliage of plants [212]— and a classification phase, in which a Random Forest algorithm is applied to those polygons.
Polygons containing the georeferenced and labeled plants acquired in the GNSS-RTK surveys are used for the model training/testing phases (2436 polygons in total). In particular, polygons in A1 and A2 were used for training, while those in A3 were used for testing, resulting in an average accuracy of 75%. The model performance in the detection of each species is evaluated through the F1 score, summarized in table 3.1.

The output dataset is composed of a shapefile containing more than 600,000 polygons, each one labeled with an abbreviation of the object class name. The reader may refer to [231] for further details about the classification technique. Morphometric parameters of the polygons, such as the coordinates of the centroids, areas, and perimeters have been extracted using QGIS.

Since Juniperus shrubs and Pine trees predominantly constitutes the backdune vegetation patch, a first cleaning of the dataset removed all the polygons corresponding to these species. Then, all the polygons with an area less than 0.01 m^2 have been removed.
The abundance of each plant species in each study area has been computed as the ratio between the number of elements of a single species and the total amount of plants in the whole area [210]. Species having an abundance of less than 1% has been considered not statistically relevant and therefore, neglected in successive analysis.
To support some of the key results, we implemented a two-dimensional visualization of the spatial distribution of the vegetation in the form of vegetation cover maps, as shown in the example in figure 3.1b. The complete set of ground cover maps for the sites A1-A3 are reported in the Supporting Information S1-S3. After subdividing

the study area with a 5 m equally-spaced grid, the vegetation cover $\psi_{i,j}$ has been computed for each cell defined as the ratio between the total area of the polygons of the i-th plant species inside the j-th cell and the area of the cell itself, namely $\psi_{i,j}$=A_i^{veg}/A_j^{cell}, where A_i^{veg} is the area of a segmentation polygon (or a portion of polygon) of the i-th plant species and A_j^{cell} is the cell area. A scheme for the computation of $\psi_{i,j}$ is represented in figure 3.2a.

Geometric indices

To analyze vegetation patterns, we used morphometric indicators focused on plant size and local spatial density. Plant size was quantified using the equivalent diameter (ED), defined as the diameter of a circle with the same area as the plant's canopy cover (Figure 3.2b) [237], namely

$$\mathrm{ED} = 2\sqrt{\frac{A_i^{veg}}{\pi}}. \tag{3.2}$$

The local spatial density is instead represented by the Mean Neighbour Distance (MND), namely the mean distance of the centroid of an individual plant from its neighbor plants of the same species. Neighboring points are defined as connected nodes in a two-dimensional first-order Delaunay triangulation network [238]

$$\mathrm{MND}_i = \frac{1}{m}\sum_{j=1}^{m} t_{i,j}, \tag{3.3}$$

where $t_{i,j}$ is the Euclidean distance between a nodes i and j of the Delaunay triangulation network, and m is the number of nodes connected to the node i (Figure 3.2c). Triplets of points constituting the network meshes have been computed with the MATLAB *Delaunay* function.

Spatial Autocorrelations

The spatial autocorrelation of ED and MND has been addressed through a geostatistical analysis by using semivariograms. The semivariance $\gamma(h)$ is defined as the half the average of the squared differences between values assumed by a spatially distributed quantity, Z, at locations x_i and x_j separated at distance h [239]. When

Plant Species	Abbreviation	Role	F1 score
Achillea maritima (L.) Ehrend. & Y.P.Guo	Am	pioneer	0.37
Dittrichia viscosa (L.) Greuter	Dv	pioneer	0.15
Echinophora spinosa	Es	pioneer	0.41
Eryngium maritimum	Em	pioneer	0.62
Euphorbia paralias	Ep	pioneer	0.67
Helycrisum stoechas (L.) Moench	Hes	pioneer	0.72
Pancratium maritimum	Pm	pioneer	0.76
Ammophila arenaria (L.) Link	Aa	dune-building	0.85
Daphne gnidium	Dg	evergreen	0.63
Juniperus oxycedrus	Jo	evergreen	0.81
Pinus pinaster	Pp	evergreen	0.65
Yucca gloriosa	Yg	evergreen	0.42

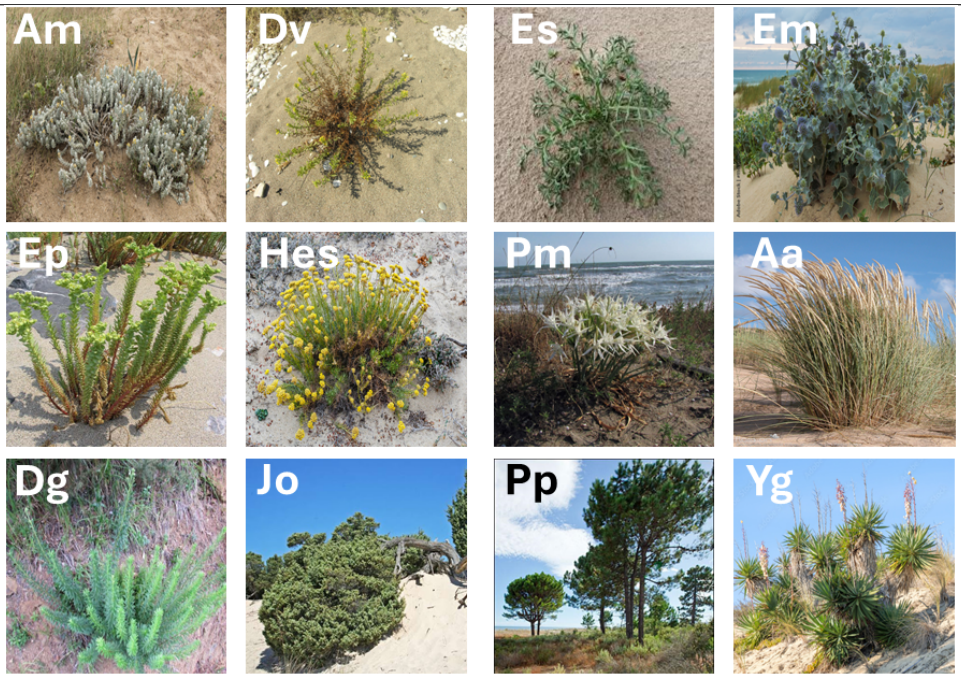

Table 3.1 List of plant species detected by the OBIA algorithm, along with their name abbreviation and phytosociological role.

dealing with field measurements, Z is a discrete quantity and not a continuous field, so we consider the set of all the pair of points whose distance is within $h+\frac{\delta}{2}$ and $h-\frac{\delta}{2}$, where δ is an suitable bin width.

$$\gamma(h) = \frac{1}{\sigma_Z^2}\frac{1}{2|n(h\pm\frac{\delta}{2})|}\sum_{(i,j)\in n(h\pm\frac{\delta}{2})}|Z_i - Z_j|^2. \tag{3.4}$$

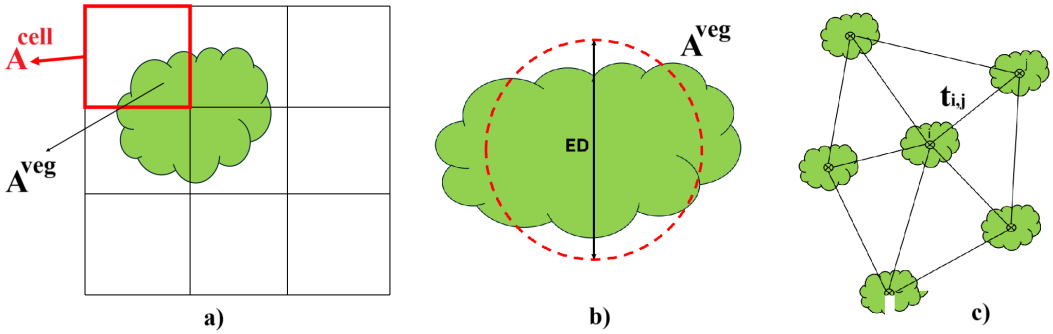

Fig. 3.2 Scheme for calculating: (a) Vegetation Cover: the ratio between the area of the plant's polygon within a cell (A_i^{veg}) and the area of the cell itself (A_j^{cell}) (red square). (b) Equivalent Diameter (ED): the diameter of a circle (red dotted line) with the same area as the plant's polygon (A_i^{veg}). (c) Mean Nearest Distance (MND): the centroid of each polygon representing a single plant (black circle with an 'x'), with centroids connected by a Delaunay triangulation network (black lines). $t_{i,j}$ are the lengths of the network links.

In the above equation, the semivariance has been normalized with the variance of Z, eliminating scale effects, to compare different semivariograms.
The spatial structure of the geometric features of vegetation was identified by fitting the experimental semivariograms onto four widely used semivariogram models: *i*) Gaussian: $\gamma(h)=d+C(1-e^{-h^2/a^2})$; *ii*) Exponential: $\gamma(h)=d+C(1-e^{-h/a})$; *iii*) Spherical: $\gamma(h)=d+C(\frac{3}{2}\frac{h}{a}-\frac{1}{2}(\frac{h}{a})^2)$; *iv*) Pure nugget: $\gamma(h)=d$.
In these models, C is the *sill* (i.e. the theoretical limit of γ for $h\to\infty$, equal to the variance of Z if it is randomly distributed in space), d is the *nugget* (i.e., the height of the jump of the semivariogram at the discontinuity at the origin), and a is the *range* (i.e., the value of h for which the difference between the sill and the semivariogram is negligible and roughly corresponds to the integral length scale at which Z loses spatial correlation with itself). For a sensible autocorrelation analysis, we neglected semivariograms showing *i*) too-low coefficient of determination, $R^2 < 0.7$.; *ii*) too-high noise level, $d > 0.9$; *iii*) unclear structure, $C-d < 0.1$.

Point Pattern Analysis

The characterization of vegetation spatial arrangements has been performed using point pattern analysis. Point pattern analysis methods fall into two predominant categories: *i)* nearest neighbor-based and *ii)* distance-based methodologies. The former centers around nearest neighbor distance, denoting the minimum distance

between one element and another within the population, while the latter is based on the enumeration of elements contained within a specified distance.

The mean nearest neighbor (MNN) method is based on the nearest neighbor distance $\overline{d_o}$, denoting the minimum distance between two a zero-dimensional objects within a population, [240]:

$$\overline{d_o} = \frac{1}{N}\sum_{i=1}^{N} min(d_{i,j}), \tag{3.5}$$

where $min(d_{i,j})$ is the distance of a given event i to its closest neighbor and N is the size of the sample taken into exam. For comparison purposes, we will refer to the case of a random distribution of points, in the following referred to as Complete Spatial Randomness (CSR), which is originated by a homogeneous Poisson process, namely, the probability of finding a number k of points in a region randomly chosen within the study area follows the Poisson distribution. In the case of CSR, the expected value of the MNN is $\overline{d_e} = \sqrt{\rho}/2$, where $\rho = N/A$ is the number of points per unit area and A is the study area [241].

The nearest neighbor index (NNI) refers to the ratio $r = \overline{d_o}/\overline{d_e}$, and represents a measure of the departure from a random distribution of a set of points. Therefore the spatial arrangement is clustered if $r < 1$, or uniformly dispersed if $r > 1$. The reliability of the prediction of the spatial pattern through the NNI is assessed by statistically testing the departure of the null hypothesis, i.e. the CSR. The testing variable in this case is the standardized mean nearest neighbor which follows a standardized normal distribution [241]:

$$Z = \frac{\overline{d_o} - \overline{d_e}}{\sigma_{\overline{d_e}}}, \tag{3.6}$$

where $\sigma_{\overline{d_e}}$=$0.261/\sqrt{\rho N}$ is the standard deviation of nearest neighbor distances in the case of CSR [241]. We choose a double-tailed test with a 95% confidence interval to test the departure from the null hypothesis. To indicate a statistically significant clustering or dispersion of the observed point pattern, the value of Z must be less than -1.96 – indicating clustering– or greater than 1.96 –indicating dispersion–. The values Z=-1.96 and Z=1.96 respectively correspond to the 2.5th and the 97.5th percentile of the distribution of Z.

In addition, Ripley's K-function $K(r)$ has been used to perform a distance-based point pattern analysis. It measures the average number of points that fall within a circle of a given radius r centered on each point of the population [242]

$$K(r) = \frac{1}{N}\frac{1}{\rho}\sum_{i}\sum_{j\neq i} I(d_{i,j} < r)w(x_i, x_j), \tag{3.7}$$

where: ρ is the number of points per unit area, N is the size of the sample, $I(r_{i,j} < r)$ is the indicator function [235] (I=1 if the distance between points i and j is less than r and assumes value I=0 otherwise), $w(x_i, x_j)$ is Ripley's edge-effect correction factor [243], wherein$w$=1 if the circle centered in x_i with radius r lies completely within the study area, otherwise w assumes a value less than 1, equal to the ratio between the total circumference of the circle of radius r and its sector inside the study area.
The edge effect is more significant at greater values of r because the research circle is more likely to fall partially outside the study area. Similarly to the Nearest Neighbour method, the type of spatial arrangement can be identified by comparing the observed K-function with its expected value in the case of CSR, equal to πr^2. Therefore, $K(r) > \pi r^2$ indicates a clustered pattern, and $K(r) < \pi r^2$ indicates a uniformly dispersed pattern.
Both the expected and observed K-function increase with the square of the distance, and, at higher values of r, small differences in the spatial arrangement of points become barely distinguishable. To circumvent such a scale-effect problem, Besag (1977) [244] suggested the use of a modified version of the K-function, the L-function, expressed as follows:

$$L(r) = \sqrt{\frac{K(r)}{\pi}} - r, \tag{3.8}$$

whose the expected value for the CSR case is L=0. It follows that positive values of the observed $L(r)$ indicate clustering, otherwise, negative values indicate dispersion.

As evidenced by [245], in the case of a clustered point pattern, the value of r at which occurs the maximum of the observed $L(r)$ gives a slight overestimate of the radius of the clusters. Although the L-function can provide an initial assessment of whether the observed point pattern differs from complete spatial randomness, it's unclear how much the observed function should deviate from its expected values (e.g., zero for the L-function) to indicate significant clustering or dispersion in a statistical

sense. For this study, we used a Monte Carlo simulation approach to build the confidence envelope of the CSR hypothesis. A number m of samples composed by N points (10^4 in our case) are randomly placed within the study area. $L_{i,i=2,\ldots,m}(r_j)$ is computed for various distances r_j for each i-th sample and sorted in ascending order. The 95% confidence interval limits are given by the 250th and the 9750th largest value of $L(r_j)$, corresponding to the 2.5th and 97.5th percentile of the distribution of $L(r_j)$. Repeating this procedure for each distance r_j, the 95% confidence envelope is therefore constructed [246]. A statistically significant clustering (or dispersion) is determined whereas the observed L-function lies above (or below) the confidence envelope.

3.3 Results & Discussion

3.3.1 Overview of dune morphology and biogeography

	Aa	Em	Ep	Es	Hes	Pm	Dg	Yg
A1	0.05	0.23	0.04	0.44	0.12	0.09	-	0.01
A2	0.34	0.07	0.28	-	0.19	0.03	0.09	0.0005
A3	0.41	0.006	0.05	0.0001	0.32	0.0002	0.12	0.07

Table 3.2 Abundance of plant species expressed as the ratio between the number of elements of a single species and the total amount of plants detected in the three study areas. Abundance values are represented using a red-to-green color gradient, where green indicates more dominant species and red highlights scarcer ones. (Abbreviations: *Aa, Ammophola Arenaria; Em, Eryngium Maritimum; Ep, Auphorbia Paralias; Es, Echinophora Spinosa; Hes, Helichrysum Stoechas; Pm, Pancratium Maritimum; Dg, Daphne Gnidium; Yg, Yucca Gloriosa*)

Upon initial examination of the digital terrain models (DTMs) within the study areas, three distinct structures that characterize the dune systems become evident (see Figure 3.3). Area A1 stands out from the other two due to anthropogenic disturbances. It consists of multiple bands of embryonic dunes running parallel to the shoreline, spaced approximately 25-30 meters apart, with a height not exceeding 70-80 centimeters. This is reflected in the limited proliferation of dune-building species, such as *Ammophila arenaria*, in this environment, as their presence is notably scarce compared to A2 and A3, where they are more abundant (see Table 3.2).

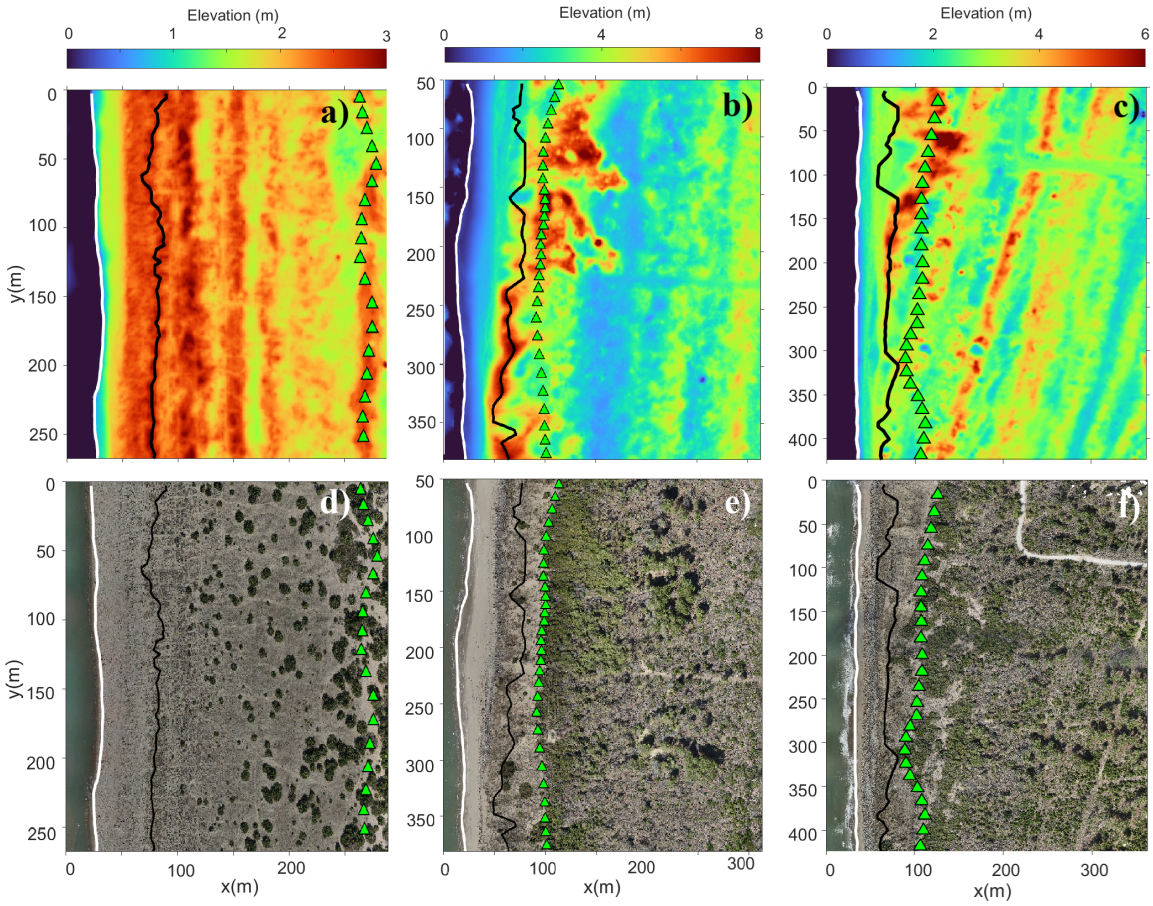

Fig. 3.3 DTMs of areas A1(a), A2(b) and A3(c). The shoreline (white line), the foredune crestline (black line), and the limit of the patch of tree vegetation (green triangles) are also reported. Orthoimagery of A1(d) A2(e) and A3(f) are portraited for visual comparison with DTMs.

Area A2 exhibits the characteristic structure of a mature coastal dune, featuring a well-developed foredune primarily colonized by ammophyte species, which can attain heights of up to 8 meters. It also includes a humid backdune slack and a fixed dune with patches of coniferous plant species like *Pinus Pinaster*. In contrast, despite being within the confines of the Regional Park like A2, Area A3 displays a different structural pattern. The orientation of its dune bands deviates approximately 17° from alignment with the shoreline (see Figure 3.3c), influenced by ongoing coastal erosion attributed to the proximity of the Morto Nuovo river outlet [13]. In this area, a nascent system of foredunes is emerging, though still in the process of formation. Consequently, it presents a more rugged structure and a lower crestline elevation compared to the foredunes of A2.

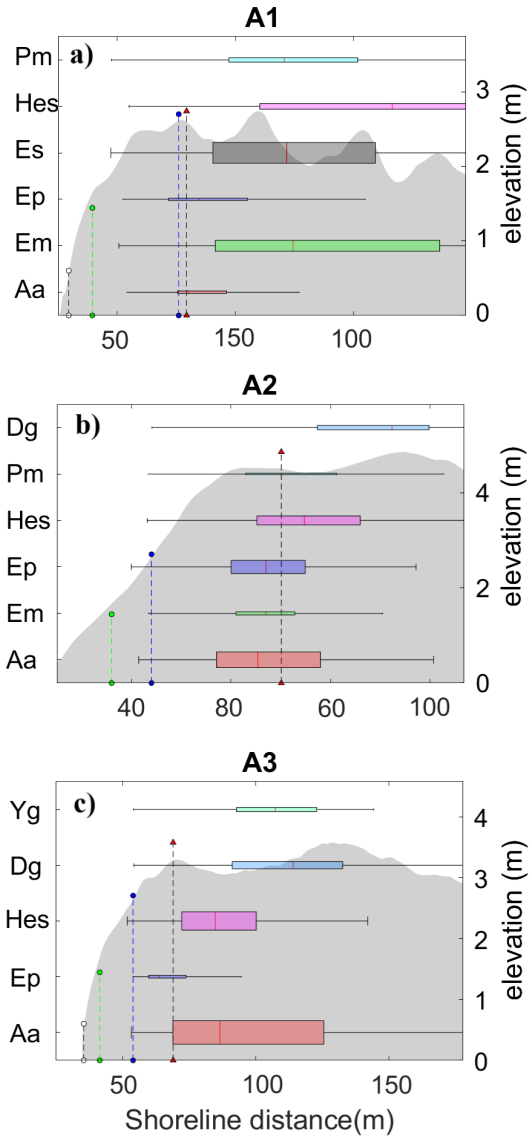

Fig. 3.4 Boxplot depicting the species spatial distribution of plant species and the mean topographic profile (depicted in grey) along the cross-shore direction for A1 (a), A2 (b) and A3 (c). The width of the boxes corresponds to the abundance of the species within the study area. Additionally, the positions of the mean foredune crest (black dashed line with red triangles), mean total water level (blue dashed line with blue dots), 95th percentile (green dashed line with green dots), and 99th percentile (black dashed line with white dots) are highlighted. (Abbreviations: *Aa, Ammophila arenaria; Em, Eryngium maritimum; Ep, Euphorbia paralias; Es, Echinophora spinosa; Hes, Helichrysum stoechas; Pm, Pancratium maritimum; Dg, Daphne gnidium; Yg, Yucca gloriosa*)

A notable distinction between A1 and A2-A3 lies in the width of the coastal zone colonized by shrub and herbaceous species, delineated as the distance between the shoreline and the vegetative cover. In A2 and A3, this distance measures approximately 70-80 meters, whereas in A1, it extends to about 250 meters, as illustrated in Figure 3.3a-c.

In A2 and A3, foredunes exhibit significant development, attaining elevations of 5-6 meters. The barrier effect of these dunes engenders marked variations in wind exposure, influencing abrasive forces, nutrient dispersion, and moisture levels [210]. These pronounced gradients in environmental conditions manifest in the spatial distribution of plant species across distinct morphological units of the dune system (e.g., foredune, slack, secondary dune, etc.), contingent upon their ecological tolerance levels. An exemplary demonstration of the tight coupling between terrain morphology, environmental gradients, and plant zonation is observed in halophytic species, such as *Ammophila arenaria* and *Euphorbia paralias*. These species predominantly populate the vicinity surrounding the crest of the foredune (as depicted by the distribution of *Aa* and *Ep* in Figure 3.4b-c). Conversely, species like *Helichrysum stoechas* and *Daphne gnidium*, which thrive in more moisture-rich habitats and are shielded from adverse environmental stressors, are primarily situated within dune slacks and stabilized dune formations (refer to the distribution of *Hes* and *Dg* in Figure 3.4b-c).

Conversely, in A1, the predominantly flat terrain results in a notably less pronounced gradient of environmental factors, yielding a vegetation zonation that is more diffuse and less distinct. Indeed, across the entire area, species exhibit a more homogeneous distribution pattern. This is evident in the interquartile ranges (IQRs) and whiskers depicted in the boxplots presented in Figure 3.4a, which illustrate the spatial distribution of vegetation species. Notably, these boxplots show significantly wider IQRs and whiskers in comparison to those observed in A2 and A3 (see Figure 3.4b-c).

In A2 and A3, the narrowness of the shore precludes the formation of embryonic dunes on the seaward side of the foredune, largely due to limited space exacerbated by accumulations of wooden debris. Consequently, the scarcity of vegetation species typical of embryonic dunes, such as *Eryngium maritimum*, *Echinophora spinosa*, and *Pancratium maritimum* [11], mirrors the morphology of these areas, which lack

embryonic dune structures. Conversely, these species thrive in A1, where the terrain primarily comprises embryonic dunes.

Another notable difference in vegetation distribution between A1 and the other two areas involves *Daphne gnidium*, a species typically associated with fixed dunes and dune slacks, along with Juniperus shrubs or Pine trees [11]. In A1, where fixed dunes are absent, *Daphne gnidium* is scarce, contrasting with its presence in A2 and A3. This pattern aligns with the distribution of Juniperus, sparsely scattered from the shoreline to the patch of tree vegetation.

Helichrysum stoechas, a species favored in areas sheltered from direct onshore winds and waves, exhibits similar abundances across all three areas (see Table 3.2). In A2 and A3, it primarily occupies the landward slope of the foredune and the dune slack (see Figure 3.4b-c), whereas in A1, it proliferates not only in such sheltered areas but also between the second and fourth rows of embryonic dunes (illustrated by the boxplot of *Hes* in Figure 3.4a).

3.3.2 Thresholds

The literature extensively underscores the significance of a critical threshold distance from the shoreline, commonly denoted as L_{veg}, beyond which vegetation survival becomes viable [211]. This threshold delineates a zone where environmental forces exceed levels conducive to vegetation encroachment (see Figure 3.1c). L_{veg} holds particular importance in coastal ecomorphodynamic modeling, serving as a pivotal determinant for vegetation colonization and thus exerting control over the dune-building process.

Figure 3.5 illustrates the ratio between the average overall L_{veg} and the mean distance of the foredune crestline from the shoreline x_{crest}, which consistently remains around 0.6 across the three areas, specifically 0.62 for A2 and A3, and 0.54 for A1. Hence, this ratio appears minimally influenced by terrain morphology. Nonetheless, further case studies are necessary to extend the applicability of this finding. The L_{veg}/x_{crest} ratio has been calculated individually for each plant species (Figure 3.5).

Species shared between A2 and A3, namely *Ammophila arenaria*, *Euphorbia paralias*, *Helichrysum stoechas*, and *Daphne gnidium*, display consistency in their respective L_{veg}/x_{crest} values, regardless of their abundance. Coherently with their zonation, halophyte species, proliferating closer to the coastline, exhibit L_{veg} values

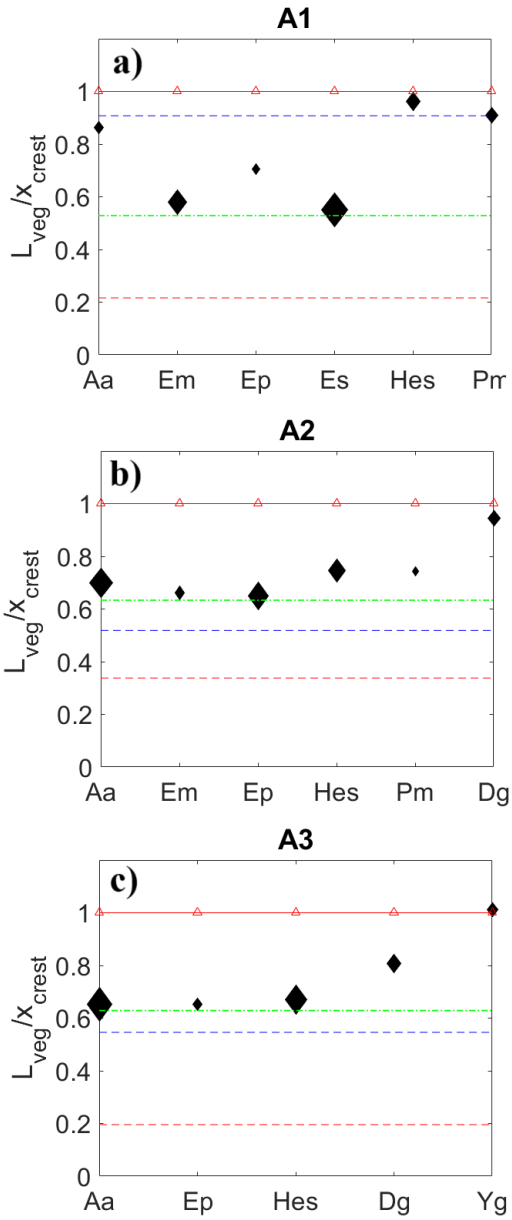

Fig. 3.5 Plots of normalized L_{veg} for different plant species. The size of the diamonds is proportional to the abundance of each species. The plots highlight the mean distances from the shoreline of the 95th (red dotted line) and 99th (blue dotted line) water level contour lines, the mean overall threshold vegetation line (green dotted line), and the crestline (red triangles).(Abbreviations: *Aa, Ammophila arenaria; Em, Eryngium maritimum; Ep, Euphorbia paralias; Es, Echinophora spinosa; Hes, Helichrysum stoechas; Pm, Pancratium maritimum; Dg, Daphne gnidium; Yg, Yucca gloriosa*)

closely aligned with each other and with the overall L_{veg} (Figure 3.5b-c). In A1, L_{veg}/x_{crest} values for individual species are inconsistent with those found for the same species in A2 and A3 (Figure 3.5b-c). For instance, *Ammophila arenaria* and *Euphorbia paralias* respectively display L_{veg}/x_{crest} ratios of about 0.9 and 0.7 in A1 (Figure 3.5a), contrasting with values around 0.63 observed in A2 and A3.

Despite these discrepancies, some similarities are remarkable: (*i*) L_{veg} of halophyte species such as *Eryngium maritimum* and *Echinophora spinosa*, abundant in A1, overlaps with the overall L_{veg} (Figure 3.5a), akin to observations in A2 and A3 (Figure 3.5b-c); (*ii*) L_{veg} of *Ammophila arenaria*, scarce in A1 but abundant in A2 and A3, closely aligns with the h_{99} line (Figure 3.5a), resembling trends observed in A2 and A3 (Figure 3.5b-c). This correlation suggests that flooding may be the primary determinant of L_{veg} for *Ammophila arenaria*, while not necessarily for other halophytes.

3.3.3 Effects of wave forcing on vegetation boundaries

In the present study, a preliminary assessment of wave runup has been conducted by using Stockdon's empirical model (Eq. 3.1), as a simplified function of the beach steepness, to examine the interaction between hydrodynamic forcing and vegetation. A more advanced wave modeling analysis guided by computational fluid dynamics (CFD) approaches (e.g., Delft3D software) will be adopted in forthcoming works. The average steepness for A1, A2, and A3 results in 0.136, 0.075, and 0.127, respectively. Since the mean total water levels associated with these three different values differ among each other by less than 10 cm, for simplicity, a mean value of $\beta_f = 0.11$ has been assumed for all the areas, with the resulting mean total water level h_m=0.65 m. Accordingly, the whole time series of the mean sea level and the total water level is reported in Fig. 3.6.

The best fitting of the probability distribution function of h was evaluated by using the χ^2 test and by by minimizing the RMSE between the theoretical and observed cumulative distribution functions (CDFs). We set a significance level of α=5% and used k=20 classes, resulting in a degree of freedom l=$k-n_p-1$, where n_p represents the number of parameters for a given distribution. We considered three distinct two-parameter distribution models: Lognormal, Gamma, and Weibull. As reported in figure 3.6b-c (see also Supporting Information Table S1), all three

distributions are well fitted onto the sample data (low p-values for χ^2 test and low RMSE). The Lognormal distribution emerged as the most statistically robust choice, so it was adopted to compute three characteristic values: the mean total water level, the 95th percentile, and the 99th percentile, respectively equal to 0.52 m, 1.63 m, and 2.61 m. For ease of reference, we will denote these water levels as h_{50}, h_{95}, and h_{99}.

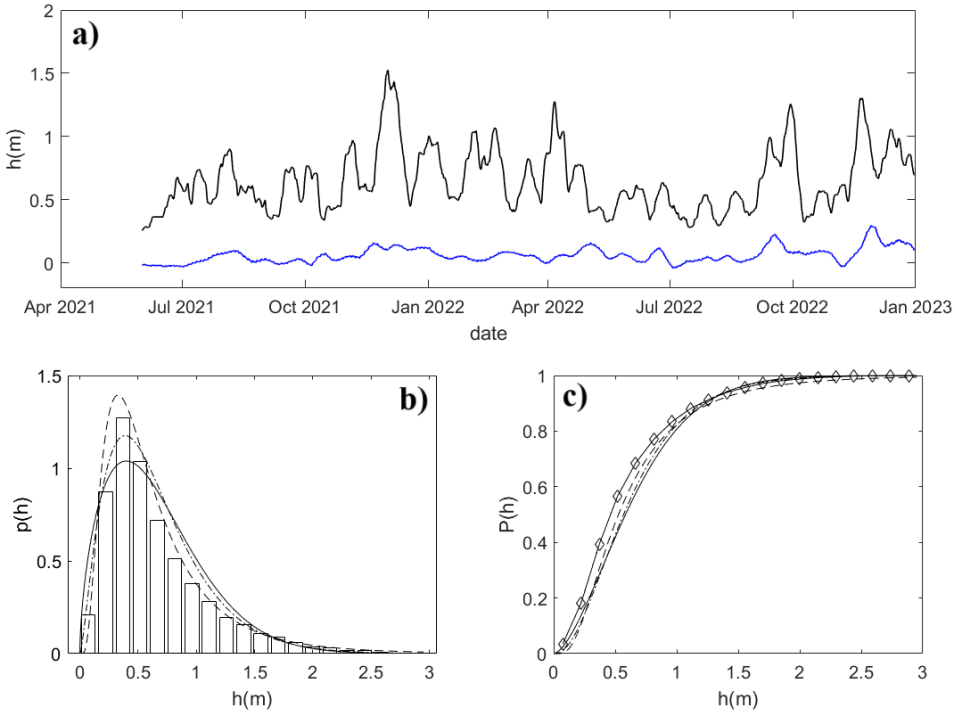

Fig. 3.6 (a) Time series of the mean sea level η from RMN database (blue line) and total water level h for β_f=0.11 (black line). (b) PDF of Lognormal (dashed lines), Gamma (dot-dashed line), Weibull (solid line), and histogram of the observed sample. (c) CDF of Lognormal (dashed lines), Gamma (dot-dashed line), Weibull (solid line) and observed CDF (solid line with diamonds).

Figure 3.7 shows a comparison between the vegetation threshold line L_{veg} and contour lines of elevations corresponding to h_{95} and h_{99}, which mark the limits of the flooded areas on the shore. Instead, the shoreline has been computed as the contour line of the DTM corresponding to 0 m elevation on the mean sea level.

In the areas A2 and A3 (Fig. 3.7b-c), h_{99} corresponds to the front edge of the fore-dune and almost overlaps with the L_{veg} edge, which is slightly higher elevation and closer to the crestline (the average distance between the two lines is approximately 5.7 m and 2.8 m, for A2 and A3, respectively). Therefore, exposure to waves during

severe autumnal and winter storms prevents the growth of any type of vegetation, acting like a cut-off for vegetation zonation. On the contrary, in area A1, the h_{99} line reaches past the L_{veg} border, actually interacting with the vegetation which is very sparsely distributed on the seaward side of the first dune crest.

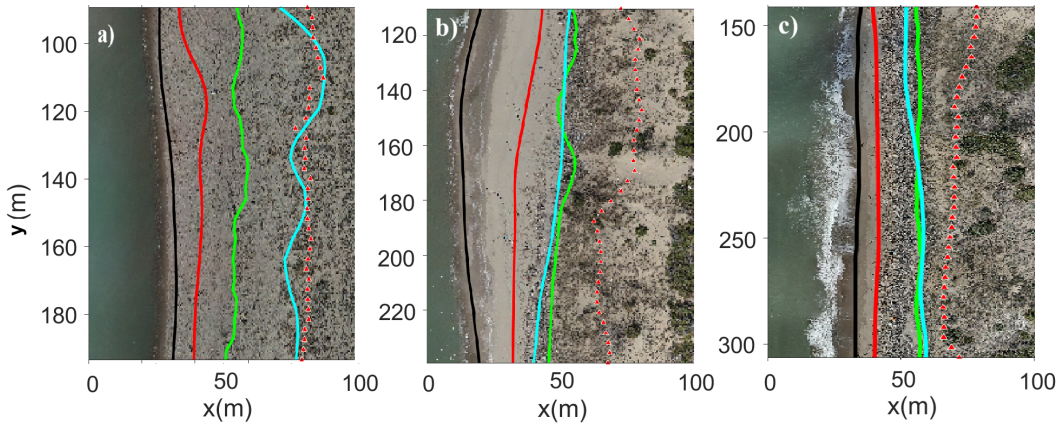

Fig. 3.7 Orthoimages of A1(a), A2(b), A3(c) with contour lines corresponding to 0m elevation, marking the reference shoreline position (solid black line), 95th (solid red line) and 99th (solid cyan line) total water level percentile. Overall vegetation threshold line (solid green line) and foredune crestline (red triangles) are also highlighted

3.3.4 Geometrical Features

The computation and distribution of the Equivalent diameter (ED, cfr. eq. 3.2) is reported in figure 3.8a-c. The statistical distributions of the same species in different areas are coherent with each other, as shown by the similarity of boxplots (in terms of median and IQR) of *Aa, Em, Ep, Pm, Dg* in figures 3.8a-c. This suggests that different morphology, environmental conditions and abundance do not affect significantly the size distribution of vegetation species. The main exception is *Helichrysum stoechas*, which measures 0.27 m in A1, notably less than the 0.4-0.5 m in A2 and A3. This could be due to either: (i) its concentration in heavily trodden areas of A1, leading to more anthropogenic impact, or (ii) heightened inter-species competition since species are evenly spread in A1, resulting in fewer resources per species. A significant 30% decrease in *Helichrysum stoechas* distribution across the shore (from 0.35 m to 0.25 m) around 40 m behind the initial crestline may mark where overtrampling effects intensify.

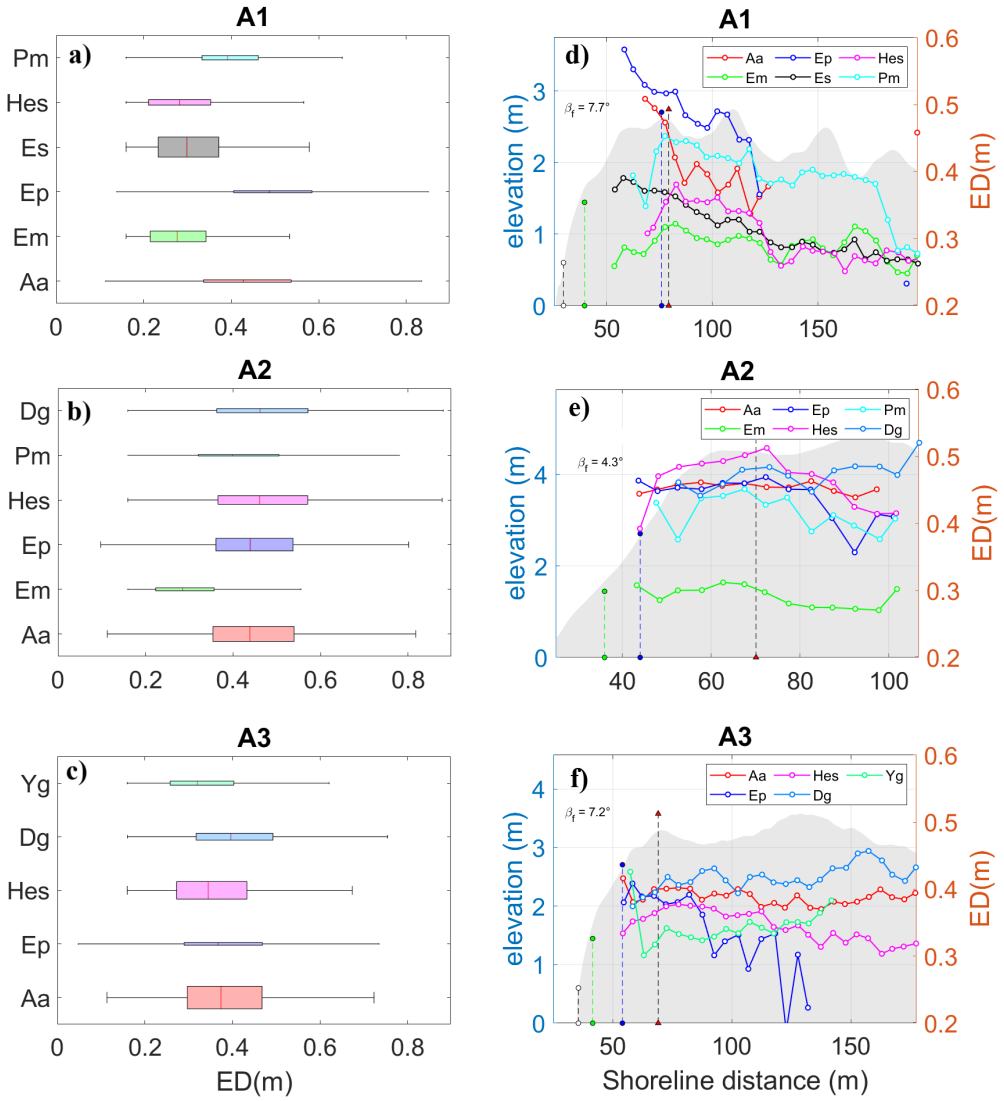

Fig. 3.8 Boxplot of ED for every plant species in A1(a), A2(b) and A3(c). The width of the boxes is proportional to the abundance of the species in the study area. Distribution of mean Equivalent Diameter (ED) of each plant species along the direction perpendicular to the shoreline for A1 (d), A2 (e), and A3 (f). The mean topographic profile in this direction is highlighted in grey. The positions of the mean foredune crest (black dashed line with red triangles), mean total water level (blue dashed line with blue dots), 95th percentile (green dashed line with green dots), and 99th percentile (black dashed line with white dots) are also indicated. Abbreviations: *Aa* (Ammophila arenaria), *Em* (Eryngium maritimum), *Ep* (Euphorbia paralias), *Es* (Echinophora spinosa), *Hes* (Helichrysum stoechas), *Pm* (Pancratium maritimum), *Dg* (Daphne gnidium), *Yg* (Yucca gloriosa).

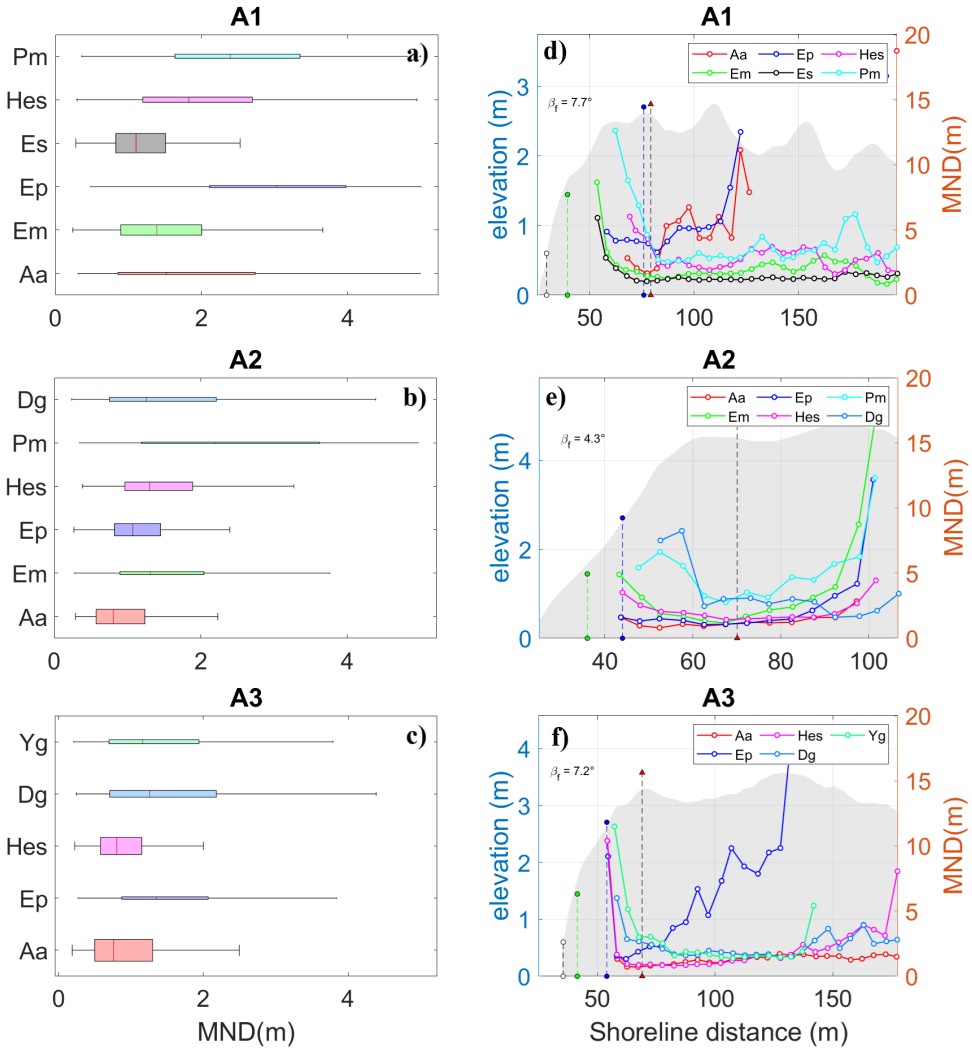

Fig. 3.9 Boxplot of MND for every plant species in A1(a), A2(b) and A3(c). The width of the boxes is proportional to the abundance of the species in the study area. Distribution of MND of every plant species along the direction perpendicular to the shoreline for A1(d), A2(e) and A3(f). In grey, it's highlighted the mean topographic profile along the direction perpendicular to the shoreline. Are also highlighted the position of the mean foredune crest(black dashed line with red triangles), mean total water level(blue dashed line with blue dots), 95th percentile(green dashed line with green dots), 99th percentile(black dashed line with white dots).Abbreviations: *Aa* (Ammophila arenaria), *Em* (Eryngium maritimum), *Ep* (Euphorbia paralias), *Es* (Echinophora spinosa), *Hes* (Helichrysum stoechas), *Pm* (Pancratium maritimum), *Dg* (Daphne gnidium), *Yg* (Yucca gloriosa).

Figures 3.8d-f illustrate a consistent trend in the spatial distribution of ED among all species, namely a notable decline as the distance from the peak point increases.

Notably, *Ammophila arenaria* in A2 and A3 bucks this trend, maintaining relatively stable ED regardless of distance from the shoreline. Moreover, in A1, where wave runup extends beyond the vegetation threshold, ED diminishes rapidly toward the swash zone, particularly between the 95th and 99th percentile line (figure 3.2a). This underscores how severe flooding events impede plant growth, hindering their size.

Figure 3.9a-c illustrates the remarkable variability of the Mean Neighbor Distance (MND) across three study areas, contrasting with the Equivalent Diameter (ED) patterns. In A1, species exhibit notably wider intra-species distances, with median values surpassing 2 m, observed in species like *Euphorbia paralias*, *Helichrysum stoechas*, and *Pancratium maritimum*. Conversely, A2 and A3 show consistent MND distributions among shared species, with narrower intra-species distances, generally below 2 m.

Interestingly, species with lower abundance tend to display wider Interquartile Ranges (IQRs) and higher medians across all areas. This suggests that abundance influences not only average spatial density but also spatial distribution patterns. Narrow IQRs indicate more uniform spacing, while wider IQRs suggest a more irregular, patchy distribution.

Less abundant species, as the cases of *Ammophila arenaria* and *Euphorbia paralias* in A1 (Fig. 3.9a), *Eryngium maritimum* and *Pancratium maritimum* in A2 (Fig. 3.9b), and *Euphorbia paralias* and *Daphne gnidium* in A3 (Fig. 3.9c), with high IQR, show a decrease of MND within a short distance from the minimum, indicating a 'quick' spread out from the region of maximum density. Instead, more abundant species like *Echinophora spinosa* in A1 (Fig. 3.9a), *Ammophila arenaria*, *Euphorbia paralias*, and *Helichrysum stoechas* in A2 (Figure 3.9b), and *Ammophila arenaria* and *Helichrysum stoechas* in A3 (Figure 3.9c), also tend to spread out with distance from the peak density region, but to a much lesser magnitude and within wider distances.

The decrease in vegetation density within the swash zone in A1 and A3 (figure 3.9d-3.9f) is much more pronounced compared to the slight decrease of ED in the same region. Therefore, vegetation density appears to be more significantly impacted by runup than vegetation size. This may suggest that extreme wave events occur at intervals shorter than the time it takes for plants to reach maximum growth.

Vegetation size and density are crucial eco-morphological variables, reflecting the 'health state' of plant species. We examined the relationship between these two by

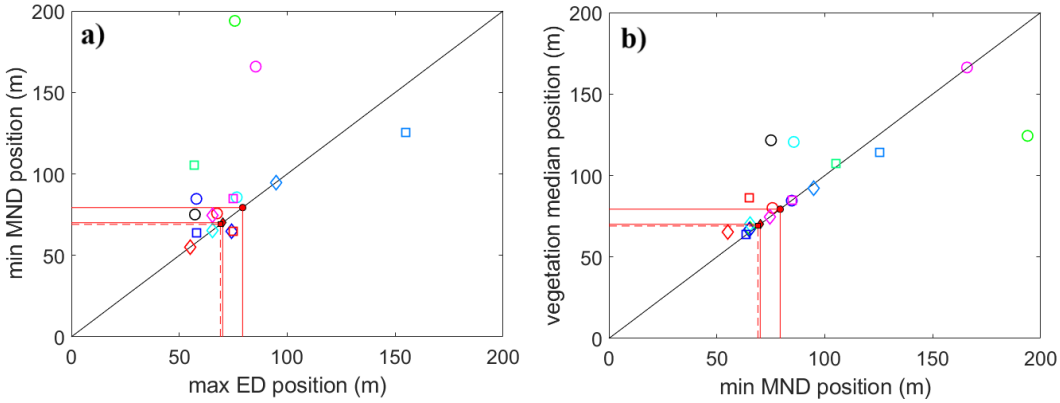

Fig. 3.10 (a)Coordinate of maximum ED vs minimum MND in the across-shore direction; (b)Coordinate of minimum MND vs spatial distribution median in the across-shore direction. Circular, diamond and square dots represents data respectively from A1, A2 and A3. Each plant species is identified by a color: Red, Ammophila arenaria; green, Eryngium maritimum; blue, Euphorbia paralias; black, Echinophora spinosa; magenta, Helichrysum stoechas; cyan, Pancratium maritimum; sky blue, Daphne gnidium; water green, Yucca gloriosa. Positions of crestlines (red lines) and the bisector line (solid black line) are also highlighted.

comparing the distance from the coastline of regions of maximum ED, denoting areas of greatest vegetation growth, and regions of minimum MND, indicating regions of highest vegetation density. Figure 3.10a illustrates that in A1, the maximum ED for all species occurs near the first crestline, as indicated by the abscissa of circles clustered around the A1 crestline's abscissa (marked with a small red dot). This suggests that in A1, areas of maximum ED are more closely associated with the crestline rather than regions of minimum MND, where higher vegetation growth is also expected. This is shown by the separation of circles from the bisector line in Figure 3.10a. Consequently, due to the uniform environmental conditions resulting from a flatter terrain morphology, the areas where plant species exhibit the most significant growth do not always align with the areas that provide optimal conditions for larger growth.

In A2 and A3, instead, the regions of maximum ED of all species show a correlation with regions of minimum MND, as we can see in figure 3.10a, with square and diamond points clustering around the bisector line. Hence, in these cases, there exists a duality between the spatial density and plant size distribution for which regions of higher density correspond to regions of greatest growth. Furthermore, Fig. 3.10b shows that all species have a clear correlation between the regions of

minimum MND and the position along the cross-shore direction of median of their spatial distribution (Figure 3.4), as denoted by diamond and square points aligning on the axis bisector.

3.3.5 Spatial Autocorrelation Analysis of Geometric features

Experimental semivariograms and best-fitting models of ED and MND have been computed to analyze their spatial autocorrelation. The parameters of best-fitting theoretical semivariograms (i.e., *nugget*, *range*, *sill*), are summarized in tables 3.3 and 3.4. The complete set of semivariograms are reported in the Supporting Information S4-S9.

In nearly half of the cases, ED semivariograms show no discernible structure, with low R^2 values indicating a poor fit of theoretical models to the data. Consequently, these cases lack a noticeable spatial autocorrelation. Conversely, the remaining cases demonstrate well-defined semivariogram structures with high R^2 values, suggesting discernible spatial autocorrelation. However, despite clear structures, high nugget values (around 0.9) imply low autocorrelation even at distances shorter than the minimum lag distance (1 m in this study). This discrepancy may stem from either genuinely weak autocorrelation among neighboring plant sizes or noise in the dataset due to segmentation inaccuracies in the OBIA algorithm. Exceptions to this trend include *Helichrysum stoechas* and *Eryngium maritimum* in A1, which exhibit nugget values below 0.8, indicating slightly stronger spatial correlation.

Overall, the *range* of effective diameter (ED) remains within approximately 10 m, consistent with similar studies [247], suggesting that vegetation diameter correlation diminishes over relatively short distances. This pattern may be attributed to the spatial cohesion of plants within individual patches of vegetation, which are correlated with neighboring plants but not with those outside their patch. Notably, *Ammophila arenaria* in A1 and A2 display wider ranges (33.7 m and 66.0 m, respectively) compared to other species and even compared to the same species in A3 (range of 3.8 m).

Regarding the MND patterning, Table 3.4 reveals that over two-thirds of the cases have been excluded. These cases fail to align with any theoretical semivariogram model ($R^2 < 0.7$). In contrast, the accepted cases exhibit MND semivariance nugget values significantly lower (ranging from 0.34 to 0.65) than those of EMD

cases. This discrepancy suggests a notably less noisy dataset and a stronger spatial autocorrelation at distances within the range. The quantity MND demonstrates a tendency to lose spatial autocorrelation over much greater distances compared to ED. Specifically, the range values fall between 17 and 36.7 m, with exception of *Helichrysum stoechas*, which displays a lower range of 4.02 m. This range is notably greater than the ED cases, where ranges span from 2 to 10.7m (Table 3.3), excluding the outliers of 33.7 m and 66 m for *Ammophila arenaria* in A1 and A2, as discussed previously.

ED

Best Fit Model

	Aa	**Em**	**Ep**	**Es**	**Hes**	**Pm**	**Dg**	**Yg**
A1	gauss	exp	exp	exp	gauss	exp	-	-
A2	gauss	gauss	spherical	-	spherical	spherical	gauss	-
A3	exp	-	gauss	-	exp	-	spherical	spherical

R^2

	Aa	**Em**	**Ep**	**Es**	**Hes**	**Pm**	**Dg**	**Yg**
A1	0.75	0.99	0.37	0.91	0.89	0.87	-	-
A2	0.96	0.28	0.98	-	0.60	0.13	0.37	-
A3	0.93	-	0.71	-	0.77	-	0.49	0.38

Nugget(m)

	Aa	**Em**	**Ep**	**Es**	**Hes**	**Pm**	**Dg**	**Yg**
A1	0.87	0.7	0.82	0.8	0.73	0.8	-	-
A2	0.91	0.93	0.85	-	1.02	0.96	0.94	-
A3	0.93	-	0.96	-	0.89	-	0.98	0.97

Range(m)

	Aa	**Em**	**Ep**	**Es**	**Hes**	**Pm**	**Dg**	**Yg**
A1	33.7	10.7	63.5	3.5	6.11	45.9	-	-
A2	66.0	3.4	9.6	-	22.9	32.6	10.32	-
A3	3.8	-	-	-	2.0	-	39.2	18.2

Sill(m)

	Aa	**Em**	**Ep**	**Es**	**Hes**	**Pm**	**Dg**	**Yg**
A1	0.95	0.91	0.87	0.89	0.87	0.86	-	-
A2	0.96	0.98	1.03	-	1.04	1.02	0.99	-
A3	0.99	-	0.97	-	1.01	-	1.01	0.98

Table 3.3 Feature parameters of ED semi-variograms, for every plant species and study area. Are highlighted in green the parameters of those semi-variograms satisfying the acceptance conditions described in paragraph 3.2.3.

MND								
Best Fit Model								
	Aa	**Em**	**Ep**	**Es**	**Hes**	**Pm**	**Dg**	**Yg**
A1	gauss	gauss	spherical	gauss	exp	exp	-	-
A2	gauss	spherical	gauss	-	spherical	gauss	gauss	-
A3	gauss	-	exp	-	gauss	-	spherical	spherical
R^2								
	Aa	**Em**	**Ep**	**Es**	**Hes**	**Pm**	**Dg**	**Yg**
A1	0.33	0.52	0.32	0.47	0.82	0.66	-	-
A2	0.49	0.69	0.96	-	0.41	0.36	0.35	-
A3	0.81	-	0.92	-	0.66	-	0.88	0.77
Nugget(m)								
	Aa	**Em**	**Ep**	**Es**	**Hes**	**Pm**	**Dg**	**Yg**
A1	1.02	0.75	0.71	0.85	0.62	0.76	-	-
A2	0.69	0.57	0.47	-	1.07	1.19	1.13	-
A3	1.22	-	0.34	-	1.17	-	0.65	0.51
Range(m)								
	Aa	**Em**	**Ep**	**Es**	**Hes**	**Pm**	**Dg**	**Yg**
A1	3.8	2.2	22.1	8.35	4.02	5.62	-	-
A2	5.4	20.9	27.19	-	5.2	32.2	36.28	-
A3	31.3	-	17	-	9.4	-	34.7	36.7
Sill(m)								
	Aa	**Em**	**Ep**	**Es**	**Hes**	**Pm**	**Dg**	**Yg**
A1	1.35	0.82	1.06	1.05	0.97	0.98	-	-
A2	1.11	0.57	0.78	-	0.99	0.8	0.95	-
A3	0.9	-	1.17	-	0.96	-	1.03	1.13

Table 3.4 Feature parameters of MND semi-variograms, for every plant species and study area. Are highlighted in green the parameters of those semi-variograms satisfying the acceptance conditions described in paragraph 3.2.3.

3.3.6 Point Pattern Analysis

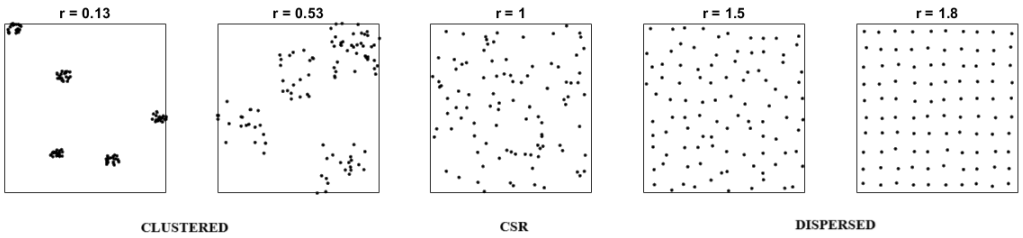

Fig. 3.11 Example of five different synthetic spatial point patterns with their nearest neighbor index r. The lower the value of r, the higher the level of clustering or aggregation of points. The higher r, the higher the level of dispersion

The results from the MNN analysis reveal a distinct clustered spatial arrangement among all species, as indicated by the r index being consistently less than 1 with high statistical significance, as Z-scores are below -1.96 (see Table 3.5). This clustering suggests that in environments with limited space, such as coastal dunes, short-range spatial variability in soil properties and environmental factors may play a more prominent role in determining vegetation patterns than competition for resources. This is in contrast to ecosystems like forests, where resource competition is the main factor determining the spatial arrangement of vegetation, leading to more dispersed patterns [248].

It's worth noting that the same plant species in different study areas exhibit varying degrees of clustering, as lower r values indicating higher levels of clustering and more distinct patches, while higher r values, closer to 1, indicate a more uncertain and 'fuzzier' clustering pattern [241]. An example is shown in figure 3.11. Therefore, the degree of clustering cannot be considered as an attribute depending on the species of the plant.

In discussing the behavior of MND distribution in Sect. 3.3.4, we hypothesized a correlation between MND deviation (indicated by the inter-quartile range, IQR) and pattern type, noting that less abundant species tend to exhibit greater MND deviation, potentially leading to a more clustered pattern, and vice versa. The clustering degree, expressed by the nearest neighbor index r, can therefore be related to species abundance. To explore this relationship, the index r has been reported against abundance (Figure 3.12). The linear regression model shows an increase in r as a function of abundance, with a coefficient of determination R^2=0.64. While not ideal, this R^2 value is significant considering it reflects only abundance, without accounting

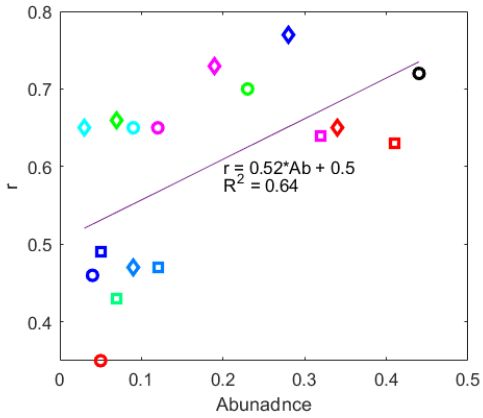

Fig. 3.12 Abundance vs nearest neighbor index *r*. Linear regression of observed data is represented by the black solid line.

					r			
	Aa	**Em**	**Ep**	**Es**	**Hes**	**Pm**	**Dg**	**Yg**
A1	0.35	0.7	0.46	0.72	0.65	0.65	-	-
A2	0.65	0.66	0.77	-	0.73	0.65	0.47	-
A3	0.63	-	0.49	-	0.64	-	0.47	0.43
					Z-score			
	Aa	**Em**	**Ep**	**Es**	**Hes**	**Pm**	**Dg**	**Yg**
A1	-43.3	-63.63	-30.67	-75.94	-52.75	-35.7	-	-
A2	-57.84	-37.41	-34.11	-	-32.37	-18.11	-43.61	-
A3	-101.87	-	-50.45	-	-93.95	-	-77.11	-76.96

Table 3.5 Nearest neighbour index, *r*, and Z-score values for every plant species and study area.

for other potential error sources or the various factors influencing clustering, such as soil type, pH, and humidity.

Therefore, although the pattern type is always clustered for all cases ($r < 1$), less abundant species tend to exhibit higher levels of clustering compared to more abundant ones, coherently with the results of MND analysis.

The behavior of the modified Ripley's *L*-function confirms a statistically significant clustering pattern for all vegetation species, as $L(r)$ remains mostly in the top half of the graph, above the confidence interval (figure 3.13). From figure 3.13a, the *L*-function of *Ammophila arenaria* in A1 has 2 peaks at 22 and 50 m, indicating a clear clustering at 2 distinct spatial scales, as shown in the example in figure 3.13d-e.

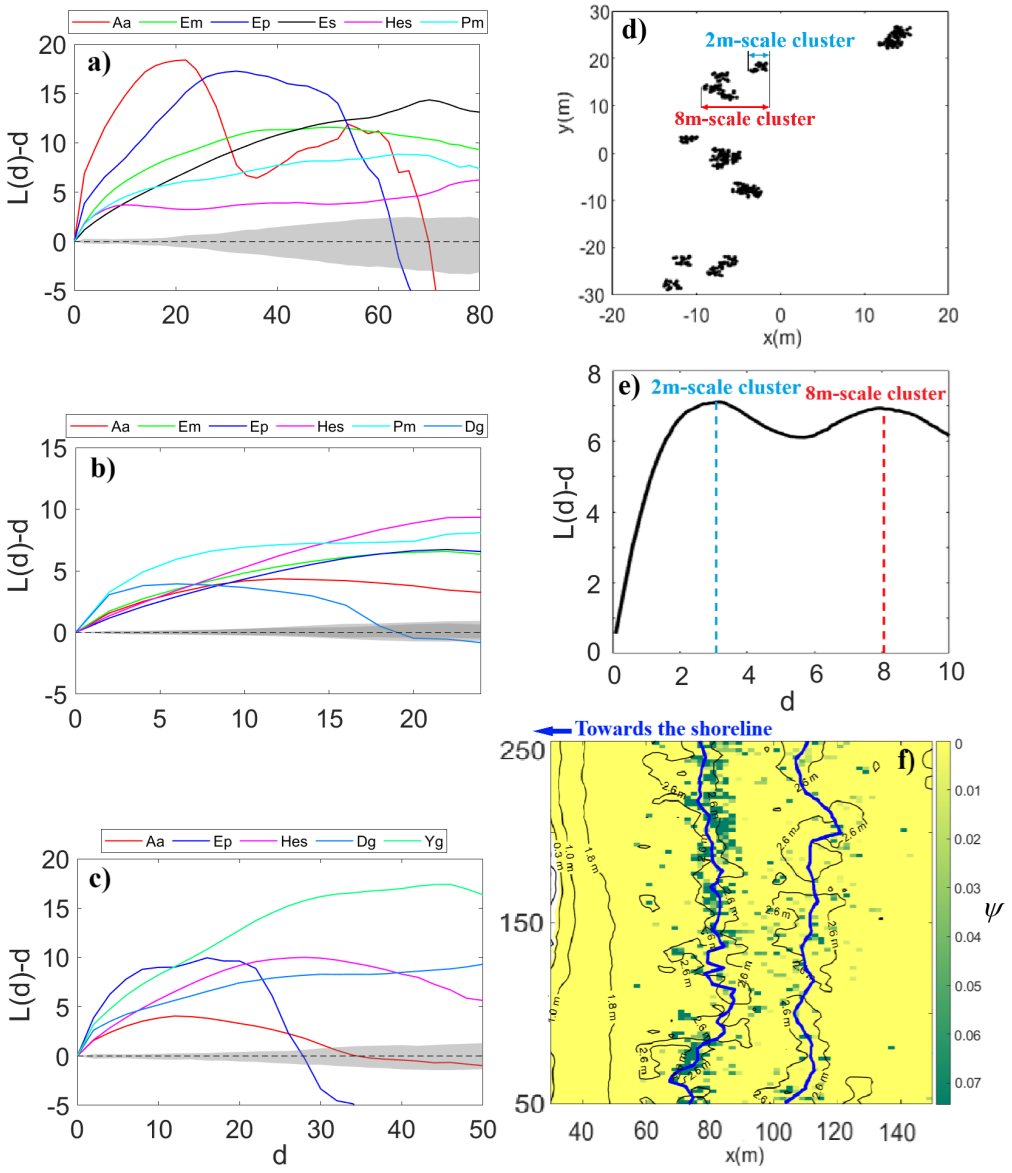

Fig. 3.13 L-function for different plant species in A1(a), A2(b) and A3(c). The 95% confidence interval for the L-function computed through Monte Carlo simulation is highlighted in grey. (d) Example of a synthetic clustered spatial point pattern at two different scales: larger clusters at 8 m scale constituted by smaller clusters at 2 m scale. The two peaks in $L(d)$ graph (e) represents those two cluster scales and fall at distances d very close to 2 and 8m. (f) Two-dimensional 2m-resolution Ground Cover map of *Ammophila arenaria* in A1. Contour lines of the elevation model (solid black lines) and crestline of the first and second row of shadow dunes (solid blue lines) are also plotted.

Those two scales can be related to the topography of the study area, as they are multiples of the wavelength of the embryonic dunes in A1 which is about 25 m. Furthermore, at the largest scale of about 70 m, the pattern turns from clustered to dispersed, as the red $L(r)$ curve in figure 3.13a drops below the confidence interval. Ground cover map of *Ammophila arenaria* shows clusters on the crest of the first two rows of dunes (Figure 3.13f). Other cases of multi-scale clusters can also be identified in those $L(d)$ curves that exhibit a plateau or multiple local maxima followed by a decrease. This could be the case of *Euphorbia paralias* in A1 (figure 3.13a), with cluster scales ranging from about 30 to 50 m; *Daphne gnidium* in A2 (figure 3.13b), with cluster scales from about 5 to 15 m; *Euphorbia paralias* in A3 (figure 3.13c), with clusters scales from about 5 to 20m.

The pattern of *Euphorbia paralias* in A1 and A3 (figure 3.13a-3.13c), shows a transition from a multi-scale cluster – even though with different sizes, probably due different extensions of study areas – to a dispersed pattern at largest scales, alike the case of *Ammophila arenaria* in A1. Other peculiar cases are the patterns of *Euphorbia paralias* in A2 (figure 3.13b) and *Ammophila arenaria* in A3 (figure 3.13c) which present a transition from clustered to random pattern as the scale increases, as $L(d)$ falls into the confidence interval, around 0. For all other cases, sizes of the main clusters are summarized in table 3.6.

	Cluster size(m)							
	Aa	**Em**	**Ep**	**Es**	**Hes**	**Pm**	**Dg**	**Yg**
A1	22	50	32	70	8	9	-	64
A2	12	22	22	-	26	27	6	-
A3	12	18	16	-	28	-	30	46

Table 3.6 Approximate size of plants clusters estimated with L-function.

3.4 Conclusions

A large vegetation dataset, derived by a machine learning classification algorithm, applied to ultra-high-resolution imagery of study areas, opens the possibility for a better insight into the complex inter-relationships between plant communities, terrain morphology, environmental forcings, and human presence, shaping sandy coastal dunes. Here we resume the key findings of the present research.

From the analysis of hydrodynamic forcings, we observed that, in well-formed dunefields, the threshold distance for vegetation growth is imposed by the reaching distance of wave runup during extreme events, acting as a cut-off for vegetation spatial distribution.

The morphology of the foredune is closely related to the abundance of dune-building species, like *Ammophila arenaria*, which also appears to be one of the most sensitive species to direct human disturbances. Abundance, in general, stands out as one of the main eco-morphological parameters in coastal vegetation pattern as the dune morphology is commanded by the role of predominant species. Morphology, in turn, highly impacts the zonation: the higher the foredune, the more distinct the plant zonation; on the contrary, the flatter the terrain, the fuzzier and indistinct the zonation.

Interestingly, we found that the ratio of the vegetation threshold distance L_{veg} to the distance from the foredune crestline x_{crest} remains relatively consistent, independently from the terrain morphology. This aspect suggests further validation in other sites. Furthermore, in well-formed dunes systems, species exhibit consistent L_{veg}/x_{crest} ratios regardless of morphology. In all three study areas, among halophyte species, flooding appears to influence the L_{veg} only of *Ammophila arenaria*, highlighting the role of hydrodynamic forces on the spatial distribution of dune-building species and, consequently, on dune morphology.

Our analysis of Equivalent Diameter (ED) revealed that plant size statistical distribution is minimally affected by terrain morphology and abundance but is related to the species type. Instead, the spatial distribution of plant sizes is influenced by species abundance, with higher-abundance species exhibiting more uniform spatial distribution. In well-formed dune systems, there is a strong correlation between the distances from the coastline and the peaks of ED and Mean Neighbour Distance (MND). In contrast, on flatter and disturbed dunes, the peak ED is located around the first dune crestline, independent of the peak MND. Wave runup has a moderate detrimental effect on plant size, likely due to the frequency of extreme flooding events surpassing plant growth rates

From the MND analysis, we observed that abundance strongly influences not only the mean plant density but also the pattern type of vegetation, with lower abundance species exhibiting a wider variation of local density, resulting in a clustering spatial pattern.

Semivariograms turned out not to be the best tool to analyze this type of dataset for the high level of noise in the dataset. Noise emerges when there are errors in measures and, in this case, the measure of ED and MND heavily depends on the accuracy of the classification algorithm. Despite the challenges posed by noise in the dataset, semivariograms highlighted the limited spatial autocorrelation of plant size and the larger-scale autocorrelation of plant density.

The Mean Nearest Neighbour point pattern analysis revealed a clustered spatial arrangement for all species taken into exam, although, the degree of clustering is correlated with the abundance, confirming that abundance is the main factor controlling the pattern type of a plant species: Notably, the L-function emerged as a valuable tool for elucidating the type and scales of vegetation clusters, revealing multi-scale clustering patterns for many coastal species.

We provided here a species-by-species extensive qualitative and quantitative description of vegetation spatial patterns using different geostatistical tools, widely used in spatial analysis and vegetation studies. Patterns identified in our study can represent a valid benchmark to tune and validate eco-morphodynamic models, e.g. the physically-based model proposed by Duràn [211], and a knowledge advancement for the monitoring of coastal dune health and preservation of coastal environments.

Chapter 4

Recovery Time of Coastal Dune Vegetation

In this chapter, a novel formulation for the recovery time of coastal dune vegetation using a stochastic approach is presented.

4.1 Introduction

Vegetation recovery in coastal dunes is measured over timeframes ranging from roughly one year to several decades. Field and remote-sensing studies report that recovery following disturbances such as hurricanes or trampling proceeds rapidly on elevated, wide beaches with ample sediment supply and favorable species traits [249]. For instance, one study using NDVI measurements indicates roughly one-year recovery post-hurricane, while a 21-year field study recorded up to a 12% annual increase in vegetation cover [250]. Faster recovery supports sustained dune elevation and reduced erosion, thereby enhancing coastal protection [251]; slower recovery, in contrast, is associated with increased dune mobility and vulnerability to overwash [250].

Several modeling approaches have been developed to study vegetation dynamics in coastal dune ecosystems. Process-based models like XBeach-Duna integrate nearshore, aeolian, and ecological processes to simulate long-term dune morphological responses to sediment supply and vegetation changes over decadal timescales

[252]. Another example is DOONIES model, undergoing an ecogeomorphological approach, simulating vegetation growth through photosynthesis-respiration balance and its feedback effects on sediment dynamics, with maximum daily photosynthesis being a key driver [47]. Cellular models have been used to examine biogeomorphic evolution under climate change scenarios, showing that vegetation growth rates critically determine dune recovery after disturbances [**?**]. The AeoLiS model focuses on wind-driven accretion and wave-driven erosion patterns, showing that vegetation density influences sediment deposition patterns, with high-density plantings trapping sediment near dune toes while low-density plantings allow broader accretion [253].

Stochastic models in ecology have been increasingly applied to understand vegetation dynamics, offering insights that differ significantly from traditional deterministic approaches. While deterministic models emphasize predictable outcomes like climax communities, stochastic models incorporate randomness in disturbance timing, dispersal, and colonization processes [254]. Research shows that the relative importance of stochastic versus deterministic processes varies across successional stages, with stochasticity typically dominating early succession before giving way to more deterministic, niche-driven dynamics [255]. Stochastic models have proven particularly valuable in floodplain ecosystems, where Poisson-distributed flood disturbances drive vegetation-sediment dynamics, successfully reproducing observed vegetation cover changes with high accuracy [256, 257]. Recent stochastic models incorporate finite vegetation colonization times and flooding frequency to better understand dune formation and recovery dynamics [258]. The field increasingly recognizes that both processes operate simultaneously, with their relative importance being context-dependent on factors such as disturbance regimes, management practices, and functional groups involved [259].
Taken together, these approaches demonstrate the importance of vegetation–sediment feedbacks but also reveal the need for simplified, tractable frameworks able to capture recovery dynamics explicitly.

In this work, we adopt a minimal stochastic framework [260] capable of capturing the essential physical and biological mechanisms driving coastal vegetation dynamics, while still allowing analytical treatment. This choice avoids the need for computationally intensive numerical simulations. Importantly, the framework explicitly incorporates the role of stochasticity, making it particularly well-suited to investigate how random forcing influences coastal ecomorphodynamics.

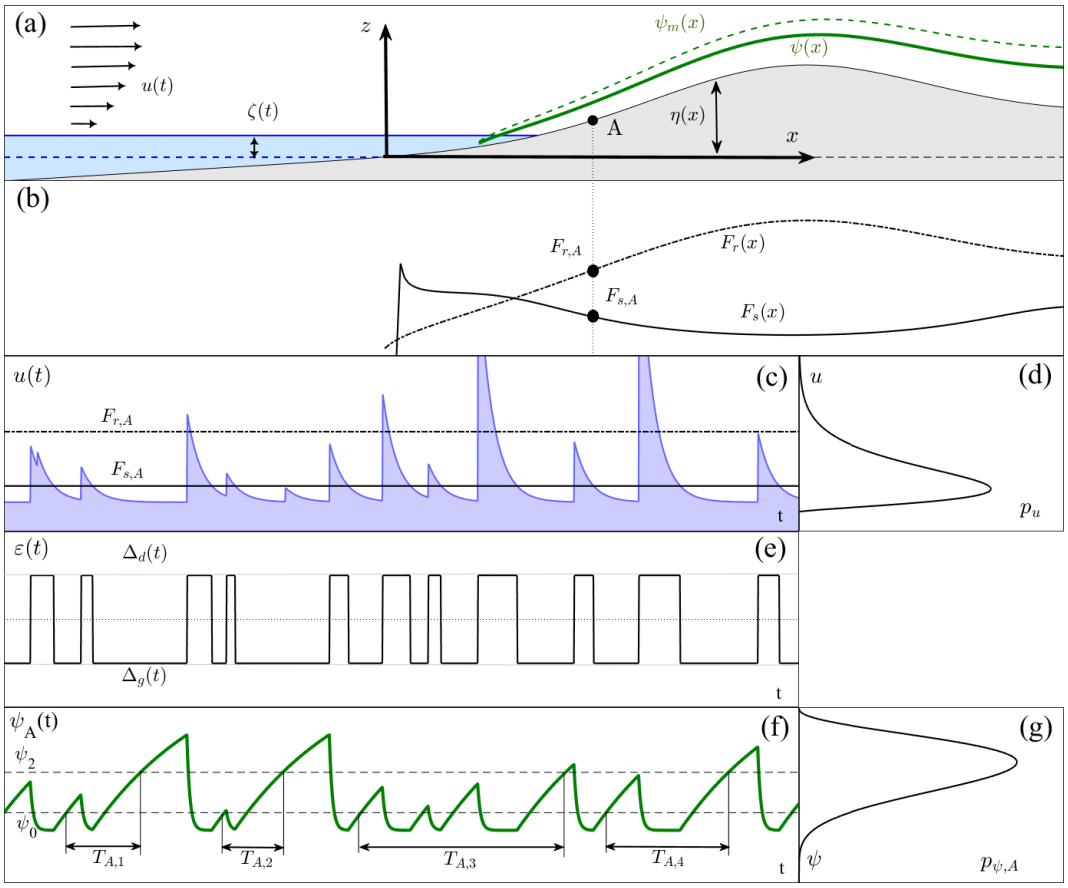

Fig. 4.1 (a)Sketch of a coastal dune cross-section. The solid blue line represents the water table at a generic time t, at elevation ζ from the mean sea level, marked with the dashed blue line; the solid green lines represent respectively the vegetation cover at a given time and the reachable vegetation cover threshold along the cross-shore direction. (b)Distribution along the transect of the wave runup threshold F_r (black dot-dashed line) and scour threshold F_s (black solid line). (c-d)Qualitative wind speed time series and its PDF. The thresholds at plot A are marked with the dot-dashed and solid lines. (e)Time series of the dichotomous noise ε at plot A. (f-g)Qualitative vegetation cover time series at plot A and its relative PDF. The sequence of recovery times, $T_{A,i}$, going from ψ_0 to ψ_2, are highlighted.

4.2 Theoretical Framework

4.2.1 Concept

The complex dynamics of dune vegetation is here simplified into a one-dimensional spatio-temporal framework along the cross-shore direction (Fig. 4.1a). Vegetation is

represented by the dimensionless ground cover index, $\psi(x,t)$ (i.e., vegetation coverage per unit area), which evolves in response to two types of environmental forcings, (*i*)wind and (*ii*)wave run-up, which can both induce a state of decay in the vegetation. For instance, vegetation in the swash zone is primarily subjected to flood-induced damage, such as anoxia or uprooting, whereas vegetation on foredune slopes and in dune slacks may experience wind-induced scour, leading to root exposure.
Another key aspect of this framework is that the vegetation at any given plot (i.e. the distance from the shoreline) can switch between two possible states, a growing state ($d\psi/dt > 0$) and a decaying state ($d\psi/dt < 0$) depending on the environmental forcings exceed a critical thresholds triggering a scour or a flooding process (Fig. 4.1c-f).
Both wind and run-up can be described as a function of the wind speed at the atmospheric boundary layer $u_\infty(t)$ [261–263], which is commonly treated as a random variable and modeled as a stochastic process with ensemble average $\mu_u = \langle u \rangle$, coefficient of variation c_u, an integral timescale $\mathscr{I}_u$ and a probability density function [264] (i.e., a Gamma-distributed compound Poisson process, described in Appendix D). It follows that, at any given plot, there's an alternation of periods of random duration of growth and decay, making the vegetation dynamics a stochastic process itself, which can be described by plot-specific PDFs [265].
Within this framework, we address the problem of computation of the mean vegetation recovery time, namely the time required for the vegetation to recover from a state ψ_0 to ψ_1 (with $\psi_0 < \psi_2$) in the presence of stochastic forcing (Fig. 4.1f).

4.2.2 Stochastic Modeling

This section summarizes the key aspects of the stochastic model developed by Camporeale and Latella (2025) [260] -CL25 from now on-, which serves as the foundation for evaluating the vegetation recovery time. It is therefore advisable to consult the original work for more detailed information.
Let us first define the geometry of a simplified cross-section of a coastal dune field, consisting of a linear swash zone with slope angle θ_0, followed by a Gaussian-like dune shape. To this purpose, the following dimensionless quantities are introduced: the across-shore coordinate X, the dune steepness β, the relative roughness ξ, and

the perturbation parameter ε.

$$X = \frac{x}{l}, \qquad \beta = \frac{h}{l}, \qquad \xi = \frac{z_0}{l}, \qquad \varepsilon = \frac{u_*}{u} = -\frac{\kappa}{\log(2\xi\sqrt{-\log 2\xi})}.$$

Where h is the dune height, l is the wavelength of the dune (i.e. the dune toe-heel distance), z_0 is the wall roughness height (2.5 times the median sand diameter D_{50}), κ is the von Karmann constant.

The topology of the dune $\eta(X)$ can therefore be expressed in dimensionless terms so that at $X = 0$, $\eta = 0$, marking the shoreline, while at $X = 1$, $d\eta/dX = 0$, marking the dune crest:

$$\eta(X) = \tan\theta_0 \arctan X + \beta e^{-4(X-1)^2} \tag{4.1}$$

The temporal evolution of vegetation at each plot X is represented as a dichotomous process of two possible states, decay and growth, reading:

$$\dot{\psi} = \begin{cases} f_d = -k\psi & F > F_{s|r}(a) \\ f_g = \psi_m - \psi - \alpha & F < F_{s|r}(b) \end{cases} \tag{4.2}$$

Equations 4.2 depicts an exponential decay of vegetation when the wind forcing F exceeds the critical threshold for scouring/flooding $F_{s|r}$ (eq. 4.2a), and a logarithmic growth otherwise (eq. 4.2b).

$\dot{\psi}$ is the time derivative of the vegetation cover relative to a dimensionless time $t^* = t/t_g$, with t_g representing a species-specific characteristic growth time scale of the vegetation; $k = t_g/t_d$ is the ratio between vegetation growth and decay timescales; ψ_m is maximum reachable vegetation cover, which can be assumed equal to 1 (i.e. 100% vegetation cover); $\alpha = \mathscr{K}|\dot{\eta}|$, with $|\dot{\eta}|$ is the local sedimentation/erosion rate and $\mathscr{K}$ is a multiplicative coefficient. The term α accounts for the positive response of some coastal species, such as halophyte plants like the *Ammophila Arenaria (L.) Link* (i.e., *Marram grass*) to sand erosion/accumulation. These species exhibit a high tolerance to both scouring and burial and can even benefit from these processes up to a specific critical threshold [266]. From now on, we refer to this type of vegetation as *type-II* vegetation, while with *type-I* we indicate vegetation with low tolerance to scour/burial, for which $\alpha = 0$. The expressions to compute the term α are reported in Appendix D.

The conditions in equations 4.2a-b are posed in terms of a dimensionless windy "Froud-like" number, $F = u(t)/\sqrt{gl}$, which can be greater or less than a control

threshold value $F_{s|r}$, namely the minimum value between the scouring threshold F_s and the run-up threshold F_r, reading respectively:

$$F_r = \left(\frac{\eta(X) - a/l}{g_r(\theta_0) c_0 \sqrt{2\pi r}} \right)^{\frac{1}{2}} \quad (a); \quad \begin{cases} F_{s,I} = \left(\frac{\tau_{*c}}{\mathscr{A}\Phi} g_{s,I} \right)^{\frac{1}{2n}} & typeI \\ F_{s,II} = \left(\frac{(1+\Gamma\psi)^n (\psi_m - \psi)}{\mathscr{K}_1 g_{s,II}} \right)^{\frac{1}{2n}} & typeII \end{cases} \quad (b) \tag{4.3}$$

In eq. 4.3a, a is the maximum tidal range (i.e. the difference between water levels reached during high tide and low tide); $g_r(\theta_0)$ is a factor accounting for the beach slope (see Appendix D); $c_0 = 0.8$ is the ratio between wave celerity in deep waters and wind velocity; $r = \zeta_{dw} g/u^2$ is a proportionality coefficient between the significant wave height in deep waters ζ_{dw} and wind speed. In eq. 4.3b, $\tau_{*c0} \approx 0.02$ is the critical Shields parameter for incipient mobilization of small sand sediments in the absence of vegetation; $\mathscr{A} = 10^{-3}\varepsilon^2/\xi$; $\Phi(X)$ is the distribution of the Shields parameter over the dune profile (see Appendix D); $g_{s,I-II}$ is a correction function for the critical Shields stress due to the local slope (see Appendix D); Γ is a dimensionless roughness factor ($\Gamma = 16$ [267]); $\mathscr{K}_1$ is a multiplicative factor; n is the power in the Heng total sediment load transport formula [268].
It is worth pointing out the physical meaning of the aforementioned thresholds expressed in eq. 4.3. The runup threshold is derived by setting the equality between the altitude reached by water due to run-up on the swash zone [189] and the topographic height $\eta(X)$. In other words, the decay state is triggered in the points where the altitude is lower than the level reached during the wave run-up. The scouring threshold for *type-I* vegetation is derived by setting the Shields shear stress equal to the critical threshold for incipient mobilization, meaning that the vegetation cannot withstand any amount of erosion or deposition. Differently, the scouring threshold for *type-II* corresponds to an erosion/deposition rate at which the vegetation is no more able to keep up with, and is derived by setting the growth function,$f_g = 0$ (Eq. 4.2b).
According to the theory of stochastic processes [264], the two equations can be combined into one stochastic ordinary differential equation:

$$\frac{d\psi}{dt} = f(\psi) + g(\psi)\varepsilon(t) \tag{4.4}$$

Where $\varepsilon(t)$ is a dichotomous Markov noise (DMN), switching between two arbitrary values, Δ_d and Δ_g. $f(\psi)$ and $g(\psi)$ are functions allowing the eq.4.4 to reduce to either f_d or f_g (eq. 4.2a-b) when ε assumes, respectively, values Δ_d or Δ_g, namely:

$$f(\psi) = -\frac{\Delta_g f_d - \Delta_d f_g}{\Delta_d - \Delta_g}, \qquad g(\psi) = \frac{f_d - f_g}{\Delta_d - \Delta_g} \tag{4.5}$$

It can be assumed the noise $\varepsilon(t)$ having zero average, such that $k_g\Delta_d + k_d\Delta_g = 0$, with $k_d = \langle t_{F>F_{s|r}} \rangle^{-1}$ and $k_g = \langle t_{F<F_{s|r}} \rangle^{-1}$ average shifting rates of the two states, namely, the inverse of the average permanence times in the decay or growth state (See Appendix D for the computation of $\langle t_{F>F_{s|r}} \rangle^{-1}$ and $\langle t_{F<F_{s|r}} \rangle^{-1}$). By setting $\Delta_d = 1$, we can deduce $\Delta_g = -k_g/k_d$, so, with little manipulation, eq. 4.5 become

$$f(\psi) = \frac{-k_g k\psi + k_d(\psi_m - \psi - \alpha)}{k_d + k_g}, \qquad g(\psi) = \frac{k_d(\psi + \alpha - k\psi - \psi_m)}{k_d + k_g} \tag{4.6}$$

The master equation for eq. 4.4 is the plot-specific probability density function of ψ at any given time t [269], of which, the stationary solution at steady-state (for $t \to \infty$) reads:

$$p_\psi = \mathscr{N} \frac{(k-1)\psi + \psi_m - \alpha}{\psi^{1-k_d/k}(\alpha + \psi - \psi_m)^{1-k_g}} \tag{4.7}$$

Here $\mathscr{N}$ is a normalization constant to make the integral of the pdf equal to 1.

4.2.3 Mean Recovery Time

The computation of the mean recovery time (RT) of vegetation is based on the theory of Mean First Passage Time (MFPT) in a bi-stable dynamical system driven by a dichotomous Markov noise, described by the stochastic eq.4.4 [270, 257]. Considering an interval (x_1, x_2) (with $x_1 < x_2$) out of the possible values of a stochastic variable $x(t)$, if initially $x(t=0) = x_0 \in (x_1, x_2)$, the MFPT, $T(x_0)$, is the expected time for the $x(t)$ to "escape" from the domain (x_1, x_2) (Figure 4.1f). The MFPT, satisfies

the Kolmogorov backward equation, which describes the evolution in time of the probability density of a Markov stochastic process, under the boundary conditions $\partial T(x)/\partial x\big|_{x=x_1} = 0$ and $T(x = x_2) = 0$. The former condition denotes a reflecting boundary at x_1, while the latter an absorbing boundary at x_2 [271, 272].
In this particular context of vegetation dynamics, the MFPT, $T(\psi_0)$, describes the mean time for the vegetation cover to reach a value ψ_2 for the first time, from an initial state ψ_0. The analytical expression of the dimensionless MFPT, proposed by Sancho (1985) [270], reads

$$T(\psi_0) = \int_{\psi_0}^{\psi_2} \frac{(k_d + k_g)d\psi}{\Psi(\psi)\Phi(\psi)} \int_{\psi_a}^{\psi} \Psi(\psi')d\psi' \tag{4.8}$$

Where $\psi_a = 0$ is the lower natural boundary of $\psi(t)$ (i.e., $f_d(\psi_a) = 0$), while $\psi_b = \psi_m - \alpha$ is the upper natural boundary of the system (i.e., $f_g(\psi_b) = 0$) [273]. The functions $\Psi(\psi)$ and $\Phi(\psi)$ represent respectively the stationary probability and the diffusion term of a substitutive Fokker-Plank process [272]. They read as follows:

$$\Phi(\psi) = -[f(\psi) + \Delta_g g(\psi)][f(\psi) + \Delta_d g(\psi)] \tag{4.9}$$

$$\Psi(\psi) = [f(\psi) + \Delta_d g(\psi)]^{-1} exp\left[\int^{\psi} \frac{(k_d + k_g)f(\psi')}{\Phi(\psi')} d\psi'\right] \tag{4.10}$$

The analytical expressions for $\Phi(\psi)$, $\Psi(\psi)$ and $T(\psi_0)$ are reported below:

$$\Phi(\psi) = k\psi(\psi_m - \psi - \alpha), \tag{4.11}$$

$$\Psi(\psi) = -\frac{\psi^{-(k_d/k-1)}(\alpha + \psi - \psi_m)}{k}, \tag{4.12}$$

that substituted into (4.8) provides the final expression fo the recovery time

$$T(\psi_0) = \frac{(k_d + k_g)\psi}{k_d(\psi_m - \alpha)} {}_3F_2\left[\left(1, 1, 1 + \frac{k_d}{k} + k_g\right); \left(2, 1 + \frac{k_d}{k}\right); \frac{\psi}{(\psi_m - \alpha)}\right]\Bigg|_{\psi_0}^{\psi_2}, \tag{4.13}$$

where ${}_pF_q[(a_1, ..., a_p); (b_1, ..., b_q), z]$ is the generalized hypergeometric function [274, 275], converging for values $|\psi/(\psi_m - \alpha)| < 1$.

In this study we investigated the RT of the vegetation in each specific plot from ψ_0 to ψ_2. ψ_0 is set as the fifth percentile of the ψ PDF as it may well represent a degraded state of the vegetation induced by extreme events like storm surges or hurricanes. ψ_2, instead, is set equal to the mean vegetation cover at the equilibrium state, μ_ψ, representing the optimal condition (Fig. 4.2).

4.3 Results and Discussion

4.3.1 Spatial Behavior of Dunal vegetation

Before exploring vegetation recovery dynamics, it is important to understand the spatial behavior of dunal vegetation, according to the stochastic model. Figures 4.2a-b portrait spatial distributions of the mean and 5-th percentile of the vegetation cover —derived from Eq.4.7— along the dune transect for the two types of vegetation, while Figures 4.2c-e show how the shape of the PDF varies along the X-axis.

At locations close to the shoreline, dune slopes are only sparsely vegetated, as they are more frequently exposed to swash flooding. In these areas, $F_r < F_s$; in other words, the impact of wind-induced stresses is negligible compared to those generated by waves. As we move away from the shoreline, the effects of wave runup weaken (although they remain predominant with respect to wind), and consequently, vegetation cover increases. CL25 shows that the Shields parameter $\Phi(X)$—and hence sand mobilization—also increases along the seaward slope of the dune, reaching a maximum near the dune crest. This implies that the scouring threshold decreases below the wave runup threshold ($F_s < F_r$), and wind stress becomes the dominant driver of vegetation dynamics. In Figures 4.2a–b, the local maxima in the green lines at low values of X (i.e., along the seaward slope of the dune) indicate the boundary between the wave-dominated and wind-dominated regions, where $F_s = F_r$.
type-I vegetation dynamics switches from wave to wind-dominated at a very short distance from the shoreline ($X \sim 0.05$) due to the low tolerance to sand mobilization, as discussed in paragraph 2.2. Furthermore, μ_ψ reaches a minimum in proximity of the dune crest, where the bed shear-stress is maximum, and it's higher in front and behind the dune crest. This kind of spatial pattern is typical of *(i)* pioneer species like the Sea Spurge (*Euphorbia Paralias L.*), colonizing the the flatter region in front of the dune; *(ii)* secondary species like the Mediterranean Strawflower (*Helichrysum*

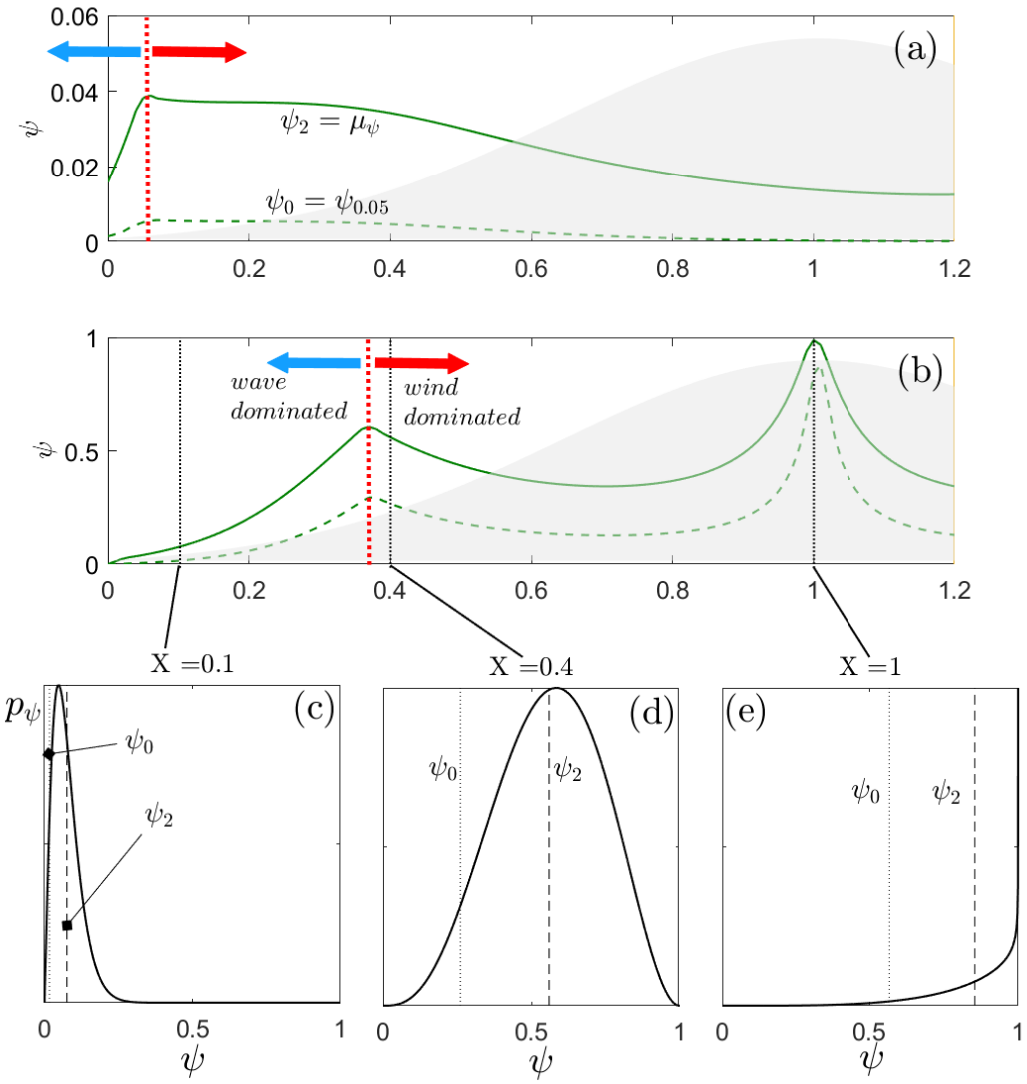

Fig. 4.2 (a-b)Distribution of the plot-specific vegetation cover for *type-I*(a) and *type-II*(b) vegetation. The solid green lines represent the mean vegetation cover, μ_ψ, while the dashed green lines is the fifth percentile $\psi_{0.05}$. The red dotted line marks the boudary between the wave-dominated and wind-dominated regions. The dune profile is represented by the gray area on the background. (c-e)Plot-specific PDFs of vegetation cover at $X = 0.1, 0.4$ and 1. The parameters of the stochastic model used for this simulation are $\{\beta, \mu_F, c_F, \xi, k\} = \{0.1, 0.2, 1, 10^{-5}, 365\}$.

stoechas (L.) Moench) found in the slack behind the dune crest on Mediterranean coasts [276].

Conversely, in *type-II* vegetation, the greater tolerance to sand mobilization allows

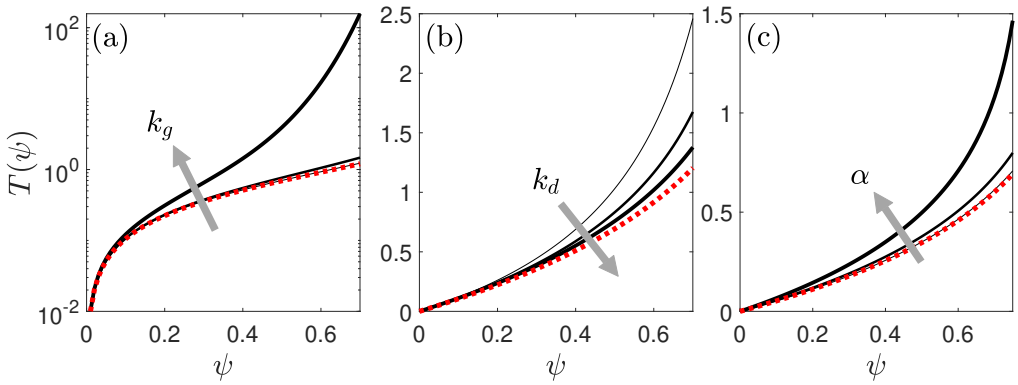

Fig. 4.3 (a-c)Sensitivity analysis of the function $T(\psi)$ changing the parameters $k_g = \{10^{-1}, 10^0, 10^1\}$, $k_d = \{10^2, 10^3, 10^4\}$, $\alpha = \{0, 0.05, 0.2\}$. Dotted red lines indicates the Recovery Time in undisturbed case, T_u.

wave-induced stresses to govern vegetation distribution over a much broader area ($X \sim 0.4$). Additionally, in this case μ_ψ shows a peak near the dune crest, denoting the positive feedback of this type of vegetation (e.g., *Ammophila Arenaria*) to sand mobilization [266]. In summary, *type-II* vegetation typically shows two peaks: a smaller one along the lower seaward slope and a larger one near the dune crest. In both cases, vegetation is more abundant where the terrain slope is gentle, while it remains scarce on the steepest sections of the dune, where the sand is less stable and prone to slumping [276, 227].

4.3.2 Exploratory Analysis on Recovery Time

Understanding the potential and limitations of the proposed approach for computing RT requires a preliminary assessment of key factors that provide a context for the following analysis.

To emphasize the impact of random environmental disturbances, it is useful to compute the RT also in the case of "undisturbed" conditions, where the vegetation dynamics is described only by the growth equation (Eq. 4.2b). The recovery time in this scenario can be immediately evaluated by simple integration of eq. 4.2b:

$$T_u(\psi_0) = \ln\left(\frac{\psi_m - \psi_0}{\psi_m - \psi_2}\right) \tag{4.14}$$

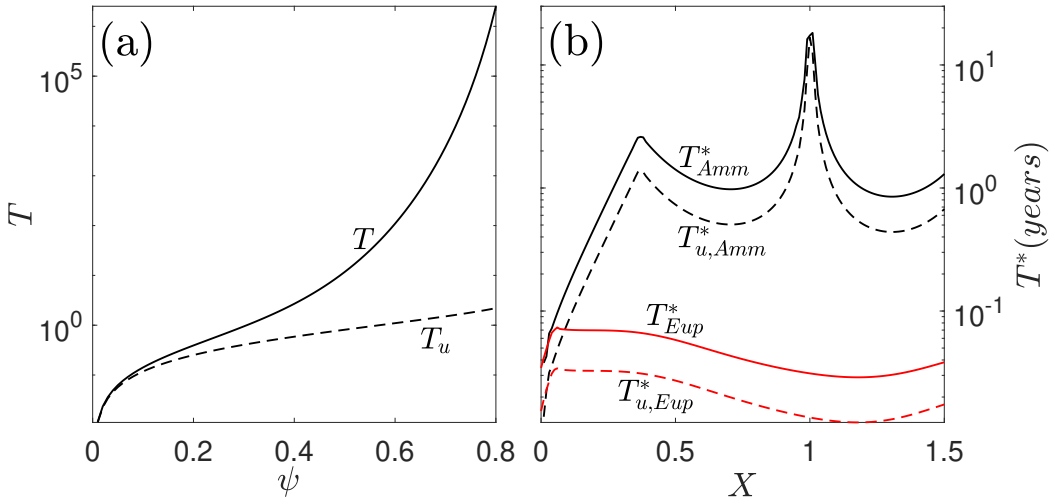

Fig. 4.4 (a)Example of RT, $T(\psi_0)$, in disturbed (solid line) and undisturbed (dashed line) case. The benchmark parameters set is here used. (b)Dimensional RT, $T^*(\psi_0)$, in disturbed (solid lines) and undisturbed conditions (dashed lines) for *type-I* species, *Euphorbia Paralias (L.)*, with $t_g = 3.5 years$ and *type-II* species, *Ammophila arenaria (L.) Link*, with $t_g = 7.5 years$.

The intrinsic property of the logarithmic growth equation of the dichotomous model (Eq. 4.2b) makes T_u approach infinity as ψ tends to its threshold value (ψ_m for *type-I* and $\psi_m - \alpha$ for *type-II*), meaning the vegetation grows much slower at higher ψ values compared to lower ones, hence, even in this favorable scenario, the time required for the vegetation to grow from ψ to $\psi + \Delta\psi$ increases exponentially as ψ increases. Firstly, we tested the sensitivity of the function $T(\psi_0)$ (Fig. 4.3) to the parameters appearing in the expression 4.13: k_g, k_d and α. The range values assigned to the parameters have been extrapolated after running the stochastic model under a number of reasonable environmental conditions. Figure 4.3a illustrates that the curve steepens with increasing k_g, an effect that becomes particularly evident for $k_g > 1$. This trend arises because k_g is directly proportional to the probability of vegetation being in the decay state [264]. Consequently, larger values of k_g (which can be associated to more severe environmental conditions) entail longer average times to reach a given value of ψ. On the contrary, T-curves become less steep with increasing k_d (Fig. 4.3), since increases the probability, hence, the permanence time in the growth state.

Accordingly, Figures 4.3a–b show that, as k_g tends to 0 (or equivalently as k_d tends to infinity), the curves converge toward the undisturbed condition.

Figure 4.4c portrait how higher values of $\alpha(\propto |\langle d\eta/dt \rangle|)$, implies longer RT, indi-

cating that sand mobilization slows down vegetation growth rate and, even though we discussed earlier that sand mobilization could *locally* entrain biomass growth -especially in *type-II* vegetation-, it is nonetheless a stressor, so it limits the maximum reachable vegetation cover.

In order to evaluate the magnitude of RT in real cases, two common species populating the Mediterranean coastal dunes -already cited in the previous paragraph- are considered as representative of the two types of vegetation: *Ammophila arenaria (L.) Link* and *Euphorbia Paralias (L.)* [49, 230, 276]. A typical time span for the *Ammophila* to reach a fully-grown state is $5-10$ years [277], while for the *Euphorbia* is estimated to be $2-5$ years [278] . Averages of 7.5 and 3.5 years which are considered as growth time t_g in the calculations.
A set of geometrical and environmental parameters, to confine the analysis to real contexts have been chosen. In line with CL25, a reasonable set of parameters are assumed to be $\{\tan\theta_0, \beta, \mu_F, c_F, \xi\} = \{0.05, 0.1, 0.2, 1, 10^{-5}\}$, which we use as benchmark set also for the next analysis. In figure 4.4b are compared the recovery times along a dune transect of the two plant species. Despite the *Euphorbia* being much vulnerable to environmental stressors (i.e., subjected to long permanence time in the decay state), inhibiting the growth, the average times for reaching the "optimal" steady state biomass level, $\psi_2 = \mu_\psi$, are $1-2$ order of magnitude lower than the case of the *Ammophila*. Beside of the shorter growth time t_g of the *Euphorbia*, under the same environmental conditions, $T(\psi_0)$ mainly scales with the vegetation cover "goal", ψ_2, much lower than *Ammophila*, as also shown in figure 4.2a-b. In other terms, although the growth rate is low, the maximum reachable vegetation biomass is low, leading to a short overall RT.

4.3.3 Sensitivity analysis

In this chapter, we delve into sensitivity analysis of the mean recovery time model to have a deeper insight on its response to the variations of the main morphological, environmental and biological parameters. According to CL25, the space of all possible parameters of the stochastic model can be reduced to a subspace of four independent controlling parameters, $\{\beta, \mu_F, c_F, \xi\}$.
As reference parameters, we used the benchmark set, as previously discussed ($\{\beta, \mu_F, c_F, \xi\} = \{0.1, 0.2, 1, 10^{-5}\}$), and making the parameter vary by $\pm 50\%$ one at the time.

Dune Aspect-Ratio, β

On *type-I* vegetation, an increase of the dune aspect-ratio, hence, a steepening of the seaward slope, increases RT in the near-shoreline region and in the back-dune slack, wile lowers it around the dune crest (Fig. 4.5a).

On *type-II* vegetation, β have a negligible effect on the hight of the peak in the near-shore area and a positive effect on the peak, in the dune-crest area where RT slightly

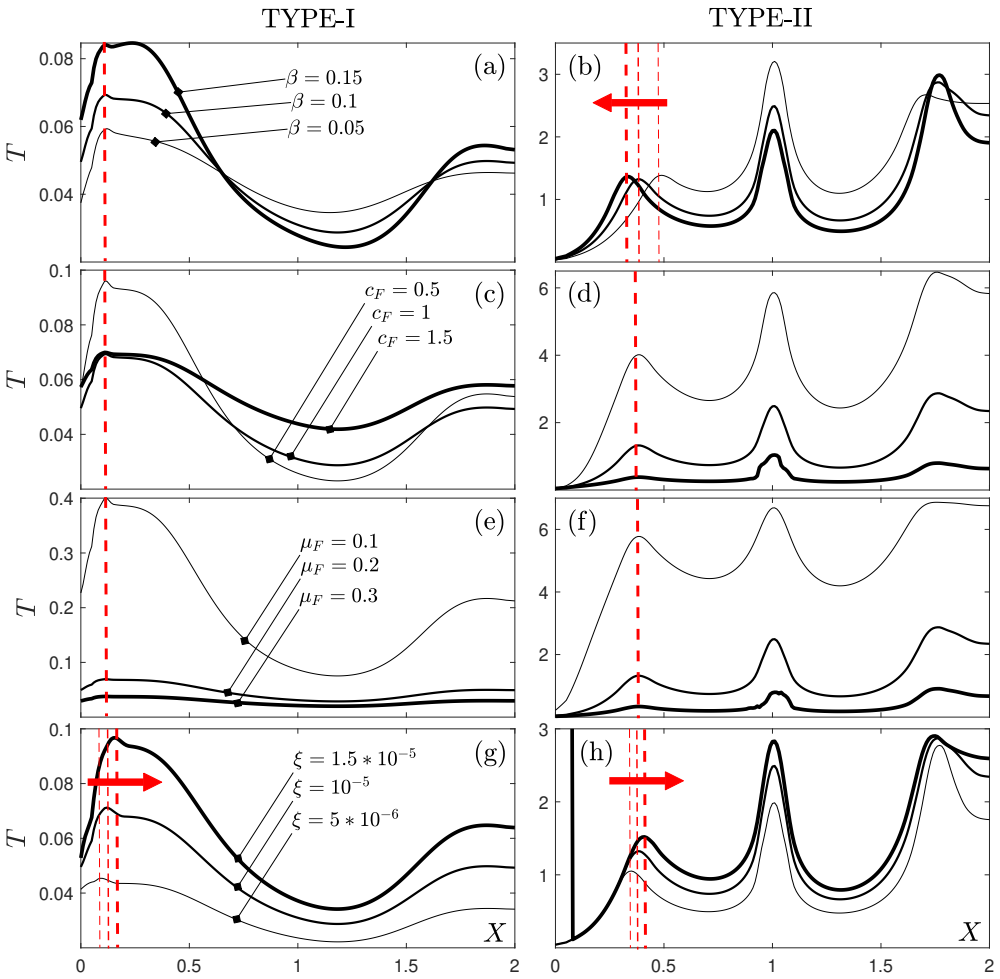

Fig. 4.5 Sensitivity analysis of $T(\psi_0)$ for *type-I* (left column panels) and *type-II* (right column panels) to the main model parameters. It has been changed one parameter at a time, relative to the benchmark set $\{\beta, \mu_F, c_F, \xi\} = \{0.1, 0.2, 1, 10^{-5}\}$. Red lines mark the transition from the runup-dominated zone ($F_r < F_S$) to the scour-dominated zone ($F_s < F_r$). (a-b)Sensitivity to β. (c-d)Sensitivity to c_F. (e-f)Sensitivity to μ_F. (g-h)Sensitivity to ξ.

diminishes as β rises. Noticeable is that the boundary separating the wave-dominated from the wind-dominated region shifts forward as β increases (Fig. 4.5b).

Wind Coefficient of Variation, c_F

On *type-I* appears an interesting pattern in the near-shore and back-dune regions, since T-curve is lower for $c_F = 1$, compared to the cases with $c_F = 0.5$ and $c_F = 1.5$. Hence, $c_F = 1$, in this instance, represents a sort of "optimal" case, since it minimizes the RT. In the dune-crest region a more clear trend shows an increase of RT with increasing c_F (Fig. 4.5c).

On *type-II*, an increase of c_F is associated with drop of RT curves. c_F clearly shows a much more dramatic impact on the values RT, almost halving for each step of variation of c_F (Fig. 4.5d).

Wind Mean, μ_F

On *type-I*, an increase of μ_F induces a strong decrease of RT all along the dune transect (Fig. 4.5e). The same trend is observed for *type-II* vegetation (Fig. 4.5f).

Surface Roughness, ξ

On *type-I*, as well as in *type-II*, to the increase of ξ corresponds an increase of RT curves and a landward shift of the wind-wave regions boundary (Fig. 4.5g-h). Especially on *type-II*, ξ is not a strong driving factor for RT, which is barley affected by its variation, compared to the effect of μ_F and c_F

Some observed behaviors of RT may seem counterintuitive. For instance, an increase on the average wind speed μ_F, is expected to lead to longer RT, due to higher stress on vegetation, hence a longer permanence time in the decay state; yet, figure 4.5e-f shows an opposite trend. Similarily, increasing roughness ξ (Fig. 4.5g-h) is expected to mitigate stresses induced by sediment transport —due to the increase of the mobilization stress threshold— hence, lowering the RT, but the results doesn't match this trend.

These apparent contradictions can be resolved by considering the role of the mean vegetation cover μ_ψ, which has been shown to encapsulate the combined effects of environmental and morphological drivers [260]. Since RT essentially reflects the dynamics of μ_ψ, its trends are consistent with those of mean vegetation cover rather than with the effect of single drivers taken in isolation. In other words, μ_ψ acts as the true mediator: parameters such as μ_F, c_F, and ξ influence RT indirectly through their impact on average vegetation cover. Consequently, the spatial distribution and

magnitude of RT are primarily determined by μ_ψ, while external drivers modulate its behavior.

4.4 Conclusions

In this chapter we developed and applied a minimal stochastic framework to quantify the mean recovery time (RT) of coastal dune vegetation under the action of wind and wave-induced disturbances. The model explicitly incorporates environmental randomness through dichotomous noise, thus capturing the alternation between phases of vegetation growth and decay. Unlike computationally demanding process-based or cellular approaches, this framework retains analytical tractability while still representing the essential eco-morphodynamic processes.

Our results highlight that recovery dynamics of vegetation is most strongly controlled by its position along the dune transect and by species-specific tolerance to sediment mobilization. *Type-I* vegetation, such as *Euphorbia paralias*, shows low tolerance to scouring and burial, leading to sharp spatial transitions and relatively short recovery times due to its lower biomass ceiling. Conversely, *type-II* vegetation, such as *Ammophila arenaria*, benefits from moderate sand mobilization and can achieve higher biomass levels, but exhibits substantially longer recovery times. This species-dependent contrast underscores the importance of functional traits on dune resilience.

The analysis further revealed that recovery times depend nonlinearly on environmental and morphological parameters. In particular, wind variability and mean intensity emerged as dominant drivers of recovery dynamics, while surface roughness and dune geometry exert secondary but non-negligible influences. Importantly, the role of mean vegetation cover acts as a mediator: parameters affect recovery time primarily through their impact on equilibrium vegetation states, rather than directly.

By providing an analytical expression for RT grounded in MFPT theory, this study offers a generalizable framework for linking stochastic disturbances to vegetation resilience in coastal dunes. Beyond advancing theoretical understanding, the approach has practical relevance for coastal management, as it enables estimation of species-specific recovery rates without resorting to extensive numerical simulations.

Future work should aim to couple this stochastic vegetation framework with morphological evolution models, thereby bridging vegetation recovery and long-term

dune dynamics. Moreover, systematic validation through Earth Observation techniques (e.g., multi-temporal remote sensing indices of vegetation cover) and targeted field surveys would be essential to test and calibrate the theoretical predictions, improving both robustness and applicability across different coastal environments.

Chapter 5

Conclusions

This thesis set out to develop an integrated monitoring and predictive framework for coastal dunes, explicitly linking vegetation—treated as a key ecological indicator—to geomorphic and hydrodynamic drivers. Coastal dunes were framed as socio–ecological buffers: ecosystems providing biodiversity, economic value, and protection from storms and sea-level hazards, yet highly dynamic and pressured by climate change and human disturbance. Because dune behavior emerges from tightly coupled physical, biological, and anthropogenic processes acting across scales, the work proceeded from the premise that a genuinely multi-disciplinary and multi-scale approach is required. High-resolution field data, UAV surveys, remote sensing, machine learning classification, stochastic theory, and process-based modeling were therefore combined to generate coherent datasets and predictive tools for robust management and restoration.

Chapter 2 documents the practical costs of assembling coherent multi-disciplinary datasets in coastal environments and proposes an operational workflow combining field surveys (RTK, in-situ measurements), UAV photogrammetry, nearshore bathymetry (including a USV prototype), and standardized post-processing. Notably, we explored the feasibility of USV prototypes for mapping near-shore seafloor, especially where other and more common type of vessels are not easily deployable. The resulting dataset proved capable of capturing seasonal to interannual dune behavior, demonstrating that such integrated systems are feasible and significantly improve detection of subtle responses.

A comparison between a process-based nearshore model (XBeach) and empirical

runup formulations (Stockdon, 2006, tuned on local data) shows broad agreement in runup estimates for gently sloping sandy beaches with limited seabed variability. This indicates that a calibrated large-scale wave simulation, coupled with S06-type empirical relations, can provide computationally efficient and reliable operational estimates. Nonetheless, the results highlight the need for targeted observations to validate setup and infragravity components and to constrain calibration uncertainties. Multi-year analysis of volumetric change and crestline migration revealed oscillatory, out-of-phase behavior between paired zones (A2 and A3), with A2 erosional phases corresponding to A3 accretional phases and vice-versa. Despite these oscillations, both areas exhibited a net erosive trend from 2021–2025. Crestline displacement magnitudes differed between sites, emphasizing strong spatial heterogeneity even within a single protected area and reaffirming the need for frequent, spatially extended monitoring.

In Chapter 3, a species-resolved vegetation dataset derived through machine-learning classification of ultra-high-resolution imagery enabled detailed eco-morphological analysis. The results show that vegetation inland limits in well-formed dunefields correspond closely to extreme runup levels, indicating a strong hydrodynamic control on vegetation zonation. Foredune morphology was found to correlate strongly with the abundance of dune-building species, which are particularly sensitive to human disturbance. The ratio between vegetation-threshold distance and crest distance remained relatively stable across different dune morphologies, suggesting a potentially generalizable spatial descriptor. Equivalent diameter distributions depended mainly on species-specific biological traits, while spatial uniformity increased with species abundance. Furthermore, nearest-neighbor metrics and L-function analyses revealed multi-scale clustering patterns driven predominantly by abundance. Overall, these spatial and statistical descriptors provide robust benchmarks for both ecosystem and morphodynamic model validation.
The spatial arrangement of vegetation emerged as a robust proxy for environmental forcings and underlying geomorphology, exhibiting distinct signatures at each site. Such spatial information represents a critical asset for the calibration and validation of up-scaled coastal modeling frameworks.

In chapter 4, a minimal stochastic framework based on dichotomous environmental noise and mean first-passage time analysis produced analytical expressions for vegetation recovery time. Results show strong species-dependent behavior: low-tolerance, low-biomass species show sharp transitions and short recovery times,

while dune-building species with higher biomass ceilings exhibits substantially longer recovery times. Wind variability and mean intensity emerged as dominant drivers, while roughness and dune morphology contributing to second-order effects.

As noted in Chapter 1, this study seeks to address two primary research questions. The following section outlines how the key findings and the accumulated experience contribute to answering these questions.

RQ1: What monitoring frequency, spatial resolution, and indicators are required to assess mid- to long-term dune dynamics?

First, the work demonstrates that high-resolution, multi-source monitoring is feasible but demanding in terms of time, cost, personnel, and technical skills. The acquisition and processing of UAV imagery, RTK surveys, and USV bathymetry proved capable of capturing key seasonal-to-interannual dune metrics (crestline displacement, volumetric change, vegetation structure). While this shows that high-resolution, multi-source datasets are effective, the question of a possible optimal spatio-temporal monitoring resolution remains still open to debate.

Second, The monitoring carried out in this thesis revealed several meaningful cross-correlations between environmental forcing, dune morphology, and vegetation patterns.
For instance, extreme runup levels were shown to set the inland limit of vegetation in well-formed dunes, demonstrating a direct link between hydrodynamics and ecological zonation. Morphological indicators such as crestline position, foredune height, and volumetric change also exhibited clear connections with biological variables, in fact, areas with greater abundance of dune-building species corresponded to more developed foredune forms, while flatter or disturbed terrains displayed weaker and more diffuse zonation. Similarly, the spatial metrics derived from vegetation mapping (ED, MND, clustering patterns) reflected underlying geomorphological conditions and exposure to hydrodynamic disturbance. These cross-correlations—empirically observed and analyzed across the study sites—underscore the tight coupling among physical, ecological, and morphological processes and demonstrate the value of integrated, multi-disciplinary indicators for interpreting dune system behavior.

RQ2: How can geomorphological and ecological information be processed and validated for effective assimilation into physically based eco-morphodynamic

models, and which modeling architectures best support this integration to improve predictions under diverse meteo-hydrological forcing conditions?

Chapters 2, 3, and 4 of this thesis present insights derived from a comprehensive workflow and outline several concrete steps toward constructing an integrated database suitable for future eco-morphodynamic modeling—ranging from in-field measurements to data processing and comparative data analysis.
Although still in its early stages, a framework for modeling vegetation recovery times within a stochastic eco-morphodynamic model has been proposed, but it has not yet been validated.
The actual assimilation of these datasets into a predictive model is not carried out in this thesis; although, the work emphasizes the need for improved validation—particularly through hydrodynamic measurements and multi-temporal vegetation observations—and the development of a structured protocol to convert geomorphological and ecological indicators into model-ready inputs, which remains an important objective for future research.

Several directions emerge from this work.
First, efforts should continue along the path of validating the stochastic eco-morphodynamic model, with particular focus on scaling up coastal dune observations from high-resolution, small-scale measurements to broader, lower-resolution satellite-derived datasets.
Further progress requires the coupling of models across disciplines: integrating the stochastic vegetation recovery framework with morphodynamic models will enable the development of site-specific digital twins capable of testing alternative management and restoration scenarios.
Equally important is the systematic improvement and validation of the in-field data, necessary to identify and reduce biases in the predictive models (e.g., hydrodynamic process-based models, eco-morphodynamic vegetation model).

This thesis demonstrates that a tightly integrated, multi-disciplinary approach —combining high-resolution remote sensing, vegetation mapping, hydrodynamic analysis, stochastic theory, and process-based modeling— provides a pragmatic and effective roadmap toward operational dune monitoring, prediction, and management, strengthening coastal dune resilience under accelerating climatic and anthropogenic pressures.

References

[1] J.R Clark. *Coastal ecosystem management*. Conservation Foundation., 1977.

[2] P Hesp. Ecological processes and plant adaptations on coastal dunes. *Journal of arid environments*, 21(2):165–191, 1991.

[3] M Luisa Martínez and Norbert P Psuty. *Coastal dunes*. Springer, 2004.

[4] Udo Nehren, Hoang Ho Dac Thai, Muh Aris Marfai, Claudia Raedig, Sandra Alfonso, Junun Sartohadi, and Consuelo Castro. Ecosystem services of coastal dune systems for hazard mitigation: Case studies from vietnam, indonesia, and chile. *Ecosystem-based disaster risk reduction and adaptation in practice*, pages 401–433, 2016.

[5] Jacob M Sigren, Jens Figlus, and Anna R Armitage. Coastal sand dunes and dune vegetation: restoration, erosion, and storm protection. *Shore Beach*, 82(4):5–12, 2014.

[6] Carmelo Maximiliano-Cordova, M Luisa Martínez, Rodolfo Silva, Patrick A Hesp, Roger Guevara, and Rosario Landgrave. Assessing the impact of a winter storm on the beach and dune systems and erosion mitigation by plants. *Frontiers in Marine Science*, 8:734036, 2021.

[7] A Acosta, Maria Laura Carranza, and CF Izzi. Combining land cover mapping of coastal dunes with vegetation analysis. *Applied Vegetation Science*, 8(2):133–138, 2005.

[8] RL Gadgil. Marram grass (ammophila arenaria) and coastal sand stability in new zealand. *New Zealand Journal of Forestry Science*, 32(2):165–180, 2002.

[9] UM Hertling and RA Lubke. Use of ammophila arenaria for dune stabilization in south africa and its current distribution—perceptions and problems. *Environmental Management*, 24(4):467–482, 1999.

[10] DG Hewett. The colonization of sand dunes after stabilization with marram grass (ammophila arenaria). *The Journal of Ecology*, pages 653–668, 1970.

[11] A.T.R. Acosta and S. Ercole. *Gli habitat delle coste sabbiose italiane: ecologia e problematiche di conservazione. ISPRA, Serie Rapporti, 215/2015.* Eds, 2015.

[12] Liz Creel. Ripple effects: population and coastal regions. population reference bureau. *Washington, DC: Population Reference Bureau and Measure Communication*, 2003.

[13] Enzo Pranzini, Giorgio Anfuso, Irene Cinelli, Marco Piccardi, and Giovanni Vitale. Shore protection structures increase and evolution on the northern tuscany coast (italy): Influence of tourism industry. *Water*, 10(11):1647, 2018.

[14] K French. Competition strength of two significant invasive species in coastal dunes. *Plant Ecology*, 213:1667–1673, 2012.

[15] Andrea Bertacchi, Marco Alberto Luca Zuffi, and Tiziana Lombardi. Foredune psammophilous communities and coastal erosion in a stretch of the ligurian sea (tuscany, italy). *Rendiconti Lincei*, 27:639–651, 2016.

[16] M Luisa Martínez, Patrick A Hesp, and Juan B Gallego-Fernández. Coastal dunes: human impact and need for restoration. *Restoration of coastal dunes*, pages 1–14, 2013.

[17] Debora Lithgow, ML Martínez, JB Gallego-Fernández, PA Hesp, P Flores, S Gachuz, Natalia Rodríguez-Revelo, Oscar Jiménez-Orocio, G Mendoza-González, and LL Álvarez-Molina. Linking restoration ecology with coastal dune restoration. *Geomorphology*, 199:214–224, 2013.

[18] Peter R Darke, Michael K Brady, Ray L Benedicktus, and Andrew E Wilson. Feeling close from afar: The role of psychological distance in offsetting distrust in unfamiliar online retailers. *Journal of Retailing*, 92(3):287–299, 2016.

[19] AP Grootjans, HWT Geelen, AJM Jansen, and EJ Lammerts. Restoration of coastal dune slacks in the netherlands. *Ecological restoration of aquatic and semi-aquatic ecosystems in the Netherlands (NW Europe)*, pages 181–203, 2002.

[20] Jordan BR Eamer, Ian B Darke, and Ian J Walker. Geomorphic and sediment volume responses of a coastal dune complex following invasive vegetation removal. *Earth Surface Processes and Landforms*, 38(10):1148–1159, 2013.

[21] Chris Houser and Stuart Hamilton. Sensitivity of post-hurricane beach and dune recovery to event frequency. *Earth Surface Processes and Landforms*, 34(5):613–628, 2009.

[22] William Ritchie and Shea Penland. Cyclical changes in the coastal dunes of southern louisiana. *Journal of coastal research*, pages 111–114, 1988.

[23] Matthias Mengel, Alexander Nauels, Joeri Rogelj, and Carl-Friedrich Schleussner. Committed sea-level rise under the paris agreement and the legacy of delayed mitigation action. *Nature communications*, 9(1):601, 2018.

[24] Christine Schleupner. Evaluation of coastal squeeze and its consequences for the caribbean island martinique. *Ocean & Coastal Management*, 51(5):383–390, 2008.

[25] Lindsey S Smart, Jelena Vukomanovic, Erin O Sills, and Georgina Sanchez. Cultural ecosystem services caught in a 'coastal squeeze'between sea level rise and urban expansion. *Global Environmental Change*, 66:102209, 2021.

[26] Talia Tamarin-Brodsky and Yohai Kaspi. Enhanced poleward propagation of storms under climate change. *Nature geoscience*, 10(12):908–913, 2017.

[27] Asbury H Sallenger Jr. Storm impact scale for barrier islands. *Journal of coastal research*, pages 890–895, 2000.

[28] Hilary F Stockdon, Asbury H Sallenger Jr, Rob A Holman, and Peter A Howd. A simple model for the spatially-variable coastal response to hurricanes. *Marine Geology*, 238(1-4):1–20, 2007.

[29] Tomas Beuzen. pybeach: A python package for extracting the location of dune toes on beach profile transects. *Journal of Open Source Software*, 4(44):1890, 2019.

[30] Nicole A Elko, Asbury H Sallenger Jr, Kristy K Guy, Hilary F Stockdon, and Karen LM Morgan. Barrier island elevations relevant to potential storm impacts; 1, techniques. Technical report, 2002.

[31] Martin Flood. Commercial implications of topographic terrain mapping using scanning airborne laser radar. *Photogramm. Eng. Remote Sens.*, 63:327–366, 1997.

[32] Victor Klemas. Beach profiling and lidar bathymetry: An overview with case studies. *Journal of Coastal Research*, 27(6):1019–1028, 2011.

[33] Jeremy Mull and Peter Ruggiero. Estimating storm-induced dune erosion and overtopping along us west coast beaches. *Journal of Coastal Research*, 30(6):1173–1187, 2014.

[34] Tomasz A Łabuz. A review of field methods to survey coastal dunes—experience based on research from south baltic coast. *Journal of Coastal Conservation*, 20(2):175–190, 2016.

[35] Chris Houser, Phil Wernette, Elizabeth Rentschlar, Hannah Jones, Brianna Hammond, and Sarah Trimble. Post-storm beach and dune recovery: Implications for barrier island resilience. *Geomorphology*, 234:54–63, 2015.

[36] Norbert P Psuty. Sediment budget and dune/beach interaction. *Journal of Coastal Research*, (3):1–4, 1988.

[37] Andrew D Short and Patrick A Hesp. Wave, beach and dune interactions in southeastern australia. *Marine geology*, 48(3-4):259–284, 1982.

[38] JGS Keijsers, AV De Groot, and MJPM Riksen. Modeling the biogeomorphic evolution of coastal dunes in response to climate change. *Journal of Geophysical Research: Earth Surface*, 121(6):1161–1181, 2016.

[39] Wenyan Zhang, Ralf Schneider, Jakob Kolb, Tim Teichmann, Joanna Dudzinska-Nowak, Jan Harff, and Till JJ Hanebuth. Land–sea interaction and morphogenesis of coastal foredunes—a modeling case study from the southern baltic sea coast. *Coastal Engineering*, 99:148–166, 2015.

[40] Caroline Hallin. *Long-term beach and dune evolution: Development and application of the CS-model*. PhD thesis, Lund University, 2019.

[41] Nicholas Cohn, Bas M Hoonhout, Evan B Goldstein, Sierd De Vries, Laura J Moore, Orencio Durán Vinent, and Peter Ruggiero. Exploring marine and aeolian controls on coastal foredune growth using a coupled numerical model. *Journal of Marine Science and Engineering*, 7(1):13, 2019.

[42] Dano Roelvink and Susana Costas. Coupling nearshore and aeolian processes: Xbeach and duna process-based models. *Environmental Modelling & Software*, 115:98–112, 2019.

[43] Peter Ruggiero, Nicholas Cohn, Bas Hoonhout, Evan Goldstein, Sierd de Vries, Laura Moore, Sally Hacker, and Orencio Durán Vinent. Simulating dune evolution on managed coastlines: Exploring management options with the coastal recovery from storms tool (crest). *Shore & Beach*, 87(2):36, 2019.

[44] Umberto Pernice. D3. 1 framework for developing funding and finance arrangements for coastal restoration. 2023.

[45] Sandro De Muro, Carla Buosi, Nicola Pusceddu, Paolo Frongia, Marinella Passarella, and Angelo Ibba. Geomorphology and anthropogenic impact including military constraints in a microtidal wave-dominated embayment in south western sardinia (porto pino beach, sci itb040025, mediterranean sea). implications for beach management. In *EGU General Assembly Conference Abstracts*, pages EPSC2016–12981, 2016.

[46] Maurizio Simeone, Paola Masucci, Alessio Usai, Daniela Giordano, Caterina De Vivo, Oscar Saccone, M Moraca, Alberto Pagliarani, Giusy De Luca, Martina Genovese, et al. Medpan project "territorial analysis for the integrated management of the posillipo coastline"(gulf of naples). *Monit Mediterr Coast AREAS Probl Meas Tech*, 1:299–308, 2016.

[47] Bianca R. Charbonneau, Adam Duarte, Todd M. Swannack, Bradley D. Johnson, and Candice D. Piercy. Doonies: A process-based ecogeomorphological functional community model for coastal dune vegetation and landscape dynamics. *Geomorphology*, 398:108037, 2 2022.

[48] Thomas R Allen, George McLeod, Heather Richter, and Alex Nielsen. Digitally twinning coastal resilience via multsensor imagery, in situ sensors, and geospatial analysis. In *IGARSS 2022-2022 IEEE International Geoscience and Remote Sensing Symposium*, pages 4739–4742. IEEE, 2022.

[49] Andrea Bertacchi. Dune habitats of the migliarino–san rossore–massaciuccoli regional park (tuscany–italy). *Journal of Maps*, 13(2):322–331, 2017.

[50] Costanza Scopetani, David Chelazzi, Tania Martellini, Jukka Pellinen, Alberto Ugolini, Chiara Sarti, and Alessandra Cincinelli. Occurrence and characterization of microplastic and mesoplastic pollution in the migliarino san rossore, massaciuccoli nature park (italy). *Marine Pollution Bulletin*, 171:112712, 2021.

[51] Alessandro Barducci, Donatella Guzzi, Paolo Marcoionni, and Ivan Pippi. Aerospace wetland monitoring by hyperspectral imaging sensors: A case study in the coastal zone of san rossore natural park. *Journal of environmental management*, 90(7):2278–2286, 2009.

[52] Giovanni Leucci, Lara De Giorgi, and Giuseppe Scardozzi. Geophysical prospecting and remote sensing for the study of the san rossore area in pisa (tuscany, italy). *Journal of Archaeological Science*, 52:256–276, 2014.

[53] R Gellini, F Pantani, P Grossoni, F Bussotti, E Barbolani, and C Rinallo. Survey of the deterioration of the coastal vegetation in the park of san rossore in central italy. *European journal of forest pathology*, 13(5-6):296–304, 1983.

[54] Luigi E Cipriani, Antonio Perfetti, Enzo Pranzini, and Giovanni Vitale. Azioni di tutela delle dune costiere del parco regionale migliarino san rossore massaciuccoli (toscana settentrionale). *Studi costieri*, 17:165–179, 2010.

[55] F Alquini, D Bertoni, Giovanni Sarti, et al. Extreme erosion of a dune crest within a short timespan (january–september 2016): the recent case in the migliarino–san rossore–massaciuccoli regional park (tuscany, italy). *Atti Della Società Toscana di Scienze Naturali (Pisa). Memorie. Serie A*, 123:5–11, 2016.

[56] Nicola Silvestri, Chiara Pistocchi, Tiziana Sabbatini, Rudy Rossetto, and Enrico Bonari. Diachronic analysis of farmers' strategies within a protected area of central italy. *Italian Journal of Agronomy*, 7(2):e20, 2012.

[57] Maria Chiara Torricelli. Es-lca e patrimonio naturale: Life cycle analisi ambientale e sociale di un'area protetta. 2015.

[58] Daniela Ciccarelli, Elena Cini, Alessio Mo, Marco Paterni, Luciano Massetti, Nelson Rangel-Buitrago, and Silvia Merlino. The assessment and management of plant invasions with unmanned aerial vehicles. the yucca gloriosa case, italy. *Regional Studies in Marine Science*, 57:102759, 2023.

[59] S Cavazza. Regionalizzazione geomorfologica del trasporto solido in sospensione dei corsi d'acqua tra il magra e l'ombrone. *Atti della Società Toscana di Scienze Naturali, Memorie Serie A*, 91:119–132, 1984.

[60] Enzo Pranzini et al. Caratteristiche morfologiche e sedimentologiche di una zona di convergenza del trasporto litoraneo (versilia, toscana). *Studi costieri*, 8:135–149, 2004.

[61] Enzo Pranzini. Updrift river mouth migration on cuspate deltas: two examples from the coast of tuscany (italy). *Geomorphology*, 38(1-2):125–132, 2001.

[62] M Kukavicic and Enzo Pranzini. Beach ridges and dunes of the arno river delta. *Proceedings of the Sixth International Conference on the Mediterranean Coastal Environment, MEDCOAST*, 3:1413–1424, 2003.

[63] Enzo Pranzini. Airborne lidar survey applied to the analysis of the historical evolution of the arno river delta (italy). *Journal of Coastal Research*, 50(sp1):400–409, 2007.

[64] RWG Carter, TGF Curtis, and MJ Sheehy-Skeffington. *Coastal Dunes: Geomorphology, Ecology and Management for Conservation: Proceedings of the Third European Dune Congress, Galway, Ireland, 17-21 June 1992*. AA Balkema Rotterdam, 1992.

[65] Norbert P Psuty. Spatial variation in coastal foredune development. 1992.

[66] Saverio Devoti, Marco Fulvio Nisi, and Sergio Silenzi. Caratteri geologici ed evoluzione paleogeografica. *Studi costieri*, 6:73–89, 2003.

[67] Margherita Azzari et al. Il rinnovamento della cartografia a grande scala in toscana tra quattro e cinquecento: indicazioni di ricerca e primi risultati. *Rivista Geografica Italiana*, 1:271–290, 1993.

[68] R Caselli. Indagini sulle zone umide della toscana. xvii. le industrie neolitiche ed eneolitiche del lago di massaciuccoli. *Collana di indagini tecniche e scientifiche per una migliore conoscenza del lago di Massaciuccoli*, 2:33–38, 1981.

[69] Enzo Pranzini et al. A model for cuspate delta erosion. *6th Symp. on Coastal and Ocean Management/ASCE. Charleston, SC. Coastal Zone '89*, pages 4345–4357, 1989.

[70] Pierluigi Aminti, Luigi E Cipriani, and Enzo Pranzini. 'back to the beach': converting seawalls into gravel beaches. In *Soft Shore Protection: An Environmental Innovation in Coastal Engineering*, pages 261–274. Springer, 2003.

[71] Enzo Pranzini et al. L'intervento di stabilizzazione del litorale de le lame (parco san rossore migliarino massaciuccoli, toscana). *Studi costieri*, 14:29–42, 2008.

[72] Dan Bowman and Enzo Pranzini. Reversed responses within a segmented detached breakwater, the tuscany coast italy—a case study. *Coastal Engineering*, 49(4):263–274, 2003.

[73] LUIGI E Cipriani, SERENA Ferri, PIERLUIGI Iannotta, FRANCESCA Paolieri, Enzo Pranzini, et al. Morfologia e dinamica dei sedimenti del litorale della toscana settentrionale. *Studi costieri*, 4:119–156, 2001.

[74] Annalisa Di Bernardino, Anna Maria Iannarelli, Stefano Casadio, Giovanna Pisacane, Gabriele Mevi, and Marco Cacciani. Classification of synoptic and local-scale wind patterns using k-means clustering in a tyrrhenian coastal area (italy). *Meteorology and Atmospheric Physics*, 134(2):30, 2022.

[75] G Mastrantonio, I Petenko, A Viola, S Argentini, L Coniglio, Paolo Monti, and Giovanni Leuzzi. Influence of the synoptic circulation on the local wind field in a coastal area of the tyrrhenian sea. In *IOP Conference Series: Earth and Environmental Science*, volume 1, page 012049. IOP Publishing, 2008.

[76] S Federico, L Pasqualoni, Anna Maria Sempreviva, L De Leo, E Avolio, CR Calidonna, and C Bellecci. The seasonal characteristics of the breeze circulation at a coastal mediterranean site in south italy. *Advances in Science and Research*, 4(1):47–56, 2010.

[77] Roberto Iacono, Ernesto Napolitano, Massimiliano Palma, and Gianmaria Sannino. The tyrrhenian sea circulation: A review of recent work. *Sustainability*, 13(11):6371, 2021.

[78] Eleonora Rinaldi, B Buongiorno Nardelli, Enrico Zambianchi, R Santoleri, and P-M Poulain. Lagrangian and eulerian observations of the surface circulation in the tyrrhenian sea. *Journal of Geophysical Research: Oceans*, 115(C4), 2010.

[79] Stefano Pierini and A Simioli. A wind-driven circulation model of the tyrrhenian sea area. *Journal of Marine Systems*, 18(1-3):161–178, 1998.

[80] Danièle Hauser, Hubert Branger, S Bouffies-Cloché, S Despiau, WM Drennan, H Dupuis, P Durand, X Durrieu de Madron, C Estournel, Laurence Eymard, et al. The fetch experiment: An overview. *Journal of Geophysical Research: Oceans*, 108(C3), 2003.

[81] Flora Karathanasi, Angeliki Karperaki, Theodoros Gerostathis, and Kostas Belibassakis. Offshore-to-nearshore transformation of wave conditions and directional extremes with application to port resonances in the bay of sitiacrete. *Atmosphere*, 11(3):280, 2020.

[82] V Katsardi and C Swan. The evolution of large non-breaking waves in intermediate and shallow water. i. numerical calculations of uni-directional seas. *Proceedings of the Royal Society A: Mathematical, Physical and Engineering Sciences*, 467(2127):778–805, 2011.

[83] Genowefa Bendykowska and Gosta Werner. Transformation of shallow water wave spectra. In *Coastal Engineering 1988*, pages 612–623. 1988.

[84] G Anfuso, Enzo Pranzini, and G Vitale. An integrated approach to coastal erosion problems in northern tuscany (italy): Littoral morphological evolution and cell distribution. *Geomorphology*, 129(3-4):204–214, 2011.

[85] Hafsa Bouhrim, Abdellatif El Marjani, Rajae Nechad, and Imane Hajjout. Ocean wave energy conversion: A review. *Journal of Marine Science and Engineering*, 12(11):1922, 2024.

[86] ALESSANDRA Sani, PAOLO EMILIO Tomei, et al. La vegetazione psammofila del litorale di san rossore (toscana settentrionale) e la sua importanza conservazionistica. *Parlatorea*, 8:99–119, 2006.

[87] Renzo Mazzanti. *La pianura di Pisa ei rilievi contermini: la natura e la storia*. na, 1994.

[88] Jean-Marie Géhu, Edoardo Biondi, and Jeannette Franck. *La végétation du littoral de la Corse: essai de synthèse phytosociologique*. Dipartimento ed ecologia dell'Università; Station internationale de ..., 1994.

[89] I Vagge and E Biondi. La vegetazione delle coste sabbiose del tirreno settentrionale italiano. *Fitosociologia*, 36(2):61–95, 1999.

[90] J-M Géhu, M Costa, A Scoppola, E Biondi, S Marchiori, and JB Peris. Essai synsystématique et synchorologique sur les végétations littorales italiennes dans un but conservatoire. *Documents phytosociologiques*, 8:393–474, 1984.

[91] Pier Virgilio Arrigoni. Flora e vegetazione della macchia lucchese di viareggio (toscana). *Webbia*, 44(1):1–62, 1990.

[92] Paolo Tomei, Andrea Bertacchi, A Sani, MO Consiglio, et al. La vegetazione della tenuta di s. rossore. note esplicative della carta della vegetazione di s. rossore 1: 10000. 2004.

[93] PIER VIRGILIO Arrigoni. La vegetazione del complesso dunale di capo comino (sardegna nord-orientale). *Parlatorea*, 1:35–45, 1996.

[94] Sebastian D'Oleire-Oltmanns, Irene Marzolff, Klaus Daniel Peter, and Johannes B Ries. Unmanned aerial vehicle (uav) for monitoring soil erosion in morocco. *Remote sensing*, 4(11):3390–3416, 2012.

[95] Ryan Hruska, Jessica Mitchell, Matthew Anderson, and Nancy F Glenn. Radiometric and geometric analysis of hyperspectral imagery acquired from an unmanned aerial vehicle. *Remote Sensing*, 4(9):2736–2752, 2012.

[96] Per Skoglar, Umut Orguner, David Törnqvist, and Fredrik Gustafsson. Road target search and tracking with gimballed vision sensor on an unmanned aerial vehicle. *Remote sensing*, 4(7):2076–2111, 2012.

[97] Daniele Giordan, Andrea Manconi, Fabio Remondino, and Francesco Nex. Use of unmanned aerial vehicles in monitoring application and management of natural hazards, 2017.

[98] Jaime Paneque-Gálvez, Michael K McCall, Brian M Napoletano, Serge A Wich, and Lian Pin Koh. Small drones for community-based forest monitoring: An assessment of their feasibility and potential in tropical areas. *Forests*, 5(6):1481–1507, 2014.

[99] Morris F Glenn. Introducing an operational multi-beam array sonar. *The International Hydrographic Review*, 1970.

[100] John E Hughes Clarke. Multibeam echosounders. In *Submarine geomorphology*, pages 25–41. Springer, 2017.

[101] Harold K Farr. Multibeam bathymetric sonar: Sea beam and hydro chart. *Marine Geodesy*, 4(2):77–93, 1980.

[102] E Hammerstad, A Lovik, S Minde, L Krane, and M Steinset. Field performance of the benigraph high-resolution multibeam seafloor mapping system. In *OCEANS'85-Ocean Engineering and the Environment*, pages 682–685. IEEE, 1985.

[103] John E Hughes Clarke, Larry A Mayer, and David E Wells. Shallow-water imaging multibeam sonars: A new tool for investigating seafloor processes in the coastal zone and on the continental shelf. *Marine Geophysical Researches*, 18(6):607–629, 1996.

[104] Wayne D Wilson. Equation for the speed of sound in sea water. *The Journal of the Acoustical Society of America*, 32(10):1357–1357, 1960.

[105] Claude C Leroy. Development of simple equations for accurate and more realistic calculation of the speed of sound in seawater. *The Journal of the Acoustical Society of America*, 46(1B):216–226, 1969.

[106] Herman Medwin. Speed of sound in water: A simple equation for realistic parameters. *The Journal of the Acoustical Society of America*, 1975.

[107] Vincent A Del Grosso. New equation for the speed of sound in natural waters (with comparisons to other equations). *The Journal of the Acoustical Society of America*, 56(4):1084–1091, 1974.

[108] Chen-Tung Chen and Frank J Millero. Speed of sound in seawater at high pressures. *The Journal of the Acoustical Society of America*, 62(5):1129–1135, 1977.

[109] Joe Breman et al. *Ocean globe*. ESRI Press Academic, 2010.

[110] Adam Zielinski, Xueyi Geng. Precise multibeam acoustic bathymetry. *Marine Geodesy*, 22(3):157–167, 1999.

[111] Keir Colbo, Tetjana Ross, Craig Brown, and Tom Weber. A review of oceanographic applications of water column data from multibeam echosounders. *Estuarine, coastal and shelf science*, 145:41–56, 2014.

[112] RE Francois and GR Garrison. Sound absorption based on ocean measurements: Part i: Pure water and magnesium sulfate contributions. *The Journal of the Acoustical Society of America*, 72(3):896–907, 1982.

[113] Xavier Lurton and Jean-Marie Augustin. A measurement quality factor for swath bathymetry sounders. *IEEE Journal of Oceanic Engineering*, 35(4):852–862, 2010.

[114] John E Hughes Clarke. Dynamic motion residuals in swath sonar data: Ironing out the creases. *The International hydrographic review*, 2003.

[115] International Hydrographic Organization. Standards for hydrographic surveys: S-44 edition 6.1. 0. 2022.

[116] Garret P Duffy and John E Hughes-Clarke. Application of spatial cross correlation to detection of migration of submarine sand dunes. *Journal of Geophysical Research: Earth Surface*, 110(F4), 2005.

[117] Mirjam Snellen, Kerstin Siemes, and Dick G Simons. A model-based method for reducing the sound speed induced errors in multi-beam echo-sounder bathymetric measurements. In *OCEANS 2009-EUROPE*, pages 1–7. IEEE, 2009.

[118] Brian D Dushaw and John A Colosi. Ray tracing for ocean acoustic tomography. Technical report, 1998.

[119] Sana Gul, S Sajjad Haider Zaidi, Rehan Khan, and Ammar Banduk Wala. Underwater acoustic channel modeling using bellhop ray tracing method. In *2017 14th International Bhurban Conference on Applied Sciences and Technology (IBCAST)*, pages 665–670. IEEE, 2017.

[120] Yoann Ladroit, Geoffroy Lamarche, and Arne Pallentin. Seafloor multibeam backscatter calibration experiment: comparing 45°-tilted 38-khz split-beam echosounder and 30-khz multibeam data. *Marine Geophysical Research*, 39(1):41–53, 2018.

[121] Anna M Crawford. Removing roll and heave artifacts from high-resolution multibeam bathymetric data. 2003.

[122] Andre Godin. *The calibration of shallow water multibeam echo-sounding systems*. PhD thesis, University of New Brunswick, 1997.

[123] S Zieger, Thomas Stieglitz, and S Kininmonth. Mapping reef features from multibeam sonar data using multiscale morphometric analysis. *Marine Geology*, 264(3-4):209–217, 2009.

[124] John Joseph Bowman Rooney. Cruise report, vessel oscar elton sette, cruise se-10-02 (se-78), 11 february-14 march 2010, guam and commonwealth of the northern mariana islands (cnmi: Rota, farallon de medinilla and saipan). 2010.

[125] Donald F Dinn, Bosko D Loncarevic, and Gerard Costello. The effect of sound velocity errors on multi-beam sonar depth accuracy. In *'Challenges of Our Changing Global Environment'. Conference Proceedings. OCEANS'95 MTS/IEEE*, volume 2, pages 1001–1010. IEEE, 1995.

[126] Kenneth V Mackenzie. A decade of experience with velocimeters. *The Journal of the Acoustical Society of America*, 50(5B):1321–1333, 1971.

[127] Julian Le Deunf, Nathalie Debese, Thierry Schmitt, and Romain Billot. A review of data cleaning approaches in a hydrographic framework with a focus on bathymetric multibeam echosounder datasets. *Geosciences*, 10(7):254, 2020.

[128] Chao He, Kai Vannahme, and Arnold Gillner. High-efficiency sub-micrometer multi-beam interference structuring for large-scale surface using ultrashort laser pulses. *Journal of Laser Micro Nanoengineering*, 14(1):95–99, 2019.

[129] Daniel R Herlihy, Bruce F Hillard, and Timothy D Rulon. National oceanic and atmospheric administration sea beam system'patch test'. *The International Hydrographic Review*, 1989.

[130] Oddbjorn Bergem. Bathymetric navigation of autonomous underwater vehicles using a multibeam sonar and a kalman filter with relative measurement covariance matrices. 1993.

[131] Brian R Calder and Larry A Mayer. Robust automatic multi-beam bathymetric processing. 2001.

[132] Charu C Aggarwal. An introduction to outlier analysis. In *Outlier analysis*, pages 1–34. Springer, 2016.

[133] Md Mahabub Alam and Md Nuruzzaman. Comparative analysis of interpolation methods commonly used in bathymetric data generation. *World J. Adv. Res. Rev*, 25(3):2018–2029, 2025.

[134] Christopher J Amante and Barry W Eakins. Accuracy of interpolated bathymetry in digital elevation models. *Journal of Coastal Research*, (76):123–133, 2016.

[135] Didier Guériot, Julien Chèdru, Sylvie Daniel, and Eric Maillard. The patch test: a comprehensive calibration tool for multibeam echosounders. In *OCEANS 2000 MTS/IEEE Conference and Exhibition. Conference Proceedings (Cat. No. 00CH37158)*, volume 3, pages 1655–1661. IEEE, 2000.

[136] Thomas B Curtin, James G Bellingham, Josko Catipovic, and Doug Webb. Autonomous oceanographic sampling networks. *Oceanography*, 6(3):86–94, 1993.

[137] Justin E Manley. Development of the autonomous surface craft" aces". In *Oceans' 97. MTS/IEEE Conference Proceedings*, volume 2, pages 827–832. IEEE, 1997.

[138] Massimo Caccia. Autonomous surface craft: prototypes and basic research issues. In *2006 14th Mediterranean Conference on Control and Automation*, pages 1–6. IEEE, 2006.

[139] Michael R Benjamin, Henrik Schmidt, Paul M Newman, and John J Leonard. Nested autonomy for unmanned marine vehicles with moos-ivp. *Journal of Field Robotics*, 27(6):834–875, 2010.

[140] Les Elkins, Drew Sellers, and W Reynolds Monach. The autonomous maritime navigation (amn) project: Field tests, autonomous and cooperative behaviors, data fusion, sensors, and vehicles. *Journal of Field Robotics*, 27(6):790–818, 2010.

[141] Christopher Kitts, Paul Mahacek, Thomas Adamek, Ketan Rasal, Vincent Howard, Steve Li, Alexi Badaoui, William Kirkwood, Geoffrey Wheat, and Sam Hulme. Field operation of a robotic small waterplane area twin hull boat for shallow-water bathymetric characterization. *Journal of field Robotics*, 29(6):924–938, 2012.

[142] Alfredo Martins, Hugo Ferreira, Carlos Almeida, Hugo Silva, José Miguel Almeida, and Eduardo Silva. Roaz and roaz ii autonomous surface vehicle design and implementation. In *International lifesaving congress*, volume 2007, 2007.

[143] Jürgen Majohr, Thomas Buch, and Cathleen Korte. Navigation and automatic control of the measuring dolphin (messin™). *IFAC proceedings volumes*, 33(21):399–404, 2000.

[144] Massimo Caccia, Riccardo Bono, Gabriele Bruzzone, E Spirandelli, G Veruggio, AM Stortini, and G Capodaglio. Sampling sea surfaces with sesamo: an autonomous craft for the study of sea-air interactions. *IEEE robotics & automation magazine*, 12(3):95–105, 2005.

[145] J Alves, P Oliveira, Rodolfo Oliveira, A Pascoal, M Rufino, L Sebastiao, and C Silvestre. Vehicle and mission control of the delfim autonomous surface craft. In *2006 14th mediterranean conference on control and automation*, pages 1–6. IEEE, 2006.

[146] Dominik Iwen and Mariusz WĄż. Benefits of using asv mbes surveys in shallow waters and restriced areas. In *2019 European Navigation Conference (ENC)*, pages 1–3. IEEE, 2019.

[147] Giuseppe Stanghellini, Fabrizio Del Bianco, and Luca Gasperini. Openswap, an open architecture, low cost class of autonomous surface vehicles for geophysical surveys in the shallow water environment. *Remote Sensing*, 12(16):2575, 2020.

[148] Minas Spetsakis and John Yiannis Aloimonos. A multi-frame approach to visual motion perception. *International Journal of Computer Vision*, 6(3):245–255, 1991.

[149] Matthew J Westoby, James Brasington, Niel F Glasser, Michael J Hambrey, and Jennifer M Reynolds. 'structure-from-motion'photogrammetry: A low-cost, effective tool for geoscience applications. *Geomorphology*, 179:300–314, 2012.

[150] Mark A Fonstad, James T Dietrich, Brittany C Courville, Jennifer L Jensen, and Patrice E Carbonneau. Topographic structure from motion: a new development in photogrammetric measurement. *Earth surface processes and Landforms*, 38(4):421–430, 2013.

[151] Sunil Arya, David M Mount, Nathan S Netanyahu, Ruth Silverman, and Angela Y Wu. An optimal algorithm for approximate nearest neighbor searching fixed dimensions. *Journal of the ACM (JACM)*, 45(6):891–923, 1998.

[152] Richard Szeliski and Sing Bing Kang. Recovering 3d shape and motion from image streams using nonlinear least squares. *Journal of Visual Communication and Image Representation*, 5(1):10–28, 1994.

[153] Yasutaka Furukawa and Jean Ponce. Accurate, dense, and robust multiview stereopsis. *IEEE transactions on pattern analysis and machine intelligence*, 32(8):1362–1376, 2009.

[154] Yasutaka Furukawa. Clustering views for multi-view stereo. *http://grail. cs. washington. edu/software/cmvs*, 2010.

[155] Berthold KP Horn. Closed-form solution of absolute orientation using unit quaternions. *Journal of the optical society of America A*, 4(4):629–642, 1987.

[156] BeamworX. Autoclean, 2025. Accessed: 2025-11-04.

[157] Daniel Devote BASIL. Analysis of three selected automated multibeam bathymetric filters in beamworx autoclean software. *Nova Geodesia*, 5(2):335–335, 2025.

[158] Deltares. *Delft3D-WAVE Simulation of short-crested waves with SWAN. Delft, Deltares.* Deltares, 2025.

[159] N Booij, LH Holthuijsen, and RC Ris. The" swan" wave model for shallow water. In *Coastal engineering 1996*, pages 668–676. 1996.

[160] JC Dietrich, Marcel Zijlema, JJ Westerink, LH Holthuijsen, C Dawson, RA Luettich Jr, RE Jensen, JM Smith, GS Stelling, and GW Stone. Modeling hurricane waves and storm surge using integrally-coupled, scalable computations. *Coastal Engineering*, 58(1):45–65, 2011.

[161] Juan L Garzon and Celso M Ferreira. Storm surge modeling in large estuaries: Sensitivity analyses to parameters and physical processes in the chesapeake bay. *Journal of Marine Science and Engineering*, 4(3):45, 2016.

[162] Richard M Gorman and Cameron G Neilson. Modelling shallow water wave generation and transformation in an intertidal estuary. *Coastal Engineering*, 36(3):197–217, 1999.

[163] NRRC Booij, Roeland C Ris, and Leo H Holthuijsen. A third-generation wave model for coastal regions: 1. model description and validation. *Journal of geophysical research: Oceans*, 104(C4):7649–7666, 1999.

[164] RC Ris, LH Holthuijsen, and NJJoGRO Booij. A third-generation wave model for coastal regions: 2. verification. *Journal of Geophysical Research: Oceans*, 104(C4):7667–7681, 1999.

[165] Deepak Vatvani, NC Zweers, M Van Ormondt, AJ Smale, H De Vries, and VK Makin. Storm surge and wave simulations in the gulf of mexico using a consistent drag relation for atmospheric and storm surge models. *Natural Hazards and Earth System Sciences*, 12(7):2399–2410, 2012.

[166] Susanne Hasselmann, Klaus Hasselmann, JHm Allender, and TP Barnett. Computations and parameterizations of the nonlinear energy transfer in a gravity-wave spectrum. part ii: Parameterizations of the nonlinear energy transfer for application in wave models. *Journal of Physical Oceanography*, 15:1378–1391, 1985.

[167] Gerald Beresford Whitham. Linear and nonlinear waves(book). *New York, Wiley-Interscience, 1974. 651 p*, 1974.

[168] Chiang C Mei. *The applied dynamics of ocean surface waves*, volume 1. World scientific, 1989.

[169] MW Dingemans, AC Radder, and HJ De Vriend. Computation of the driving forces of wave-induced currents. *Coastal Engineering*, 11(5-6):539–563, 1987.

[170] Norman A Phillips. A coordinate system having some special advantages for numerical forecasting. *Journal of Atmospheric Sciences*, 14(2):184–185, 1957.

[171] John W Miles. On the generation of surface waves by shear flows. *Journal of Fluid Mechanics*, 3(2):185–204, 1957.

[172] GJ Komen, Susanne Hasselmann, and Klaus Hasselmann. On the existence of a fully developed wind-sea spectrum. *Journal of physical oceanography*, 14:1271–1285, 1984.

[173] André J van der Westhuysen, Marcel Zijlema, and Jurjen A Battjes. Nonlinear saturation-based whitecapping dissipation in swan for deep and shallow water. *Coastal Engineering*, 54(2):151–170, 2007.

[174] O Shemdin, Klaus Hasselmann, SV Hsiao, and Klaus Herterich. Nonlinear and linear bottom interaction effects in shallow water. In *Turbulent fluxes through the sea surface, wave dynamics, and prediction*, pages 347–372. Springer, 1978.

[175] Luciana Bertotti and Luigi Cavaleri. Accuracy of wind and wave evaluation in coastal regions. In *Coastal Engineering 1994*, pages 57–67. 1995.

[176] Klaus Hasselmann, Tim P Barnett, E Bouws, H Carlson, David E Cartwright, K Enke, JA Ewing, A Gienapp, DE Hasselmann, P Kruseman, et al. Measurements of wind-wave growth and swell decay during the joint north sea wave project (jonswap). *Ergaenzungsheft zur Deutschen Hydrographischen Zeitschrift, Reihe A*, 1973.

[177] Jurjen A Battjes and JPFM Janssen. Energy loss and set-up due to breaking of random waves. In *Coastal engineering 1978*, pages 569–587. 1978.

[178] Yasser Eldeberky. Parameterization of triad interaction in wave energy model. In *Proc. Coastal Dynamics Conf. Gdansk, Poland, 1995*, 1995.

[179] Dano Roelvink, Ad Reniers, AP Van Dongeren, Jaap Van Thiel De Vries, Robert McCall, and Jamie Lescinski. Modelling storm impacts on beaches, dunes and barrier islands. *Coastal engineering*, 56(11-12):1133–1152, 2009.

[180] van Dongeren Roelvink, AP Van Dongeren, Robert McCall, Bas Hoonhout, Arnold van Rooijen, Pieter van Geer, L De Vet, K Nederhoff, and E Quataert. Xbeach technical reference: Kingsday release. *Model. Desc. Func*, 77:125–184, 2015.

[181] D Roelvink, A Van Dongeren, R McCall, B Hoonhout, A Van Rooijen, P Van Geer, L De Vet, K Nederhoff, and E Quataert. Xbeach documentation: Release xbeach v1. 23.5527 xbeachx final. *Deltares: Delft, The Netherlands*, 2018.

[182] LH Holthuijsen, N Booij, and THC Herbers. A prediction model for stationary, short-crested waves in shallow water with ambient currents. *Coastal engineering*, 13(1):23–54, 1989.

[183] TE Baldock, P Holmes, S Bunker, and P Van Weert. Cross-shore hydrodynamics within an unsaturated surf zone. *Coastal Engineering*, 34(3-4):173–196, 1998.

[184] Christopher Daly, Dano Roelvink, Ap van Dongeren, Jaap van Thiel de Vries, and Robert McCall. Validation of an advective-deterministic approach to short wave breaking in a surf-beat model. *Coastal Engineering*, 60:69–83, 2012.

[185] Owen M Phillips. The dynamics of the upper ocean. *(No Title)*, 1977.

[186] DGandmcintyre Andrews and ME McIntyre. An exact theory of nonlinear waves on a lagrangian-mean flow. *Journal of fluid Mechanics*, 89(4):609–646, 1978.

[187] Marcel Zijlema, Guus Stelling, and Pieter Smit. Swash: An operational public domain code for simulating wave fields and rapidly varied flows in coastal waters. *Coastal Engineering*, 58(10):992–1012, 2011.

[188] Paul Wintersteller and Knut Hartmann. The european harmonised bathymetry grid emodnet bathymetry-introduction, outlook and contribution from german partners. 2020.

[189] Hilary F Stockdon, Rob A Holman, Peter A Howd, and Asbury H Sallenger Jr. Empirical parameterization of setup, swash, and runup. *Coastal engineering*, 53(7):573–588, 2006.

[190] Hilary F Stockdon, David M Thompson, Nathaniel G Plant, and Joseph W Long. Evaluation of wave runup predictions from numerical and parametric models. *Coastal Engineering*, 92:1–11, 2014.

[191] Michael S Longuet-Higgins and RW Stewart. Radiation stresses in water waves; a physical discussion, with applications. In *Deep sea research and oceanographic abstracts*, volume 11, pages 529–562. Elsevier, 1964.

[192] AJ Bowen, DL Inman, and VP Simmons. Wave 'set-down'and set-up. *Journal of geophysical research*, 73(8):2569–2577, 1968.

[193] Todd L Walton. Wave setup. *Handbook of Coastal and Ocean Engineering*, page 1, 2010.

[194] George Vosselman. Slope based filtering of laser altimetry data. *International archives of photogrammetry and remote sensing*, 33(B3/2; PART 3):935–942, 2000.

[195] Seungyong Lee, George Wolberg, and Sung Yong Shin. Scattered data interpolation with multilevel b-splines. *IEEE transactions on visualization and computer graphics*, 3(3):228–244, 1997.

[196] Richard Williams. Dems of difference. *Geomorphological techniques*, 2(3.2), 2012.

[197] Jessica D DeWitt and Francis X Ashland. Investigating geomorphic change using a structure from motion elevation model created from historical aerial imagery: A case study in northern lake michigan, usa. *ISPRS International Journal of Geo-Information*, 12(4):173, 2023.

[198] Maged Marghany. Dem reconstruction of coastal geomorphology from dinsar. In *International Conference on Computational Science and Its Applications*, pages 435–446. Springer, 2012.

[199] Olivier Burvingt, Bruno Castelle, Vincent Marieu, Bertrand Lubac, Alexandre Nicolae Lerma, and Nicolas Robin. Using pleiades satellite imagery to monitor multi-annual coastal dune morphological changes. *Remote Sensing*, 17(9):1522, 2025.

[200] P Hesp. Morphology, dynamics and internal stratification of some established foredunes in southeast australia. *Sedimentary geology*, 55(1-2):17–41, 1988.

[201] P Hesp. Foredunes and blowouts: initiation, geomorphology and dynamics. *Geomorphology*, 48(1-3):245–268, 2002.

[202] Ian J Walker, Jordan BR Eamer, and Ian B Darke. Assessing significant geomorphic changes and effectiveness of dynamic restoration in a coastal dune ecosystem. *Geomorphology*, 199:192–204, 2013.

[203] RWG Carter and Peter Wilson. Aeolian processes and deposits in northwest ireland. *Geological Society, London, Special Publications*, 72(1):173–190, 1993.

[204] José Carlos Muñoz-Reinoso. Doñana mobile dunes: what is the vegetation pattern telling us? *Journal of Coastal Conservation*, 22(4):605–614, 2018.

[205] RHF Curr, A Koh, E Edwards, AT Williams, and P Davies. Assessing anthropogenic impact on mediterranean sand dunes from aerial digital photography. *Journal of Coastal Conservation*, 6:15–22, 2000.

[206] Catherine Bressolier and Y-F Thomas. Studies on wind and plant interactions on french atlantic coastal dunes. *Journal of Sedimentary Research*, 47(1):331–338, 1977.

[207] R Silva, ML Martínez, I Odériz, E Mendoza, and RA Feagin. Response of vegetated dune–beach systems to storm conditions. *Coastal Engineering*, 109:53–62, 2016.

[208] Martin T Sykes and J Bastow Wilson. An experimental investigation into the response of some new zealand sand dune species to salt spray. *Annals of Botany*, 62(2):159–166, 1988.

[209] Henry J Oosting. Tolerance to salt spary of plants of coastal dunes. *Ecology*, 26(1):85–89, 1945.

[210] Daehyun Kim and Keun Bae Yu. A conceptual model of coastal dune ecology synthesizing spatial gradients of vegetation, soil, and geomorphology. *Plant Ecology*, 202:135–148, 2009.

[211] Orencio Durán and Laura J Moore. Vegetation controls on the maximum size of coastal dunes. *Proceedings of the National Academy of Sciences*, 110(43):17217–17222, 2013.

[212] Bill Coulloudon, Kris Eshelman, James Gianola, Ned Habich, Lee Hughes, Curt Johnson, Michael L Pellant, Paul Podborny, Allen Rasmussen, Ben Robles, et al. Sampling vegetation attributes: interagency technical reference. 1999.

[213] Lise Frederiksen, Johannes Kollmann, Peter Vestergaard, and Hans Henrik Bruun. A multivariate approach to plant community distribution in the coastal dune zonation of nw denmark. 2006.

[214] Lloyd W Morrison. Observer error in vegetation surveys: a review. *Journal of Plant Ecology*, 9(4):367–379, 2016.

[215] Yichun Xie, Zongyao Sha, and Mei Yu. Remote sensing imagery in vegetation mapping: a review. *Journal of plant ecology*, 1(1):9–23, 2008.

[216] Duo Chu and Duo Chu. Fractional vegetation cover. *Remote sensing of land use and land cover in mountain region: a comprehensive study at the central Tibetan Plateau*, pages 195–207, 2020.

[217] Compton J Tucker. Red and photographic infrared linear combinations for monitoring vegetation. *Remote sensing of Environment*, 8(2):127–150, 1979.

[218] CP Lo and Dale A Quattrochi. Land-use and land-cover change, urban heat island phenomenon, and health implications. *Photogrammetric Engineering & Remote Sensing*, 69(9):1053–1063, 2003.

[219] Raimundo Bermúdez and Rubén Retuerto. Living the difference: alternative functional designs in five perennial herbs coexisting in a coastal dune environment. *Functional Plant Biology*, 40(11):1187–1198, 2013.

[220] John Nay, Emily Burchfield, and Jonathan Gilligan. A machine-learning approach to forecasting remotely sensed vegetation health. *International journal of remote sensing*, 39(6):1800–1816, 2018.

[221] Arbab Mansoor Ahmad, Nasru Minallah, Nasir Ahmed, Arbab Masood Ahmad, and Nouman Fazal. Remote sensing based vegetation classification using machine learning algorithms. In *2019 International Conference on Advances in the Emerging Computing Technologies (AECT)*, pages 1–6. IEEE, 2020.

[222] Teja Kattenborn, Jens Leitloff, Felix Schiefer, and Stefan Hinz. Review on convolutional neural networks (cnn) in vegetation remote sensing. *ISPRS journal of photogrammetry and remote sensing*, 173:24–49, 2021.

[223] Ricardo Martínez Prentice, Miguel Villoslada Peciña, Raymond D Ward, Thaisa F Bergamo, Chris B Joyce, and Kalev Sepp. Machine learning classification and accuracy assessment from high-resolution images of coastal wetlands. *Remote Sensing*, 13(18):3669, 2021.

[224] Timothy G Whiteside, Guy S Boggs, and Stefan W Maier. Comparing object-based and pixel-based classifications for mapping savannas. *International Journal of Applied Earth Observation and Geoinformation*, 13(6):884–893, 2011.

[225] Tedros M Berhane, Charles R Lane, Qiusheng Wu, Oleg A Anenkhonov, Victor V Chepinoga, Bradley C Autrey, and Hongxing Liu. Comparing pixel- and object-based approaches in effectively classifying wetland-dominated landscapes. *Remote sensing*, 10(1):46, 2017.

[226] Sonia Silvestri, Marco Marani, and Alessandro Marani. Hyperspectral remote sensing of salt marsh vegetation, morphology and soil topography. *Physics and Chemistry of the Earth, Parts a/B/C*, 28(1-3):15–25, 2003.

[227] F Yousefi Lalimi, S Silvestri, LJ Moore, and M Marani. Coupled topographic and vegetation patterns in coastal dunes: Remote sensing observations and ecomorphodynamic implications. *Journal of Geophysical Research: Biogeosciences*, 122(1):119–130, 2017.

[228] Adrien Michez, Hervé Piégay, Jonathan Lisein, Hugues Claessens, and Philippe Lejeune. Classification of riparian forest species and health condition using multi-temporal and hyperspatial imagery from unmanned aerial system. *Environmental monitoring and assessment*, 188:1–19, 2016.

[229] Yifang Shi, Tiejun Wang, Andrew K Skidmore, and Marco Heurich. Improving lidar-based tree species mapping in central european mixed forests using multi-temporal digital aerial colour-infrared photographs. *International Journal of Applied Earth Observation and Geoinformation*, 84:101970, 2020.

[230] Elena Belcore, Marco Pittarello, Andrea Maria Lingua, and Michele Lonati. Mapping riparian habitats of natura 2000 network (91e0*, 3240) at individual tree level using uav multi-temporal and multi-spectral data. *Remote Sensing*, 13(9):1756, 2021.

[231] E. Belcore, M. Latella, M. Piras, and C. Camporeale. Enhancing precision in coastal dunes vegetation mapping: Ultra-high resolution hierarchical classification at the individual plant level. *Int. J. of Remote Sens.*, 45(13):4527–4552, 2024.

[232] Pedzisai Kowe, Onisimo Mutanga, John Odindi, and Timothy Dube. Exploring the spatial patterns of vegetation fragmentation using local spatial autocorrelation indices. *Journal of Applied Remote Sensing*, 13(2):024523–024523, 2019.

[233] Peter Haase. Spatial pattern analysis in ecology based on ripley's k-function: Introduction and methods of edge correction. *Journal of vegetation science*, 6(4):575–582, 1995.

[234] Raphaël Pélissier and François Goreaud. A practical approach to the study of spatial structure in simple cases of heterogeneous vegetation. *Journal of Vegetation Science*, 12(1):99–108, 2001.

[235] Philip M Dixon. Nearest-neighbor contingency table analysis of spatial segregation for several species. *Ecoscience*, 9(2):142–151, 2002.

[236] Ira A Hunt Jr. Design of seawalls and breakwaters. *Journal of the waterways and harbors division*, 85(3):123–152, 1959.

[237] Niklas Schandry and Claude Becker. Allelopathic plants: models for studying plant–interkingdom interactions. *Trends in plant science*, 25(2):176–185, 2020.

[238] NV Joshi, HS Suresh, HS Dattaraja, and R Sukumar. The spatial organization of plant communities in a deciduous forest: A computational-geometry-based analysis. *Journal of the Indian Institute of Science*, 77(4):365, 1997.

[239] Georges Matheron. Principles of geostatistics. *Economic geology*, 58(8):1246–1266, 1963.

[240] Yukio Sadahiro. Event pattern analysis: Peak detection and pattern comparison. *Geographical Analysis*, 56(1):143–162, 2024.

[241] P.J. Clark and F.C. Evans. Distance to nearest neighbor as a measure of spatial relationships in populations. *Ecology*, 35(4):445–453, 1954.

[242] BD Ripley. 198 1. spatial statistics, 1984.

[243] François Goreaud and Raphaël Pélissier. On explicit formulas of edge effect correction for ripley's k-function. *Journal of Vegetation Science*, 10(3):433–438, 1999.

[244] Julian Besag and Peter J Diggle. Simple monte carlo tests for spatial pattern. *Journal of the Royal Statistical Society Series C: Applied Statistics*, 26(3):327–333, 1977.

[245] Maria A Kiskowski, John F Hancock, and Anne K Kenworthy. On the use of ripley's k-function and its derivatives to analyze domain size. *Biophysical journal*, 97(4):1095–1103, 2009.

[246] Mari Myllymäki, Tomáš Mrkvička, Pavel Grabarnik, Henri Seijo, and Ute Hahn. Global envelope tests for spatial processes. *Journal of the Royal Statistical Society Series B: Statistical Methodology*, 79(2):381–404, 2017.

[247] Fernando T Maestre, Francisco Rodríguez, Susana Bautista, Jordi Cortina, and Juan Bellot. Spatial associations and patterns of perennial vegetation ina semi-arid steppe: a multivariate geostatistics approach. *Plant Ecology*, 179:133–147, 2005.

[248] Janusz Szmyt. Spatial structure of managed beech-dominated forest: applicability of nearest neighbors indices. *Dendrobiology*, 68, 2012.

[249] Alicia Teresa Rosario Acosta, Tommaso Jucker, Irene Prisco, and Riccardo Santoro. *Passive Recovery of Mediterranean Coastal Dunes Following Limitations to Human Trampling*, pages 187–198. Springer Berlin Heidelberg, 2013.

[250] Steven T. Brantley, Spencer N. Bissett, Donald R. Young, Catherine W. V. Wolner, and Laura J. Moore. Barrier Island Morphology and Sediment Characteristics Affect the Recovery of Dune Building Grasses following Storm-Induced Overwash. *PLoS ONE*, 9(8):e104747, aug 22 2014.

[251] Glenn M. Suir, Sam Jackson, Christina Saltus, and Molly Reif. Multi-Temporal Trend Analysis of Coastal Vegetation Using Metrics Derived from Hyperspectral and LiDAR Data. *Remote Sensing*, 15(8):2098, apr 16 2023.

[252] Susana Costas, Katerina Kombiadou, and Dano Roelvink. Exploring the role of vegetation and sediment supply to coastal dune states using integrated process-based modelling. *EGU General Assembly2. Online. https://doi. org/https://doi. org/10.5194/egusphere-egu2020-18568*, 2020.

[253] Selwyn S Heminway, Nicholas Cohn, Elizabeth H Davis, Andrew White, Christopher J Hein, and Julie C Zinnert. Exploring ecological, morphological, and environmental controls on coastal foredune evolution at annual scales using a process-based model. *Sustainability*, 16(8):3460, 2024.

[254] Guillaume Decocq. Determinism, chaos and stochasticity in plant community successions: consequences for phytosociology and conservation ecology. In *Nature Conservation: Concepts and Practice*, pages 254–266. Springer, 2006.

[255] Inger Elisabeth Måren, Jutta Kapfer, Per Arild Aarrestad, John-Arvid Grytnes, and Vigdis Vandvik. Changing contributions of stochastic and deterministic processes in community assembly over a successional gradient. *Ecology*, 99(1):148–157, 2018.

[256] Paolo Perona, P Molnar, M Savina, and Paolo Burlando. An observation-based stochastic model for sediment and vegetation dynamics in the floodplain of an alpine braided river. *Water Resources Research*, 45(9), 2009.

[257] Riccardo Vesipa, Carlo Camporeale, and Luca Ridolfi. Recovery times of riparian vegetation. *Water Resources Research*, 52(4):2934–2950, 2016.

[258] Kiran Adhithya Ramakrishnan and Orencio Duran Vinent. Modelling the Influence of Vegetation on the Stochastic Dynamics of Coastal Dunes. *Ecohydrology*, 18(1), 1 2025.

[259] Sergio Estrada-Villegas, Niv DeMalach, Miguel Martinez Ramos, Laura M Ladwig, Scott J Meiners, Leland K Werden, and Stefan A Schnitzer. Review of the symposium determinism and stochasticity in ecological succession in esa-louisville, 2019. *Bulletin of the Ecological Society of America*, 101(3):1–6, 2020.

[260] Carlo Camporeale and Melissa Latella. Stochastic dynamics of coastal dune vegetation. *Authorea Preprints*, 2024.

[261] B. Kang, R. A. Feagin, T. Huff, and O. Durán Vinent. Stochastic properties of coastal flooding events – part 2. *Earth Surf. Dynam.*, 12:105–115, 2024.

[262] Tobia Rinaldo, Kiran Adhithya Ramakrishnan, Ignacio Rodriguez-Iturbe, and Orencio Durán Vinent. Probabilistic structure of events controlling the after-storm recovery of coastal dunes. *Proceedings of the National Academy of Sciences*, 118(1):e2013254118, 2021.

[263] Harald Ulrik Sverdrup and Walter Heinrich Munk. *Wind, sea and swell: the theory of relations for forecasting*. Number 303. US Government Printing Office, 1952.

[264] L. Ridolfi, P. D'Odorico, and F. Laio. *Noise-Induced Phenomena in the Environmental Sciences*. Cambridge University Press, 2011.

[265] C Camporeale and Luca Ridolfi. Riparian vegetation distribution induced by river flow variability: A stochastic approach. *Water resources research*, 42(10), 2006.

[266] M Anwar Maun. *The biology of coastal sand dunes*. Oxford University Press, 2009.

[267] Orencio Duran Vinent and Laura J Moore. Vegetation controls on the maximum size of coastal dunes. *Proceedings of the National Academy of Sciences*, 110(43):17–217, 2013.

[268] F. Hengelund and E. Hansen. A monograph on sediment transport in alluvial streams. *Teknish Forlag, Technical Press, Copenhagen, Denmark*, page 62, 1967.

[269] K Kitahara, W Horsthemke, R Lefever, and Y Inaba. Exact results for a class of external coloured noise. *Progr. Theor. Phys*, 64:1233–1247, 1980.

[270] José M Sancho. External dichotomous noise: The problem of the mean-first-passage time. *Physical Review A*, 31(5):3523, 1985.

[271] Peter Hänggi and Peter Talkner. Memory index of first-passage time: a simple measure of non-markovian character. *Physical review letters*, 51(25):2242, 1983.

[272] Christian Van den Broeck and Peter Hänggi. Activation rates for nonlinear stochastic flows driven by non-gaussian noise. *Physical Review A*, 30(5):2730, 1984.

[273] Werner Horsthemke and René Lefever. *Noise-induced transitions in physics, chemistry, and biology*. Springer, 1984.

[274] Milton Abramowitz and Irene A Stegun. *Handbook of mathematical functions with formulas, graphs, and mathematical tables*, volume 55. US Government printing office, 1968.

[275] Antonius Henricus Maria Levelt. *Hypergeometric functions*. PhD thesis, Universiteit van Amsterdam, 1961.

[276] Davide Demichele, Elena Belcore, Marco Piras, and Carlo Camporeale. Species-by-species pattern analysis of coastal dune vegetation. *Journal of Geophysical Research: Biogeosciences*, 130(2):e2024JG008419, 2025.

[277] WH Van Der Putten and EH Kloosterman. Large-scale establishment of ammophila arenaria and quantitative assessment by remote sensing. *Journal of Coastal Research*, pages 1181–1194, 1991.

[278] Frances G Velvin and Darion R Embling. Sea spurge (euphorbia paralias): using plant development to inform the eradication programme in new zealand. *Nineteenth Australasian Weeds Conference*, 2014.

Appendix A

Previews of Orto-mosaics

Previews of orto-mosaics processed from UAV imagery.

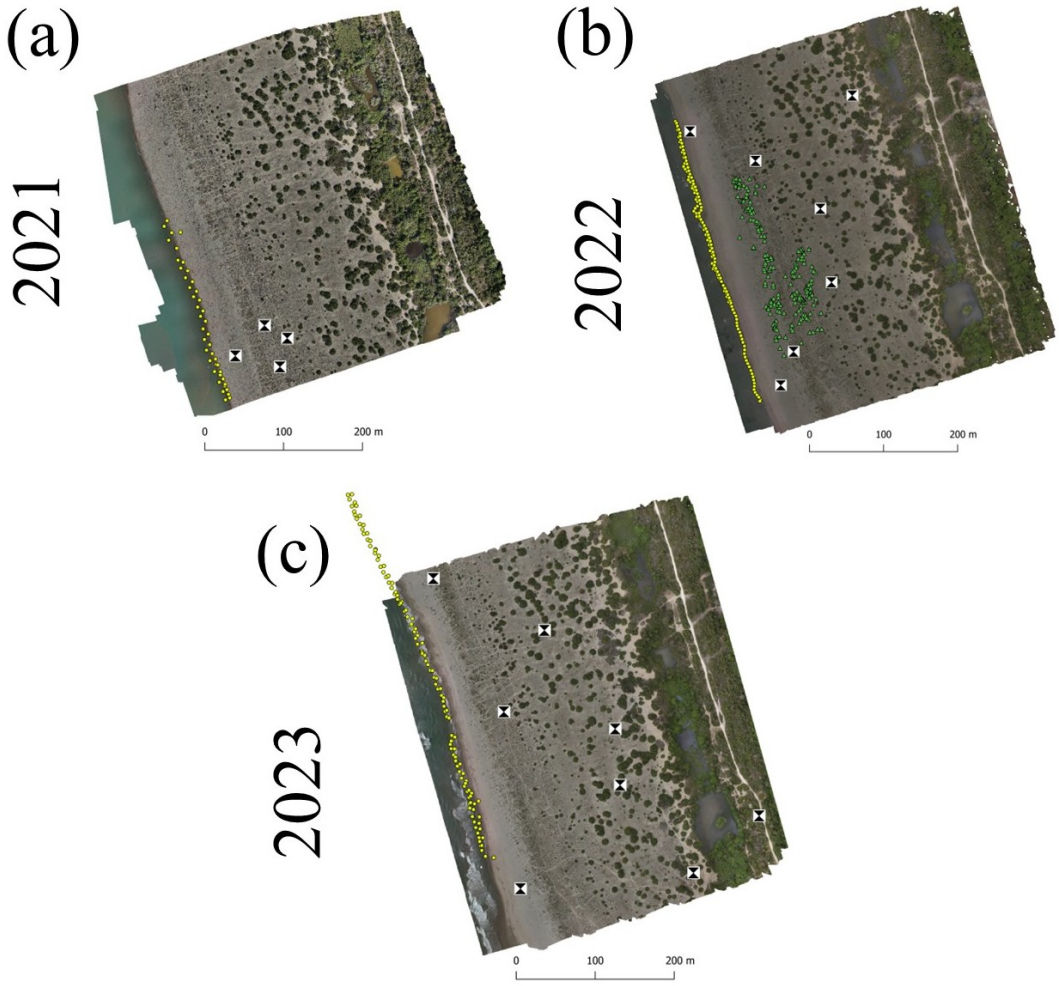

Fig. A.1 Orto-photos of A1 in (a) 2021, (b) 2022 and (c)2023. Are Highlighted the locations of manually measured points with GNSS antennas: GCPs (black-white squares), shallow-water bathymetry(yellow dots), plants sampled (green triangles).

Fig. A.2 Orto-photos of A2 in (a)2021, (b)2022, (c)2023, (d)2024, (e)2025 and (f) A2-bis in 2025. Are Highlighted the locations of manually measured points with GNSS antennas: GCPs (black-white squares), shallow-water bathymetry (yellow dots), plants sampled (green triangles).

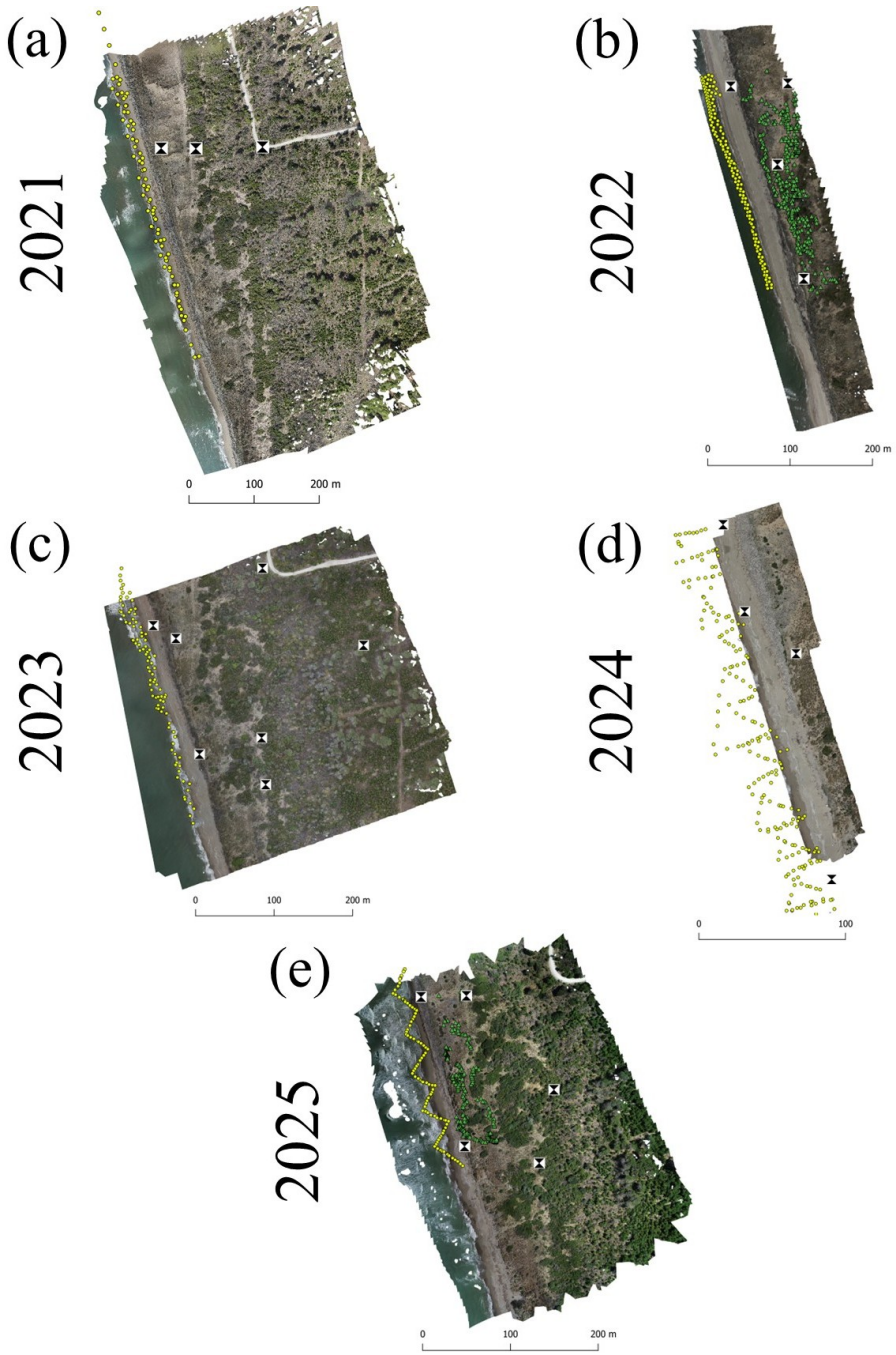

Fig. A.3 Orto-photos of A3 in (a)2021, (b) 2022, (c)2023, (d) 2024 and (e) 2025. Are Highlighted the locations of manually measured points with GNSS antennas: GCPs (black-white squares), shallow-water bathymetry (yellow dots), plants sampled (green triangles).

Appendix B

Previews of DEMs

Previews of DEMs processed from UAV imagery.

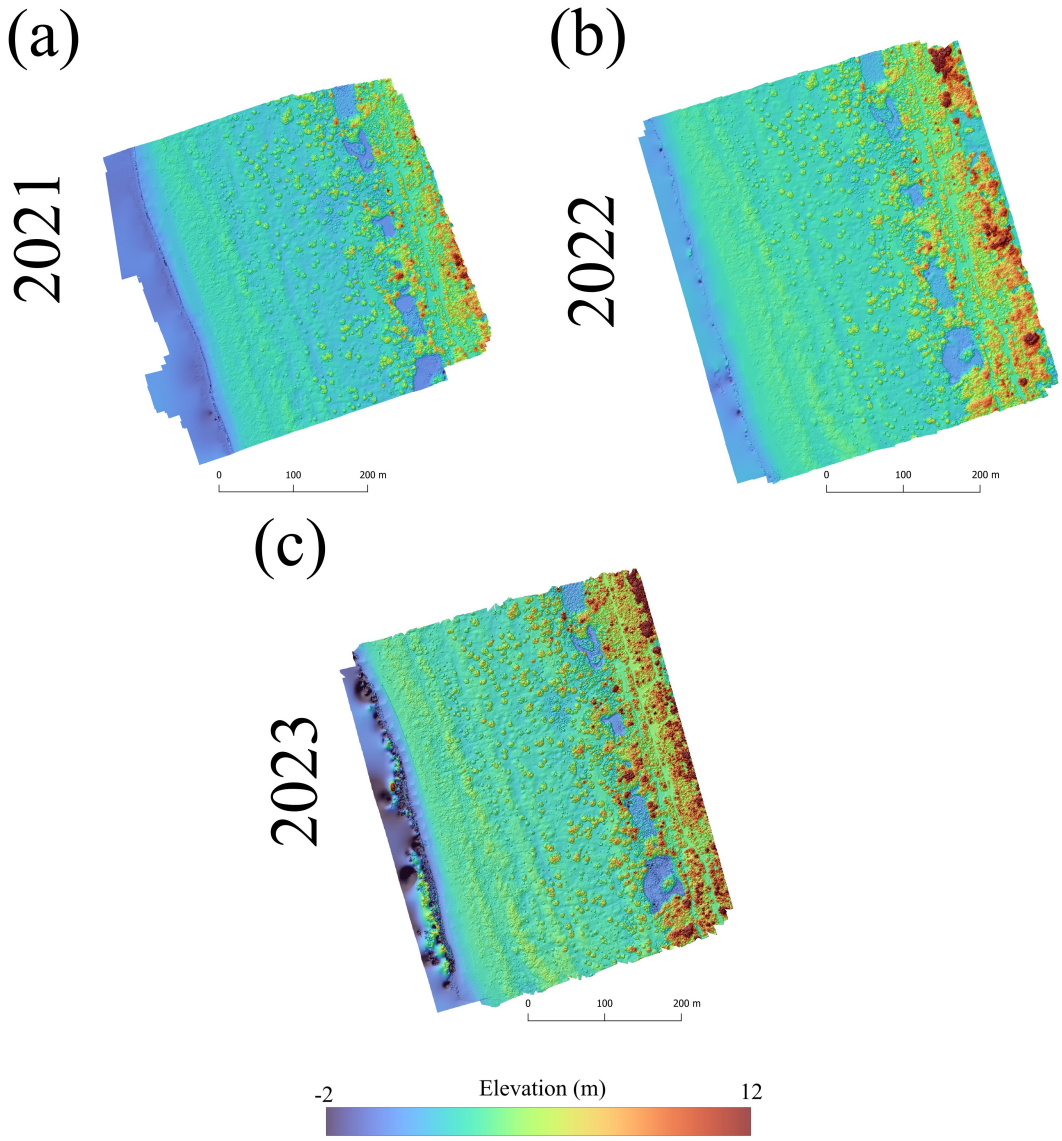

Fig. B.1 Digital Elevation Model of A1 in (a) 2021, (b) 2022 and (c) 2023.

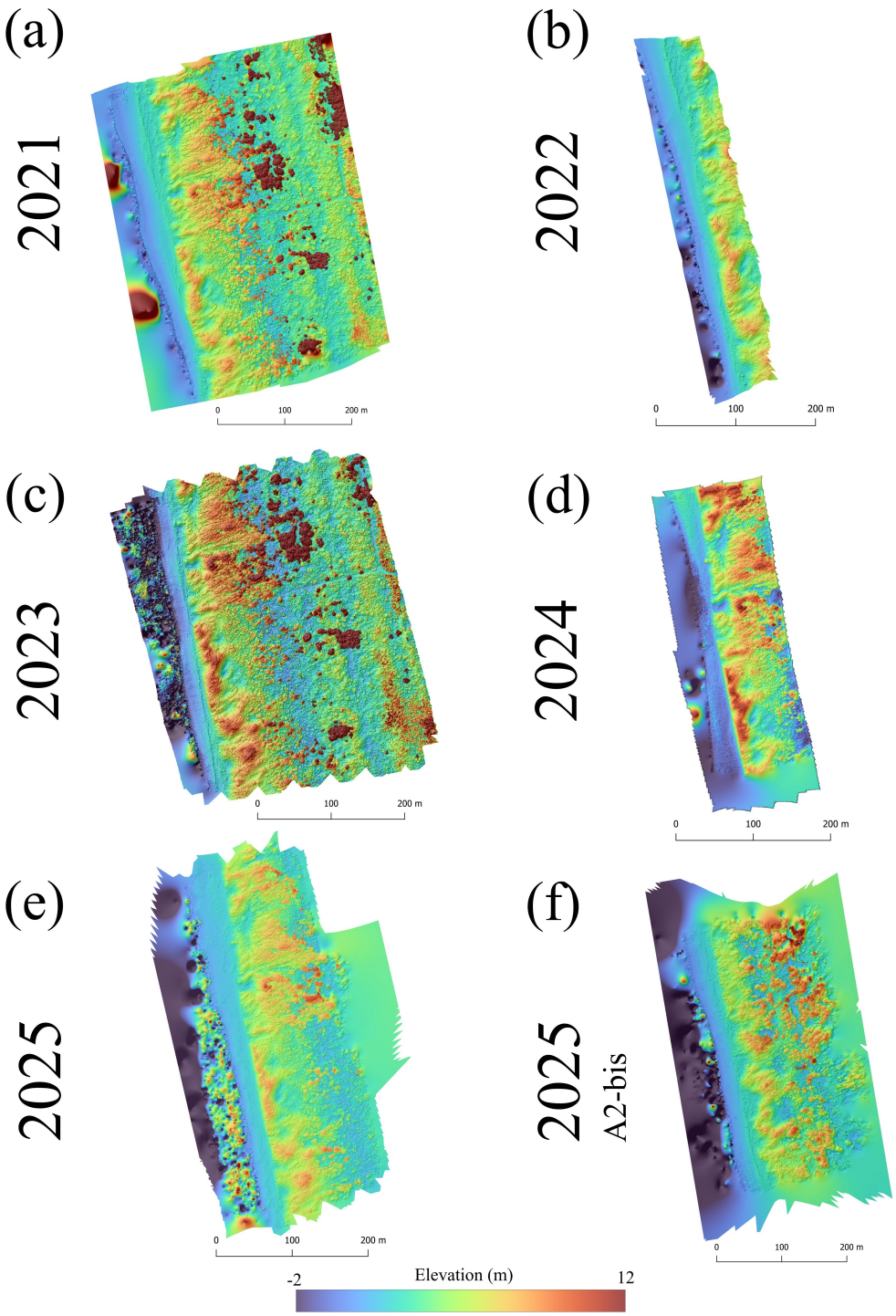

Fig. B.2 Digital Elevation Model of A2 in (a) 2021, (b) 2022 and (c) 2023. of A2 in (a) 2021, (b) 2022, (c) 2023, (d) 2024, (e) 2025 and (f) A2-bis in 2025.

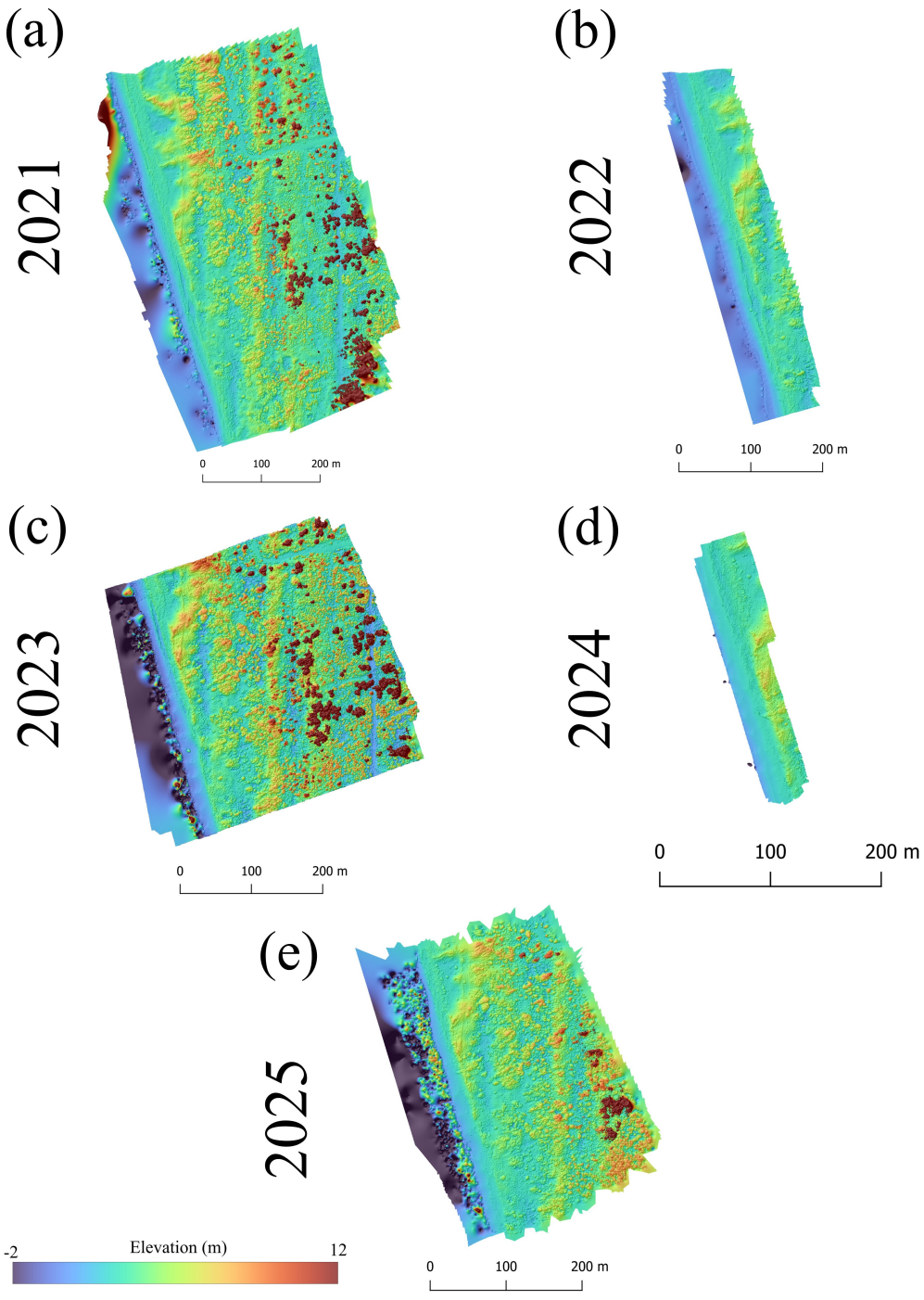

Fig. B.3 Digital Elevation Model of A3 in (a) 2021, (b) 2022 and (c) 2023. of A3 in (a) 2021, (b) 2022, (c) 2023, (d) 2024 and (e) 2025.

Appendix C

Previews of Bathymetries

Previews of Bathymetries processed from MBES surveys.

In the 2024 survey (Fig. C.2a), intermittent positioning emerged due to degraded GNSS signal quality and/or instability in the positioning solution, which resulted in reduced spatial reliability of the associated soundings.
As a consequence, the affected dataset exhibited inconsistencies in georeferencing that prevented a direct generation of a high-resolution bathymetry. To ensure the usability of the overall dataset, soundings acquired during periods of unreliable positioning were flagged and excluded from the primary high-resolution grid generation. The remaining points were subsequently interpolated.
It is important to note that, while the interpolated surface provides a continuous representation of the seabed morphology, the resolution and confidence level within the affected area are inherently lower than other surveys.

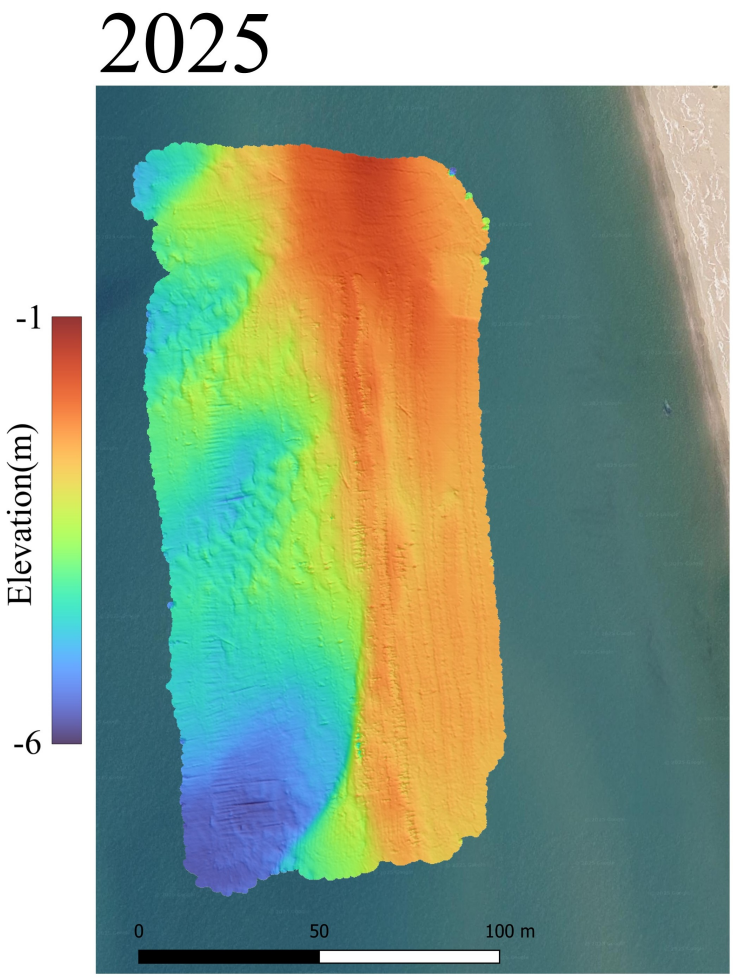

Fig. C.1 Near-shore bathymetry of A2-bis in 2025.

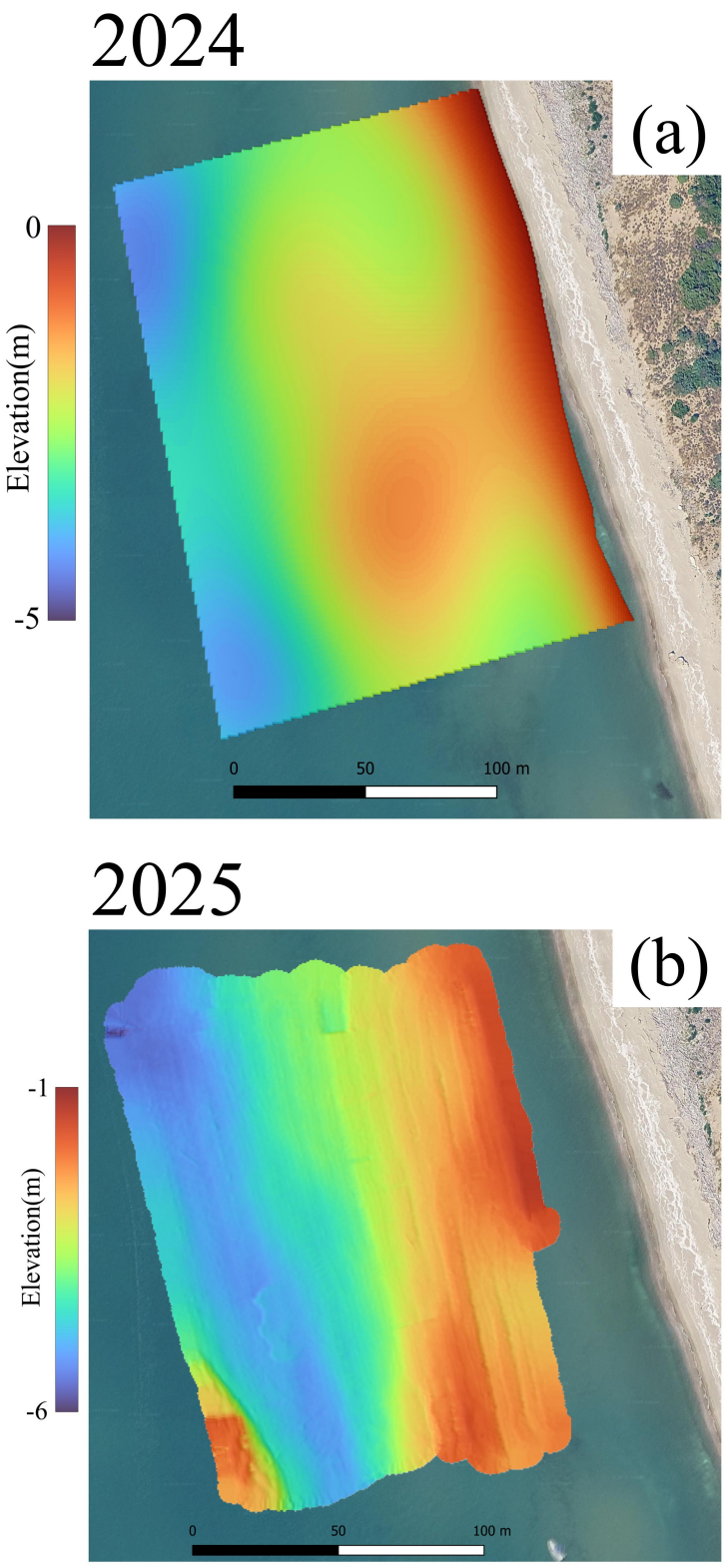

Fig. C.2 Near-shore bathymetry of A3 in (a) 2024 and (b)2025.

Appendix D

CL25 Model Functions

Gamma probability density function as theoretical wind-speed distribution

$$p_u = \frac{c_u^{-2q}}{\mu_u \Gamma_q} \left(\frac{u}{\mu_u} \right)^{q-1} e^{-\frac{uq}{\mu_u}} \tag{D.1}$$

Where μ_u and c_u are the wind-speed mean and coefficient of variation; $q = c_u^{-2}$; Γ_a is the Euler Gamma function.

Average time of F exceeding -or not exceeding- the threshold $F_{s|r}$

$$\langle t_{F>F_{s|r}} \rangle = \mathscr{I}_u e^{\hat{u}} E(1-q,\hat{u}), \qquad \langle t_{F<F_{s|r}} \rangle = \left(\frac{\Gamma_q}{\Gamma_{q,\hat{u}}} \right) \mathscr{I}_u e^{\hat{u}} E(1-q,\hat{u})$$

Where $\hat{u} = qu/\mu_u$; $E(a,z)$ is the exponential integral function and $\Gamma_{a,b}$ is the incomplete Gamma function.

Distribution of the Shield parameter over the dune profile

$$\Phi(X) = 1 + \frac{4\beta f}{\sqrt{\pi}} \{1 - 4(X-1)Da[2(X-1)]\} + \frac{f \tan\theta_0}{1+X^2} \left(\frac{X}{2} + \frac{\log X}{\pi} \right) \tag{D.2}$$

Where $Da[z]$ is the Dawson function.

Deposition/erosion rate factor

$$\alpha(\psi) = \mathscr{K} \left| \left\langle \frac{d\eta}{dt} \right\rangle \right| = \mathscr{K} \left| \frac{\Lambda \mathscr{G}(X,\psi)}{I(X)} - 1 \right| \frac{\langle F^{2n} \rangle}{I(X)} \tag{D.3}$$

Where $\mathscr{G} = \left(\frac{1+\Gamma\psi}{\Phi(X)}\right)^n$ and $I = \int_\Lambda^X e^{(\zeta-X)/\Lambda}\mathscr{G}(\zeta,\psi(\zeta))d\zeta$.

Slope correction functions for wave runup, g_r and critical Shields stress, g_s:

$$g_r(\theta_0) = 0.38 + \tan\theta_0\sqrt{0.172 + \frac{0.001}{\tan^2\theta_0}} \tag{D.4}$$

$$g_s(X) = \cos\left[\arctan\left(-\frac{d\eta}{dX}\right)\right]\left[1 + 1.67\arctan\left(-\frac{d\eta}{dX}\right)\right] \tag{D.5}$$